Design Rules for Multi-Electron Systems in Next-Generation Batteries: From Mg electrode-electrolyte interface to anion redox activation in Li-rich sulfides

Thesis by

Seong Shik (Steve) Kim

In Partial Fulfillment of the Requirements for the
Degree of
Doctor of Philosophy

CALIFORNIA INSTITUTE OF TECHNOLOGY
Pasadena, California

2023
Defended May 15th, 2023

ACKNOWLEDGEMENTS

My PhD journey would not have been possible without the support and love of those around me.

I would like to start my acknowledgements by thanking my advisor Kimberly See. She was always very patient and understanding with me and taught me the fundamentals of everything I know now. There are many memories I cherish, from individual meetings with La Croix in her office to learning lab skills directly from her and going on group camping trips. I really value the lessons I learned from Kim, especially about how to think like a scientist. I really appreciate how she gets excited as much as or even more than me when I show her exciting data. Kim always fosters a positive environment in the group. She has supported me to attend conferences and also to do an internship for four months. I couldn't have asked for a better advisor and I am very grateful to have had Kim as my advisor.

I would like to thank my committee members–Zhen-Gang Wang, John Brady, and Theo Agapie. I thank them for their decision and time to be on my committee and all the inputs along the way.

I am also very grateful to my undergraduate advisor Nga Lee (Sally) Ng. I took her Intro to Chemical Engineering class back in 2015, and I ended up joining her research group because I was interested in her aerosol research. She was the first person to show me what research is like. Sally was always passionate about science and taught me how fun and exciting conducting research and discovering new things were. Thank you for making me decide to pursue a PhD.

I thank all the scientists and collaborators that helped me with various measurements–David Velde for solution-phase NMR, Paul Oyala for EPR, Chi Ma for SEM and EPMA, and Sonjong Hwang for solid-state NMR. I am especially grateful to Sonjong; I first met him during my visit weekend, and he was always welcoming and helpful whenever I had trouble with the spectrometer. It was also a great pleasure TAing for him. I also thank David Agyeman-Budu for all the help with TXM and mail-in XAS data, and Qizhang for all the TEM images and discussions at the GRC.

Now, I would like to thank all the people in the See Group. I want to thank Andy for teaching me all the basics about solid-state chemistry and how thrilling running solid-state reactions and checking XRD patterns for the first time and seeing a single phase is. Sarah was my mentor during my first year and showed me to how to run

half-cells in the glovebox. I thank Charlie who was the only other chemical engineer in the group when I joined. My sincere thanks to the anion redox subgroup–Forrest, Xiaotong, Josh, Eshaan, Michelle, Colin, and now Nick and Tori also. Especially Josh and Eshaan, I'll always look back on our beamtime trips to SSRL very fondly. Thank you to Dan for sitting next to me and letting me ask him random questions. Thank you to the 5th years in the group Skyler and Zac who have been together since day 1. Special thank you to Colin for being my mentee and being so patient with me and all the great discussions we've had. I also thank the rest of the group for the positive group environment and all the fun activities we've done together.

I would like to thank people in my personal life. Being with these people made Pasadena feel like home. My former roommates Ethan and Connor, I appreciate all the moments I've shared with them. I want to thank Alessio, Leo, Zac, Olmo, and Katrina for all the weekend trips, beach days, and camping adventures over the years. I am truly grateful for Eleonore, who has always been so supportive and brought joy in my life. Thank you for always giving me things to laugh about and to look forward to.

Most importantly, I want to thank my family. My dad taught me how to enjoy life and prioritize physical and mental health. My mom always looked out for me and encouraged me. They have sacrificed so much for me and my siblings, and I want to let them know that I truly appreciate it. I am very grateful that my sister and brother-in-law Honey and Erik and also my cousin Silvia lived in LA while I was working on my PhD. It was always great to take a break from research and spend time with family. I also appreciate Caroline and Young's continuous support, and I'm grateful to have a niece and nephew!

ABSTRACT

Li-ion batteries (LIBs) have revolutionized the modern world, powering portable electronic devices and more recently realizing electrification of transportation. With more technological advancements that further improved the performance, LIBs also play an important role as one of the most promising energy storage systems in transforming into renewable energy sources and achieving net zero emissions. However, state-of-the-art intercalation-based LIBs are beginning to mature and reach their theoretical capacity limits. To further improve the electrochemical performance of batteries and meet growing demands of energy storage applications, there have been growing efforts to increase the energy density beyond the limits of conventional LIBs. In this thesis, we examine two examples of multi-electron systems–Mg electrolytes and Li-rich sulfide cathode materials–to gain insights and establish design principles.

First, we explore the magnesium aluminum chloride complex (MACC) electrolyte to study the role of the electrode-electrolyte interface in Mg charge transfer. We demonstrate that MACC electrolyte which normally requires electrolytic conditioning can be chemically activated by the small addition of $Mg(HMDS)_2$. Solution-phase characterization reveals that $Mg(HMDS)_2$ helps prevent the formation of passivating film on the Mg surface by scavenging trace amounts of H_2O. Mg(HMDS)2 also reacts with MACC to form free Cl^- which decorates the Mg surface which facilitates Mg electrodeposition and stripping.

Next, we investigate three different alkali-rich sulfides–$LiNaFeS_2$, $LiNaCoS_2$, and $Li_{1.33-1.33z}Ti_{0.67+0.33z}\square_zS_2$–to probe the role of electronic and physical structure in governing reversible anion redox. We demonstrate that cryomilling $LiNaFeS_2$ mitigates particle fracturing by increasing microstrain and reducing crystallite size. Isostructural $LiNaCoS_2$ exhibits more covalent interactions between the transition metal-*d* and S-*p* states compared to $LiNaFeS_2$, but undergoes an irreversible conversion reaction. Lastly, Li_2TiS_3 ($Li_{1.33}Ti_{0.67}S_2$) exhibits no electrochemical activity, but introducing cationic vacancies in $Li_{1.33-1.33z}Ti_{0.67+0.33z}\square_zS_2$ activates S oxidation. $Li_{1.33-1.33z}Ti_{0.67+0.33z}\square_zS_2$ is studied further to study first-cycle activation and voltage hysteresis in Li-rich sulfides.

PUBLISHED CONTENT AND CONTRIBUTIONS

(1) **Kim, S. S.**; et al. Enabling Anion Redox through Cation Vacancies in Li-rich Sulfide Materials.
Contributions: S.S.K. conceived, designed, and performed experiments, and wrote the manuscript. *manuscript submitted*.

(2) **Kim, S. S.**; et al. Origin of First-Cycle Activation and Voltage Hysteresis in Li-Rich Sulfide Materials.
Contributions: S.S.K. conceived, designed, and performed experiments, and wrote the manuscript. *manuscript in preparation*.

(3) **Kim, S. S.**; et al. Tuning Transition Metal-Anion Covalency and Controlling Redox Species in Li-Rich Sulfide Cathode Material by Transition Metal Substitution.
Contributions: S.S.K. conceived, designed, and performed experiments, and wrote the manuscript. *manuscript in preparation*.

(4) Iton, Z. W.; **Kim, S. S.**; Patheria, E. S.; Qian, M. D.; Ware, S. D.; See, K. A. In *Comprehensive Inorganic Chemistry III*; Elsevier: 2023, pp 308–363.
Contributions: S.S.K. participated in the conception of the project and in the writing of the sections 4.10.3.1.5 and 4.10.4. **DOI:**10.1016/B978-0-12-823144-9.00110-2.

(5) **Kim, S. S.**; Agyeman-Budu, D. N.; Zak, J. J.; Dawson, A.; Yan, Q.; Cában-Acevedo, M.; Wiaderek, K. M.; Yakovenko, A. A.; Yao, Y.; Irshad, A.; Narayan, S. R.; Luo, J.; Nelson Weker, J.; Tolbert, S. H.; See, K. A. Promoting Reversibility of Multielectron Redox in Alkali-Rich Sulfide Cathodes through Cryomilling. *Chem. Mater.* **2022**, 3236–3245,
Contributions: S.S.K. conceived, designed, and performed experiments, and wrote the manuscript. **DOI:**10.1021/acs.chemmater.2c00030.

(6) Zak, J. J.; **Kim, S. S.**; Laskowski, F. A. L.; See, K. A. An Exploration of Sulfur Redox in Lithium Battery Cathodes. *J. Am. Chem. Soc.* **2022**, *144*, 10119–10132,
Contributions: S.S.K. participated in the conception of the project and in the writing the manuscript. **DOI:**10.1021/jacs.2c02668.

(7) **Kim, S. S.**; See, K. A. Activating Magnesium Electrolytes through Chemical Generation of Free Chloride and Removal of Trace Water. *ACS Appl. Mater. Interfaces* **2021**, *13*, 671–680,
Contributions: S.S.K. conceived, designed, and performed experiments, and wrote the manuscript. **DOI:**10.1021/acsami.0c19053.

(8) Martinolich, A. J.; Zak, J. J.; Agyeman-Budu, D. N.; **Kim, S. S.**; Bashian, N. H.; Irshad, A.; Narayan, S. R.; Melot, B. C.; Nelson Weker, J.; See, K. A. Controlling Covalency and Anion Redox Potentials through Anion

Substitution in Li-Rich Chalcogenides. *Chem. Mater.* **2021**, *33*, 378–391,
Contributions: S.S.K. participated in the performance of the experiments and in writing the manuscript. **DOI:**10.1021/acs.chemmater.0c04164.

(9) **Kim, S. S.**; Bevilacqua, S. C.; See, K. A. Conditioning-Free Mg Electrolyte by the Minor Addition of $Mg(HMDS)_2$. *ACS Appl. Mater. Interfaces* **2020**, *12*, 5226–5233,
Contributions: S.S.K. conceived, designed, and performed experiments, and wrote the manuscript. **DOI:**10.1021/acsami.9b16710.

TABLE OF CONTENTS

LIST OF ILLUSTRATIONS

LIST OF TABLES

Chapter 1

INTRODUCTION

1.1 Background and Context

Evidence that the climate is changing is overwhelming.[1] Global average temperature has increased about 1.8 °F from 1901 to 2016.[2] Changes of one or two degrees in the average temperature of the planet can cause potentially dangerous shifts in climate and weather. The evidence consistently points to human activities, especially emissions of greenhouse or heat-trapping gases, as the dominant cause.[2,3] Many technologies have emerged to mitigate the greenhouse gas emissions such as carbon capture and storage/utilization, fuel switch and efficiency gains, and renewable energy sources.[4] One core component of achieving net zero emissions is energy storage.[5] Energy storage systems act as the basis in the transformation into renewable energy because they allow us to charge the energy storage systems when electricity is available from wind and solar, store it for future use, and discharge it to supply electricity. Various forms of energy storage systems have been developed in the past such as pumped storage hydropower, molten salt thermal systems, flywheels, and batteries.[6] Battery systems, specifically Li-ion batteries, are emerging as attractive candidates thanks to their high energy density and independence from geographic constraints.

Since their commercialization in 1991, Li-ion batteries (LIBs) have revolutionized the modern technological world.[7] In 2019, John B. Goodenough, M. Stanley Whittingham, and Akira Yoshino were awarded the Nobel Prize in Chemistry for their groundbreaking research on electrode materials that paved the way for the development of LIB materials. LIBs have powered portable electronic devices such as camcorders, laptops, and cellphones since their inception. Recent advancements in the battery technology enabled the electrification of transportation by storing energy and supplying power to electric vehicles.[7,8] Additionally, LIBs can serve as grid energy storage solutions to account for the intermittency of renewable energy sources as they have the potential to meet the requirements of frequency regulation, peak shaving, integration with renewable energy sources, and power management.[8]

1.2 Chemistry of the Li-ion Battery

Figure 1.1 illustrates the main components of LIBs. The voltage of the battery is determined by the chemical potential difference between the anode and cathode. This potential difference dictates the flow of electrons between electrodes during charge and discharge, creating an electric current that can be used to power devices. During discharge which is spontaneous, oxidation occurs at the anode causing electrons to flow through the circuit and mobile ions to travel through the electronically insulated electrolyte and separator. The cathode is reduced by gaining the electrons and mobile ions from the anode. In rechargeable or secondary batteries, the reverse process is performed with an external source of energy to charge the battery. The separator is a thin material that physically separates the anode and cathode and prevents them from coming into contact and causing a short circuit while allowing the movement of mobile ions. Lastly, the electrolyte is a substance that allows for the transport of mobile ions between the anode and cathode.

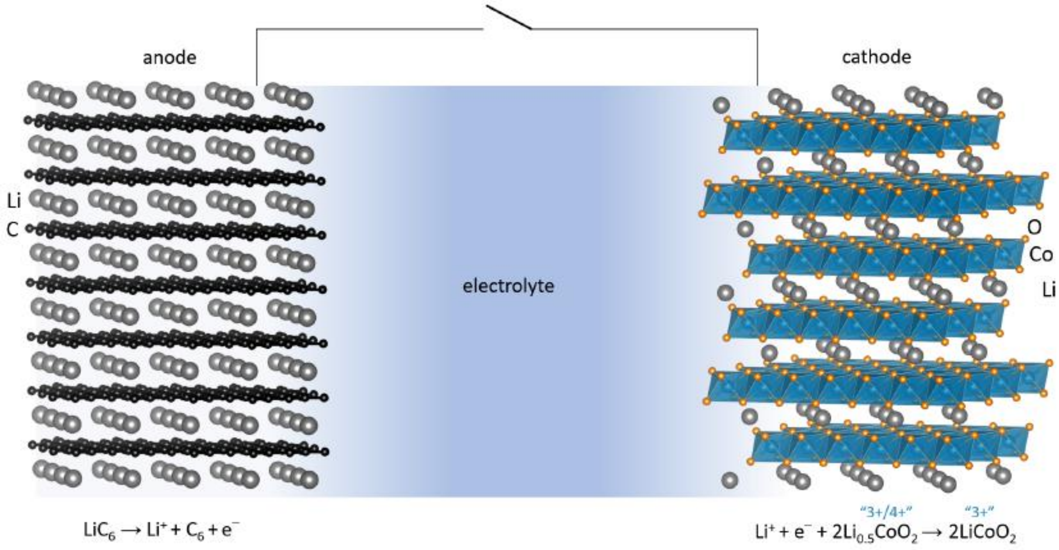

Figure 1.1: Depiction of the Li-ion battery. The original LIBs contain lithiated graphite (LiC_6) as the anode and lithiated CoO_2 as the cathode ($Li_{0.5}CoO_2$) at the fully charged state.

Of all elements, Li possesses exceptionally attractive properties owing to its small atomic weight, extremely low reduction potential (-3.04 V vs. NHE), and monovalent charge.[9] These features allow for high gravimetric capacity, constant high overall voltage, and high electronic and ionic conductivity. Thus, employing rechargeable batteries with Li metal anode has become the holy grail. However, the extreme electrode potential of Li metal also means high chemical and electrochemical reactivities.[9] Thus, first successful commercial batteries used graphite as the anode which acts as an intercalation host for Li. Graphite consists of layers of graphene sheets held together by van der Waals forces into which Li ions intercalate.[10] In fact, the term "Li-ion battery" gained its name to highlight the absence of pure Li metal within the host matrix of the electrode.[11] Using graphite as the host material was also appealing as the reduction potential is very close to that of Li metal (0.1 V vs. Li/Li^+), and lithiated graphite is less prone to dendrite formation. Therefore, although lithiated graphite delivered less gravimetric capacity of 372 mAh g^{-1} compared to that of Li metal (3856 mAh g^{-1}) because of the mass of the host matrix, lithiated graphite came to dominate as the anode material in commerical LIBs and has proven to be highly successful.

Layered structures with a host matrix dominated on the cathode side as well. Since the pioneering work of Whittingham that demonstrated reversible Li (de)intercalation in Li_xTiS_2 where $0 < x < 1$,[12] Li_xCoO_2 with $0.5 < x < 1$ was developed by Goodenough and proposed as the cathode material.[13] With O p states lying lower to Li/Li^+ couple compared to S p states, transition metal redox at higher voltages such as $Co^{3+/4+}$ can be accessed (Figure 1.2).[14] Charge compensation in $LiMO_2$ (M = a combination of transition metals) is attributed formally to transition metal redox during the (de)intercalation of Li. The first widely used intercalation–type cathode $LiCoO_2$ could only reversibly cycle 0.5 equivalents of Li before disrupting the parent phase and causing irreversible structural changes. Since then partial substitution of other metals such as Ni, Mn, and Al, has improved the structural stability at higher degrees of Li+ deintercalation and thus increased energy density of LIBs.[15–18] With decades of research and development, the experimental charge capacities of intercalation–type materials are maturing and reaching their theoretical limits.

To further improve the electrochemical performance of batteries and meet growing demands of energy storage applications, there have been increasing efforts to increase the energy density beyond the limits of conventional LIBs. One way is developing all solid-state batteries which allows for the utilization of Li metal as the anode and takes advantage of its voltage and capacity.[19] Other examples of "beyond Li-ion" batteries include Na-ion and K-ion batteries, conversion-type batteries such as Li-S, and multi-valent (Mg^{2+} and Ca^{2+}) systems.[20] The main focus of this thesis is to gain insights and establish design rules for multi-electron systems by examining two particular examples: Mg electrolytes and Li-rich cathodes.

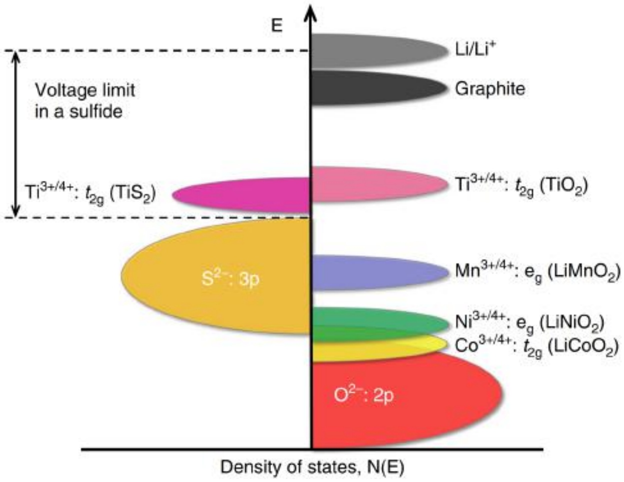

Figure 1.2: Schematic band structure of S and O p states and various transition metal d bands. Adapted from reference.[14]

1.3 Multi-Electron Systems in Next-Generation Batteries

Multi-electron systems benefit from the transfer of multiple (> 1) electrons per formula unit and can drastically increase the energy density of the material. There are many ways to achieve multi-electron storage. First, conversion-type materials such as Li-S systems and Si alloy anodes can reversibly store more than one electron per formula unit. Another example is utilizing multiple redox couples on the transition metal such as $Mn^{2+/4+}$ in $Li_2Mn_{2/3}Nb_{1/3}O_2F$ or $V^{3+/5+}$ in LiV_3O_8.[21,22] Another approach is the use of multi-valent ion such as Mg^{2+} as the charge carrier. Mg metal anode exhibits high theoretical volumetric and gravimetric specific capacities of 3833 mA h cm^{-3} and 2202 mA h g^{-1}, respectively, and its reduction potential is -2.37 V vs. NHE which is only 0.67 V higher than Li/Li^+ couple. Mg is also highly abundant in the Earth's crust, making it a cost-effective anode material. However, multi-valent ions carry high charge density which poses challenges on charge transfer and ion transport. Therefore, the importance of the electrode-electrolyte interface will be explored in Chapters 2 and 3.

The rest of the thesis will focus on a different type of multi-electron storage, anion redox in Li-rich cathode materials. While conventional $LiMO_2$-type cathode materials rely solely on the transition metal redox for charge compensation, incorporating redox activity of lattice anions can lead to higher energy density. In Chapters 4-7, different alkali-rich cathode materials will be explored to investigate the role of microstrain, transition metal-anion covalency, cation vacancies, and different kinetics between transition metal and anion, in governing reversible anion redox.

1.4 Thesis Overview

Chapter 2 focuses on the effect of the electrode-electrolyte interface on Mg electrodeposition by visiting an electrolyte called the magnesium aluminum chloride complex (MACC). While MACC requires electrolytic conditioning process before supporting reversible deposition and stripping, adding small amounts of $Mg(HMDS)_2$ to MACC improves the electrochemical performance without conditioning. The changes in electrochemical performance is discussed.

Chapter 3 expands on Chapter 2 and examines solution-phase speciation in MACC + $Mg(HMDS)_2$ electrolyte with Raman spectroscopy, ^{27}Al NMR spectroscopy, and ^{1}H-^{29}Si HMBC 2D NMR. The changes in solution-phase speciation and the subsequent changes on the electrode-electrolyte interface are discussed.

Chapter 4 explores alkali-rich material $LiNaFeS_2$ and investigates the cause of its rapid capacity fade compared to isostructural material Li_2FeS_2. Synchrotron-based transmission X-ray microscopy reveals that $LiNaFeS_2$ undergoes particle fracturing. To mitigate particle fracturing, $LiNaFeS_2$ is cryomilled to introduce defects and reduce particle size, and the effects are cryomilling are examined.

Chapter 5 builds on Chapter 4 and examines an isostructural alkali-rich material $LiNaCoS_2$. By introducing transition metal substitution, the role of transition metal-anion covalency is explored. While $LiNaCoS_2$ exhibits multi-electron capacity of ≥ 1.7 electrons per formula unit, it suffers from rapid capacity fade. The charge compensation and charge/discharge products are analyzed.

Chapter 6 focuses on the fundamental prerequisite for persulfide $(S_2)^{2-}$ formation in Li-rich sulfide materials. The negative control Li_2TiS_3 does not exhibit any meaningful electrochemical activity due to the d^0 electron configuration of Ti^{4+}. Introducing cationic vacancies in the structure via solid-state synthesis while maintaining the oxidation state of Ti activates S oxidation. The presence of cationic vacancies is confirmed with characterization techniques, and the charge compensation is examined.

Chapter 7 uses the same material as in Chapter 6 as a model system to study first-cycle activation and hysteresis in Li-rich sulfide materials. The asymmetry between cycle 1 charge and discharge curves are probed, and characterization techniques indicate that Ti^{4+} is overreduced and S is not completely reduced back to S^{2-}. It is also shown that heat treatment of cycled cell recovers the thermodynamic phase.

Chapter 8 provides a concise summary of these investigations and offers a perspective based on newly found results and insights.

Chapter 2

CONDITIONING-FREE MG ELECTROLYTE BY THE MINOR ADDITION OF MG(HMDS)$_2$

This chapter has been adapted from:

(1) **Kim, S. S.**; Bevilacqua, S. C.; See, K. A. Conditioning-Free Mg Electrolyte by the Minor Addition of Mg(HMDS) $_2$. *ACS Appl. Mater. Interfaces* **2020**, *12*, 5226–5233,

Contributions: S.S.K. conceived, designed, and performed experiments, and wrote the manuscript. **DOI:**10.1021/acsami.9b16710

2.1 Abstract

Mg-based batteries are an attractive next-generation energy storage chemistry due to the high natural abundance and inexpensive cost of Mg along with the high theoretical energy density compared to conventional Li-ion chemistry. The greater energy density is predicated on a Mg metal anode and pathways to achieving reversible Mg electrodeposition and stripping are reliant on the development of Mg electrolytes. Although Mg electrolyte chemistry has advanced significantly from the reactive Grignards of the 1920's to the carboranes of this decade, there remains significant challenges in correlating the Mg metal anode electrochemistry with the composition of the electrolyte salts due to the complicated interface of Mg metal and the electrolyte. To probe the effect of the interface on Mg electrodeposition, we turn to an electrolyte with a known solution phase composition: the magnesium aluminum chloride complex (MACC) electrolyte. The MACC electrolyte, however, requires electrolytic conditioning to support reversible Mg electrodeposition and stripping. Here, we show that a small concentration (2-5 mM) of Mg(HMDS)$_2$ to the MACC electrolyte suppresses Al^{3+} deposition and promotes reversible Mg electrodeposition and stripping on the first cycle. The significant effect of a small concentration of additive is attributed to changes to the electrode interface. The impact of the Mg interface on the observed electrochemical performance is discussed.

2.2 Introduction

Since its commercialization in 1991, the Li-ion battery has comfortably dominated the rechargeable battery market.[23] Conventional Li-ion batteries consist of a graphite anode and $LiCoO_2$, or other metal oxide, cathode in which Li ions are reversibly intercalated as charge carriers. The capacity of intercalation chemistry is intrinsically limited by the concentration of Li in the material and the reversibility of redox on the transition metals. Intercalation chemistry therefore has low energy density due to the volume and mass imposed by electrochemically inactive atoms. In addition, the scarcity of Li and Co makes Li-ion batteries costly and raises questions in regards to sustainability. Overcoming issues with Li-ion batteries requires next-generation chemistries with improved performance, cost, safety, and sustainability.

Mg-based batteries are promising alternatives that can theoretically meet the growing demands of energy storage.[24] Mg metal anodes offer higher theoretical volumetric and gravimetric specific capacities (3833 mAh cm^{-3} and 2202 mAh g^{-1}) compared to Li intercalated graphite anodes (719 mAh cm^{-3} and 339 mAh g^{-1}). Additionally, the high natural abundance of Mg in the Earth's crust makes it more economically appealing over other next-generation anode materials such as Li metal. The slightly less energetic standard reduction potential of Mg (-2.37 V vs. SHE) could offer stability and safety compared to Li metal (-3.05 V vs. SHE).[25] Additionally, the morphology of electrodeposited Mg metal is much smoother than those of Li metal, which deposits in a mossy morphology when deposited at the same current densities.[26] The head-to-head comparison suggests that Mg metal systems can accommodate higher current densities compared to Li metal, although the limitations of Mg metal anodes are currently in question[27] and need detailed study.

To realize effective Mg-metal batteries, electrolytes that solubilize and transport Mg^{2+}, remain inert at electrode interfaces, and allow for reversible desolvation at both the anode and cathode are needed. The electrolyte chemistry is directly responsible for defining the reversibility and efficiency of Mg electrodeposition and stripping at the Mg metal battery anode. The earliest electrolytes shown to support reversible Mg electrodeposition and stripping were demonstrated in the 1920s and 1930s with Grignards as such as PhMgBr and BnMgCl in tetrahydrofuran (THF)[28] and EtMgI in ether.[29] The anodic stability window of Grignard electrolytes was quickly identified as a limitation.[30] Additional issues with Grignards include low conductivity and reactivity with cell components and potential cathodes.[31]

In the 1990s, the anodic stability window was extended by reacting Grignards with Lewis acids like $AlCl_3$.[32] The so-called "organohaloaluminates" thus became the primary subject of study and were featured in the first prototype Mg battery chemistry by Aurbach and coworkers in which $Mg(AlCl_2BuEt)_2$ in THF was used as an electrolyte to demonstrate reversible Mg intercalation in the now canonical Chevrel cathode, Mo_6S_8.[33] Another notable organohaloaluminate is the "all-phenyl-complex," or APC, formed by reaction of PhMgCl with $AlCl_3$ in THF.[34] APC supports 100% Coulombic efficiency with >3 V anodic stability.[34]

Electrolytes that do not require Grignards in their preparation are now targeted to reach high anodic stability and good compatibility with candidate electrode materials. The first example of an inorganic salt supporting electrolyte was magnesium borohydride ($Mg(BH_4)_2$) in DME and THF.[35] Analogous to the lithium hexafluorophosphate salts used in Li-ion electrolytes, magnesium hexafluorophosphate, $Mg(PF_6)_2$ has also been explored.[36] $Mg(PF_6)_2$ boasts good anodic stability but poor Coulombic efficiency[36] likely due to instability of the anion at the Mg metal electrode.[32,37] Magnesium trifluorosulfonylimide (TFSI, $N[SO_2CF_3]_2{}^-$) has been reported in dimethoxyethane (DME) + digylme (G2) but exhibits high stripping overpotentials.[38] Theory has suggested that the $Mg(TFSI)_2$ is unstable during reduction.[39] Weakly coordinating anions such *closo*-carboranes[40] and monocarboranes[41] have shown very promising electrochemistry at the Mg electrode. The magnesium monocarborane ($CB_{11}H_{12}^-$) shows high anodic stability of >3.8 V (vs. Mg/Mg^{2+}) with Coulombic efficiencies of 99%.[41] Other boron-containing anions include tris(hexafluoroisopropyl)borate (HFP: $OC(H)(CF_3)_2{}^-$),[42–44] tris(3,5-dimethylphenyl)borane,[45] and tris(2H-hexafluoroisopropyl)borate.[46–48]

Magnesium hexamethyldisilizide (HMDS, $N[Si(CH_3)_3]_2{}^-$) has been explored in Mg electrolytes due to its non-nucleophilicity which prevents unwanted reaction with possible cathode materials such as sulfur. Liebenow et al. reported HMDSMgCl in THF as the first $HMDS^-$–containing electrolyte system that demonstrated reversible deposition/stripping of Mg in 2000.[49] The current density and anodic stability was improved by adding Lewis acid $AlCl_3$ at an optimal ratio of 3:1 HMDSMgCl:$AlCl_3$.[50] The products of the reaction between HMDSMgCl and $AlCl_3$ are identified as $[Mg_2(\mu{-}Cl)_3 \cdot 6\,(THF)]^+[HMDSAlCl_3]^-$ by single-crystal X-ray diffraction of the crystallized electrolyte.[50] Further improvement to the Mg electrodeposition and stripping metrics were achieved by replacing MgHMDSCl with $Mg(HMDS)_2$ at an optimized ratio of 1:2 to yield an electrolyte that exhibits a high anodic stability of 3.5 V (vs. Mg/Mg^{2+}) and a high Coulombic efficiency (98 %).[51] Single-crystal X-ray diffraction revealed the same active species, $[Mg_2(\mu{-}Cl)_3 \cdot 6\,(THF)]^+[HMDSAlCl_3]^-$, and additional chemical analysis by mass spectroscopy of the mother liquor after crystallization suggested the presence of $AlCl_2HMDS$.[51] $MgCl_2$ was then introduced to react with $AlCl_2HMDS$ to increase the concentrations of the active species via a transmetalation reaction $2\,MgCl_2 + R_xAlCl_{3\text{-}x} \longrightarrow [Mg_2Cl_3]^+[R_xAlCl_{4\text{-}x}]^-$, and the resulting electrolyte – 1:2:1 $MgCl_2$:$AlCl_3$:$MgHMDS_2$ – exhibited superior reversible Mg deposition/stripping in G4.[52,53] Merrill et al. reported a $Mg(HMDS)_2$–$2AlCl_3$ electrolyte in G4 that results in different speciation, as the chelating effect of the bulkier solvent molecules causes the dissociation of $AlCl_3$ into $AlCl_4{}^-$ and $AlCl_2{}^+$, and the binuclear magnesium complex to no longer exist.[54] Aurbach and coworkers identified cationic $AlCl_2{}^+$ and $HMDSAlCl^+$ as undesirable species that reduce the performance of the electrolyte and proposed that in G4, 1:2:1 $MgCl_2$:$AlCl_3$:$Mg(HMDS)_2$ exhibits higher Coulombic efficiencies and lower overpotential than 1:2 $Mg(HMDS)_2$:$AlCl_3$ because the excess $MgCl_2$ prevents the formation of cationic Al species.[55] Liao et al. presented a similar electrolyte system based on $Mg(HMDS)_2$ and free of Al by utilizing the reverse Schlenk equilibrium $Mg(HMDS)_2 + MgCl_2 \rightleftharpoons 2\,(HMDS)MgCl$, yielding $[Mg_2(\mu{-}Cl)_3 \cdot 6\,(THF)]^+[(HMDS)MgCl_2]^-$ as the final products.[56] The optimized 1:4 $Mg(HMDS)_2$:$MgCl_2$ electrolyte in THF has an anodic stability of up to 2.8 V and Coulombic efficiency of 99%.[56] The 1:4 $Mg(HMDS)_2$:$MgCl_2$ electrolyte does not exhibit effective Mg stripping/deposition in THF/glyme mixtures, but shows a Coulombic efficiency of 92 % in 1:1 THF:butyl sulfone.[56,57]

The magnesium aluminum chloride complex (MACC) electrolyte is an additional, relatively simple non-Grignard electrolyte and is the subject of this study. MACC is prepared by dissolving commercially available salts $MgCl_2$ and $AlCl_3$ in THF resulting in a Lewis acid-base reaction to yield:[25]

$$AlCl_3 + 2\,MgCl_2 + 6\,THF \longrightarrow AlCl_4{}^- + [Mg_2(\mu{-}Cl)_3 \cdot 6\,(THF)]^+. \tag{2.1}$$

The MACC electrolyte requires electrolytic conditioning before it supports reversible Mg electrodeposition and stripping.[58] During electrolytic conditioning, $AlCl_4{}^-$ is irreversibly deposited at the working electrode, resulting in the oxidation of Mg at the counter electrode and formation of free Cl^-:[59]

$$4\,AlCl_4^- + 6\,Mg_{(s)} \longrightarrow Al_{(s)} + 3\,[Mg_2(\mu{-}Cl)_3 \cdot 6\,(THF)]^+ + 7\,Cl^-. \tag{2.2}$$

Once conditioned, MACC achieves high Coulombic efficiencies (>99%), good anodic stability (approx. 3 V vs. Mg/Mg^{2+}), and a low deposition overpotential of approx. 150 mV.[25,58–60] The deposition overpotential can be further decreased by increasing the concentration of the salts.[61] MACC is most commonly prepared in THF, but reversible Mg deposition and stripping has also been reported in DME,[25,58] G2,[62] 1,3-dioxolane (DOL) and DME,[63] and tetraglyme and DOL.[63]

Ideally, the electrolyte should support electrodeposition and stripping as-prepared without the need to condition. To this end, routes to conditioning-free MACC have been reported in which chemical reducing agents are introduced that mimic the electrochemical conditioning reaction. For example, addition of $Mg_{(s)}$ to $CrCl_3$ + $AlCl_3$ solutions[64] and $Mg_{(s)}$ to MACC[62] result in electrolytes that support Mg electrodeposition and stripping on the first cycle. Interestingly, addition of 30 mM $Mg(TFSI)_2$ to MACC (at 60 mM $MgCl_2$) also results in higher Coulombic efficiency over the first 50 cycles but Al plating is still observed during the first cycles.[65]

We hypothesize that the addition of an anion capable of displacing Cl^- in ${AlCl_4}^-$ can cause the production of solvated Cl^- in solution and activate the MACC electrolyte. Assuming the effect of Cl^- is regulated to the interface as hypothesized previously,[59,66,67] only small concentrations of anion would be needed. Here, we add small concentrations of magnesium hexamethyldisilazide ($HMDS^-$: $N[Si(CH_3)_3]_2{}^-$) to the MACC electrolyte. $Mg(HMDS)_2$ does not introduce new cations to the electrolyte, is electrochemically stable over a wide potential window,[49] and has been shown to displace Cl^- in $AlCl_3$.[52] Addition of (HMDS)MgCl to $AlCl_3$ solutions results in transmetallation to form $[AlCl_{3-x}(HMDS)_x]^-$ by the following suggested reaction:[50]

$$Mg(HMDS)Cl + AlCl_3 \longrightarrow MgCl^+ + Al(HMDS){Cl_3}^- . \qquad (2.3)$$

The Al species in the MACC electrolyte, however, are mostly $AlCl_4^-$. Reaction of $Mg(HMDS)_2$ with $AlCl_4^-$ could result in the formation of free Cl^-. Here we show that upon addition of only 2 mM $Mg(HMDS)_2$, the electrolyte supports Mg electrodeposition and stripping on the first cycle with greatly suppressed Al^{3+} reduction. Because of the low concentration of $Mg(HMDS)_2$ required to affect such significant changes in the electrochemistry, we infer that the effect must be interface-related. Future work will involve detailed characterization of the species in solution to determine the mechanism of performance enhancement upon $Mg(HMDS)_2$ addition.

2.3 Experimental Section

Electrolyte Preparation

The MACC electrolyte was prepared in an Ar-filled glovebox according to the procedure outlined in Barile et al.[58] Anhydrous tetrahydrofuran (THF, Fisher Scientific) was dried on a solvent purification system and brought into the glovebox without exposure to air. The water content of THF measured by Karl Fischer titration was 22 ppm. Anhydrous $AlCl_3$ (99.999%, Sigma–Aldrich), anhydrous $MgCl_2$ (99.9%, Fisher Scientific), and $Mg(HMDS)_2$ (97%, Sigma–Aldrich) were opened in the glovebox. The MACC electrolyte was prepared at 30 mM $AlCl_3$ and 60 mM $MgCl_2$. MACC in THF was prepared by cooling 2.5 mL of THF and $AlCl_3$ (0.020 g) in separate vials with a Peltier plate (approx. 0°C). Cold THF was added dropwise to $AlCl_3$ and agitated to yield a clear, colorless solution. $MgCl_2$ (0.0286 g) was added to 2.5 mL room temperature THF. The $AlCl_3$ solution was added dropwise to the $MgCl_2$ suspension while stirring, and the solution was allowed to stir for at least 6 h to yield a clear, colorless solution. 2 mL of the as-prepared MACC was added to $Mg(HMDS)_2$ (0.0014 g, 0.0035 g, and 0.0069 g for 2 mM, 5 mM, and 10 mM $Mg(HMDS)_2$ solutions in MACC, respectively) and stirred for at least 6 h to yield a clear, colorless solution. The water content of electrolytes was measured with Coulometric Karl Fischer Titrator (Mettler Toledo C20S).

Addition of H_2O to solutions was achieved by first purging a flame-dried vial with Ar with a venting needle through a septum. A drop of water (3 mg, for instance) was then added to the vial and the mass was recorded. The vial was additionally sealed with parafilm to prevent the evaporation of water during transfer into the glovebox. In the glovebox, a desired concentration of H_2O was prepared by adding THF into the vial containing the H_2O drop (1.67 mL of THF to 3 mg of H_2O to reach 100 mM). The wet THF was then added to electrolytes in a 1:9 ratio to reach desired H_2O concentrations.

Electrochemical Characterization

Mg electrodeposition and stripping was evaluated in a vial cell with 0.5 mm Pt wire (Sigma–Aldrich) working electrodes with a Mg foil (Solution Materials LLC and MTI Corp.) reference/counter electrode in an Ar-filled glovebox. The Pt wire was cleaned in concentrated HNO_3 and heated in a H_2 flame prior to use. The Mg foil was mechanically cleaned with a razor blade in the glovebox prior to use. Electrochemical cells were assembled in an Ar glovebox with 1.0 mL of electrolyte in vials. The cells were cycled using cyclic voltammetry (CV) from -1.2 to 3 *V* *vs.* Mg/Mg^{2+} at 5 mV s^{-1}. The electrochemistry was controlled with a VMP-3 BioLogic potentiostat. All subsequent references to voltage are referenced to a Mg foil electrode.

Scanning Electron Microscopy

Scanning electron microscopy (SEM) of the Pt electrodes was performed using a ZEISS 1550VP Field Emission SEM with an acceleration voltage of 20 kV. Energy-dispersive X-ray spectroscopy (EDS) was performed with an Oxford X-Max SDD X-ray Energy Dispersive Spectrometer system. The surfaces were rinsed with THF inside the glovebox and vacuum-dried overnight in preparation for SEM. The samples were transported to the SEM air-free, but were briefly exposed to air (less than 10 s) upon introduction of the sample to the SEM chamber.

2.4 Results

To study the effect of adding small concentrations of $Mg(HMDS)_2$ to MACC on the conditioning process, 2 mM to 10 mM $Mg(HMDS)_2$ was added to as-prepared MACC at 60 mM $MgCl_2$ and 30 mM $AlCl_3$ in THF. The first CV obtained with of MACC electrolyte neat and with varying concentrations of $Mg(HMDS)_2$ added are shown in Figure 2.1a and b. The first cycle of neat MACC shows significant cathodic current above 0 *V vs.* Mg/Mg^{2+} due to reduction of Al species.[58,59] The fourth quadrant of the CV is the region associated with Al reduction and is highlighted in red in both Figure 2.1a and b. The CV does not show features associated with Mg electrodeposition and stripping, consistent with previous studies on the MACC electrolyte.[58] Upon addition of only 2 mM $Mg(HMDS)_2$ to MACC, the CV shape changes significantly (Figure 2.1a). The cathodic current in the fourth quadrant decreases substantially, and Mg electrodeposition and stripping features are observed even on the first cycle. Increasing the $Mg(HMDS)_2$ concentration to 5 mM and 10 mM results in CVs that show only Mg electrodeposition and stripping characteristics with negligible cathodic current in the fourth quadrant, as shown in Figure 2.1b.

The Coulombic efficiency (η) is also affected by the addition of $Mg(HMDS)_2$ and is plotted as a function of cycle index in Figure 2.1c. The average of replicate cells is shown and the error bar represents the standard deviation. Addition of just 2 mM $Mg(HMDS)_2$ increases the Coulombic efficiency of cycle one from 13%±6% to 60%±15%. The poor Coulombic efficiency at low cycle numbers is associated with the irreversible Al^{3+} deposition processes that plague unconditioned MACC

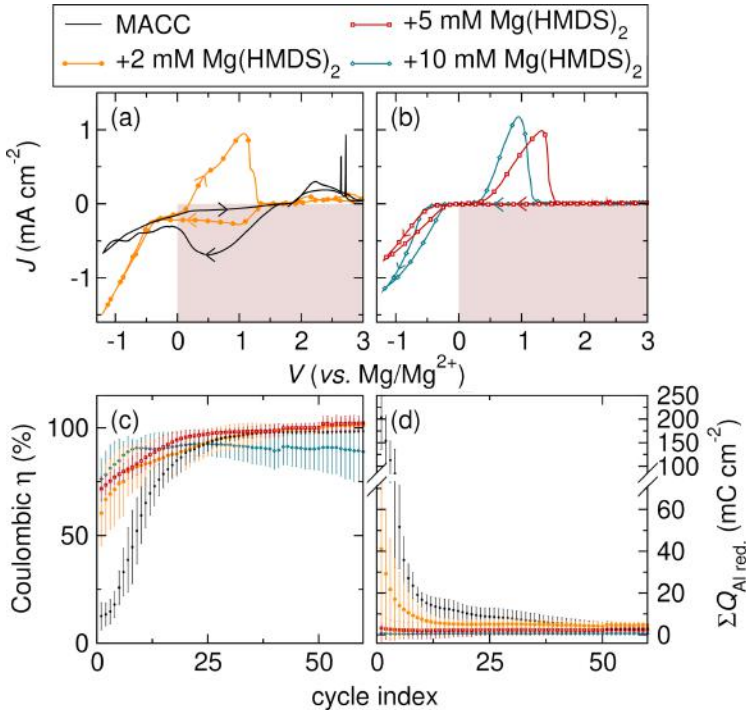

Figure 2.1: Cyclic voltammetry of MACC and MACC + Mg(HMDS)$_2$. The first CV cycles of (a) MACC (60 mM MgCl$_2$ and 30 mM AlCl$_3$, MACC + 2 mM Mg(HMDS)$_2$, (b) MACC + 5 mM Mg(HMDS)$_2$, and + 10 mM Mg(HMDS)$_2$. CVs are obtained with a Pt working electrode and Mg foil counter/reference electrode at 5 mV s^{-1}. The region highlighted in red is the fourth quadrant of the CV, or cathodic current above 0 *V vs.* Mg/Mg^{2+}. (c) The Coulombic efficiency (η) as a function of cycle index upon sequential CVs. The Coulombic η is defined as the sum of the anodic current over the sum of the cathodic current in the entire CV range. (d) The integrated charge passed on the negative sweep in the fourth quadrant, which is associated with Al deposition, during extended CV cycling.

electrolytes. After addition of 5 mM and 10 mM Mg(HMDS)$_2$, the Coulombic efficiency on the first cycle remains high at 72%±6% and 76%±9%, respectively. Interestingly, 10 mM Mg(HMDS)$_2$ causes lower Coulombic efficiencies. In this case, we observe a black film on the working electrode and upon removal, the electrolyte returns to high (>90%) Coulombic efficiency (see Figure 2.5 for Coulombic efficiency profile). The effect of Mg(HMDS)$_2$ on the deposition morphology is unknown at this time.

To evaluate the effect of adding Mg(HMDS)$_2$ on the Al^{3+} deposition processes, the cathodic current in the fourth quadrant of the CV (highlighted in red in Figure 2.1a and b), was integrated and summed over cycling (Figure 2.1d). We assume that a majority of the current in this region of the CV is associated with Al^{3+} deposition (*vide infra*), although some additional side reactions likely contribute, as well.

Without $Mg(HMDS)_2$, the negative sweep in the MACC electrolyte is plagued by significant cathodic current during the initial CVs. With only 2 mM $Mg(HMDS)_2$, the Al deposition current drops from 203 ±68 mC cm^{-2} to 41 ±35 mC cm^{-2}. Addition of 5 mM $Mg(HMDS)_2$ decreases the initial Al deposition current to nearly 0 mC cm^{-2} (3 ±6 mC cm^{-2}).

Although we assume the current in the fourth quadrant of the CV is associated with Al deposition, side reactions could also contribute to cathodic current in this region. To evaluate the origin of current in the fourth quadrant, the electrolytes were cycled between 0 V and 1.7 *V vs.* Mg/Mg^{2+} with a Pt working electrode. The CVs of the MACC electrolyte and the MACC electrolyte + 10 mM $Mg(HMDS)_2$ are shown in Figure 2.2a. Significant cathodic current is observed in the absence of $Mg(HMDS)_2$ while addition of 10 mM $Mg(HMDS)_2$ causes the cathodic current density to drop nearly to 0 mA cm^{-2}. The cumulative charge passed over sequential cycling is plotted in Figure 2.2b. The MACC electrolyte accumulates significant cathodic current summing to approx. -300 mC cm^{-2} over 10 CV cycles while MACC + 10 mM $Mg(HMDS)_2$ passes only approx. -5 mC cm^{-2}. The Pt working electrode was then characterized with SEM and EDS. The SEM images of the pristine Pt electrode, the Pt electrode after cycling in MACC, and the Pt electrode after cycling in MACC + 10 mM $Mg(HMDS)_2$ are shown in Figure 2.2c-e. The SEM shows deposits on the Pt electrode after cycling in MACC that are not present on the pristine Pt surface. The EDS shows the presence of Pt, Al, O, and C on the electrode. Mapping the Al EDS signal onto the SEM image, shown in Figure 2.2d, reveals high Al counts that correspond to the new deposited material suggesting that the deposits are primarily composed of Al. The deposits also contain O (EDS map not shown) due to brief exposure of the electrode to air prior to imaging. The Al EDS suggests that the cathodic current in the MACC electrolyte is at least partially due to Al electrodeposition, as suggested previously.[58] We note that other side reactions could be occurring in this region of the CV to form soluble or gaseous products unobservable by SEM. The SEM of the Pt electrode after cycling in MACC + 10 mM $Mg(HMDS)_2$ reveals a clean surface indistinguishable from the pristine Pt electrode. The lack of deposits on the electrode combined with the negligible cathodic current between 0 *V* and 1.7 *V* (vs. Mg/Mg^{2+}) confirms that addition of 10 mM $Mg(HMDS)_2$ inhibits Al electrodeposition.

Addition of a small concentration of $Mg(HMDS)_2$ changes the behavior of the MACC electrolyte by inhibiting Al electrodeposition and supporting reversible Mg

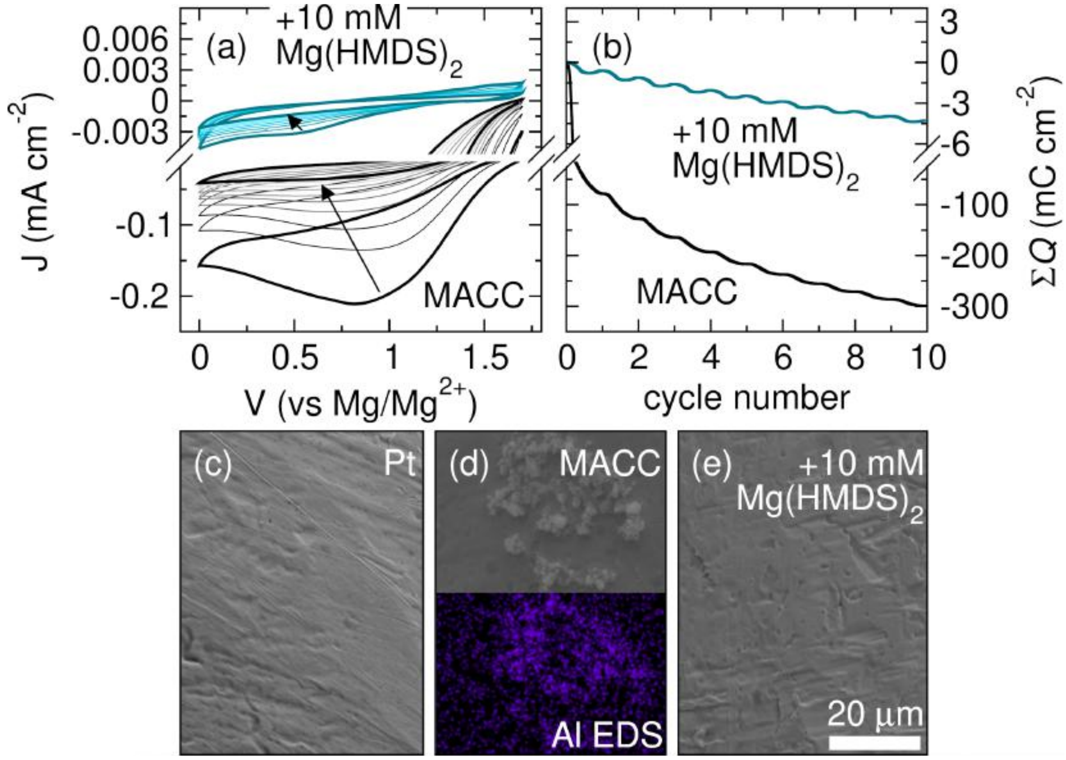

Figure 2.2: Cyclic voltammograms over cycles and SEM images. (a) Cyclic voltammograms of MACC and MACC + 10 mM $Mg(HMDS)_2$ from 0 V to 1.7 V at 5 mV s^{-1} for 10 cycles. The evolution of the CVs with continued cycling is indicated by the arrow for each electrolyte. (b) The cumulative charge as a function of cycle number from the CVs in (a). SEM images of the Pt working electrode (a) before cycling, (d) after cycling in MACC, and (e) after cycling in MACC + $Mg(HMDS)_2$. The Al EDS map is shown for the image in panel (d).

electrodeposition from cycle one. Without $Mg(HMDS)_2$, efficient Mg deposition and stripping is only observed in neat MACC after electrochemical conditioning during which free Cl^- is generated as a result of irreversible Al^{3+} electrodeposition.[59] The electrolyte ages, however, as the solvated Cl^- is metastable resulting in decreased performace over time. Barile *et al.* reported a decreased Coulombic efficiency and an increased overpotential when conditioned MACC was aged for a week.[58] The aging behavior of the MACC electrolyte ages is counter the suggestion that the electrochemical conditioning of MACC is merely electrolytic removal of electrolyte impurities.

To determine if the MACC + $Mg(HMDS)_2$ electrolyte ages similar to neat MACC, a solution of MACC + 5 mM $Mg(HMDS)_2$ was allowed to age in a sealed glass vial in the glovebox absent from electrodes. Aliquots were extracted from the vial after 3 d and 4 d of aging and used as electrolytes in Pt|Mg cells. The first CVs obtained for the electrolyte as-prepared, after aging for 3 d, and after aging for 4 d are shown in Figure 2.3a. The electrolyte shows reversible Mg electrodeposition and stripping behavior as-prepared, with essentially no cathodic current in the fourth quadrant as reported above. As the electrolyte ages, cathodic current in the fourth quadrant increases and the current density in this region increases as the electrolyte continues to age suggesting that Al deposition is enabled as a result of aging. The current at 0.5 *V vs.* Mg/Mg^{2+} measured during the negative sweep of the first cycle is plotted *vs.* aging time in Figure 2.3b to observe the effect of aging on the Al deposition current density. Three replicate electrolyte batches are shown. In all cases, as the electrolyte ages, the current density associated with Al deposition increases. To determine if the aged electrolytes could be conditioned like neat MACC, the electrolytes were subjected to continuous CV cycling. The associated Coulombic efficiency and Al reduction current as a function of cycle index are plotted in Figure 2.3c and d. The Coulombic efficiency is 34% and 16% after the electrolyte is aged for 3 d and 4 d, respectively, but increases over continuous CV cycles similar to the behavior of the MACC electrolyte without $Mg(HMDS)_2$. The increase in Coulombic efficiency is correlated with a decrease in the charge passed associated with Al deposition.

2.5 Discussion

Addition of a small concentration of $Mg(HMDS)_2$ to the MACC electrolyte greatly suppresses Al^{3+} deposition and increases Coulombic efficiency on cycle one. The concentration of $Mg(HMDS)_2$ is 6-30 times smaller than that of the $MgCl_2$ supporting electrolyte, which is too low to cause bulk changes in speciation of the Mg complexes. For small concentrations of an electrolyte additive to have such a pronounced effect on the electrochemistry, we hypothesize that addition of $Mg(HMDS)_2$ instead causes changes in the interface at the Mg electrode that activates Mg electrodeposition and stripping. We hypothesize two possible mechanisms. First, the $Mg(HMDS)_2$ could quench electrolyte impurities that would otherwise have a detrimental effect at the electrode interface. The most obvious role of $Mg(HMDS)_2$ in this regard is its role as a water scavenger. Trace water is not only important to control in Mg electrolytes, but also in electrolytes containing PF_6^-. PF_6^- reacts with water to form highly corrosive HF that can leach metals from Li-ion cathodes. Addition of HMDS, $HN[Si(CH_3)_2)]_2$, to $LiPF_6$ electrolytes with $Li_{1.01}Mn_{1.99}O_4$ cathodes has resulted in increased capacity retention and reduced the dissolution of Mn.[68] $Mg(HMDS)_2$ should only act as a stronger water scavenger compared to its HMDS counterpart $HN[Si(CH_3)_3)]_2$. In the area of Mg electrolytes, heptamethyldis-

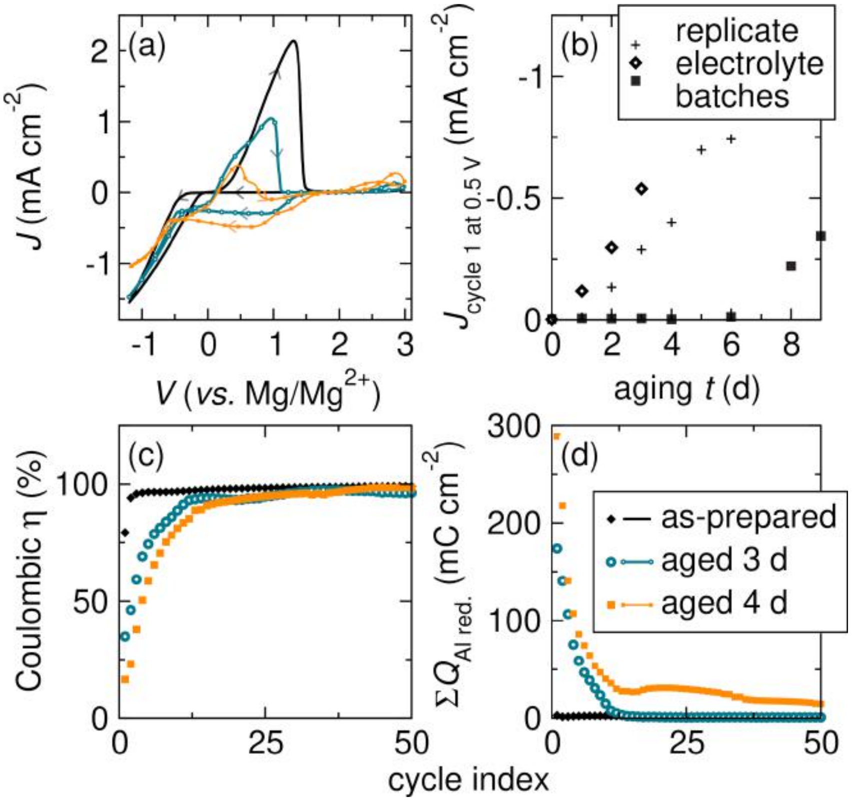

Figure 2.3: Aged electrolytes cyclic voltammetry. (a) The first CV obtained in the MACC + 5 mM Mg(HMDS)$_2$ electrolyte as-prepared and after aging for 3 d and 4 d. (b) The current density (J) on the negative sweep at 0.5 V of the first cycle as a function of aging time. The cathodic current increases as the electrolyte ages. Three replicate electrolyte batches are shown. (c) The Coulombic efficiency (η) during conditioning of the MACC + 5 mM Mg(HMDS)$_2$ as-prepared and after aging for 3 d and 4 d. (d) The sum of the cathodic current in the fourth quadrant taken to be the Al reduction current as a function of cycle index.

ilazane $CH_3N[Si(CH_3)_3]_2$ has been added to Mg electrolytes with sulfone and glyme solvents and $MgCl_2$ and Mg(TFSI)$_2$ supporting electrolytes resulting in Mg electrodeposition and stripping on the first cycle. The change in behavior was attributed to the ability of heptamethyldisilazane to scavenge water in the electrolyte.[69] Similarly, Aurbach and coworkers introduced Bu_2Mg as a reducing agent to Mg(TFSI)$_2$ + 2 $MgCl_2$ in DME to react with traces of oxygen, water, and other protic moieties and observed enhanced electrolyte performance.[70] In fact, the MACC electrolyte + 2 mM Mg(HMDS)$_2$ has a lower water content measured by Karl Fischer titration of 46 ppm compared to MACC (71 ppm).

The second possibility is that addition of Mg(HMDS)$_2$ forms beneficial species in the electrolyte that activate the interface. Activation of Mg electrolytes has been attributed to the formation of solvated Cl^- previously. In the MACC electrolyte, metastable solvated Cl^- is formed *via* an electrolytic reaction shown in reaction 3.2.[59] In fact, the majority of Mg electrolytes contain Cl^- and several studies have suggested that it is actively involved in the charge transfer mechanism.[49–53,55,56,58,59] Cl^- could act to depassivate the Mg electrode by dissolving surface oxides or removing adsorbed THF. Cl^- could also act as an electron transfer bridge to the multivalent Mg^{2+}, reminiscent of Cu^{2+} electroplating mechanisms.

Next we discuss the interplay between the two possible roles of $Mg(HMDS)_2$ in MACC. The ability of $Mg(HMDS)_2$ to scavenge water is certainly improving the electrochemistry as water is known to be detrimental to Mg deposition and stripping behavior. The removal of water, however, does not explain the aging behavior of the electrolytes. Water removal by reaction with $HMDS^-$ to form HMDS and OH^-, for example, will not reverse over time and require re-conditioning, as we observe in the experiments. Water could be reintroduced into the electrolyte during aging; however, we take care during the aging experiments to prevent contamination of the electrolytes. The electrolytes are kept in a sealed vials in the glovebox. The glovebox was stable at <0.1 ppm H_2O and O_2 during the aging experiments and no new chemicals are introduced into the box that were not already present when the electrolytes were first prepared. Aliquots were taken from the electrolyte with a clean needle each time. Regardless, it is possible that water is absorbed into the electrolyte causing the electrolytes to age. To probe this hypothesis, water was intentionally added to the MACC + 5 mM $Mg(HMDS)_2$ electrolyte. Figure 2.4 shows the first CV sweep of the as-prepared electrolyte and the as-prepared electrolyte with varying concentrations of water added. Addition of water reduces the current density and causes a new oxidative feature to appear confirming that water is detrimental to the Mg electrochemistry. The cathodic current in the fourth quadrant associated with Al^{3+} reduction is not observed after adding water. Aged MACC + 5 mM $Mg(HMDS)_2$ is also shown in Figure 2.4 for comparison. In the aged electrolyte, significant cathodic current in the fourth quadrant is observed, and because we do not see such behavior in the wet electrolyte, the aging of the electrolyte is, therefore, a different process than simply water introduction. In all cases, the electrolyte can be re-conditioned by electrochemical conditioning (sequential CVs). The cycling evolution of these electrolytes can be found in Figure 2.6.

We therefore suggest that the aging of MACC + $Mg(HMDS)_2$ is not due to introduction of impurities such as water. We hypothesize that the aging mechanism of

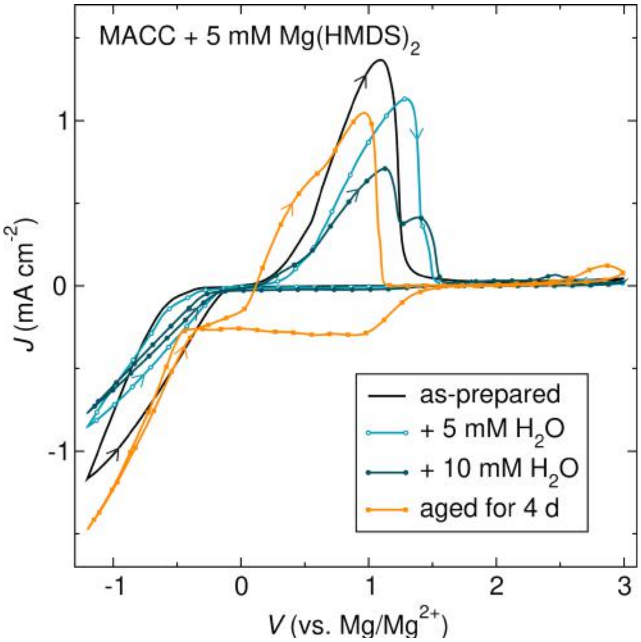

Figure 2.4: Aged electrolytes comparison. First cycle of MACC + 5 mM Mg(HMDS)$_2$ electrolytes scanned at 5 mV s^{-1} with a Pt working electrode and Mg counter/reference electrode. The as-prepared electrolyte is shown *versus* the electrolyte + 5 mM H_2O and + 10 mM H_2O. The as-prepared electrolyte was allowed to age in the glovebox for 4 days, and the resulting trace obtained with new electrodes is also shown. Addition of H_2O lowers the current density and causes a new oxidative wave, but the cathodic current in the fourth quadrant as a result of aging is not observed.

MACC + Mg(HMDS)$_2$ electrolytes is similar to that of conditioned MACC. Namely, the metastable Cl^- species, formed either through electrochemical conditioning in the case of neat MACC or addition of Mg(HMDS)$_2$, is slowly depleted from solution through precipitation of $MgCl_2$. Connell et al. explored the competition between Cl^- and H_2O in Mg(TFSI)$_2$ + $MgCl_2$ in DME by varying their concentrations and discovered that H_2O forms films of MgO and Mg(OH)$_2$ that slow down the deposition of Mg^{2+}. Cl^- is able to protect the Mg surface via the formation of Mg-Cl$_{(ad)}$ and/or $MgCl_2$ resulting in higher reversibility.[71] Because formation of Cl^- results in both an active electrolyte, and an electrolyte that ages, we hypothesize that the addition of Mg(HMDS)$_2$ causes Cl^- formation from a chemical step rather than an electrochemical step. Therefore, in addition to Mg(HMDS)$_2$ acting as a water scavenger, we hypothesize that it also acts to form free Cl^- in solution to activate the surface. We are currently pursuing detailed characterization of the solution complexes to probe this hypothesis.

2.6 Conclusions

The MACC electrolyte continues to be a useful electrolyte to study the fundamental mechanisms associated with Mg electrodeposition and stripping. Addition of just 2 mM $Mg(HMDS)_2$ suppresses Al^{3+} reduction and promotes Mg^{2+} electrodeposition and stripping in the electrolyte from cycle one. The small concentration implies that the change in the electrochemistry is likely due to interactions at the electrode interface. We hypothesize the effect of the $Mg(HMDS)_2$ is not only to scavenge water from the electrolyte but also to generate solvated Cl^- to activate the Mg electrodeposition and stripping. Because MACC + $Mg(HMDS)_2$ ages similarly to neat MACC, it is more likely that the formation of Cl^- is the cause for improved behavior on cycle one. In fact, the CV measured with a wet electrolyte does not cause the cathodic current in the fourth quadrant associated with Al^{3+} reduction seen in the aged electrolytes. As the electrolyte ages, Cl^- could be depleted from solution thereby deactivating the electrolyte and requiring the electrochemical conditioning step necessary in neat MACC. Current studies are focused on probing the speciation of the Al and Mg complexes in the electrolyte solution as a function of $Mg(HMDS)_2$ to probe this hypothesis.

solution	THF	MACC	MACC + 2 mM Mg(HMDS)$_2$
water content (ppm)	22	71	46

Table 2.1: Water content of various solutions measured by Karl Fischer Titration.

2.A Supplementary Information

Increased water content in MACC is attributed to water present in the salts. In MACC + 2 mM Mg(HMDS)$_2$, although more salt is added to the solution, water content decreases, confirming the water-scavenging effect of Mg(HMDS)$_2$.

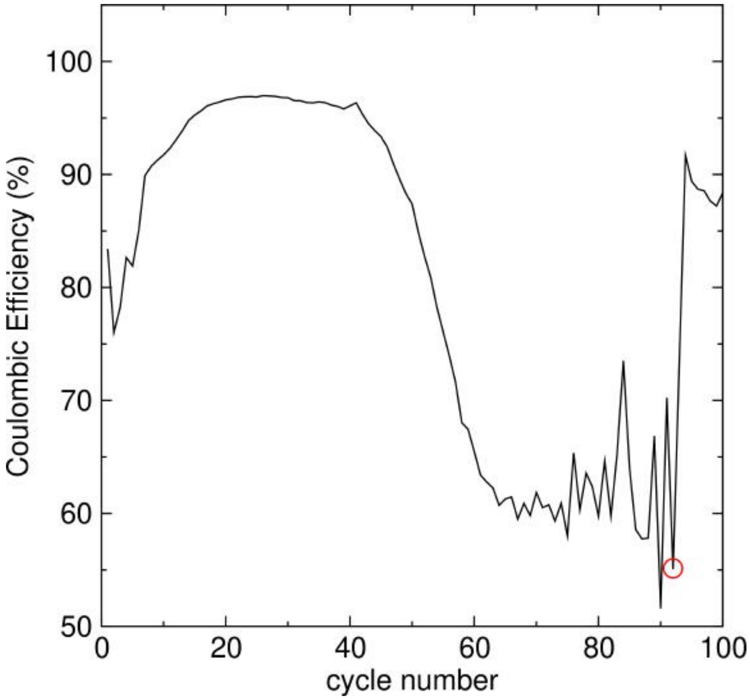

Figure 2.5: Coulombic efficiency as a function of cycling. Typical Coulombic efficiency profile of MACC + 10 mM Mg(HMDS)$_2$. CE decreases due to the formation of a black film. The black film is easily removed from the Pt wire by simple agitation. The electrolyte reaches >90% CE upon when the black film is removed from the electrolyte (red circle).

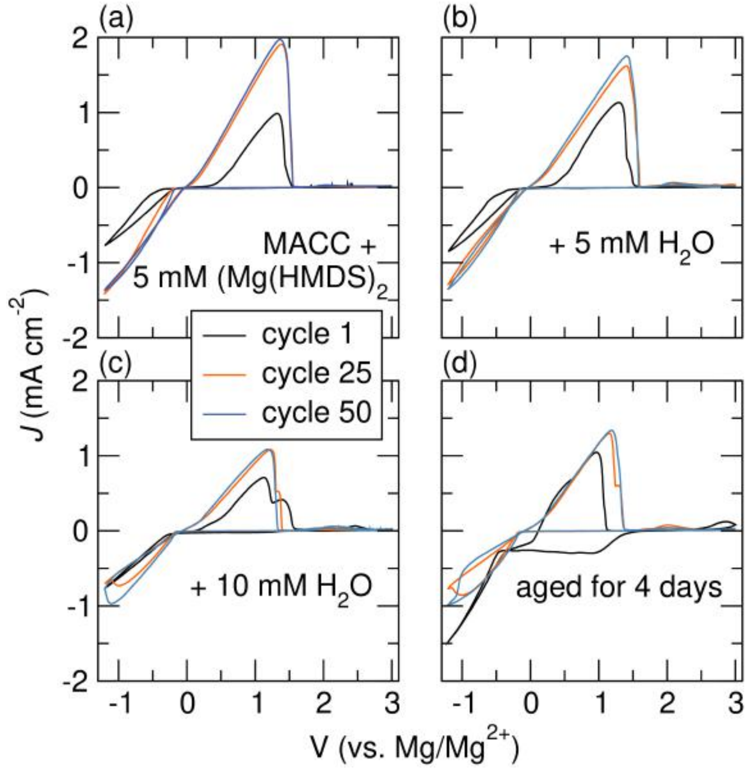

Figure 2.6: Aged electrolytes comparison. Cyclic voltammograms of cycles 1, 25, and 50 of (a) MACC + 5 mM Mg(HMDS)$_2$, (b) MACC + 5 mM Mg(HMDS)$_2$ + 5 mM and (c) 10 mM H_2O, and (d) MACC + 5 mM Mg(HMDS)$_2$ aged for 4 days. MACC + 5 mM Mg(HMDS)$_2$ with and without H_2O exhibit similar electrochemical behavior, including Mg deposition/stripping and no cathodic current in the fourth quadrant from cycle 1. MACC + 5 mM Mg(HMDS)$_2$ + 5 mM H_2O exhibits >99% Coulombic efficiency at cycle 50 while MACC + 5 mM Mg(HMDS)$_2$ + 10 mM H_2O exhibits 84% at cycle 50, likely due to the high concentration of H_2O in the solution. The electrolyte does not exhibit cathodic current in the fourth quadrant with 10 mM of H_2O addition. In comparison, MACC + 5 mM Mg(HMDS)$_2$ aged for 4 days exhibits cathodic current in the fourth quadrant, the region attributed to Al deposition, in cycle 1. The cathodic current in aged MACC + 5 mM Mg(HMDS)$_2$ that disappears in subsequent cycles may be due to the depletion of free Cl^- during aging.

C h a p t e r 3

ACTIVATING MG ELECTROLYTES THROUGH CHEMICAL GENERATION OF FREE CHLORIDE AND REMOVAL OF TRACE WATER

This chapter has been adapted from:

(1) **Kim, S. S.**; See, K. A. Activating Magnesium Electrolytes through Chemical Generation of Free Chloride and Removal of Trace Water. *ACS Appl. Mater. Interfaces* **2021**, *13*, 671–680,

Contributions: S.S.K. conceived, designed, and performed experiments, and wrote the manuscript. **DOI:**10.1021/acsami.0c19053

3.1 Abstract

Mg batteries are attractive next-generation energy storage systems due to their high natural abundance, inexpensive cost, and high theoretical volumetric capacity compared to conventional Li-ion based systems. The high energy density is achieved by electrodeposition and stripping of a Mg metal anode and requires the development of effective electrolytes enabled by a mechanistic understanding of the charge transfer mechanism. The magnesium aluminum chloride complex (MACC) electrolyte is a good model system to study mechanism as the solution phase speciation is known. Previously, we reported that minor addition of $Mg(HMDS)_2$ to the MACC electrolyte causes significant improvement in the Mg deposition and stripping voltammetry resulting in good Coulombic efficiency on cycle one and, therefore, negating the need for electrochemical conditioning. To determine the cause of the improved electrochemistry, here we probe the speciation of the electrolyte after $Mg(HMDS)_2$ addition using Raman spectroscopy, ^{27}Al nuclear magnetic resonance spectroscopy, and ^{1}H-^{29}Si heteronuclear multiple bond correlation spectroscopy on MACC + $Mg(HMDS)_2$ at various $Mg(HMDS)_2$ concentrations. $Mg(HMDS)_2$ scavenges trace H_2O, but it also reacts with MACC complexes, namely $AlCl_4^-$, to form free Cl^-. We suggest that although both the removal of H_2O and the formation of free Cl^- improve electrochemistry by altering the speciation at the interface, the latter has a more profound effect on electrodeposition and stripping of Mg.

3.2 Introduction

Rechargeable Mg batteries are attractive next-generation systems that could help meet growing energy storage demands.[24] Mg^{2+} working ions with a Mg metal anode allow higher theoretical volumetric and gravimetric specific capacities (3833 mA h cm^{-3} and 2202 mA h g^{-1}, respectively) than the commercialized Li intercalated graphite anode (719 mA h cm^{-3} and 339 mA h g^{-1}). Another advantage of Mg is its high natural abundance in the Earth's crust, which makes it more economically appealing over anodes reliant on Li^+ working ions.[72,73] At the same current densities, Mg^{2+} ions electrodeposit a smoother morphology compared to Li^+ ions suggesting Mg may be a more viable metal anode.[74] Mg is not immune to dendrites;[75,76] however, and it will be important moving forward to determine Mg deposition limitations.

A primary challenge facing Mg metal battery technology is developing effective electrolytes. The Mg electrolyte must support reversible Mg deposition and stripping with high Coulombic efficiency without reacting at the electrodes. The earliest electrolytes that demonstrated reversible Mg electrodeposition and stripping were based on Grignards such as PhMgBr and BnMgCl in tetrahydrofuran (THF)[28] or EtMgI in ether.[29] However, these systems suffer from issues such as poor anodic stability, low conductivity, and incompatibility with electrode materials and cell components.[30,31] Several electrolytes have been developed since the Grignards that address some of these limitations. Interestingly, a majority of Mg electrolytes contain Cl, although a few electrolytes have been shown to support Mg deposition and stripping without halides such as the carboranes[41,77,78] and the borates.[79,80] The active complex in electrolytes that contain Cl is often suggested as $[Mg_2(\mu{-}Cl)_3]^+$.[34,51,81–87] The magnesium aluminum chloride complex (MACC) electrolyte, first reported by Doe et al., is a good example of a non-Grignard, Cl–containing electrolyte that supports Mg deposition and stripping with high Coulombic efficiency and low deposition overpotential.[85] MACC is prepared by dissolving 2:1 ratio of $MgCl_2$ and $AlCl_3$ in THF, which undergo a Lewis acid-base reaction to yield:[88]

$$AlCl_3 + 2\,MgCl_2 + 6\,THF \rightleftharpoons AlCl_4^- + [Mg_2(\mu{-}Cl)_3 \cdot 6\,(THF)]^+. \tag{3.1}$$

MACC requires an undesirable conditioning process before reaching high Coulombic efficiency and low deposition overpotential. During electrolytic conditioning, Al^{3+} from $AlCl_4^-$ is irreversibly reduced and deposited at the working electrode while Mg is oxidized at the counter electrode, resulting in the formation of free Cl^-

and $[Mg_2(\mu{-}Cl)_3 \cdot 6\,(THF)]^+$:[88]

$$4\,AlCl_4^- + 6\,Mg_{(s)} \longrightarrow 4\,Al_{(s)} + 3\,[Mg_2(\mu{-}Cl)_3 \cdot 6\,(THF)]^+ + 7\,Cl^-. \qquad (3.2)$$

MACC requires electrochemical conditioning to achieve high Coulombic efficiency (>99%), low deposition overpotential (150 mV), and an anodic stability of 3 V vs. Mg/Mg^{2+}.[88,89] The conditioning process involves irreversible Al^{3+} reduction and results in the formation of free Cl^- which is hypothesized to interact with the Mg interface.[88] Recent experimental and theoretical works have suggested that the Cl^- plays a pivotal role in activating Mg electrodeposition and stripping via these interfacial interactions. Esbenshade *et al.* reported that the deposition of Cl–containing species on the electrode enhanced Mg electrodeposition in the all phenyl complex (APC) electrolyte.[90] Cene *et al.* reported that the adsorption of Cl^- on Mg surfaces is thermodynamically favorable.[91,92] Also, Benmayza *et al.* and Ta *et al.* have suggested that the adsorption of $MgCl^+$ onto the Mg electrode precedes Mg electrodeposition and identified Mg electrodeposition as a chemical-electrochemical (CE) mechanism, further corroborating the role of Cl^- in Mg electrodeposition and stripping.[93,94] Therefore, although there is a need to ultimately develop effective Cl–free electrolytes due to its reactivity toward battery cell components,[95] understanding the charge transfer mechanisms in Cl–containing electrolytes and the role of Cl^- is necessary to establish design principles.

It is difficult to directly study the role of Cl^- in the deposition mechanism. We have instead pursued various ways to produce Cl^- in solution and study its affect on the electrochemistry. For example, we have shown that addition of small concentrations of $Mg(HMDS)_2$ shows electrochemistry similar to the conditioned electrolyte without electrochemical conditioning and hypothesized that the beneficial electrochemistry is due to generation of Cl^-.[96] The acronym "HMDS" will be used to refer to the $[[(CH_3)_3Si]_2N]^-$ anion henceforth. Addition of $Mg(HMDS)_2$ suppresses the Al^{3+} reduction current typical of unconditioned MACC electrolyte and reveals Mg electrodeposition and stripping with high reversibility without conditioning.[96] The small concentration of the $Mg(HMDS)_2$ additive suggests that the effects of the additive are not due to bulk speciation changes and must be due to either the formation of a complex that is active at the interface, like Cl^-, or the removal of a detrimental trace species, like H_2O.[96] The presence of H_2O is detrimental as highly oxophilic Mg[97] reacts with H_2O to form an oxide layer that passivates the Mg surface and slows the kinetics of Mg electrodeposition.[98–100] Additives such as heptamethyldisilazane ($CH_3N[Si(CH_3)_3]_2$),[99] $MgBu_2$,[100] Mg metal,[101] and hexamethyldisilazane

($[(CH_3)_3Si]_2NH$), denoted here as H(HMDS),[102] have been introduced to various electrolyte systems to scavenge trace levels of H_2O resulting in decreased overpotential and increased reversibility. In the MACC system, we observed decreased H_2O content upon $Mg(HMDS)_2$ addition which could explain the beneficial effects of the additive.[96] However, we also observed that MACC + $Mg(HMDS)_2$ ages similarly to conditioned MACC resulting in an electrolyte that must be electrolytically conditioned, suggesting some contribution from Cl^-. We therefore hypothesized that $Mg(HMDS)_2$ is able to not only scavenge H_2O, but also chemically generate Cl^- to activate the Mg electrodeposition and stripping.[96] Here, through the combination of Raman spectroscopy, ^{27}Al NMR spectroscopy, and ^{1}H–^{29}Si heteronuclear multiple bond correlation spectroscopy, we probe these hypotheses by characterizing the speciation of the Al and Mg complexes in the electrolyte as a function of $Mg(HMDS)_2$ concentration. The data are evaluated in concert to identify changes in bulk speciation and devise possible reactions. We find that $Mg(HMDS)_2$ not only scavenges H_2O in solution, but also undergoes a ligand exchange reaction with $AlCl_4^-$ to release Cl^- and activate the MACC electrolyte by facilitating Mg electrodeposition and stripping at the electrode-electrolyte interface.

3.3 Experimental Section

Electrolyte Preparation

The MACC electrolyte was prepared according to the procedure outlined by Barile et al. in an Ar-filled glovebox. Anhydrous tetrahydrofuran (THF, Fisher Scientific) was dried on a solvent purification system and brought into the glovebox without exposure to air. The H_2O content of THF measured by Karl Fischer titration was 21 ppm. Anhydrous $MgCl_2$ (99.9%, Fisher Scientific), anhydrous $AlCl_3$ (99.999%, Sigma–Aldrich), and $Mg(HMDS)_2$ (97%, Sigma–Aldrich) were opened in the glovebox. The MACC electrolyte was prepared at 30 mM $AlCl_3$ and 60 mM $MgCl_2$ in THF. THF (2.5 mL) and $AlCl_3$ (0.020 g) were cooled in separate vials on a Peltier plate (approx. 0°C). Cold THF was added dropwise to $AlCl_3$ and agitated to yield a clear, colorless solution. $MgCl_2$ (0.0286 g) was added to a separate vial with 2.5 mL room temperature THF. The $AlCl_3$ solution was added dropwise to the $MgCl_2$ suspension while stirring, and the solution was stirred for at least 6 h to yield a clear, colorless solution. The as-prepared MACC (2 mL) was added to $Mg(HMDS)_2$ (0.0014 g, 0.0035 g, and 0.0069 g $Mg(HMDS)_2$ for 2 mM, 5 mM, and 10 mM $Mg(HMDS)_2$ solutions in MACC, respectively) and stirred for at least 6 h to yield clear, colorless solutions.

Characterization Details

Raman spectra were measured on a Horiba Instruments XplorRA PLUS Raman spectrometer with an excitation wavelength of 785 nm. The samples were measured in capped and epoxy sealed 5 mm N51A borosilicate glass tubes. The spectra were collected with an 1800 grooves mm^{-1} grating, a slit of 200 μm, and a hole of 500 μm. The signal was averaged over 100 acquisitions lasting 2 s each.

^{27}Al NMR spectroscopy was performed on a 400 MHz Varian instrument in 5-mm thin wall precision screw-cap NMR sample tubes (Wilmad-LabGlass). Samples were measured with 1 M of $Al(NO_3)_3$ in D_2O as a standard in a coaxial, sealed capillary. Each spectrum was baseline-subtracted with a spectrum of THF measured with the same NMR tube to remove features due to Al artifacts present from the NMR tubes and the probe. ^{27}Al NMR was measured with a 90 degree pulse width of 7.125 μs, an acquisition time of 0.4 s, and a relaxation delay of 0.1 s. ^{1}H–^{29}Si heteronuclear multiple bond correlation (HMBC) measurements were performed on a 400 MHz Bruker instrument in 5 mm screw-cap NMR tubes. Spectra were referenced based on the chemical shift of Si grease present in the tubes.[103] ^{1}H–^{29}Si HMBC was measured with a 90 degree pulse width of 8.7 μs, an acquisition time of 0.197 s, and a relaxation delay of 2 s.

3.4 Results

Raman Spectroscopy: Raman spectroscopy is used to study the changes in MACC speciation upon $Mg(HMDS)_2$ addition. The Raman spectra of the electrolytes and standard solutions are shown in Figure 3.1, and the assignments of the observed modes are tabulated in Table 3.1. The spectra are shown normalized to a strong THF mode at 913 cm^{-1}. The Raman spectrum of the as-prepared MACC exhibits the A_1 breathing mode of $[Mg_2(\mu{-}Cl)_3]^+$, the twisting mode of $\alpha CH_2{-}\beta CH_2$ (mode *b*), and the F_2 bending and A_1 stretching of $AlCl_4^-$ (modes *a* and *e*) in addition to prominent THF modes (modes *c*, *g*, *j*), consistent with previous reports.[104–106] Addition of $Mg(HMDS)_2$ to MACC causes the $AlCl_4^-$ mode at 347 cm^{-1}, mode *e*, to decrease in intensity as the $Mg(HMDS)_2$ concentration increases. The decrease in intensity of mode *e* with increasing $Mg(HMDS)_2$ concentration is accompanied by the appearance of two new modes, labeled *f* and *i* in Figure 3.1a. Mode *f* at 569 cm^{-1} aligns with the A_{1g} stretch of H(HMDS) shown in Figure 3.1b.[107] The presence of H(HMDS) suggests a reaction of $Mg(HMDS)_2$ with H_2O to form H(HMDS), which is supported by ^{1}H–^{29}Si 2D NMR (*vide infra*).

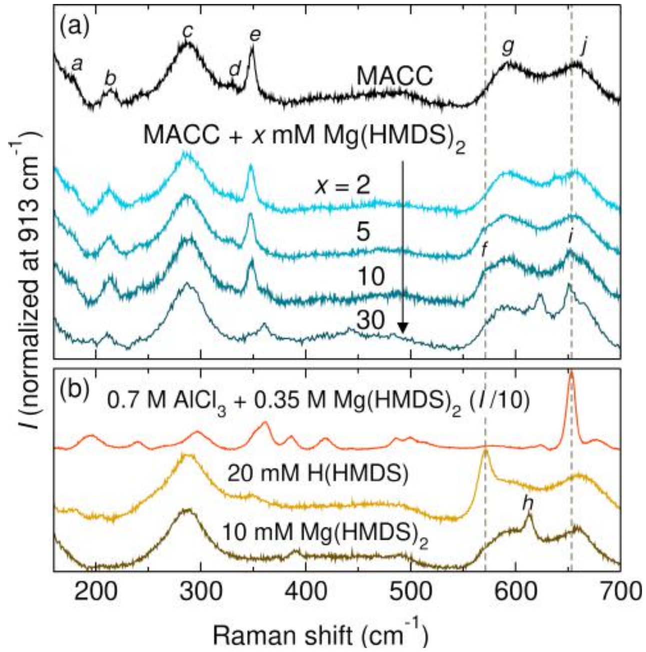

Figure 3.1: Raman spectroscopy data of electrolytes. (a) Raman spectra of as-prepared MACC and MACC with 2, 5, 10, and 30 mM of Mg(HMDS)$_2$ along with (b) reference solutions of 0.7 M AlCl$_3$ + 0.35 M Mg(HMDS)$_2$ (Raman intensity divided by 10), 20 mM H(HMDS), and 10 mM Mg(HMDS)$_2$. All intensities are normalized to a THF mode at 913 cm^{-1}. Tabulated mode assignments can be found in Table 3.1.

	Raman shift (cm^{-1})					**assignment**		
mode ID	THF	MACC	$Mg(HMDS)_2$ 10 mM	MACC + $Mg(HMDS)_2$ 10 mM	$AlCl_3$ + $Mg(HMDS)_2$ 0.7:0.35 M	species	mode(s)	ref.
a		176		178		$AlCl_4^-$	F_2 bending	105,106
b		214		213		$[Mg_2(\mu{-}Cl)_3 \cdot 6\,THF]^+$	A_1 $Mg_2(\mu{-}Cl)_3$ breathing mode + $\alpha CH_2{-}\beta CH_2$ twist	104
c	283	285	285	286	285	THF	βCX_2 (bend + rock) + ring pucker	108,109
d		328				$AlCl_3 \cdot THF$	Al–Cl	105,110
e		347		349		$AlCl_4^-$	A_1 symmetric stretching	105,106
f				569		H(HMDS)	A_{1g} Si–C	
g	592	591	590	588	590	THF	αCH_2 (bend + twist) + $C_\alpha C_\beta$ asym. stretch + ring pucker	108,109
h			610			$Mg(HMDS)_2$	A_{1g} Si–C	
i				651	651	$AlCl_3HMDS^-/AlCl_2HMDS$	A_{1g} Si–C	
j	658	659	660	663	660	THF	αCH_2 (bend + twist + rock) + βCH2 (twist + rock) + ring bend	108,109

Table 3.1: Raman Shift Assignments for Peaks in the MACC, MACC-$Mg(HMDS)_2$, and $AlCl_3$-$Mg(HMDS)_2$.

To assign mode *i*, we turn to the Raman spectrum of a reference solution of 0.7 M $AlCl_3$ + 0.35 M $Mg(HMDS)_2$ shown in Figure 3.1b. Mode *i* is observed at 651 cm^{-1} which aligns with a mode in the reference solution that is assigned by Merrill *et al.* to the A_{1g} stretch of HMDS when HMDS is coordinated to Al to form a species such as $AlCl_3HMDS^-$ or $AlCl_2HMDS$. The A_{1g} stretch of HMDS is located at 610 cm^{-1} in $Mg(HMDS)_2$ (mode *h*) and at 569 cm^{-1} in H(HMDS) (mode *f*).[107] Based on the emergence of mode *i* at 651 cm^{-1} in MACC + $Mg(HMDS)_2$ and the decrease in intensity of mode *e*, we hypothesize that $Mg(HMDS)_2$ reacts with $AlCl_4^-$ to form an HMDS–containing Al species.

The changes in the Raman spectra as a function of $Mg(HMDS)_2$ concentration show reactivity of $Mg(HMDS)_2$ beyond just removal of H_2O, and the species are further characterized with NMR below. At 5 mM $Mg(HMDS)_2$, however, the prominent modes in the Raman spectrum associated with MACC complexes such as $[Mg_2(\mu{-}Cl)_3 \cdot 6\,THF]^+$ and $AlCl_4^-$ remain, suggesting the bulk speciation remains. The low concentration of $Mg(HMDS)_2$, nonetheless, is enough to suppresses Al deposition completely and increase Coulombic efficiency at cycle one from less than 25% to 71%.[96]

^{27}Al NMR Spectroscopy: ^{27}Al NMR is used to investigate Al-containing species in MACC + $Mg(HMDS)_2$ electrolytes. Line broadening due to the quadrupolar nature of ^{27}Al offers information about the symmetry around the Al center while the chemical shifts are diagnostic of the coordination number and shielding of the Al center.[111,112] First, $Mg(HMDS)_2$ is added to solutions of 30 mM $AlCl_3$ to probe reactivity with $AlCl_3{\cdot}2THF$, the dominate complex in 30 mM $AlCl_3$. Figure 3.2a shows the ^{27}Al NMR spectra of 30 mM $AlCl_3$ with increasing concentrations of $Mg(HMDS)_2$. The neat $AlCl_3$ solution displays a small resonance at 102 ppm, *a*, which corresponds to $AlCl_4^-$,[113,114] and a strong resonance at 64 ppm, *b*, associated with $AlCl_3{\cdot}2THF$.[113–115] Upon addition of $Mg(HMDS)_2$, resonance *b* decreases in intensity and a new peak at 101 ppm emerges. The 101 ppm peak is in the region of four-coordinate anions, but it is broader than $AlCl_4^-$[88,110,114] (12.5 ppm compared to 7.7 ppm), suggesting a $[AlCl_{4\text{-}x}HMDS_x]^-$ complex. After addition of 20 mM $Mg(HMDS)_2$, $AlCl_3{\cdot}2THF$ is consumed, and the only resonance observed is that at 101 ppm. The reaction between $AlCl_3$ and $Mg(HMDS)_2$ has been probed previously with single crystal diffraction and ^{1}H NMR and is suggested as:[51]

$$4\,AlCl_3 + 2\,Mg(HMDS)_2 \longrightarrow [Mg_2(\mu{-}Cl)_3 \cdot 6\,(THF)]^+[AlCl_3HMDS]^- + 3\,AlCl_2(HMDS). \tag{3.3}$$

Therefore, we assign the broad resonance at 101 ppm to $AlCl_3HMDS^-$. We note that a second resonance for $AlCl_2(HMDS)$ is not observed in our ^{27}Al NMR. It is not uncommon for a ^{27}Al resonance to be undetectably broad.[112,116] We propose that quadrupolar interactions around the Al center in $AlCl_2$HMDS cause the resonance to be too broad to be detected. The ^{27}Al NMR spectrum of the 0.7 M $AlCl_3$ + 0.35 $Mg(HMDS)_2$ solution is shown in Figure 3.5 and also exhibits a single resonance at 101 ppm, suggesting that $AlCl_2$HMDS is undetectable by ^{27}Al NMR independent of concentration.

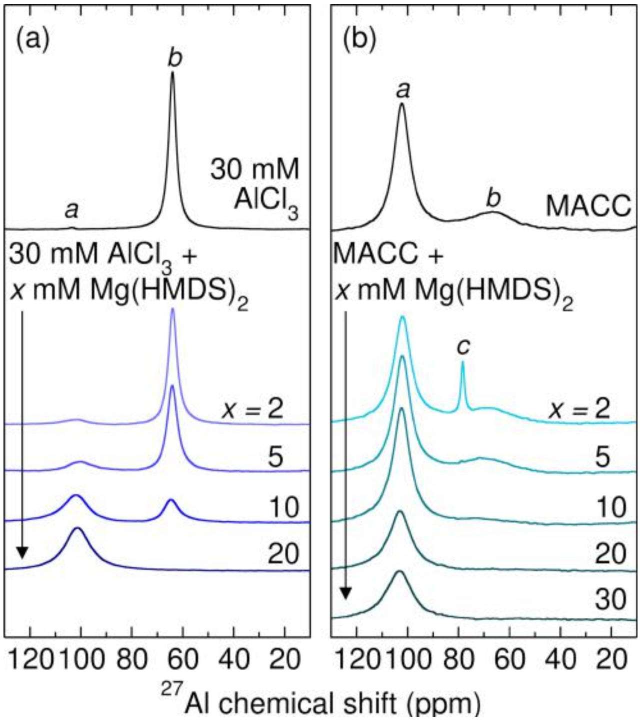

Figure 3.2: ^{27}Al NMR data of electrolytes. (a) ^{27}Al NMR of 30 mM $AlCl_3$ and 30 mM $AlCl_3$ + various concentrations of Mg(HMDS). Addition of $Mg(HMDS)_2$ causes the intensity of mode *b*, $AlCl_3{\cdot}2THF$, to decrease at the expense of a new, broad mode at 101 ppm ascribed to $AlCl_3HMDS^-$. (b) ^{27}Al NMR of MACC and MACC + various concentrations of $Mg(HMDS)_2$. Addition of $Mg(HMDS)_2$ to MACC causes resonance *a*, ascribed to $AlCl_4{}^-$, to broaden suggesting the formation of $AlCl_3HMDS^-$. The ^{27}Al spectra are referenced to $Al(NO_3)_3$ at 0 ppm. Tabulated fit values can be found in Table 3.2.

Next, we turn to the reactivity of $Mg(HMDS)_2$ with the MACC solution. The ^{27}Al NMR spectra of MACC and MACC with various concentrations of $Mg(HMDS)_2$ are shown in Figure 3.2b. The Al complexes in MACC are mostly $AlCl_4{}^-$, resonance *a*, with some unreacted $AlCl_3{\cdot}2THF$, resonance *b*.[88] Both species are observed because reaction (3.1) is in equilibrium. Thus, addition of excess $MgCl_2$ consumes

	resonance *a*		resonance *b*		resonance *c*	
	shift (ppm)	fwhm (ppm)	shift (ppm)	fwhm (ppm)	shift (ppm)	fwhm (ppm)
$AlCl_3$			64	3.78		
+ 2 mM $Mg(HMDS)_2$	101	9.6	64	4.18		
+ 5 mM $Mg(HMDS)_2$	101	12.2	64	5.23		
+ 10 mM $Mg(HMDS)_2$	101	12.5	64	7.06		
+ 20 mM $Mg(HMDS)_2$	101	12.4				
MACC	102	7.7	66	21.8		
+ 2 mM $Mg(HMDS)_2$	102	8.4	66	24.3	78	2.0
+ 5 mM $Mg(HMDS)_2$	102	8.4	70	22.1		
+ 10 mM $Mg(HMDS)_2$	102	8.7				
+ 20 mM $Mg(HMDS)_2$	102	10.9				
+ 30 mM $Mg(HMDS)_2$	102	12.1				

Table 3.2: Positions and Widths of the Resonances in ^{27}Al NMR Spectra

the unreacted $AlCl_3·2THF$ as evidenced by the loss of resonance *b* in the ^{27}Al NMR and the loss of the Al–Cl mode of $AlCl_3·2THF$ in the Raman spectrum (Figure 3.6).

The ^{27}Al NMR spectrum of MACC changes significantly upon addition of $Mg(HMDS)_2$. First, resonance *b* ascribed to unreacted $AlCl_3·2THF$ decreases in intensity with increasing $Mg(HMDS)_2$ concentration and completely disappears at 10 mM $Mg(HMDS)_2$. Concurrently, the full width at half maximum (fwhm) of resonance *a* increases from 7.7 ppm in MACC to 8.7 ppm in MACC + 10 mM $Mg(HMDS)_2$, and ultimately to 12.1 ppm in MACC + 30 mM $Mg(HMDS)_2$. The reactivity of $Mg(HMDS)_2$ in MACC is therefore similar to that in the 30 mM $AlCl_3$ solution to form $AlCl_3HMDS^-$. However, even after all the $AlCl_3·2THF$ is consumed at 10 mM $Mg(HMDS)_2$, resonance *a* continues to broaden with increasing $Mg(HMDS)_2$ concentration suggesting that $Mg(HMDS)_2$ also reacts with $AlCl_4^-$ to form $AlCl_3HMDS^-$. The increased fwhm is attributed to the exchange between multiple species which we suggest are $AlCl_4^-$ and $AlCl_3HMDS^-$. The ^{27}Al NMR spectrum of MACC + 30 mM $Mg(HMDS)_2$ contains a broad anionic resonance with a fwhm similar to that of the anionic resonance in 30 mM $AlCl_2$ + 20 mM $Mg(HMDS)_2$. The presence of $AlCl_3HMDS^-$ is further corroborated by the Raman spectrum of MACC + 30 mM $Mg(HMDS)_2$ (Figure 3.1), in which the $AlCl_4^-$ mode completely disappears and the $AlCl_3HMDS^-$ mode appears. Together, these results suggest that $Mg(HMDS)_2$ reacts not only with $AlCl_3·2THF$ as previously reported,[51] but also with $AlCl_4^-$ to yield $AlCl_3HMDS^-$.

A new, sharp resonance is observed at 78 ppm in MACC + 2 mM $Mg(HMDS)_2$ (resonance *c*) that disappears at higher concentrations of $Mg(HMDS)_2$ (Figure 3.2b). The narrow fwhm suggests that this Al-containing species is highly symmetric. The chemical shift of the resonance can be explained by either an anionic species more shielded than $AlCl_4^-$, or a neutral species more deshielded than $AlCl_3$. We hypothesize that the species is related to a reaction involving the Al complexes, H_2O, and Mg(HMDS)$_2$, as the intensity of the resonance is directly correlated to H_2O content and is only observed when Mg(HMDS)$_2$ is added to the solution. This result is corroborated by ^{1}H–^{29}Si 2D NMR data (*vide infra*).

^{1}H–^{29}Si Heteronuclear Multiple Bond Correlation (HMBC): Characterization of the various HMDS-containing species is achieved with ^{1}H–^{29}Si HMBC NMR spectroscopy. Although ^{29}Si has a natural abundance of 4.7% and a spin of 1/2, its long T_1 relaxation time requires long ^{29}Si NMR experiments and yields a low signal to noise ratio. The 2D ^{1}H–^{29}Si HMBC, on the other hand, enables the transfer of polarization from ^{1}H to ^{29}Si and the observation of correlations between Si and H that are separated by two and three bond-lengths away. Thus, cross peaks in ^{1}H–^{29}Si HMBC spectra will only be observed for HMDS-containing complexes. The 2D ^{1}H–^{29}Si HMBC spectra of control solutions containing various concentrations of Mg(HMDS)$_2$ are shown in Figure 3.3. The spectra of 2, 5, and 10 mM Mg(HMDS)$_2$ (Figure 3.3a–c) exhibit two cross peaks at {0.059, -10} ppm (peak A) and {0.047, 1} ppm (peak B) while 100 mM Mg(HMDS)$_2$ shows a single cross peak: peak A (Figure 3.3d). Peak B is also the only cross peak observed in the spectrum of H(HMDS) (Figure 3.3e), allowing us to assign peak B to either freely solvated HMDS or H(HMDS). Recall that in this paper, we refer to the anion as HMDS and the protonated anion as H(HMDS) for clarity. Peak A is therefore ascribed to HMDS coordinated to Mg^{2+}. The ^{29}Si chemical shifts of Mg(HMDS)$_2$ and H(HMDS) also align with previously reported values. Although the exact stoichiometry of the complexes in the solutions is unknown, we will simply refer to them as Mg(HMDS)$_2$ and H(HMDS) hereafter.

If we assume peak B is H(HMDS), then its presence in the Mg(HMDS)$_2$ solution would require the presence of a proton source which is likely trace water. To examine this hypothesis, different concentrations of H_2O are added to 100 mM Mg(HMDS)$_2$. The ^{1}H–^{29}Si HMBC spectra of these solutions are shown in Figure 3.3f–h. With increasing H_2O concentration, the intensity of the H(HMDS) cross peak (peak B) increases, and that of the Mg(HMDS)$_2$ cross peak (peak A) decreases (Figure 3.3f–h). Thus, we assign peak B to H(HMDS). When 200 mM H_2O is added, the Mg(HMDS)$_2$ cross peak is absent. Kang *et al.* have reported that heptamethyldisilazane, $CH_3N[Si(CH_3)_3]_2$, is able to scavenge trace amounts of H_2O.[99] Yamane *et al.* also proposed that H(HMDS) reacts with H_2O and forms $(CH_3)_3SiOSi(CH_3)_3$ and NH_3.[102] Here, we show that two equivalents of H_2O com-

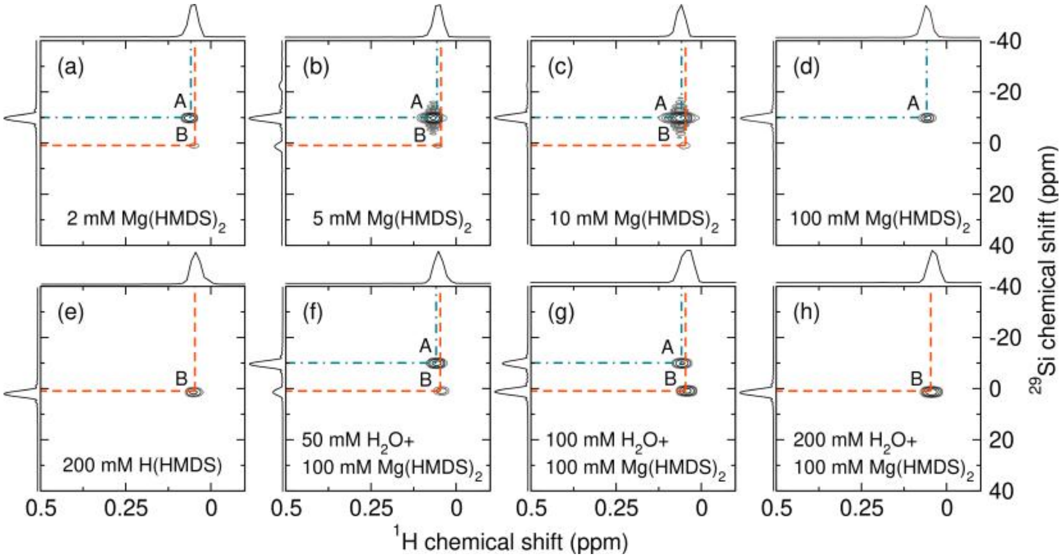

Figure 3.3: ^{1}H–^{29}Si HMBC spectra of Mg(HMDS)$_2$ with H_2O. ^{1}H–^{29}Si HMBC spectra of (a) 2, (b) 5, (c) 10, and (d) 100 mM Mg(HMDS)$_2$. Two cross peaks are observed: peak A which corresponds to Mg(HMDS)$_2$ and peak B which corresponds to H(HMDS). ^{1}H–^{29}Si HMBC spectra of (e) 200 mM H(HMDS) and 100 mM Mg(HMDS)$_2$ with (f) 50, (g) 100, and (h) 200 mM H_2O. Varying H_2O content with a fixed Mg(HMDS)$_2$ concentration reveals that the intensity of peak A decreases with increasing H_2O concentration and completely disappears when two equivalents of H_2O is present. Tabulated assignments can be found in Table 3.3. All spectra are referenced to a cross peak associated with silicone grease.[103]

pletely removes Mg(HMDS)$_2$. Thus, we hypothesize that Mg(HMDS)$_2$ reacts with H_2O in THF via the following reaction:

$$\mathrm{Mg(HMDS)_2 + 2\,H_2O \longrightarrow 2H(HMDS) + Mg(OH)_2.} \tag{3.4}$$

The presence of the H(HMDS) cross peak in the ^{1}H–^{29}Si HMBC spectra of 2, 5, 10 mM Mg(HMDS)$_2$, therefore, is attributed to the ability of Mg(HMDS)$_2$ to scavenge trace amounts of H_2O.

Next we discuss the ^{1}H–^{29}Si HMBC spectra of MACC with various concentrations of Mg(HMDS)$_2$ that are shown in Figure 4. Upon addition of Mg(HMDS)$_2$ to MACC, the Mg(HMDS)$_2$ cross peak (peak A) is not observed at any Mg(HMDS)$_2$ concentration (Figure 3.4a–d), suggesting the complete consumption of Mg(HMDS)$_2$ in MACC. The consumption of Mg(HMDS)$_2$ is consistent with the Raman spectroscopy results, but the ^{1}H–^{29}Si HMBC data are much more quantitative. In the ^{1}H–^{29}Si HMBC spectrum of the MACC + 2 mM Mg(HMDS)$_2$ solution, the H(HMDS) cross peak (peak B) is the most prominent peak. The presence of the H(HMDS) cross peak is attributed to the H_2O-scavenging effect of Mg(HMDS)$_2$.

The H_2O content in MACC originates mostly from the nominally anhydrous salts that are not perfectly anhydrous.[96] In MACC + 2 mM $Mg(HMDS)_2$, an additional cross peak is observed at {0.415, 31} ppm (peak C). Peak C is absent at higher concentrations of $Mg(HMDS)_2$, a trend also displayed by the 78 ppm resonance observed in the ^{27}Al NMR. To determine if peak C is indeed correlated to the 78 ppm resonance in ^{27}Al NMR, we measured the ^{1}H–^{29}Si HMBC spectra of MACC + 5 mM $Mg(HMDS)_2$ with 2 and 5 mM H_2O. Indeed, these solutions show both the 78 ppm ^{27}Al NMR resonance, as described above, and the peak C cross peak in the ^{1}H–^{29}Si HMBC (Figure 3.7). We hypothesize that an HMDS–containing Al species gives rise to these peaks and that this species only exists when the H_2O concentration is greater than that of $Mg(HMDS)_2$ added. A species that could be formed by reaction of HMDS-containing species with H_2O is trimethylsilanol, $(CH_3)_3SiOH$. Reaction of H(HMDS) with H_2O can cause cleavage of the Si–N bond to form $(CH_3)_3SiOH$.[102] To this end, we measured the ^{1}H–^{29}Si HMBC spectrum of trimethylsilanol ($(CH_3)_3SiOH$) (Figure 3.8), but the cross peak does not correspond to any cross peaks in the electrolyte spectra and cannot explain peak C. With the data presented here, we can only conclude that the 78 ppm resonance in the ^{27}Al NMR and peak C in the ^{1}H–^{29}Si HMBC spectra are associated with a Al-HMDS complex that forms in the presence of H_2O.

When $Mg(HMDS)_2$ is added to MACC at concentrations larger than 2 mM, the ^{1}H–^{29}Si HMBC spectra show a new cross peak labeled peak D in addition to peak A (Figure 3.4b–d), again indicating additional reactivity of $Mg(HMDS)_2$ beyond H_2O scavenging to form a new HMDS–containing species. Peak D is also observed in the ^{1}H–^{29}Si HMBC spectrum of the reference solution 0.7 M $AlCl_3$ + 0.35 M $Mg(HMDS)_2$ electrolyte (Figure 3.4e). Zhao-Karger *et al.* characterized the reference solution with ^{1}H NMR, and the ^{1}H chemical shift of peak D aligns with the reported ^{1}H chemical shift.[51] Zhao-Karger *et al.* assign the ^{1}H resonance to $AlCl_3HMDS^-$ because the ^{1}H shift lines up with that obtained from a solution of a redissolved $[Mg_2Cl_3^+][AlCl_3HMDS^-]$ crystal.[51] Thus, we assign peak D to $AlCl_3HMDS^-$. As more $Mg(HMDS)_2$ is added, peak D increases in intensity relative to peak B due to the limited concentration of H_2O, allowing $Mg(HMDS)_2$ to react with an Al–containing species to form $AlCl_3HMDS^-$.

When the concentration of $Mg(HMDS)_2$ is increased to 30 mM, peak E appears in the ^{1}H–^{29}Si HMBC spectrum (Figure 3.4d). The 0.7 M $AlCl_3$ + 0.35 M $Mg(HMDS)_2$ electrolyte also exhibits peak E (Figure 3.4e). We note that peak B does not appear

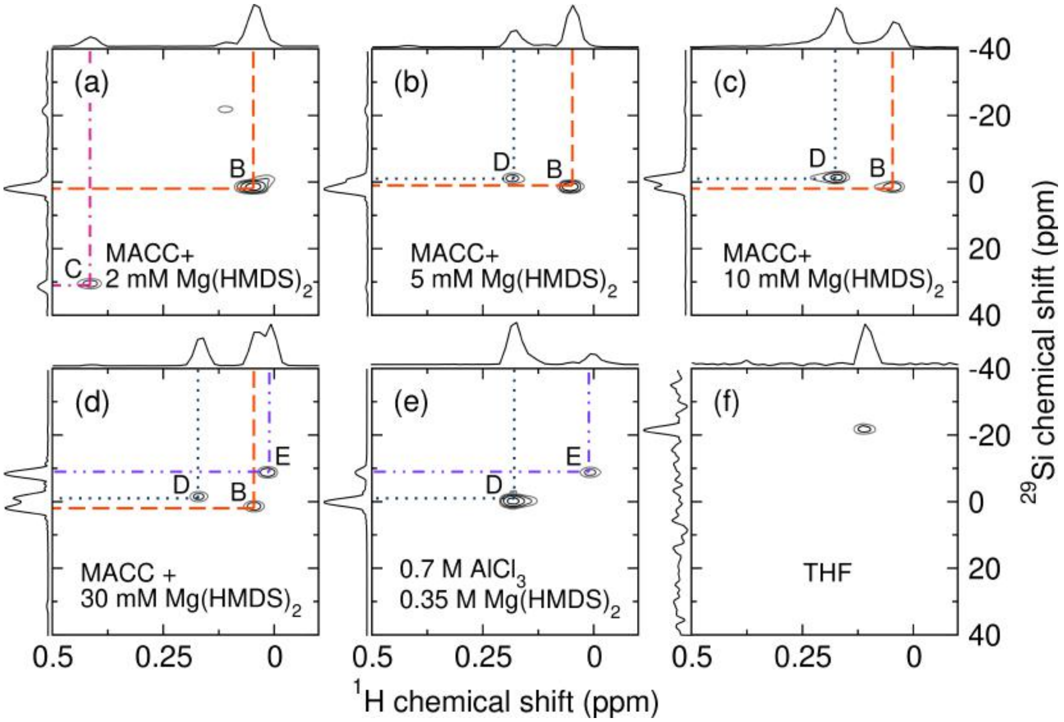

Figure 3.4: ^{1}H–^{29}Si HMBC spectra of MACC + Mg(HMDS)$_2$. ^{1}H–^{29}Si HMBC spectra of MACC + (a) 2, (b) 5, (c) 10, and (d) 30 mM Mg(HMDS)$_2$. All the spectra of MACC + Mg(HMDS)$_2$ solutions exhibit the H(HMDS) cross peak (peak B) due to reaction with H_2O. At Mg(HMDS)$_2$ concentrations higher than 2 mM, new cross peaks (peak D in 5 and 10 mM Mg(HMDS)$_2$, and peaks D and E in 30 mM Mg(HMDS)$_2$) are observed, which are also present in the (e) 0.7 M AlCl$_3$ + 0.35 M Mg(HMDS)$_2$ electrolyte. Peak D and E are attributed to $AlCl_3HMDS^-$ and $AlCl_2HMDS$, respectively, based on ^{1}H NMR.[51] (f) The ^{1}H–^{29}Si HMBC spectrum of THF shows one cross peak due to silicone grease,[103] which is used as reference in all of the spectra. Tabulated assignments can be found in Table 3.3.

peak label	A	B	C	D	E
assignment	$Mg(HMDS)_2$	H(HMDS)		$AlCl_3HMDS^-$	$AlCl_2HMDS$
solution	$\{^{1}H\ \delta,\ ^{29}Si\ \delta\}$ (ppm)	$\{^{1}H\ \delta,\ ^{29}Si\ \delta\}$ (ppm)	$\{^{1}H\ \delta,\ ^{29}Si\ \delta\}$ (ppm)	$\{^{1}H\ \delta,\ ^{29}Si\ \delta\}$ (ppm)	$\{^{1}H\ \delta,\ ^{29}Si\ \delta\}$ (ppm)
2, 5, 10 mM $Mg(HMDS)_2$	{0.059, -10}	{0.047, 1}			
MACC + 2 mM $Mg(HMDS)_2$		{0.047, 2}	{0.415, 31}		
MACC + 5 mM $Mg(HMDS)_2$		{0.048, 1}		{0.180, -1}	
MACC + 10 mM $Mg(HMDS)_2$		{0.047, 1}		{0.176, -1}	
MACC + 30 mM $Mg(HMDS)_2$		{0.046, 2}		{0.172, -1}	{0.012, -9}
0.7 M $AlCl_3$+ 0.35 M $Mg(HMDS)_2$				{0.179, -1}	{0.011, -9}

Table 3.3: Assignments of Chemical Shifts of HMDS–Containing Species from ^{1}H–^{29}Si HMBC NMR.

in the spectrum because of the relatively small concentration H_2O compared to that of HMDS–containing species in the solution. Zhao-Karger *et al.* assigned a resonance at 0.036 ppm in ^{1}H NMR to $AlCl_2HMDS$.[51] We propose that peak E is $AlCl_2HMDS$ as it shows a similar ^{1}H chemical shift as that reported by Zhao-Karger *et al.*[51] This result, combined with the ^{27}Al NMR result that the fwhm of the anioinc resonance increases with increasing $Mg(HMDS)_2$ concentration and the Raman spectroscopy data that show that the $AlCl_4^-$ mode decreases in intensity and completely disappears, suggests that the reaction between $Mg(HMDS)_2$ and $AlCl_4^-$ is able to form both $AlCl_3HMDS^-$ and $AlCl_2HMDS$, although the products are dependent on the $Mg(HMDS)_2$ concentration.

Merrill *et al.* have proposed that the mode at 651 cm^{-1} in the Raman spectrum of the 0.7 M $AlCl_3$ + 0.35 M $Mg(HMDS)_2$ electrolyte is ascribed to both $AlCl_3HMDS^-$ and $AlCl_2HMDS$. The Raman spectrum of MACC + 10 mM $Mg(HMDS)_2$ shown in Figure 3.1, whose ^{1}H–^{29}Si HMBC spectrum exhibits $AlCl_3HMDS^-$ but not $AlCl_2HMDS$, contains the 651 cm^{-1} mode. Therefore, we propose that $AlCl_3HMDS^-$ alone is able to give rise to the 651 cm^{-1} mode in Raman spectroscopy.

In ^{27}Al NMR, the resonance at 66 ppm, ascribed to unreacted $AlCl_3$ in MACC, disappears first with increasing $Mg(HMDS)_2$ concentration, which may suggest the reaction between $Mg(HMDS)_2$ and $AlCl_3$ (reaction (3.3)). However, the absence of peak D in the ^{1}H–^{29}Si HMBC spectra of MACC + 2, 5, and 10 mM $Mg(HMDS)_2$ suggests that reaction (3.3) is not the reaction at play. We hypothesize that in MACC + $Mg(HMDS)_2$, $Mg(HMDS)_2$ instead reacts with $AlCl_4^-$, and the consequent depletion of $AlCl_4^-$ causes the equilibrium in MACC preparation (reaction (3.1)) to shift to the products, consuming the trace amount of unreacted $AlCl_3$. This result also agrees with the Raman and ^{27}Al NMR spectra of 30:80 MACC which suggest that reaction (3.1) is at an equilibrium.

3.5 Discussion

Multitechnique characterization of the MACC electrolyte upon $Mg(HMDS)_2$ addition enables the identification of key reaction pathways and chemical products. Raman spectroscopy, ^{27}Al NMR, and ^{1}H–^{29}Si HMBC NMR results suggest two roles of $Mg(HMDS)_2$ in MACC. First, $Mg(HMDS)_2$ scavenges trace levels of H_2O in solution that would otherwise hinder Mg electrodeposition and stripping. H_2O can passivate the oxophilic Mg electrode surface by forming insulating MgO and $Mg(OH)_2$.[117] Addition of $Mg(HMDS)_2$ to solutions that contain H_2O results in the formation of H(HMDS) as evidenced by the ^{1}H–^{29}Si HMBC and Raman spectra. The intensity of the cross peak associated with H(HMDS) in the ^{1}H–^{29}Si HMBC data is dependent on the H_2O content of the solution prior to $Mg(HMDS)_2$ addition. Addition of $Mg(HMDS)_2$ to MACC solution indeed lowers the H_2O content as measured by Karl Fischer Titration.[96]

Although the removal of H_2O improves the electrochemistry, addition of $Mg(HMDS)_2$ to MACC forms more products than just H(HMDS), suggesting additional reactivity. Here, we show that $Mg(HMDS)_2$ can react with $AlCl_4^-$ in MACC to form $AlCl_3HMDS^-$. Evidence for the $AlCl_3HMDS^-$ product is provided by the 651 cm^{-1} mode in the Raman spectroscopy; a broad 102 ppm resonance observed in ^{27}Al NMR (resonance *a*) suggesting an asymmetric, four coordinate, anionic Al complex; and the {0.176, -1} ppm cross peak (peak D) in ^{1}H–^{29}Si HMBC NMR. Importantly, the ^{1}H–^{29}Si HMBC spectra of MACC + 5 and 10 mM $Mg(HMDS)_2$ solutions exhibit only two cross peaks, which we assign to H(HMBC) and $AlCl_3HMDS^-$, suggesting that HMDS–containing Mg species such as $MgHMDS^+$ or $MgCl_2HMDS^-$ are not present. Thus, $Mg(HMDS)_2$ reacts with complexes in the MACC solution until the additive is completely consumed. The resulting Mg species, therefore, must consist of only Mg, Cl, and THF. MACC + $Mg(HMDS)_2$ solutions remain transparent, suggesting that the solutions are free of insoluble $MgCl_2$ salts. $[Mg_2(\mu{-}Cl)_3 \cdot 6\,(THF)]^+$, on the other hand, has been demonstrated to be the active species in many Mg electrolytes.[51,84] Evidence for the presence of $[Mg_2(\mu{-}Cl)_3 \cdot 6\,(THF)]^+$ can be observed by analyzing the 210 cm^{-1} mode in the Raman spectra, which is indicative of the C_{3v} symmetric dinuclear complex.[104] In fact, the 210 cm^{-1} mode intensity in the Raman spectrum of MACC + 10 mM $Mg(HMDS)_2$ is slightly greater than that of MACC, providing further evidence for $[Mg_2(\mu{-}Cl)_3 \cdot 6\,(THF)]^+$ as a reaction product (Figure 3.9). Based on the spectroscopic analysis, we propose the following reaction:

$$4\,AlCl_4{}^- + 2Mg(HMDS)_2 \longrightarrow 4AlCl_3HMDS^- + [Mg_2(\mu{-}Cl)_3 \cdot 6\,(THF)]^+ + Cl^-. \tag{3.5}$$

With $AlCl_3HMDS^-$ and $[Mg_2(\mu{-}Cl)_3 \cdot 6\,(THF)]^+$ as products, the reaction between $AlCl_4{}^-$ and $Mg(HMDS)_2$ necessitates the formation of Cl^- as a product to complete the stoichiometry and charge balance the reaction. Reaction (3.5) shows that Cl^- is chemically produced in the solution, which has been previously shown to activate

MACC.[88] Addition of $Mg(HMDS)_2$ replaces the electrolytic conditioning process by producing Cl^- chemically instead of electrolytically. Both $[Mg_2(\mu\text{–}Cl)_3 \cdot 6\,(THF)]^+$ and Cl^-, species that have been contributed to the activation of conditioned MACC,[88] are products of the reaction. Only 5 mM $Mg(HMDS)_2$ is required to suppress Al deposition and increase Coulombic efficiency resulting in a conditioned electrolyte on cycle 1,[96] and the $Mg(HMDS)_2$ is reacting not only to form Cl^- but also to scavenge H_2O. Therefore, minimal concentrations of Cl^- are required to activate the electrolyte, suggesting the Cl^- is active only at the interface. Freely solvated Cl^- is difficult to measure directly in solution especially at the concentrations we expect here. Previous attempts at ^{35}Cl NMR, for example, have observed fast exchange with other Cl–containing complexes, preventing direct measurement of solvated Cl^-.[88] We have considered using chloride ion-selective electrodes; however, the electrodes are limited to aqueous solutions.

In addition to the spectroscopic results, the aging behavior of MACC + $Mg(HMDS)_2$ also suggests the formation of Cl^-. MACC + $Mg(HMDS)_2$ ages in a similar fashion to conditioned MACC in that allowing the electrolyte to sit at open circuit results in the return of Al deposition current and a decrease in Coulombic efficiency.[96] We previously showed that the aging of MACC + $Mg(HMDS)_2$ is not due to the introduction of impurities such as H_2O.[96] Electrolytic conditioning of both MACC and aged MACC + $Mg(HMDS)_2$ causes a reduction in the cathodic current associated with Al deposition and an increase in current associated with reversible Mg^{2+} deposition and stripping.[88,96] The improvement after conditioning has been attributed to the formation of mestasable solvated Cl^- .[88] In aged MACC solutions, we propose that Cl^- is depleted over time due to its metastability, which deactivates the electrolyte and requires electrochemical conditioning.

The presence of solvated Cl^- is able to explain not only the activation of MACC, but also the aging experiment and spectroscopic results. Cl^- has been proposed to actively partake in the charge-transfer mechanism at the Mg electrode-electrolyte interface.[94] Cl^- can also depassivate the Mg electrode by dissolving surface oxides or removing adsorbed solvent molecules.[117] Because Cl^- aids Mg deposition and stripping at the interface, only a small amount is necessary to activate the electrolyte.

Next we consider the contributions of H_2O scavenging vs. the formation of Cl^- upon addition of $Mg(HMDS)_2$ on the electrochemistry. ^1H–^{29}Si HMBC spectra of MACC + $Mg(HMDS)_2$ suggest that $Mg(HMDS)_2$ reacts first with H_2O to scavenge trace amounts of H_2O prior to undergoing reaction with $AlCl_4^-$. The biggest cross peak in the ^1H–^{29}Si HMBC spectrum of MACC + 2 mM $Mg(HMDS)_2$ is the H(HMDS) resonance, and the spectrum is free of the $AlCl_3HMDS^-$ cross peak. Reaction (3.5), and thus the formation of Cl^-, has not yet occurred at these concentrations. The CV using MACC with 2 mM $Mg(HMDS)_2$ indeed shows better behavior compared to MACC with increased Coulombic efficiency and decreased Al^{3+} deposition.[96] Although the undesired Al^{3+} deposition decreases greatly, it is not eliminated as is observed in MACC + 5 or 10 mM $Mg(HMDS)_2$. This result suggests that H_2O-scavenging indeed improves electrochemical performance of MACC, but only to an extent. Only after enough $Mg(HMDS)_2$ is added to MACC to undergo reaction (3.5) is Al deposition completely suppressed.[96] We also note that in MACC + 5 and 10 mM $Mg(HMDS)_2$, Al^{3+} deposition is completely suppressed in the absence of the unidentified cross peak in ^{27}Al NMR and ^1H–^{29}Si HMBC of MACC + 2 mM $Mg(HMDS)_2$, suggesting that the species responsible for these peaks does not actively participate in activating the MACC electrolyte. We hypothesize that free Cl^- formed from reaction (3.5) decorates the electrode surface to facilitate Mg deposition and stripping.

3.6 Conclusions

$Mg(HMDS)_2$ addition, even at minor concentrations, to MACC results in a conditioning-free electrolyte from cycle 1. Speciation after $Mg(HMDS)_2$ addition characterized by Raman spectroscopy, ^{27}Al NMR spectroscopy, and ^1H–^{29}Si HMBC spectroscopy allows for the identification of reactions responsible for Al deposition suppression and increased electrochemical reversibility of Mg deposition and stripping. Improved electrochemistry is achieved with a small concentration of $Mg(HMDS)_2$, implying that changes occur at the electrode interface to facilitate Mg electrodeposition and stripping. Spectroscopic results reveal two roles of $Mg(HMDS)_2$ that affect interactions at the electrode interface. First, $Mg(HMDS)_2$ scavenges trace levels of H_2O, likely preventing the formation of passive films of MgO and $Mg(OH)_2$ on the Mg surface. Second, $Mg(HMDS)_2$ reacts with $AlCl_4^-$ to release Cl^- which then activates Mg electrodeposition and stripping at the interface. The generation of solvated Cl^- also explains the aging behavior of MACC + $Mg(HMDS)_2$, which is similar to the aging behavior of conditioned MACC, further corroborating the presence of solvated Cl^- in MACC + $Mg(HMDS)_2$. The role of free Cl^- at the interface is still unclear as we are not able to probe it directly. The Cl^- could be directly involved at the interface or its generation could cause the formation of a secondary product that is active at the interface. The ability of small interfacial changes to activate Mg electrolytes demonstrates that it is crucial to understand the mechanism of Mg electrodeposition and stripping in designing efficient Mg electrolytes.

3.A Supplementary Information

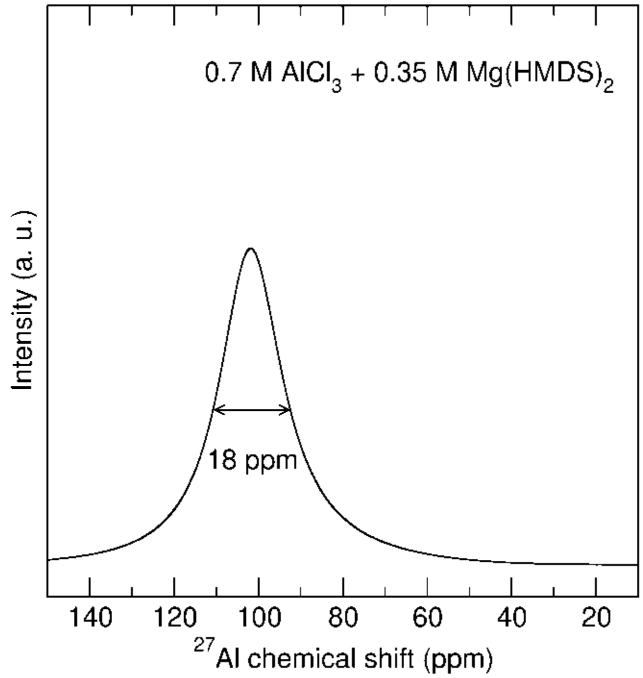

Figure 3.5: ^{27}Al NMR of 0.7 M $AlCl_3$ + 0.35 M $Mg(HMDS)_2$. Only one broad resonance is observed at 102 ppm with a full width at half maximum of 18 ppm.

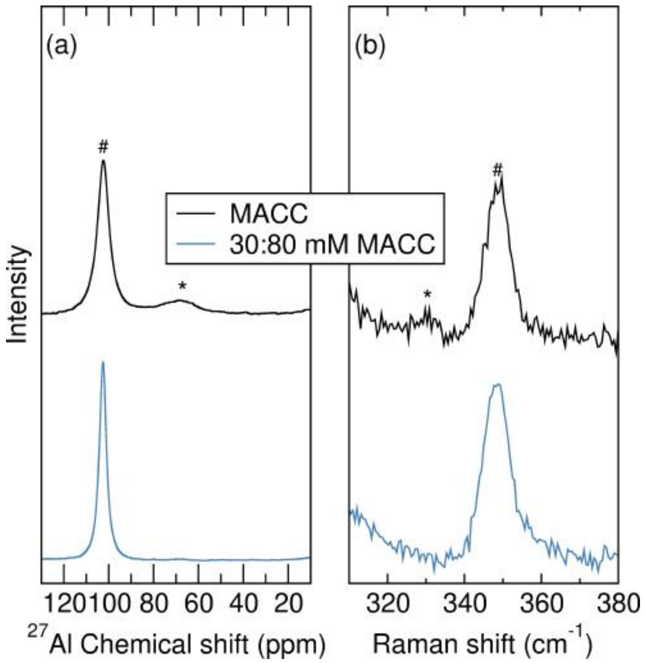

Figure 3.6: ^{27}Al NMR and Raman spectra of MACC and 30:80 mM MACC. (a) ^{27}Al NMR and (b) Raman spectra of MACC and 30:80 mM MACC. The 66 ppm resonance present in MACC (*), which corresponds to $AlCl_3$, is not present in 30:80 mM MACC. Similarly, the Al–Cl mode of $AlCl_3$ at 328 cm^{-1} present in MACC (*) is not present in 30:80 mM MACC.

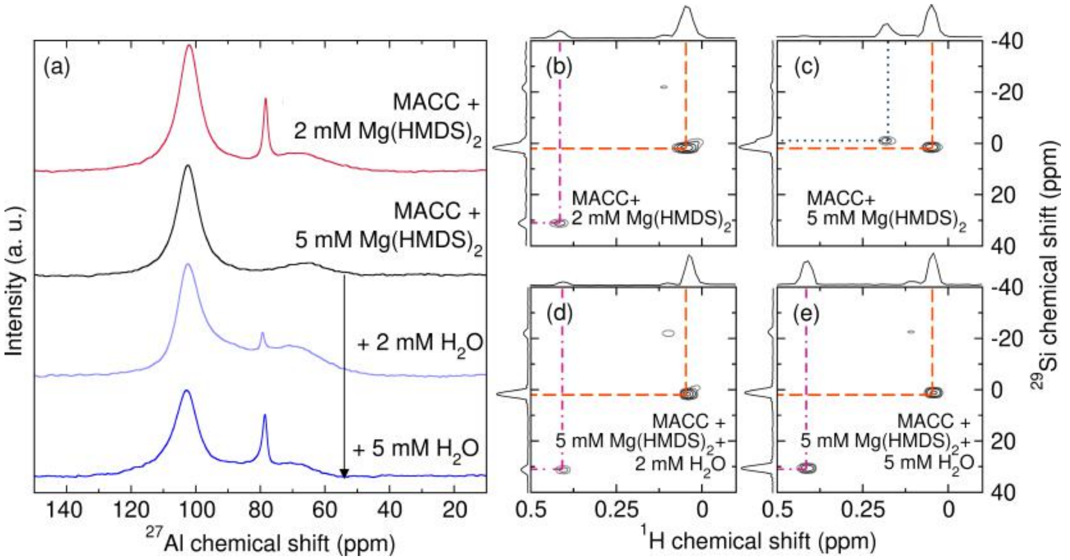

Figure 3.7: ^{27}Al NMR spectra and ^{1}H–^{29}Si HMBC spectra of MACC + x mM Mg(HMDS)$_2$. (a) ^{27}Al NMR spectra and ^{1}H–^{29}Si HMBC spectra of MACC (b) + 2 mM Mg(HMDS)$_2$, (c) + 5 mM Mg(HMDS)$_2$, (d) + 5 mM Mg(HMDS)$_2$ + 2 mM H_2O, (e) + 5 mM Mg(HMDS)$_2$ + 5 mM H_2O. The 78 ppm resonance in ^{27}Al NMR and the {0.415, 31} ppm cross peak in ^{1}H–^{29}Si HMBC are not present in MACC + 5 mM Mg(HMDS)$_2$, but appear in the presence of H_2O.

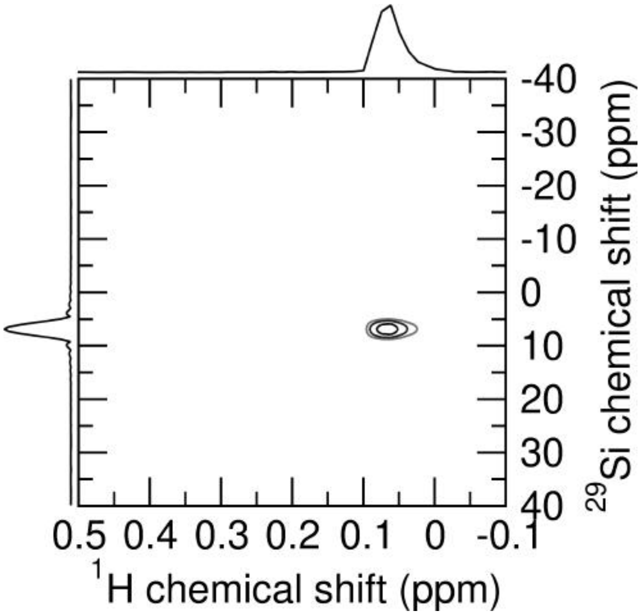

Figure 3.8: ^{1}H–^{29}Si HMBC spectrum of trimethylsilanol ($(CH_3)_3SiOH$). ^{1}H–^{29}Si HMBC spectrum of trimethylsilanol ($(CH_3)_3SiOH$), whose cross peak is located at {0.066, 7} ppm.

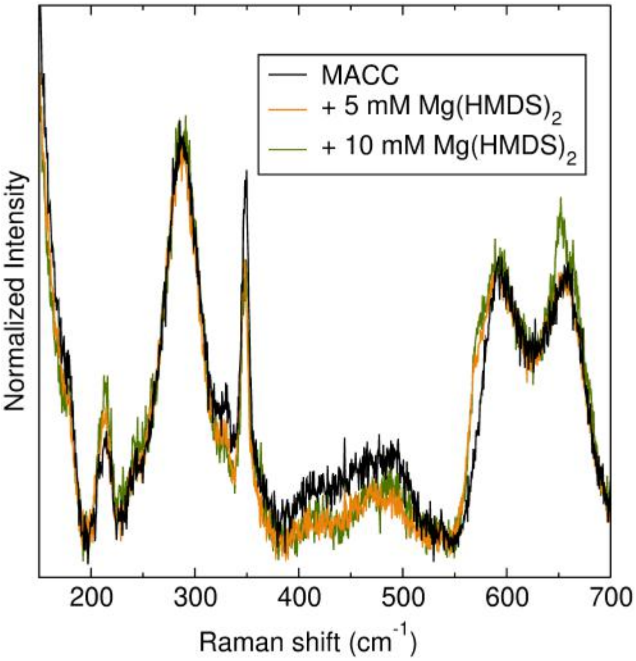

Figure 3.9: Raman spectra of as-prepared MACC, MACC + 5, and 10 mM Mg(HMDS)$_2$ overlayed on top of one another. These spectra are the same spectra as in Figure 1. All intensities are normalized to a THF mode at 913 cm^{-1}. With increasing Mg(HMDS)$_2$ concentration, the $[Mg_2(\mu{-}Cl)_3 \cdot 6\,(THF)]^+$ mode at 210 cm^{-1} increases while the $AlCl_4^-$ mode at 347 cm^{-1} decreases in intensity. Also, two new modes develop at 569 cm^{-1} and 651 cm^{-1}.

Chapter 4

PROMOTING REVERSIBILITY OF MULTIELECTRON REDOX IN ALKALI-RICH SULFIDE CATHODES THROUGH CRYOMILLING

This chapter has been adapted from:

(1) **Kim, S. S.**; Agyeman-Budu, D. N.; Zak, J. J.; Dawson, A.; Yan, Q.; Cában-Acevedo, M.; Wiaderek, K. M.; Yakovenko, A. A.; Yao, Y.; Irshad, A.; Narayan, S. R.; Luo, J.; Nelson Weker, J.; Tolbert, S. H.; See, K. A. Promoting Reversibility of Multielectron Redox in Alkali-Rich Sulfide Cathodes through Cryomilling. *Chem. Mater.* **2022**, 3236–3245,

Contributions: S.S.K. conceived, designed, and performed experiments, and wrote the manuscript. **DOI:**10.1021/acs.chemmater.2c00030

4.1 Abstract

Conventional cathodes for Li-ion batteries (LIBs) are reaching their theoretical capacity limits. One way to meet the growing demands for high-capacity LIBs is by developing so-called Li-rich cathode materials that greatly benefit from additional capacities from anionic moieties in the structure. Li-rich materials are intrinsically subject to higher degrees of (de)intercalation, leaving the particles more prone to fractures and thus rapid capacity fade. Alkali-rich $LiNaFeS_2$ reversibly cycles with capacities exceeding 300 mAh g^{-1}, but its capacity fades faster than an isostructural material Li_2FeS_2. Using synchrotron–based transmission X-ray microscopy (TXM), we demonstrate that capacity fade of $LiNaFeS_2$ stems from particle fractures in the first charge cycle. We improve the cycling performance of $LiNaFeS_2$ by means of cryomilling, which enhances capacity retention at cycle 50 by 76%. Through crystallographic and morphological characterization techniques, we confirm that cryomilling not only decreases particle and crystallite size while increasing microstrain, but also prevents particles from fracturing. Cryomilling is a powerful tool to engineer nanoscale battery materials, and TXM allows the direct observation of morphological changes of the particles, which can be leveraged to develop next-generation cathode materials for LIBs.

4.2 Introduction

Since their commercialization in the 1990s, Li-ion batteries (LIBs) have been deeply integrated in the modern technological world. LIBs power electric vehicles and have enabled the rapid development of portable electronic devices.[118,119] The cathode of LIBs most often takes the form LiMO$_2$ (M = a combination of transition metals), in which charge compensation can be attributed formally to transition metal redox during the topotactic (de)intercalation of Li$^+$. Although the first widely used intercalation–type cathode material LiCoO$_2$ could only reversibly cycle 0.5 equivalents of Li, partial substitution of other metals such as Ni, Mn, and Al, has improved the structural stability at higher degrees of Li$^+$ deintercalation and thus increased energy density of LIBs.[15–18]

As the experimental capacities of oxide materials based on transition metal redox are reaching their theoretical capacity limits, efforts to discover new chemistries that increase the cathode capacity are growing. A promising way to greatly increase the theoretical capacity is by leveraging multielectron redox, i.e., more than one electron stored per transition metal through the redox activity of anions.[120–123] However, many Li-rich oxide materials suffer from irreversible capacity loss and voltage fade due to structural transformations stemming from unstable electronic configurations as a result of anion redox at high potentials.[120,124–126] Interestingly, the substitution of redox inactive metals Sn^{4+} and Ti^{4+} into Li$_2$RuO$_3$ was used to demonstrate that Li$_2$Ru$_{1-y}$Sn$_y$O$_3$ exhibits superior voltage retention compared to Li$_2$Ru$_{1-y}$Ti$_y$O$_3$ due to the bigger size of Sn which prevents it from migrating to the tetrahedral site.[120,127,128] Thus, structural stability is an integral component to promote reversibility of anion redox.

Also critical is understanding the morphological response on the particle scale to continued removal and insertion of charge carrier ions at high degrees of (de)lithiation. LIB cathodes experience intercalation-induced stress and strain during cycling. Accelerated decay in battery performance in materials such as NMC 811 has been attributed to significant anisotropic lattice changes and subsequent fractures during cycling.[129,130] Multielectron Li-rich materials intrinsically undergo higher degrees of (de)intercalation compared to the conventional LIB cathodes, leaving the materials more prone to volumetric changes and deformations. To isolate the effect of strain upon large degrees of intercalation, we highlight alkali-rich sulfides that do not suffer from drastic structural rearrangements and irreversible capacity loss in cycle 1, Li$_2$FeS$_2$ and LiNaFeS$_2$. Previously, we reported that both Li$_2$FeS$_2$ and

$LiNaFeS_2$ exhibit $Fe^{2+/3+}$ oxidation followed by S^{2-} oxidation into the formation of persulfide ($(S_2)^{2-}$).[131] However, while both materials exhibit similar spectroscopic behavior, the capacity of $LiNaFeS_2$ fades faster, presumably due to the large strain induced by the incorporation of Na in the lattice.[131]

In this work, we turn to cryogenic milling, or cryomilling, to engineer the particle structure of $LiNaFeS_2$ in an effort to accommodate some of the strain associated with combined cation and anion redox. Cryomilling is the mechanical grinding of powders within a cryogenic medium–liquid nitrogen in this case–and has been widely used to fabricate nanostructured materials due to its ability to control the grain size.[132–135] Compared to ball milling conducted at room temperature, cryomilling effectively reduces the particle and grain size while minimizing heat-induced thermal damage to the material. The development of nanocrystalline grains is also often accompanied by an increase in defect density in the material such as dislocations and stacking faults.[132,136] In conjunction with X-ray diffraction (XRD), scanning electron microscopy (SEM), and transmission electron microscopy (TEM), we employ transmission X-ray microscopy (TXM) to characterize particle morphology. TXM is a non-invasive imaging technique that allows investigations of bulk internal structures.[137] Tunable incident X-ray energy offers element-specific chemical information, enabling the direct observation of changes in the particle morphology.[138] TXM has been widely used to monitor volume changes and fractures and to engineer nanoscale architecture.[139–143]

Here, we explore changes in the particle morphology and the electrochemical performance of as-prepared $LiNaFeS_2$ and cryomilled $LiNaFeS_2$ during cycling. XRD, SEM, and TEM reveal that cryomilling increases microstrain through the introduction of defects and decreases crystallite size while preserving its crystal structure. Importantly, we find that cryomilled $LiNaFeS_2$ demonstrates superior electrochemical performance compared to as-prepared $LiNaFeS_2$. TXM shows that particle fracturing occurs in as-prepared $LiNaFeS_2$ with cycling which causes rapid capacity fade while cryomilled $LiNaFeS_2$ is free of fractures due to the high defect density that helps accommodate strain associated with Na removal.

4.3 Experimental Section

Material Preparation

All materials were prepared in an Ar-filled glovebox in which O_2 and H_2O levels were < 1 ppm. $LiNaFeS_2$ was prepared using traditional solid state methods according to a previously reported protocol by Hansen *et al.*, from Li_2S (Beantown Chemical, 99.9%), Na_2S (prepared from the elements), Fe (Acros Organics, 99.0%) and S_8 (Acros Organics, >99.5%).[131] Stoichiometric powders of Li_2S, Na_2S, Fe, and S_8 were ground and pressed into pellets of up to 500 mg and sealed in an evacuated vitreous silica ampule. The reactants were heated at 2 °C min^{-1} to 500 °C, dwelled for 96 hours before cooling to room temperature. The resulting black pellet was ground into powder in the glovebox.

The cryomill process was conducted with a Retsch Cryomill. The ball mill jar was cooled with liquid nitrogen circulation, and the milling temperature was maintained at -196 °C with the Autofill System from the cryomill machine. $LiNaFeS_2$ (500 mg) was placed in an air-tight stainless-steel jar (65 mL) with six stainless-steel balls (5 mm diameter), resulting in a ball-to-powder ratio of 6:1 by mass. The sample was first pre-cooled for 15 min, and the milling process was performed for 2 h. The sample preparation and collection were conducted inside an Ar–filled glovebox.

Material Characterization

Powder X-ray diffraction (XRD) experiments were conducted at Stanford Synchrotron Radiation Lightsource (SSRL). Powder samples were sealed in an argon glovebox between Kapton tape and further sealed in an aluminized mylar pouch for transportation and X-ray exposure. XRD was performed at SSRL beamline 11-3 in transmission geometry. X-ray energy used was 12.70 keV (λ = 0.9763 Å). Samples were exposed to the beam for 30 seconds or 60 seconds, to increase signal due to smaller sample size. LaB_6 was placed at the same sample-to-detector distance as the powder samples for use as a calibration standard. Data integration and reduction was performed using wxDiff and GSAS-II.[144]

Scanning electron microscopy of as-prepared $LiNaFeS_2$ and cryomilled $LiNaFeS_2$ powders was performed using a ZEISS 1550VP field emission SEM with an acceleration voltage of 10 kV at 50,000 magnification. The samples were transported to the SEM air-free but were briefly exposed to air (less than 10 s) during sample loading into the SEM chamber.

Transmission electron microscopy data of as-prepared $LiNaFeS_2$ and cryomilled $LiNaFeS_2$ powders were collected using an FEI Tecnai Polar (F30) TEM at an accelerating voltage of 300 keV. TEM samples were prepared by dry transfer of the powders onto a C-Flat holey carbon Cu grid (Electron Microscopy Sciences).

Two-dimensional X-ray images of the prepared samples were collected utilizing full-field Transmission X-ray Microscopy at the 6-2c beamline at SSRL. The beam to the hutch is from SPEAR3, a 3-GeV storage ring, which operates in a top-off mode at 500 mA and is fed through a 56-pole, 0.9 Tesla wiggler. The microscope has spatial resolution of 30 nm and a field of view of around 30 μm. The X-ray energy was tuned to 7.2 keV (with a typical intensity of 10^{13} photons s^{-1}), which is 88 eV above the Fe absorption edge to enhance the image contrast of particles. For each sample position, ten 1 s exposure images were taken for averaging to obtain good image quality. Additional reference exposures were taken in air without the sample in the beam path. The reference images are for pixel-to-pixel image normalization and background removal. Normalizing also takes into account for any beam instability and intensity drift, as well as removing image artifacts such as scratches on the scintillator.

Operando X-ray diffraction studies were performed at beamline 17-BM-B ($\lambda = 0.24146$ Å) at the Advanced Photon Source, Argonne National Laboratory in AMPIX cells. Electrodes were prepared and cells were assembled in an Ar-filled glovebox. Working electrodes were 10 mm pellets (around 21.0 mg in total mass) pressed under uniaxial pressure consisting of active material, carbon black (Vulcan XC 72R), and PTFE (Sigma-Aldrich) in a ratio of 60:20:20 (wt%), respectively. Cells consisted of a Li metal foil as a combined counter and reference electrode, a glass fiber separator, and LP100 electrolyte (1 M $LiPF_6$ in ethylene carbonate, propylene carbonate, and dimethyl carbonate at 1:1:3 by volume). Cells were placed in a motor-controlled sample holder to switch between cells during experimentation and were cycled galvanostatically in the beamline using a Maccor 4300 battery cycler between 3 V and 1.7 V at C/10 based on 1 e^- per formula unit. LaB_6 standards in each sample position were used as reference to calibrate the image controls for integration of 2D diffraction images. Data analysis was carried out using the GSAS-II program.[144]

Electrochemical Characterization

All cell preparations were conducted inside Ar-filled gloveboxes in which H_2O and O_2 levels were below 0.1 ppm. As-prepared $LiNaFeS_2$ and cryomilled $LiNaFeS_2$ were mixed with polytetrafluoroethylene (PTFE, Sigma-Aldrich) and Super P carbon (Alfa Aesar, ≥99%) at a ratio of 3:1:1 by mass to make composite electrodes. The composite mixture was ground with a mortar and pestle and pressed into 0.25 inch diameter pellets with a hand driven arbor press. Therefore, the resulting active material mass loading of the electrodes in this configuration is 19 mg/cm^2. 2032 coin cells were prepared with polished Li metal counter/reference electrodes, dried 18 mm diameter glass fiber separators (Whatman GF/D), and 11 drops of the electrolyte (approx. 165 mg). The electrolyte used was a 1 M solution of $LiPF_6$ (Sigma-Aldrich, ≥99.99%) in a 1:1:3 mixture of ethylene carbonate (Sigma-Aldrich, >99%), propylene carbonate (Sigma-Aldrich, >99%), and dimethyl carbonate (Sigma-Aldrich, >99%) by volume. All potentials reported here are in reference to the Li metal counter/reference electrode potential, which is approximated to equal to that of Li/Li^+. Galvanostatic cycling data were collected at a rate of C/10 based on 1 e^- per formula unit between 2.8 V and 1.8 V. Galvanostatic intermittent titration technique (GITT) was conducted at a rate of C/10 based on 1 e^- per formula unit for 20 minutes alternating with 4 h open circuit hold steps between 3 V and 1.7 V. Electrode porosity and mass loading could affect the measured overpotentials. Here, the electrode loading is held constant (19 mg/cm^2) and the electrodes are fabricated with 10 mg of material pressed into 0.25 inch pellets yielding electrode thicknesses for the as-prepared and cryomilled materials of 0.32 mm and 0.31 mm, respectively. Thus, the electrode porosities are similar between the two.

Electrochemical impedance spectroscopy (EIS) measurements were performed in the potentiostatic mode on a VersaStat MC electrochemical workstation. The impedance was recorded over the frequency range of 100 kHz to 50 mHz with a sinusoidal excitation voltage of ±5 mV. Spectra were collected at different states of charge (SoCs), by charging or discharging the cell at C/10 rate in steps of 0.1x (where x is the total number of moles of lithium inserted/ per mole of the cathode material) between 3 V and 1.7 V. The cell was allowed to relax to an equilibrium voltage after each charge or discharge step before the EIS data were collected. Data were analyzed using ZSimpWin software for both samples. The experimental impedance data fits within 5% error when simulated using a modified Randles circuit, R_s (Q | (R_{ct} W)). Instead of an ideal capacitor, a constant phase element, Q was used to model the double layer capacitance in consideration of surface heterogeneities. The 45° tail at the low frequency end due to semi–infinite linear diffusion of electroactive ions was modeled by the Warburg element (W).

4.4 Results

Structural Characterization

The structures of as-prepared $LiNaFeS_2$ and cryomilled $LiNaFeS_2$ are characterized by synchrotron XRD. The powder XRD patterns with quantitative Rietveld refinement of as-prepared $LiNaFeS_2$ and cryomilled $LiNaFeS_2$ are shown in Figure 4.1.

$LiNaFeS_2$, isostructural to Li-rich sulfide Li_2FeS_2, adopts the P$\bar{3}$m1 space group and consists of layers of edge-sharing octahedral Na separated by layers of edge-sharing tetrahedral mixed Fe/Li.[131] Sharp diffraction peaks of $LiNaFeS_2$ and the presence of only one very small impurity at 1.12 Q in the difference curve indicate the formation of a pure crystalline phase (Figure 4.1a).

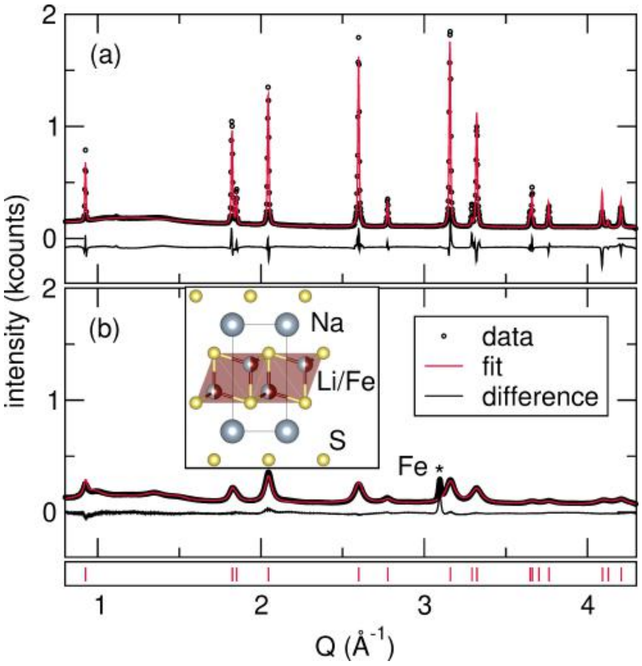

Figure 4.1: Synchrotron powder XRD patterns with quantitative Rietveld refinements of (a) as-prepared $LiNaFeS_2$ and (b) cryomilled $LiNaFeS_2$. The tick marks indicate the Bragg reflection locations of $LiNaFeS_2$ with the space group $P\bar{3}m1$. The cryomilled material shows much broader and less intense peaks, consistent with increased microstrain and/or smaller crystallite size.

Cryomilling $LiNaFeS_2$ results in broadened diffraction peaks (Figure 4.1b). Peak broadening stems from structural changes that lead to a non-ideal lattice periodicity, such as increased microstrain and smaller crystallite size. Cryomilling induces non-uniform distortions in the lattice by introducing a large amount of defects that increase microstrain in the structure. By the same token, cryomilling creates more grain boundaries and thus decreases the crystallite size in the particle. During the Rietveld refinement process, the diffraction patterns of cryomilled $LiNaFeS_2$ can be fit by varying one parameter between microstrain and crystallite size, or both concurrently. The contributions are decoupled with the Williamson-Hall analysis (Figure 4.9), an integral breadth method in which size- and microstrain-induced broadening are isolated by treating them as additive components.[145] The Williamson-Hall analysis suggests that both effects are present, with the crystallite size decreasing by an order of magnitude and microstrain increasing by a factor of four in cryomilled $LiNaFeS_2$.

Next, the particle morphology and size are probed with SEM and the images are shown in Figure 4.2a and b. SEM micrographs of as-prepared $LiNaFeS_2$ reveal that particles of as-prepared $LiNaFeS_2$ appear irregular in the arrangement of facets, with no apparent ordering features (Figure 4.2a). The particle sizes are widely distributed with an average particle size of 540 nm ± 480 nm (one standard deviation). Cryomilling for 4 h results in more fragmented particles that are homogeneously distributed in particle size, with the average size of 170 nm ± 220 nm, while maintaining the apparent irregularity in the particle morphology (Figure 4.2b). We note that many small particles observed in the SEM micrograph aggregate into clusters that cannot be distinguished as individual particles after binarization. Thus, the average size reported here is likely an overestimate. SEM confirms that there is a significant decrease in the particle size as well as an increase in particle size homogeneity as a result of cryomilling. Although the change in the domain size cannot be directly observed with SEM, it can be inferred that reducing the particle size concomitantly decreases the domain size within the particle.

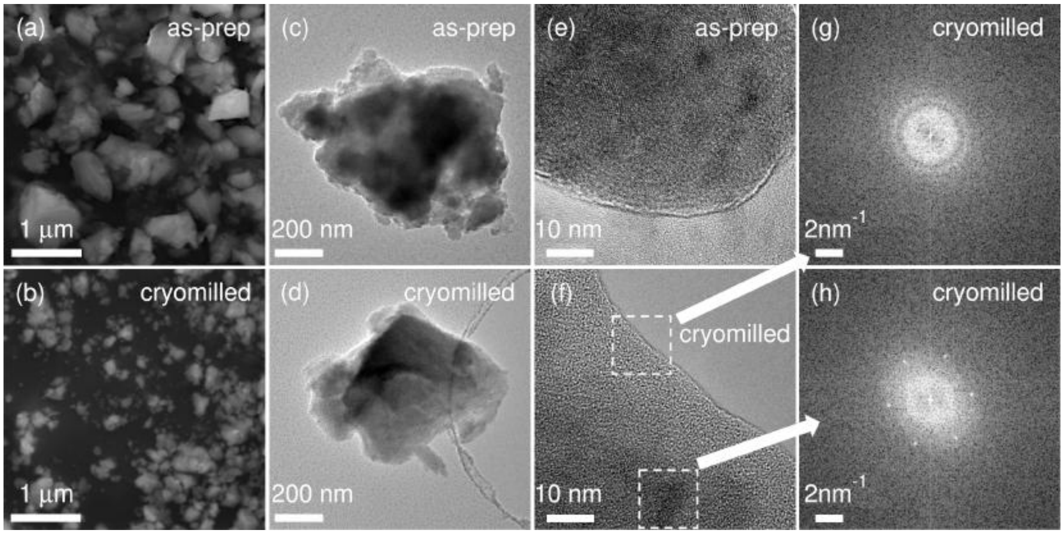

Figure 4.2: SEM images of (a) as-prepared $LiNaFeS_2$ with the average particle size 540 nm ± 480 nm and (b) cryomilled $LiNaFeS_2$ with the average particle 170 nm ± 220 nm. High-resolution TEM images of (c) as-prepared $LiNaFeS_2$ and (d) cryomilled $LiNaFeS_2$ along with magnified images of (e) as-prepared $LiNaFeS_2$ and (f) cyromilled $LiNaFeS_2$. FFT at the (g) surface region and (h) bulk region of the cryomilled $LiNaFeS_2$ particle. TEM collected by Dr. Miguel Caban-Acevedo.

Additional structural information is obtained with TEM. High-resolution images of as-prepared $LiNaFeS_2$ and cryomilled $LiNaFeS_2$ are shown in Figure 4.2c and d, respectively. Magnified micrographs of these particles (Figure 4.2e and f) reveal that as-prepared $LiNaFeS_2$ is more crystalline, as indicated by the presence of more and larger regions that show lattice fringes. This is particularly true near the edges of the particles (Figures 4.10 and 4.11). In contrast, fewer crystalline domains are observed in the cryomilled particle. Also, the fringes only exist in the bulk of the particle and the surface of the cryomilled particle appears amorphous (Figure 4.2f). Fast Fourier Transform (FFT) of a surface region (Figure 4.2g) indeed shows diffraction consisting of a single broad ring, a characteristic feature of amorphous materials. We note that the FFT of carbon background does not contain the broad ring (Figure 4.12), confirming that the FFT feature cannot be explained by the presence of the carbon support alone. Lattice fringes corresponding to single-crystal nano-domains can be observed in the core of the cryomilled $LiNaFeS_2$ particle (Figure 4.2f). The FFT of this region reveals distinct diffraction patterns, further supporting the presence of crystalline domains away from the surface (Figure 4.2h). Cryomilled $LiNaFeS_2$ contains significantly fewer fringes compared to as-prepared $LiNaFeS_2$, suggesting a loss in crystalline domains due to the presence of defects. TEM analysis suggests that cryomilling not only decreases the particle size, but also creates an amorphous surface region and introduces defects throughout the particle.

Electrochemical Characterization

The electrochemistry of as-prepared $LiNaFeS_2$ and cryomilled $LiNaFeS_2$ is examined with galvanostatic cycling to understand the influence of cryomilling on reversibility. We previously reported the electrochemical behavior of $LiNaFeS_2$ and compared it to Li_2FeS_2.[131] $LiNaFeS_2$ has a theoretical capacity of 358 mAh g^{-1}, assuming full removal of the alkali, and can reversibly cycle more than one equivalent of alkali metal.[131]

The galvanostatic cycling data for as-prepared $LiNaFeS_2$ and cryomilled $LiNaFeS_2$ are shown in Figure 4.3. The first charge of as-prepared $LiNaFeS_2$ is characterized by an initial sloping region up to 2.5 V ascribed to $Fe^{2+/3+}$ oxidation, followed by a plateau around 2.5 V associated with sulfide (S^{2-}) oxidation to persulfide ($(S_2)^{2-}$).[131] A charge capacity of 1.75 e^- per formula unit is reached on the first charge followed by rapid capacity fade. We note that the capacities measured here are lower than the capacities originally reported[131] because of the different electrode fabrication method. In our previous report, electrodes were made with the drop

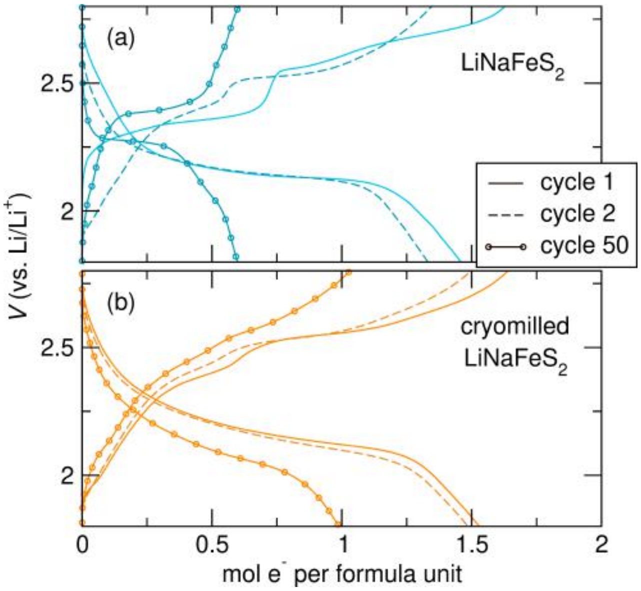

Figure 4.3: Galvanostatic cycling of (a) LiNaFeS$_2$ and (b) cryomilled LiNaFeS$_2$ cycled at a rate of C/10 based on one e$^-$ per formula unit in 1 M LiPF$_6$ in EC/PC/DMC electrolyte.

casting technique and here, electrodes are made as free-standing electrodes, which is required for the *operando* XRD experiments (videa infra), with high active mass loading (19 mg/cm^2). The capacity fade is faster during the initial cycles, showing 17.7 % capacity fade in cycle 2 (Figure 4.3a). Also, the initial sloping region of as-prepared LiNaFeS$_2$ occurs at lower voltages after the first cycle, suggesting a permanent structural change. To determine if the structural change occurs at high voltages, a cell is cycled with a charge cutoff voltage of 2.5 V (Figure 4.13). Even with the lower cuttoff voltage, the second cycle charge curve looks similar to that measured with an upper cutoff of 2.8 V suggesting the structural changes are occurring below 2.5 V. Because the material is cycled in a Li electrolyte, the structural change could be due to reincorporation of Li after the first oxidation or due to the formation of a new phase dissimilar from LiNaFeS$_2$.

In contrast, cryomilled LiNaFeS$_2$ exhibits more stable cycling behavior. The open-circuit voltage is lowered from 1.96 V to 1.81 V upon cryomilling (Figure 4.3b). We hypothesize that structural changes from defects on a local level collectively alter the electronic structure of the material. Starting from a lower OCV, the initial sloping region of the cryomilled material maintains a lower voltage profile compared to as-prepared LiNaFeS$_2$. Additionally, while a sharp increase in potential from the initial sloping region to subsequent plateau at 2.5 V is observed in as-prepared LiNaFeS$_2$, cryomilled LiNaFeS$_2$ shows a smoother transition. Importantly, the second charge curve closely resembles that of the first, suggesting more reversible redox–related structural changes.

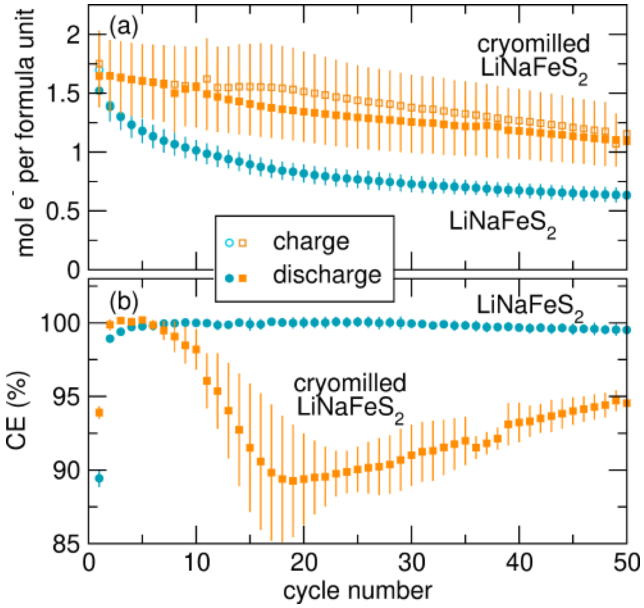

Figure 4.4: Cycling data and Coulombic efficiency of $LiNaFeS_2$ and cryomilled $LiNaFeS_2$. (a) capacity and (b) Coulombic efficiencies of as-prepared $LiNaFeS_2$ and cryomilled $LiNaFeS_2$ over 50 cycles. The cells are cycled at a rate of C/10 based on one e^- per formula unit in 1 M $LiPF_6$ in EC/PC/DMC electrolyte. The average of five replicate cells is shown, with error bars depicting one standard deviation.

The capacity and Coulombic efficiency of as-prepared $LiNaFeS_2$ and cryomilled $LiNaFeS_2$ over 50 cycles are shown in Figure 4.4. In general, the capacity of the cryomilled $LiNaFeS_2$ is higher and the capacity retention is improved compared to as-prepared $LiNaFeS_2$. After 50 cycles, cryomilled $LiNaFeS_2$ exhibits capacities over one e^- per formula unit compared to a capacity of 0.63 e^- per formula unit for as-prepared $LiNaFeS_2$ (Figure 4.4a). Capacity fade of as-prepared $LiNaFeS_2$ is fast in the initial ten cycles, after which both materials experience similar capacity fade rates. Such a drastic difference in capacity fade in early cycles further suggests that a permanent change occurs in the initial stage of cycling without cryomilling. Cycle one of cryomilled $LiNaFeS_2$ shows a higher Coulombic efficiency of 94.3% compared to that of as-prepared $LiNaFeS_2$, 89.4% (Figure 4.4b). We note that cryomilled $LiNaFeS_2$ demonstrates Coulombic efficiencies over 99% in the initial cycles, then decrease briefly to 90% and increase again. We hypothesize that an increase in surface area due to the decrease in particle size leads to greater reaction with the electrolyte, similar to other nanomaterials such as hard carbon anode and Si anode.[146,147]

To probe the effect of cryomilling on the electrode kinetics, galvanostatic intermittent titration technique (GITT) is performed on both materials (Figure 4.5a and b). In a GITT experiment, the cell is polarized for a defined time, in this case 20 m, and subsequently allowed to rest at open circuit until the voltage stabilizes to a near equilibrium value, in this case 4 h. The potential at the end of the 4 h rest period can be approximated as the equilibrium potential, V_{eq}, while the overpotential, η, represents the difference in potential between the start and the end of each rest period. Both V_{eq} and η are obtained from the GITT data and are plotted in Figure 4.5c-f. We note that the total capacity measured by GITT for the as-prepared $LiNaFeS_2$ is lower than that measured with the galvanostatic cycling experiment because the material polarizes quickly upon application of a bias after rest, causing the cell to hit the 3 V cutoff voltage earlier. Interestingly, the V_{eq} on charge is lower in the cryomilled material. Similar to the decrease in OCV before cycling, the difference in V_{eq} below 2.5 V can be explained by a multitude of local structural defects that alter the overall electronic structure. We hypothesize that the lower V_{eq} in the anion redox regime can be attributed to the ability of defects to stabilize the persulfide.

Additionally, the η is generally significantly lower for the cryomilled material on both charge and discharge suggesting that cryomilling enhances the kinetics. Below 2.5 V on charge, as-prepared $LiNaFeS_2$ exhibits η of up to 200 mV compared to 68 mV of cryomilled $LiNaFeS_2$ (Figure 4.5e). In the anion redox region of the charge curve, the η of the cryomilled material is lower by a factor of two, suggesting that structural distortions necessary to allow S–S bond formation become more facile upon cryomilling (Figure 4.5e). η of as-prepared $LiNaFeS_2$ increases toward the end of charge (> 1.2 e^-) while those of the cryomilled material remain unchanged, suggesting an additional constraint that affects reversibility in $LiNaFeS_2$. GITT profiles measured on cycle 13 reveal that the lower overpotential measured with the cryomilled $LiNaFeS_2$ remains significantly lower than as-prepared $LiNaFeS_2$ (Figure 4.14).

To further probe the effect of cryomilling, *in situ* electrochemical impedance spectroscopy (EIS) is conducted. Nyquist plots of as-prepared $LiNaFeS_2$ and cryomilled $LiNaFeS_2$ at selected states of charge are shown in Figure 4.6 (see Figure 4.15 for all states of charge). The high-frequency x-intercept and the size of the semicircles are similar in both materials before cycling, suggesting minimal difference in the Ohmic resistance values and R_{ct} of 279.5Ω and 370 Ω for as-prepared $LiNaFeS_2$ and cryomilled $LiNaFeS_2$, respectively (Figure 4.6a). The diffusion coefficient of

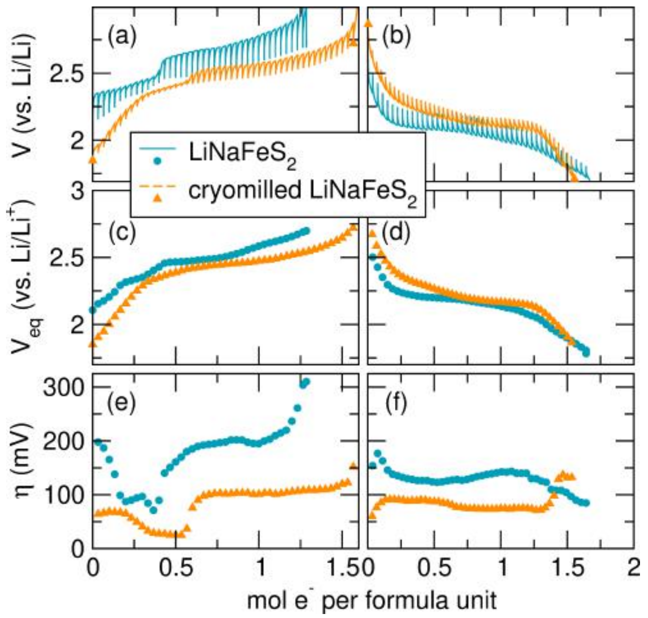

Figure 4.5: GITT curves of (a) the first charge and (b) the first discharge of as-prepared $LiNaFeS_2$ and cryomilled $LiNaFeS_2$. The polarization steps are done at C/10 based on 1 e^- per formula unit for 20 m separated by an OCV rest period of 4 h. The corresponding equilibrium potentials, V_{eq}, during (c) discharge and (d) charge. The corresponding overpotential, η, during (e) discharge and (f) charge.

cryomilled $LiNaFeS_2$ is five times larger than that of as-prepared $LiNaFeS_2$ assuming constant surface area (Figure 4.16). In all states of charge, cryomilled $LiNaFeS_2$ shows a shorter tail in the low frequency region, suggesting lower mass transfer resistance. A lower mass transfer resistance suggests faster diffusion within the particle. We hypothesize that decreased crystallite size and increased microstrain from cryomilling contribute to shorter diffusion pathways for alkali metal deintercalation.[148,149]

EIS measured after 0.5 e^- per formula unit are removed reveals a significant decrease in the impedance of both samples (Figure 4.6b). The cause for a drop in resistance is unclear and it was not observed in Li_2FeS_2 or Li_2FeSe_2. Both Li_2FeS_2 and Li_2FeSe_2 show a gradual increase in impedance as the materials are charged. Regardless, we compare the diffusion coefficients of as-prepared $LiNaFeS_2$ and cryomilled $LiNaFeS_2$ at this charge state and find that the diffusion coefficient for the cryomilled material is three times larger (Figure S8). EIS measured at the fully charged state shows that the impedance associated with the cryomilled material is significantly lower. The Nyquist plots of the fully discharged materials resemble those measured before cycling.

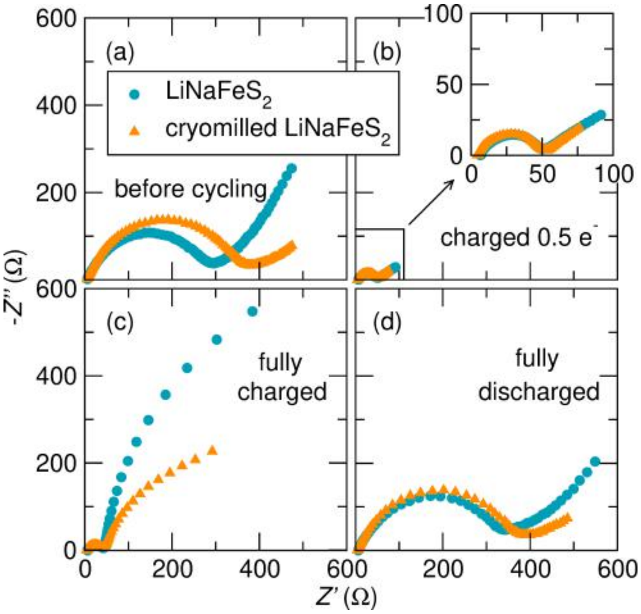

Figure 4.6: Nyquist plots of as-prepared $LiNaFeS_2$ and cryomilled $LiNaFeS_2$ (a) before cycling, (b) charged to 0.5 e^-, (c) fully charged, and (d) fully discharged. Data collected by Dr. Ahamed Irshad in the Narayan Group at USC.

Morphological and Structural Characterization

The particle structure and morphology of as-prepared $LiNaFeS_2$ and cryomilled $LiNaFeS_2$ at different states of charge are examined with transmission X-ray microscopy (TXM). TXM micrographs of as-prepared $LiNaFeS_2$ and cryomilled $LiNaFeS_2$ at various states of charge are shown in Figure 4.7. First, we discuss the morphology evolution of as-prepared $LiNaFeS_2$ during charge and discharge. Before cycling, the as-prepared $LiNaFeS_2$ particle is homogeneous with no signs of fractures (Figure 4.7a). Upon charging to 2.5 V, parallel fractures are observed in the TXM images (Figure 4.7b), and the fully charged sample shows an increased occurrence of parallel fractures (Figure 4.7c and d). The mosaic images are shown in Figure 4.17 for comparison. The fractures remain at the end of discharge (Figure 4.7e), indicating that the formation of the cracks is irreversible. We note that Li_2FeS_2 does not show any fracturing at any state of charge (Figure 4.18). The lack of fracturing in Li_2FeS_2 and the presence of fractures at low states of charge in as-prepared $LiNaFeS_2$ suggests that the fracturing is caused by the removal of large Na^+ during charge. The cause of fracturing is not the exposure to a high voltage nor a high degree of deintercalation; rather, it is the inability of the material to accommodate strain associated deintercalation of Na^+ ions–2.4 times larger in volume compared to Li^+ ions.

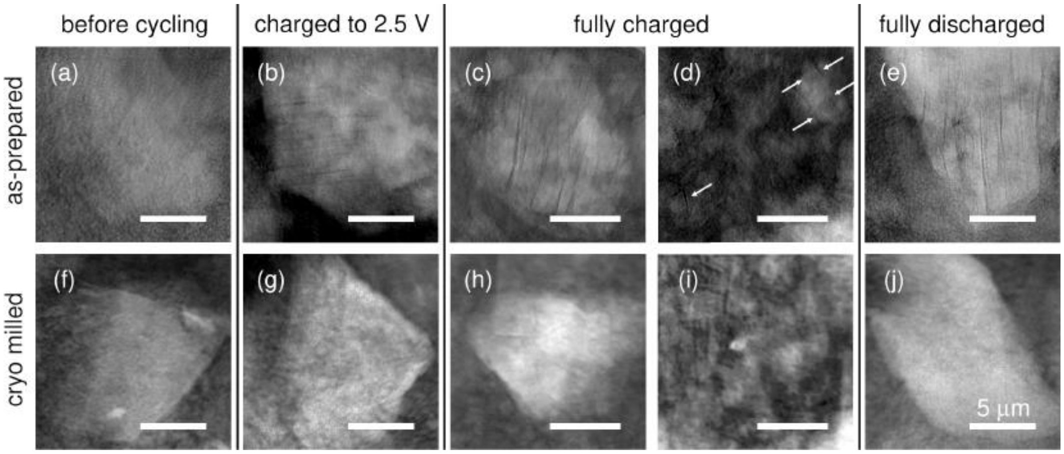

Figure 4.7: *Ex-situ* transmission X-ray microscopy micrographs of (a–e) as-prepared $LiNaFeS_2$ and (f–j) cryomilled $LiNaFeS_2$ at different states of charge. All scale bars represent 5 μm. As-prepared $LiNaFeS_2$ exhibits parallel fractures when charged to 0.5 e^- that do not recover at the end of discharge, while cryomilled $LiNaFeS_2$ does not exhibit any fractures at any state of charge.

The as-prepared $LiNaFeS_2$ particles crack in a parallel fashion, likely representative of the (001) plane through which alkali metal ions deintercalate. The directionality of crack propagation suggests that the particles are either single crystals or aggregates of smaller primary particles with a high degree of ordering that results in a preferred orientation. TEM images suggest that the particles are aggregates, not single particles (Figure 4.19).

Next, TXM micrographs of cryomilled $LiNaFeS_2$, shown in Figure 4.7f–j, are examined. We note that the spatial resolution of TXM is 30 nm; thus, single grains of the cryomilled material are too small in size and low in intensity to be easily identified in TXM (Figure 4.20). Therefore, bigger aggregates that are similar in size to those of as-prepared $LiNaFeS_2$ are first compared, although most particles observed in micrographs of cryomilled $LiNaFeS_2$ are smaller than 1 μm. Particles of cryomilled $LiNaFeS_2$ before cycling and charged to 2.5 V and 3 V do not exhibit fractures (Figure 4.7f–i) suggesting that cryomilling mitigates particle fracturing of $LiNaFeS_2$ during deintercalation. The discharged particle is also free of fractures (Figure 4.7j). Inspection of smaller particles (< 1 μm) of both materials at the end of charge (Figure 4.7d and i) reveals that even much smaller as-prepared $LiNaFeS_2$ particles fracture during charge while the cyromilled particles do not. Thus, the fractures occur across multiple length scales and the decrease in particle size alone does not prevent particle fracturing.

To probe the effect of cryomilling and fracture mitigation on the bulk structural transformations, *operando* synchrotron XRD (sXRD) is performed. Figure 4.8 shows the *operando* diffraction patterns highlighting the (001) reflection of as-prepared $LiNaFeS_2$ and cryomilled $LiNaFeS_2$ during galvanostatic cycling at C/10 based on 1 e^- per formula unit. The full Q range can be found in Figure 4.21. In the initial sloping region of as-prepared $LiNaFeS_2$ (Figure 4.8a and b), the position of the (001) reflection increases in Q, consistent with lattice contraction associated with deintercalation. Concurrent with the kink in the charge profile, the original reflection loses intensity and a new peak appears at higher Q, suggesting a two-phase mechanism. To show the new peak clearly, we have included a magnified view of the diffraction data in the SI (Figure 4.22). In the subsequent plateau region, a bigger shift to higher Q is observed, reaching a d-spacing of 6.21 Å in the fully charged state from 6.79 Å before cycling. During discharge, the trend is mirrored, characterized by a decrease in Q and the emergence of the original peak, albeit with lower intensity, toward the end of discharge.

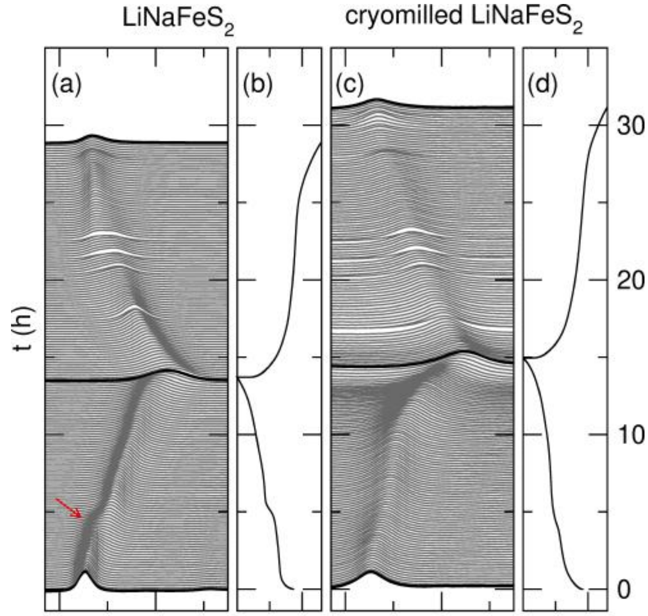

Figure 4.8: *Operando* XRD patterns of $LiNaFeS_2$ and cryomilled $LiNaFeS_2$. (a and b) *operando* sXRD and the corresponding galvanostatic cycling data of as-prepared $LiNaFeS_2$, and (c and d) those of cryomilled $LiNaFeS_2$.

Figure 4.8c and d show the diffraction patterns of the (001) reflection of cryomilled $LiNaFeS_2$ and the corresponding galvanostatic cycling data for the first cycle. In contrast to as-prepared $LiNaFeS_2$, a new peak does not emerge in the initial sloping region; rather, the original peak is retained and gradually shifts to a higher Q. A greater shift to higher Q is observed in the plateau region, reaching the same d-spacing value as that of as-prepared $LiNaFeS_2$ at the end of charge (Figure 4.23). The same trend is maintained during discharge, showing a smooth decrease in Q, suggesting the recovery of the original phase without a two-phase region. The two-phase region begins below 2.5 V in as-prepared $LiNaFeS_2$, at which particle fracturing is also observed. Thus, we hypothesize that the emergence of the two-phase region is responsible for much of the strain that ultimately results in particle fracture.

Both materials lose peak intensity during charge due to loss of long-range order, and the peak intensity is not fully recovered during discharge. While the severity of peak broadening of cryomilled $LiNaFeS_2$ precludes further analysis of the *operando* sXRD data, diffraction patterns of as-prepared $LiNaFeS_2$ offer additional information about structural transformations. For instance, the (100) reflection does not shift much during charge suggesting minimal contraction in the *a* direction (Figure 4.24). Additionally, a new peak appears next to the (101) reflection and increases in Q, which is correlated with the appearance of the new (001) peak (Figure S16).

As-prepared $LiNaFeS_2$ exhibits two-phase behavior while cryomilled $LiNaFeS_2$ does not. Nonetheless, the peak positions of both materials reach similar Q values at the end of charge and discharge in the *operando* sXRD. To obtain more accurate structural information, *ex situ* sXRD is performed. The Rietveld refinement of the materials at the end of cycle 1 reveals that the lattice parameters *a* and *c* of as-prepared $LiNaFeS_2$ and cryomilled $LiNaFeS_2$ are 3.949 Å and 6.772 Å, and 3.937 Å and 6.736 Å, respectively (Figure 4.25). Both materials revert back to a phase whose lattice parameters are more similar to those of $LiNaFeS_2$ than those of Li_2FeS_2. Lattice parameters *a* and *c* of as-prepared $LiNaFeS_2$ at the end of cycle 10 discharge are 3.967 Å and 6.735 Å, showing that the material does not undergo strain-induced phase transformation upon continued cycling despite particle fracturing.

4.5 Discussion

Cryomilling causes substantial improvement in the capacity retention of $LiNaFeS_2$. Using the data collected on the as-prepared $LiNaFeS_2$ and the croymilled $LiNaFeS_2$, we now discuss the mechanism for the improved performance. Cryomilling reduces particle size and introduces defects. Controlled nanoscale engineering, including the introduction of defects, has been shown to improve the performance of battery materials.[150–152] In the case of $LiNaFeS_2$, the reduced particle size and the introduction of defects allows the material to accommodate the strain induced by removal of the large Na^+. The volume of Na^+ is 2.4 times bigger than that of Li^+ so oxidation causes significant lattice contraction. Although the magnitude of lattice contraction is similar in the as-prepared $LiNaFeS_2$ material compared to the cryomilled $LiNaFeS_2$, the structural response is very different. The large strain imposed during oxidation causes the reaction to proceed via a first-order, discontinuous phase transition. The two-phase behavior likely arises due to the inability of the initial phase to accommodate the large strain. The cryomilled $LiNaFeS_2$, in contrast, is able to undergo the oxidation reaction via a solid-solution mechanism due to its ability to accommodate the strain.

The strain imposed by removal of large Na^+ causes significant particle fracturing in as-prepared $LiNaFeS_2$ while cryomilled $LiNaFeS_2$ particles remain intact, even at high degrees of oxidation. The particle fracturing is likely the result of nucleation of the second phase and the strain mismatch between it and the first phase. The fractures are irreversible and thus contribute to the capacity fade in as-prepared $LiNaFeS_2$. The absence of fractures in TXM micrographs of Li_2FeS_2 further confirms that fractures in as-prepared $LiNaFeS_2$ are caused by strain associated with removal of Na^+.

Furthermore, the cryomilling process facilitates the kinetics of persulfide formation during oxidation. In our original report on $LiNaFeS_2$, we hypothesize that the formation of vacancies are necessary to allow for distortions that enable the formation of a S-S bond.[131] Here, we hypothesize that exogenous vacancies introduced via cryomilling are likely facilitating the S-S bond formation, reducing the associated kinetic overpotentials.

4.6 Conclusions

We have demonstrated that cryomilling $LiNaFeS_2$ improves the cycling performance with an increased capacity retention at cycle 50 from 37% to 65%. Cryomilling decreases particle and crystallite size while increasing microstrain. TXM reveals that as-prepared $LiNaFeS_2$ undergoes particle fracturing during the first charge while cryomilled $LiNaFeS_2$ does not, indicating that cryomilling effectively prevents particle fracturing of $LiNaFeS_2$. Even though the alkali-rich materials can reach very large degrees of alkali ion removal exceeding 1.7 mol of alkali per transition metal, we find that the particle fracturing is due to the removal of the larger Na ion and can occur at low states of charge. Cryomilling is thus an effective way to engineer materials for battery systems based on larger mobile ions such as Na^+, K^+, or Ca^{2+}. Furthermore, cryomilling reduces the overpotentials associated with anion oxidation at high states of charge. Thus, understanding different mechanisms that lead to capacity fade and ways to address them in alkali-rich materials will enable the development of next-generation multielectron battery materials.

4.A Supplementary Information

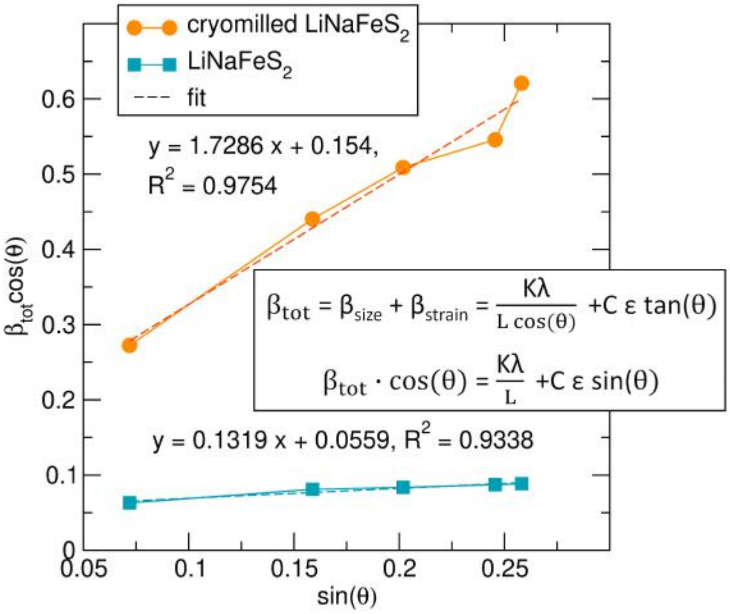

Figure 4.9: Williamson-Hall analysis of XRD peaks of as-prepared LiNaFeS$_2$ and cryomilled LiNaFeS$_2$. Calculated crystallite size decreases from 1.47 nm to 0.56 nm upon cryomilling, while microstrain increases from 29800 to 425500.

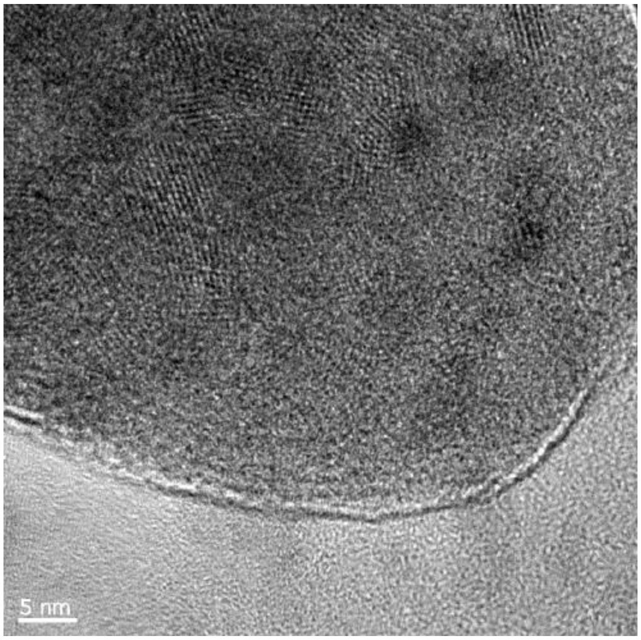

Figure 4.10: TEM image of as-prepared LiNaFeS$_2$. Regions of fringes are observed throughout the particle suggesting high crystallinity.

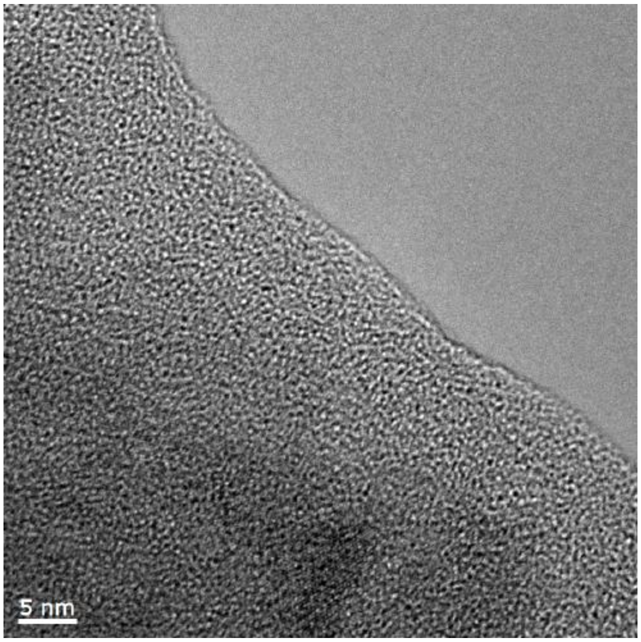

Figure 4.11: TEM image of cryomilled $LiNaFeS_2$. Fewer crystalline domains are observed, which only exist in the bulk. The surface of the particle appears amorphous.

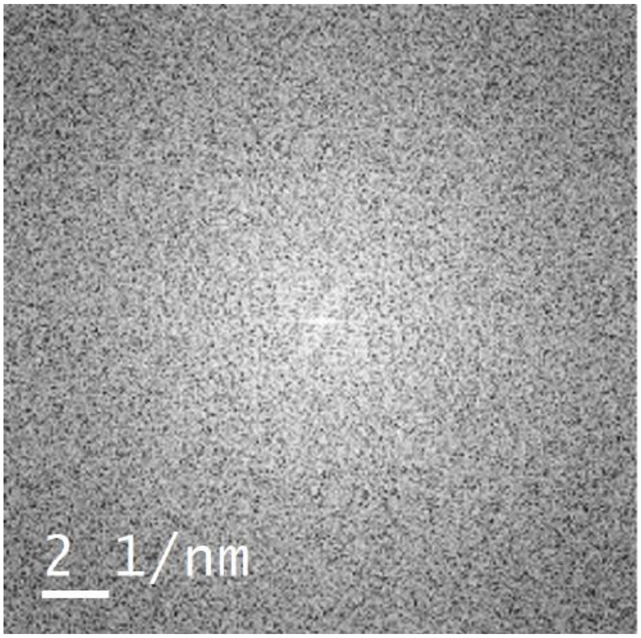

Figure 4.12: FFT of background carbon. The absence of a broad ring suggests that the broad ring observed in the FFT of the edge of cryomilled particle cannot be explained by carbon supporta lone.

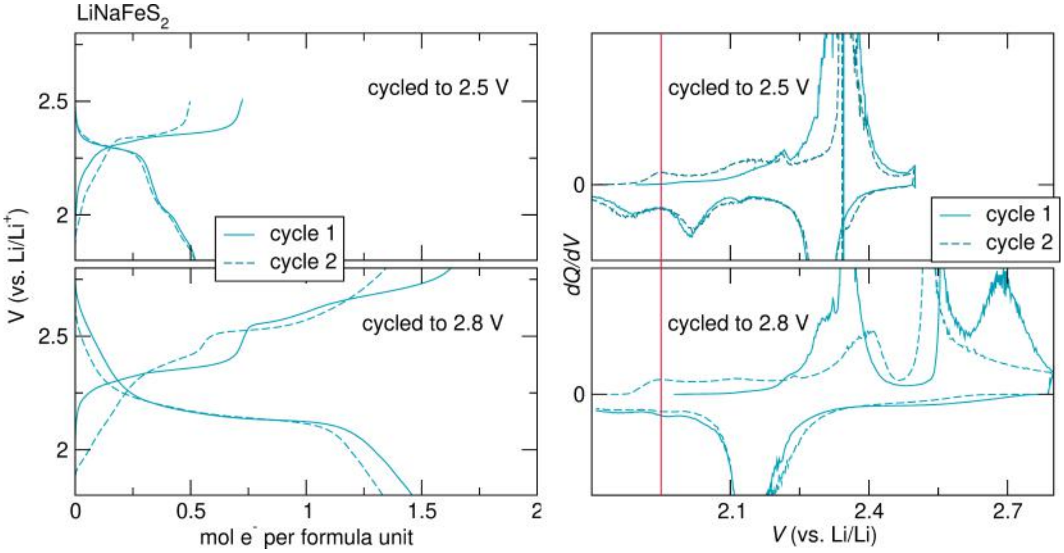

Figure 4.13: Galvanostatic cycling and corresponding dQ/dV plots of as-prepared LiNaFeS$_2$ to different upper voltage cutoffs 2.5 V and 2.8 V. Both upper cutoffs exhibit the same peak in the dQ/dV plots of cycle 2.

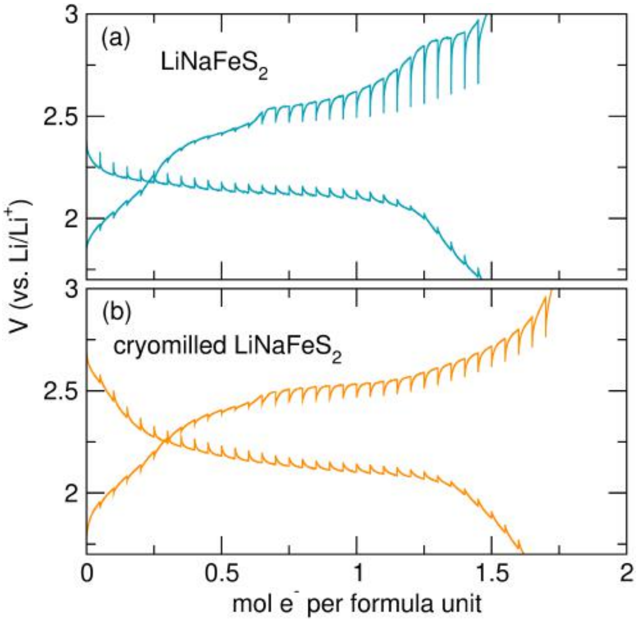

Figure 4.14: Cycle 13 GITT of (a) as-prepared LiNaFeS$_2$ and (b) cryomilled LiNaFeS$_2$. As-prepared LiNaFeS$_2$ continues to show higher overpotentials above 2.5 V.

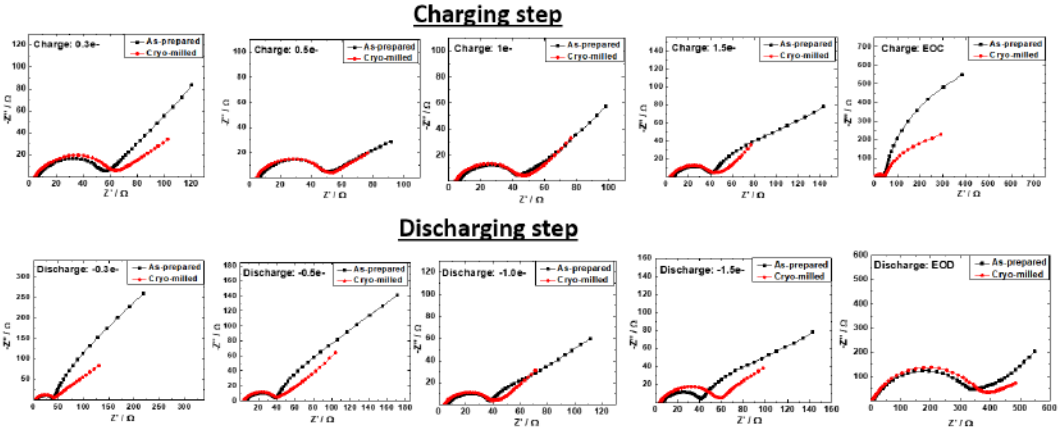

Figure 4.15: Intermittent EIS during cycle 1 at different states of charge. While high-frequency x-intercepts and the size of semicircles are similar, cryomilled $LiNaFeS_2$ always shows shorter tails, suggesting lower mass transfer resistance.

$$D = \frac{R^2T^2}{2A^2n^2F^4C^2\sigma^2}$$

Before cycling

$$(D_{Li+})_{cryo\text{-}milled} / (D_{Li+})_{as\text{-}prepared} = (\sigma^2)_{as\text{-}prepared} / (\sigma^2)_{cryo\text{-}milled}$$
$$= (120.01)^2 / (53.52)^2$$
$$= 5$$

0.5 e⁻ removed

$$(D_{Li+})_{cryo\text{-}milled} / (D_{Li+})_{as\text{-}prepared} = (\sigma^2)_{as\text{-}prepared} / (\sigma^2)_{cryo\text{-}milled}$$
$$= (22.89)^2 / (13.59)^2$$
$$= 2.8$$

Figure 4.16: Ratios of diffusion coefficients of as-prepared $LiNaFeS_2$ and cryomilled $LiNaFeS_2$ before cycling and 0.5 e^- removed assuming constant surface area. Cryomilled $LiNaFeS_2$ shows higher diffusion coefficients compared to as-prepared $LiNaFeS_2$.

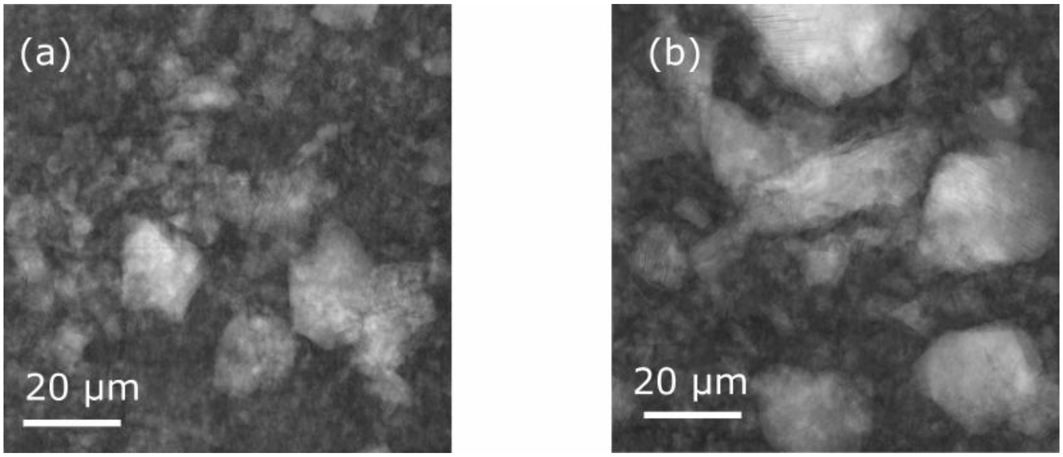

Figure 4.17: TXM mosaic micrographs of as-prepared $LiNaFeS_2$ (a) charged to 2.5 V, (b) fully charged to 3 V. Scale bars represent 20 μm. Particle fractures appear at 2.5 V, and more particle fractures are observed at the end of charge.

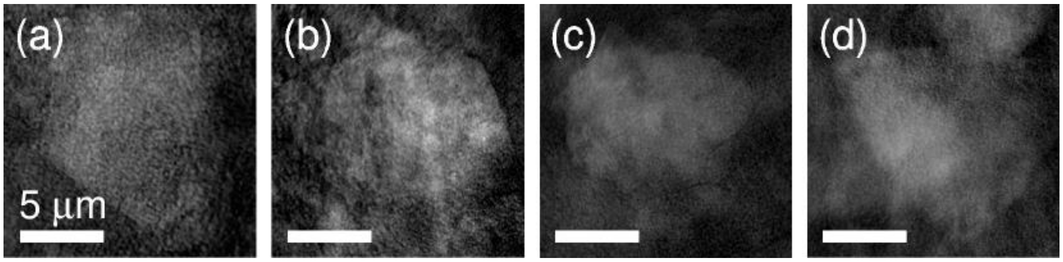

Figure 4.18: TXM micrographs of Li_2FeS_2 (a) before cycling, (b) charged to 2.5 V, (c) charged to 3 V, and (d) discharged to 1.7 V. Scale bars represent 5 μm. Li_2FeS_2 does not show signs of fracturing in all states of charge.

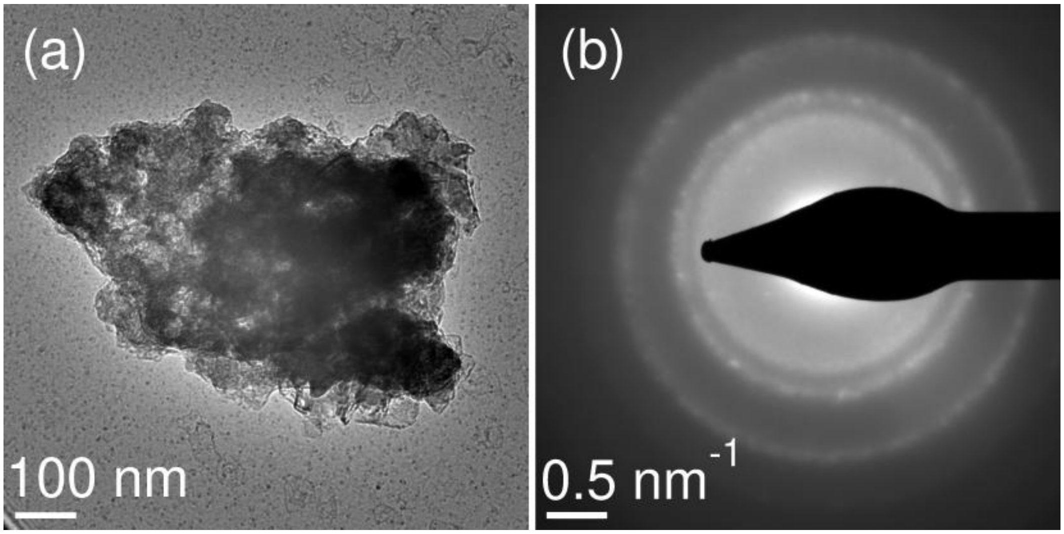

Figure 4.19: TEM of cryomilled $LiNaFeS_2$ and corresponding selected area electron diffraction patterns. (a) Particle clusters of cryomilled $LiNaFeS_2$ and (b) diffraction rings in the corresponding selected area electron diffraction (SAED) pattern. The cluster is composed of small single crystalline particles that are randomly oriented.

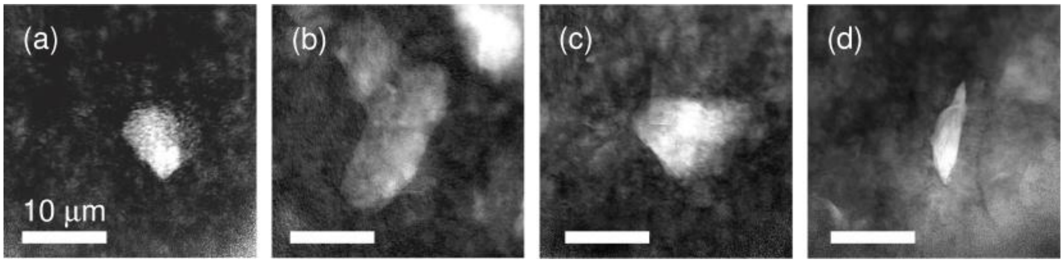

Figure 4.20: TXM micrographs of cryomilled $LiNaFeS_2$ (a) before cycling, (b) charged to 2.5 V, (c) charged to 3 V, and (d) charged to 3V then discharged to 1.7 V. Scale bars represent 10 μm. There are more smaller particles than bigger aggreagates. Brightness and contrast levels are adjusted so that smaller particles can be seen better.

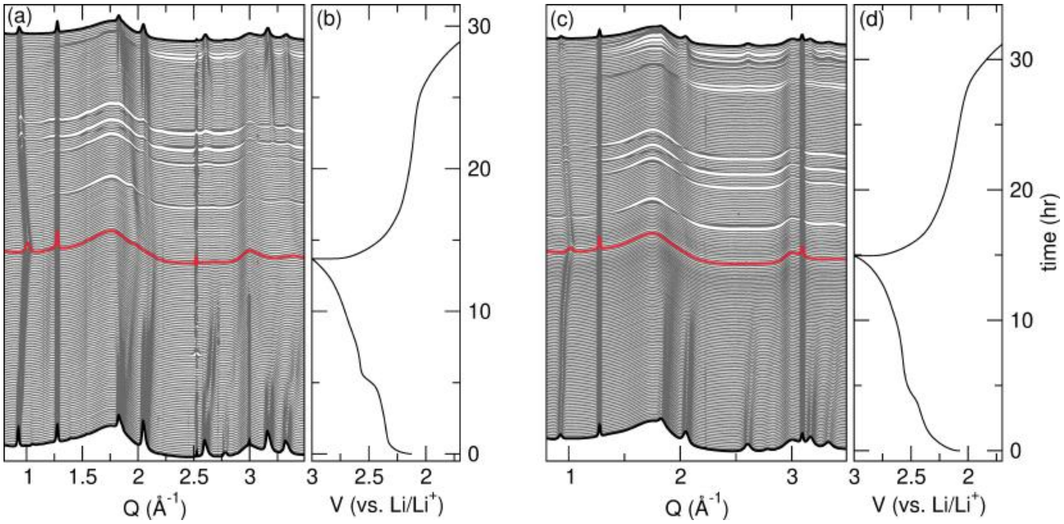

Figure 4.21: *Operando* sXRD of (a and b) as-prepared $LiNaFeS_2$ and (c and d) cryomilled $LiNaFeS_2$. The peak at 1.26 Q corresponds to PTFE binder.

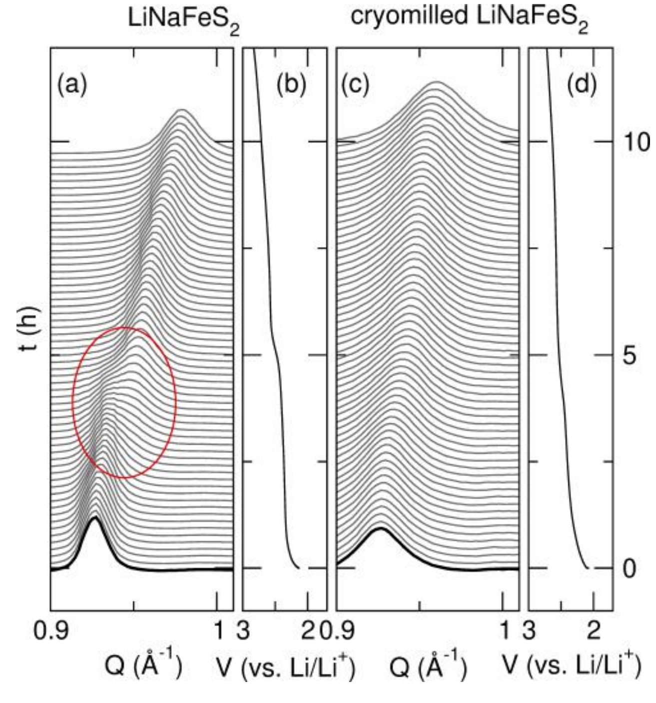

Figure 4.22: *Operando* sXRD of (a and b) as-prepared $LiNaFeS_2$ and (c and d) cryomilled $LiNaFeS_2$ magnified up to the first 10 hours of charge to highlight the new peak in as-prepared $LiNaFeS_2$.

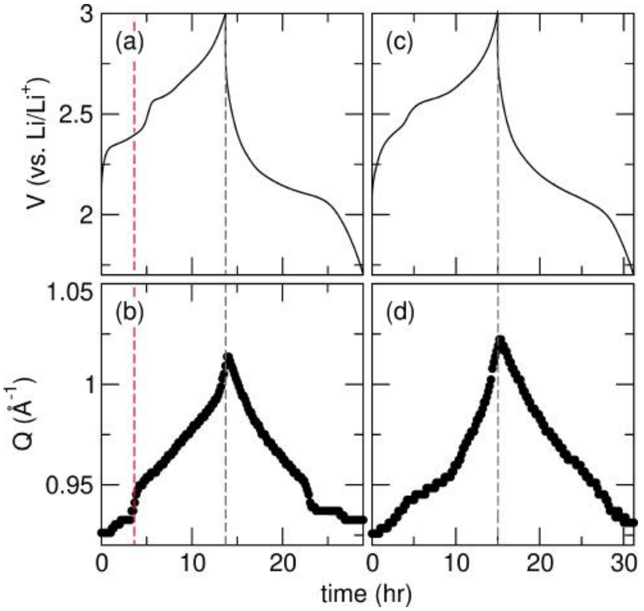

Figure 4.23: Galvanostatic cycling data and plotting the (001) reflection together. (a) Galvanostatic cycling data of as-prepared $LiNaFeS_2$ and (b) Q of the (001) reflection, and (c and d) corresponding data for cryomilled $LiNaFeS_2$. While both materials' (001) peaks reach the same Q and thus d-spacing at the end of charge, as-prepared $LiNaFeS_2$ exhibits a jump in Q suggesting a two-phase mechanism.

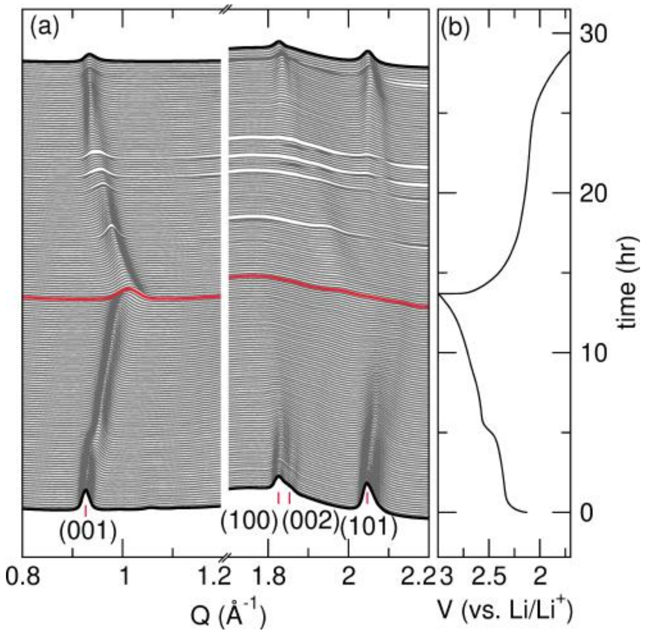

Figure 4.24: *Operando* sXRD of $LiNaFeS_2$ of selected region. (a) *Operando* sXRD of as-prepared $LiNaFeS_2$ of selected Q regions and (b) the corresponding galvanostatic cycling data.

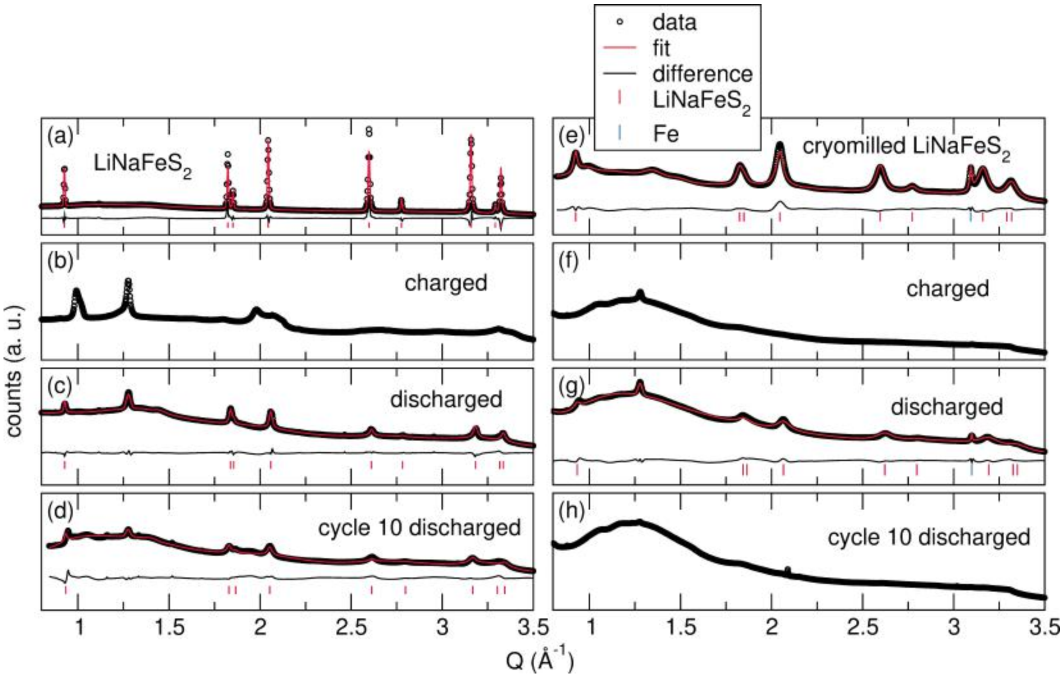

Figure 4.25: *Ex situ* sXRD of (a–d) as-prepared $LiNaFeS_2$ and (e–h) cryomilled $LiNaFeS_2$ at different states of charge. The peak at 1.26 Q corresponds to PTFE. While intensity attenuation of cryomilled $LiNaFeS_2$ precludes further analysis, diffraction patterns of discharged and cycle 10 discharged as-prepared $LiNaFeS_2$ can be fit with Rietveld refinement.

Chapter 5

TUNING TRANSITION METAL-ANION COVALENCY AND CONTROLLING REDOX SPECIES IN LI-RICH SULFIDE CATHODE MATERIAL BY TRANSITION METAL SUBSTITUTION

Contributions: S.S.K. conceived, designed, and performed experiments, and wrote the manuscript. *manuscript in preparation*

5.1 Abstract

New energy storage methods are emerging to increase the energy density of the state-of-the-art battery systems beyond the current intercalation electrode materials. Incorporating lattice anions in the cathode material is a promising method to achieve multielectron electrochemical activity and increase energy density. Li-rich sulfide materials in particular serve as great candidates thanks to their ability to form stable transition metal-anion bonds and thus benefit from both intercalation and conversion type mechanisms. In this work, we report a new alkali-rich material $LiNaCoS_2$ and probe its charge compensation mechanism to explore how transition metal-anion covalency affects the electrochemical performance. $LiNaCoS_2$ exhibits multielectron capacity of $\geq$1.7 electrons per formula unit and anion redox. However, the material suffers from irreversible phase transition and rapid capacity fade. Through a combination of solid-state nuclear magnetic resonance spectroscopy, Co and S X-ray absorption spectroscopy, X-ray diffraction, and partial density of states, we demonstrate that S oxidation and the formation of pyrite CoS_2 occurs in early states charge which triggers the formation of lithiated cobalt spinel phase such as $Li_xCo_3S_4$ and $Li_xCo_9S_8$.

5.2 Introduction

Lithium-ion batteries (LIBs) have revolutionized the modern technological era, ranging from powering portable electronic devices to realizing the commercialization of electric vehicles.[153,154] Charge compensation of cathode materials in LIBs predominantly stems from the redox activity of M in $LiMO_2$ (M = a combination of transition metals). From the original commercial intercalation-type oxide $LiCoO_2$, partial and/or full substitution of other metals such as Ni, Mn, and Al has improved the structural stability and energy density.[15–18]

To increase the energy density beyond the limits of conventional intercalation chemistry, there have been increasing efforts to leverage both cation and anion redox in the lattice to achieve multielectron storage (more than 1 e^- per formula unit).[155,156] While utilizing anion redox in so-called Li-rich oxides is highly desirable, many Li-rich oxide materials suffer from undesirable side reactions such as irreversible capacity loss, voltage fade, and electrolyte decomposition, due to the unstable electronic configurations of oxidized structures.[124–126,156] Recently, it was shown that removing e^- from O results in delocalized holes in the O-p band around the cationic vacancy created by Li removal from the center of the honeycomb in the transition metal layer that eventually leads to transition metal migration and O_2 dimer formation.[157–160]The driving force is ascribed to the lower energy of O_2 dimer–containing structures.[159] In other words, the formation of O_2 dimer leads to undesirable side reactions and thus must be suppressed in Li-rich oxides to promote high electrochemical performance.

An alternative approach to take advantage of anion redox is to replace the O with more covalent element S and develop Li-rich sulfide materials. Unlike metal oxides, metal sulfides have been known to form stable S_2 dimers without breaking the transition metal-S bond .[161–164] Also, anion redox in Li-rich sulfides occurs within the electrochemical window of conventional carbonate electrolytes making them excellent candidates to study anion redox and also as next-generation cathode materials.

Recently, researchers have controlled the relative positions of transition metal-d states and S-p states to study the nature of anion redox in Li-rich sulfide materials. Transition metal substitution in redox-inactive d^0-based Li-rich sulfides (Li_2TiS_3 + Fe^{2+}, Co^{2+}, and Ti^{3+} and Li_2SnS_3 + Fe^{2+}) has proven effective in activating S oxidation by introducing a redox-active transition metal whose d states overlap with those of S-p states.[163,165,166] Additionally, substituting S with even more covalent Se ($Li_2FeS_{2-y}Se_y$, $Li_2TiS_{3-x}Se_x$, and $(Li_2Fe)S_{1-x}Se_xO$) has demonstrated that increasing transition metal-anion covalency through increasing Se content results in systematic decrease in the redox potential as a result of the formation of hybridized states of transition metal-d, S-p, and Se-p bands.[167,168] As for comparing different redox-active transition metals in an isostructural phase, $(Li_2M)SO$ (M = Fe^{2+}, Mn^{2+}, and Co^{2+}) has been explored which revealed that although the role of S is not fully elucidated, partial substitution of Co improves the structural stability while that of Mn does not.[169–171]

In this work, we turn to alkali-rich sulfide $LiNaFeS_2$ that benefits from transition metal and $S^{2-}/(S_2)^{2-}$ redox couples and achieves reversible multielectron capacity. From $LiNaFeS_2$, we substitute Co for Fe in an isostructural manner to form $LiNaCoS_2$. By introducing Co whose $Co^{2+/3+}$ states are slightly lower in energy and thus more covalent with S-p states compared to $Fe^{2+/3+}$,[162,172] we explore the role of transition metal-anion covalency in electrochemical performance of S redox. We report that $LiNaCoS_2$ can be prepared via solid-state synthesis and is isostructural to previously reported Li_2FeS_2 and $LiNaFeS_2$.[173] $LiNaCoS_2$ exhibits multielectron capacity with anion redox in cycle 1, but the material is plagued by rapid capacity fade from irreversible conversion reaction that prevents further electrochemical activity. With a multitude of characterization techniques including X-ray diffraction, solid-state nuclear magnetic resonance spectroscopy, and X-ray absorption spectroscopy, we report that S oxidation in the formation of CoS_2 drives the irreversible phase transition in $LiNaCoS_2$.

5.3 Experimental Section

Material Preparation

All materials were stored and prepared in an Ar-filled glovebox in which the levels of O_2 and H_2O were below 1 ppm. $LiNaCoS_2$ was prepared using traditional solid state methods, from Li_2S (Beantown Chemical, ≥ 99.9%), Na_2S (Fisher Scientific ≥ 99%), Co (Fisher Scientific, ≥ 99.8%) and S_8 (Acros Organics, ≥ >99.5%). Stoichiometric amounts of Li_2S, Na_2S, Co, and S_8 were ground and pressed into pellets of up to 400 mg and sealed in a C-coated evacuated vitreous silica ampule. The reactants were heated at 2 °C min^{-1} to 600 °C, dwelled for 96 hours, and quenched with water at room temperature. The resulting black pellet was ground into powder in the glovebox. $LiNaCoS_2$ retains the pellet morphology upon the completion of the reaction. The pristine $LiNaCoS_2$ pellet is dark gray/black, and the color is retained upon grinding.

Material Characterization

Powder X-ray diffraction (XRD) patterns were collected using the Rigaku SmartLab diffractometer. The powders were placed on a 6 mm air-free sample holder (Rigaku) inside the glovebox to prevent air exposure. XRD patterns were collected with a Cu-Kα X-ray source at 3 °min^{-1} with 0.04 °step size. The diffraction patterns were fit by the Rietveld method using GSAS-II.[144] Visualization of the crystal structures was aided by VESTA.[174]

High-resolution synchrotron powder X-ray diffraction (sXRD) patterns were collected at the Advanced Photon Source at Argonne National Laboratory on beamline 11-BM-B (λ = 0.459738 Å).[175] $LiNaCoS_2$ powder was used for the pristine state, while *ex situ* charged (fully polarized to 3 V) and discharged (fully charged to 3 V then discharged to 1.7 V) samples were prepared with 15 mg of a 60:20:20 wt% pellets of $LiNaCoS_2$, Super P carbon, and PTFE. The cathode composite was recovered from the disassembled cell, washed with 200 μl of dimethyl carbonate, and vacuum dried for more than 4 hours. The sample was then sealed under vacuum in 0.7 mm (o.d.) glass capillaries (Hampton Research) to prevent air exposure and placed inside of polyimide capillaries.

Operando XRD data were collected using a Bruker D8 Advance diffractometer in Bragg-Brentano geometry equipped with a Cu Kα source (λ_1 = 1.5406 Å, λ_2 = 1.5444 Å) and a Lynxeye XE-T detector. A custom-made *operando* cell with a PEEK body, stainless steel electrical contacts, and an X-ray transparent Be window (SPI Supplies, 0.25 mm thick) was used. The Be window served as a current collector and allowed for X-ray penetration so that diffraction patterns could be collected while cycling galvanostatically. As with the *ex situ* cells, pellet electrodes composed of 60% active material, 20% carbon black, and 20% polymer binder were used and placed directly on the Be window. The pellet electrodes were cycled against Li foil using a BioLogic SP-200 potentiostat at a C/20 rate with one Whatman glass fiber separator (GF/D) flooded with 1 M LiPF6 in 1:1:1 EC:PC:DMC electrolyte. Patterns were continuously collected over a range of 10°to 45°2θ approximately every 20 min throughout the duration of the electrochemical cycling.

Solid-state nuclear magnetic resonance (ssNMR) spectroscopy was performed using Bruker Avance 500 MHz spectrometer operating at 194.31 MHz for ^{7}Li and 132.29 MHz for ^{23}Na. All samples were packed in a 4 mm ZrO_2 HR-MAS rotor with 50 μl PTFE spacer (Cortecnet). 30 mg of pristine LiNaCoS2 was packed into the rotor in an Ar-filled glovebox. *Ex situ* samples were preared in the same way as electrochemical cells with a total mass of 20 mg. ^{7}Li and ^{23}Na magic angle spinning (MAS) ssNMR was recorded at a spinning rate of 10.5 kHz. A single RF pulse of 0.5 μs with a 7 μs $\pi/2$ and 3 μs were applied for ^{7}Li and ^{23}Na, respectively. Different spinning rates were used to identify the isotropic peaks. LiCl and NaCl were used as standards at 0 ppm. Not washing the composite electrode resulted in peaks from Li-containing impurities such as the electrolyte salts.

Co and S X-ray absorption spectroscopy was conducted at beamline 2-2 at the Stanford Synchrotron Radiation Lightsource at SLAC National Accelerator Laboratory. Data processing including calibration and background correction was performed using Athena.[176] All data were calibrated to a collinear Co and S foil for each sample. *Ex situ* samples were prepared in the same way as electrochemical cells with a total mass of 20 mg. All measurements were taken within 2 weeks of completing the electrochemical acitivty. *Ex situ* samples were placed onto the sample holder using Kapton tape on each side inside an Ar-filled glovebox. During measurement, the sample holder was placed in a continuous He-flushed chamber with minimal O_2 concentration (< 500 ppm).

Electrochemical Characterization

All cells were prepared inside Ar-filled gloveboxes with H_2O and O_2 levels below 0.1 ppm. Powder of LiNaCoS2 was mixed with Super P carbon (Alfa Aesar, ≥99%) and polytetrafluoroethylene (PTFE, Sigma-Aldrich) at 60:20:20 wt% to prpare free-standing composite electrodes. Approximately 10 mg of the composite mixture was pressed into 0.25 inch diameter pellets with a hand-operated arbor press. 2032 coin cells were prepared with polished Li metal counter/reference electrodes, dried 18 mm diameter glass fiber separators (Whatman GF/D), and 11 drops of electrolyte (approximately 163 mg). 1 M solution of $LiPF_6$ (Sigma-Aldrich, ≥99.99%) in a 1:1:3 mixture of ethylene carbonate (Sigma-Aldrich, >99%), propylene carbonate (Sigma-Aldrich, >99%), and dimethyl carbonate (Sigma-Aldrich, >99%) by volume was used as the electrolyte in all cells. Potentials reported here are in reference to the Li metal electrode potential, which is approximated to equal to that of Li/Li^+. Galvanostatic cycling experiments were performed at C/10 based on 1 e^- per formula unit. Galvanostatic intermittent titration technique (GITT) was conducted at a rate of C/10 based on 1 e^- per formula unit for 20 minutes with 4 hour open circuit hold rest periods.

5.4 Results

Structural Characterization

First, synchrotron X-ray diffraction (sXRD) is employed to characterize the structure of $LiNaCoS_2$. Synchrotron XRD patterns and quantitative Rietveld refinement results of pristine $LiNaCoS_2$ are shown in Figure 5.1. $LiNaCoS_2$ adopts the $P\bar{3}m1$ space group and is isostructural to previously reported $LiNaFeS_2$.[173] In $LiNaCoS_2$, layers of edge-sharing Na octahedra are separated by layers of edge-sharing mixed Co/Li tetrahedra (Figure 5.1). The sharp reflections suggest high crystallinity, and the diffraction patterns are well-described by a two-phase fit to $LiNaCoS_2$ and 0.0008 phase fraction of Co_9S_8 (<1.6 wt %). The lattice parameters of $LiNaCoS_2$ are a = 3.95618 and c = 6.73845 Å.

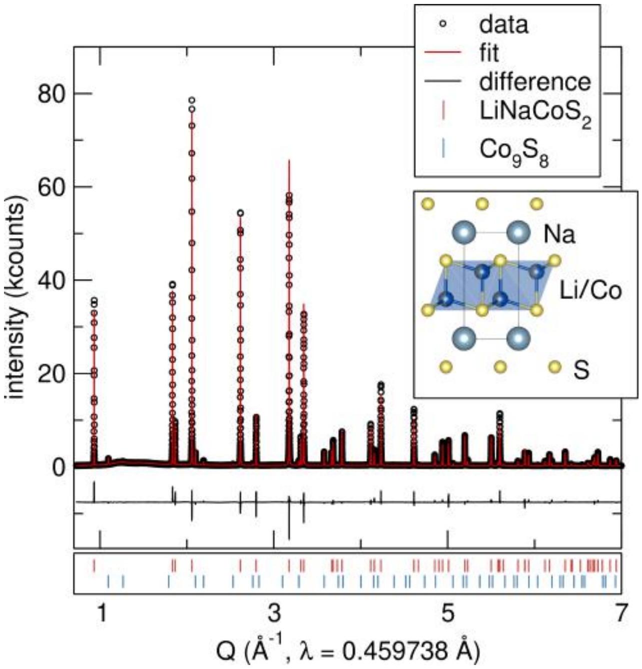

Figure 5.1: Synchrotron powder X-ray diffraction patterns and the Rietveld refinement results of $LiNaCoS_2$ and the structure. The ticks indicate the Bragg reflection locations.

Electrochemical characterization

The electrochemical performance of $LiNaCoS_2$ is examined with galvanostatic cycling to probe the effect of transition metal-anion covalency. Figure 7.1 depicts the galvanostatic cycling data of $LiNaCoS_2$ at C/10 based on 1 e^- per formula unit, which is 175.2 mAh g^{-1}. Multi-electron capacity of 1.7 e^-, or 297.8 mAh g^{-1}, is observed in the first charge. The voltage curve is characterized by a single plateau, suggesting a two-phase mechanism. The plateau occurs at 2.6 V, similar to anion oxidation in other Li-rich sulfide materials.[163,166,167,173,177] Unlike its isostructural material $LiNaFeS_2$, no distinct region associated with transition metal oxidation is observed. Nonetheless, the oxidation potential of the plateau is pinned at around 2.6 V like in $LiNaFeS_2$.[173,178] This trend differs from anion-substituted $Li_2FeS_{2-y}Se_y$ in which mixing of the S and Se states yields a systematic shift in the voltage plateau.

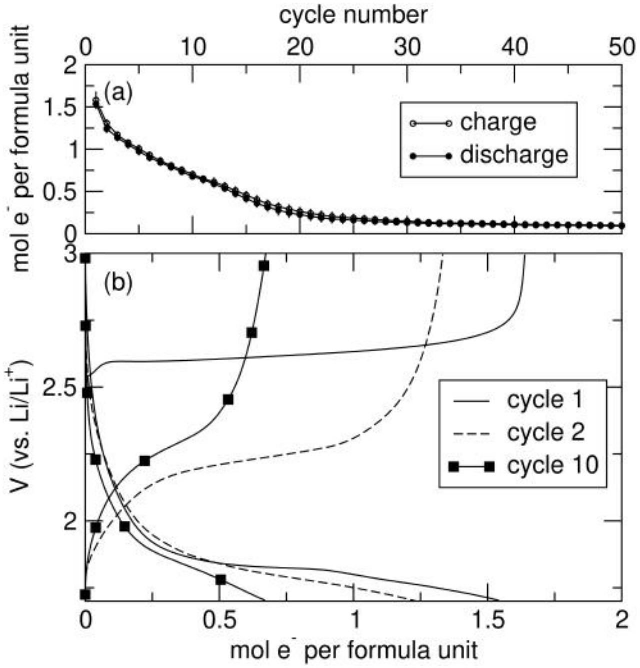

Figure 5.2: Galvanostatic cycling data of $LiNaCoS_2$. (a) charge and discharge capacities of $LiNaCoS_2$ and (b) galvanostatic cycling data of $LiNaCoS_2$ at C/10 based on 1 e^- per formula unit.

The subsequent discharge cycle is characterized by a single plateau and a sloping region, and large voltage hysteresis is observed. After cycle 1, the charge voltage profile changes drastically and loses capacity very quickly, losing most of its electrochemical activity by cycle 20 (Figure 7.1a). The charge and discharge voltage profiles after cycle 1 resemble those of CoS_2 cycled between 3 and 1.6 V suggesting a similar mechanism in $LiNaCoS_2$.[179] When charged to 3 V then discharged to below 1.7 V, the discharge curve of $LiNaCoS_2$ resembles that of CoS_2, further suggesting that charge products are similar to those of CoS_2 (Figure 5.10).

To probe the kinetics of $LiNaCoS_2$ during cycling, galvanostatic intermittent titration technique (GITT) is measured on $LiNaCoS_2$ (Figure 7.2). The cell is polarized for 20 minutes at C/10 per formula unit with 4 hour open circuit hold rest periods. The near-equilibrium potential at the end of each relaxation period is approximated as the equilibrium potential, V$_{eq}$, and the overpotential, η, represents the potential difference between the beginning and end of each rest period.

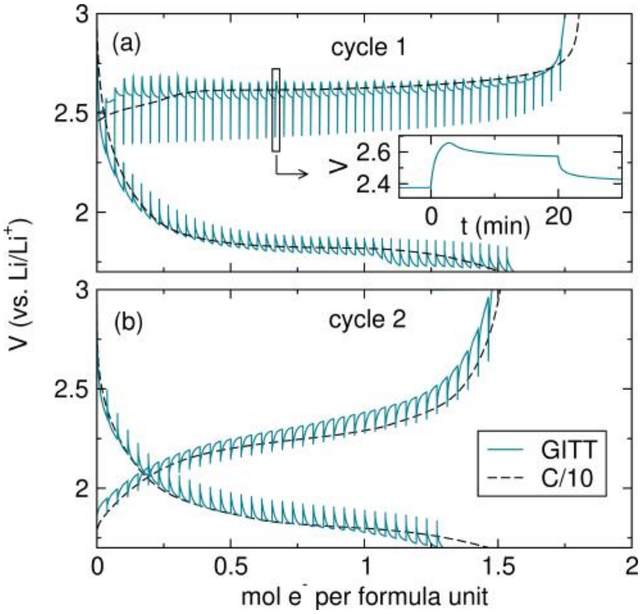

Figure 5.3: Galvanostatic cycling and galvanostatic intermittent titration technique data of $LiNaCoS_2$ (a) in cycle 1 and (b) cycle 2 at C/10 and 4-hr rest periods.

The GITT profile during first charge exhibits high overpotentials (Figure 7.2a). Voltage profile plotted as a function of time (Figure 7.2a inset) reveals that a high overpotential spike forms and relaxes during polarization similar to the nucleation and growth behavior observed in Li metal electrodeposition.[180,181] The GITT profile during charge, thus, suggests that a new phase nucleates and grows within the particle during each polarization step instead of a new phase that nucleates and propagates during polarization. When GITT is performed at C/100, the overpotential associated with the nucleation region decreases significantly (Figure 5.9), suggesting that the nucleation and growth behavior is caused by the sluggish kinetics. During discharge, an initial sloping region is followed by a plateau (Figure 7.2a). Also, the overpotential spike is no longer observed and η is lower than during charge, suggesting an irreversible phase transition at the end of cycle 1. The large voltage hysteresis between charge and discharge V$_{eq}$ further suggests that the charge and discharge pathways differ from each other. In cycle 2, the charge and discharge GITT profiles trace the galvanostatic cycling data well which resemble that of CoS_2 cycled between 1.6 and 3 V.[179]

Structural and Spectroscopic Evolution during Cycling

Next, we investigate the structural evolution of $LiNaCoS_2$ during cycling. First, solid-state nuclear magnetic resonance (ssNMR) spectroscopy is employed to explore the local Li and Na environments. ^{7}Li and ^{23}Na magic-angle spinning (MAS) ssNMR spectra of $LiNaCoS_2$ at different states of charge collected at 10.5 kHz are shown in Figure 7.4. A single resonance is observed at 87.4 ppm and 652 ppm for ^{7}Li and ^{23}Na (marked *), respectively, indicating a single unique environment for both Li and Na in pristine $LiNaCoS_2$ and confirming the Wyckoff site assignments based on sXRD.

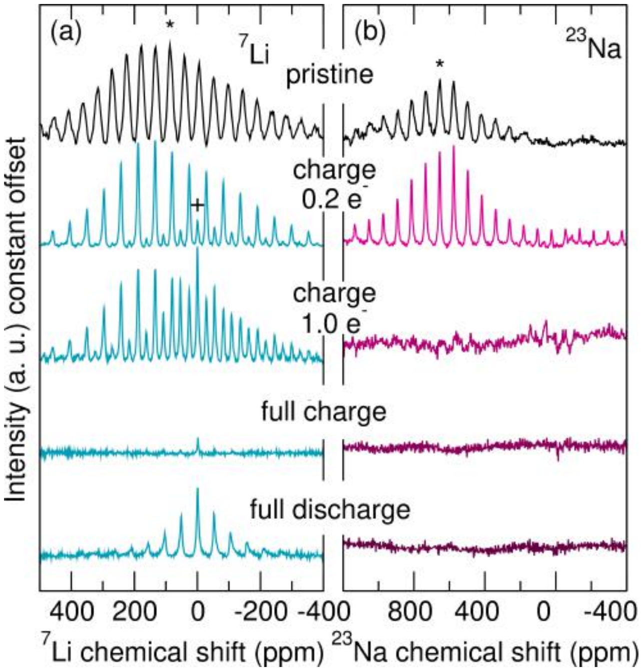

Figure 5.4: Solid-state NMR data of $LiNaCoS_2$ at different states of charge. (a) ^{7}Li and (b) ^{23}Na MAS ssNMR spectra of $LiNaCoS_2$ at different states of charge. Pristine $LiNaCoS_2$ exhibits a single resonance marked * in both ^{7}Li and ^{23}Na spectra confirming a single environment for Li and Na. During charge, a new feature (+) is observed in ^{7}Li spectra while ^{23}Na spectra exhibits a decrease in intensity of the single resonance.

At 0.2 e^- charge (charge capacity equivalent to 0.2 e^- removal per formula unit), a new resonance is observed at -1 ppm in ^{7}Li MAS ssNMR (marked +) suggesting that a new Li environment begins to grow at early states of charge. This new resonance grows in intensity during charge as evidenced by the 1.0 e^- charge spectrum while the intensity of the original resonance at 87.4 ppm decreases. This result indicates that in addition to Li removal during charge, the active material undergoes a phase transition and a new Li environment grows. At full charge (1.7 e^-), both resonances disappear in ^{7}Li MAS ssNMR, suggesting that Li proceeds to be removed from the newly formed environment. Meanwhile, ^{23}Na MAS ssNMR spectra reveal that the single resonance in the pristine sample decreases in intensity throughout charge. Na does not actively participate in the phase transition and is simply removed during charge. We also note that the overall intensity of ^{23}Na MAS ssNMR peaks decreases more quickly than ^{7}Li MAS ssNMR peaks which suggests that Na is removed faster than Li during charge although the removal of alkali metal does not occur in a discrete manner.

Upon full discharge, a single resonance is observed in the ^{7}Li spectrum while there are no resonances in the ^{23}Na spectrum implying that only Li is inserted back in the structure during discharge. The resonance observed in the ^{7}Li spectrum appears at the same chemical shift as the one formed during charge, suggesting that the same lithiated structure is recovered. The original resonance at 87.4 ppm does not return, confirming that $LiNaCoS_2$ undergoes irreversible phase transition.

Next, we probe the structural evolution of $LiNaCoS_2$ with X-ray diffraction. Figure 5.5a and b depict the *operando* XRD patterns of the (001) and (002) reflections of $LiNaCoS_2$ during cycle 1 with the corresponding galvanostatic cycling data in Figure 5.5c. The full 2θ range can be found in Figure 5.11. Existing reflections do not shift in position and lose intensity during charge indicating a two-phase mechanism. The newly formed phase is not detected in *operando* XRD due to the lack of long-range order (Figure 5.11).

Ex situ sXRD patterns are examined to gain more quantitative insights. SXRD patterns of fully charged and fully discharged $LiNaCoS_2$ are shown in Figure 5.5d and e. The sXRD diffraction patterns exhibit low intensities compared to the pristine material shown in Figure 5.1, confirming the loss of long-range order. The sXRD patterns of fully charged $LiNaCoS_2$ are fit to Co_9S_8 and CoS, with minor impurities that align with Li_2S reflections marked in * that are too low in intensity to be accurately fit. At the end of full charge, 1.7 alkali metal ions – Li and Na combined – have been removed, implying that there is a very small amount of alkali metal ions left in the structure and most of the active material is comprised of Co_xS_y. There are no visible signs of S dissolution upon disassembly of the cell, and ultraviolet-visible (UV-Vis) spectroscopy shows no evidence of S dissolution in the electrolyte (Figure 5.12). Although the Co:S ratio at the end of charge should be 1:2 or 0.5, the sXRD fit indicates the presence of species with Co:S ratios of ≥ 1, suggesting that not all phases formed during charge are observed in *ex situ* sXRD patterns. The small

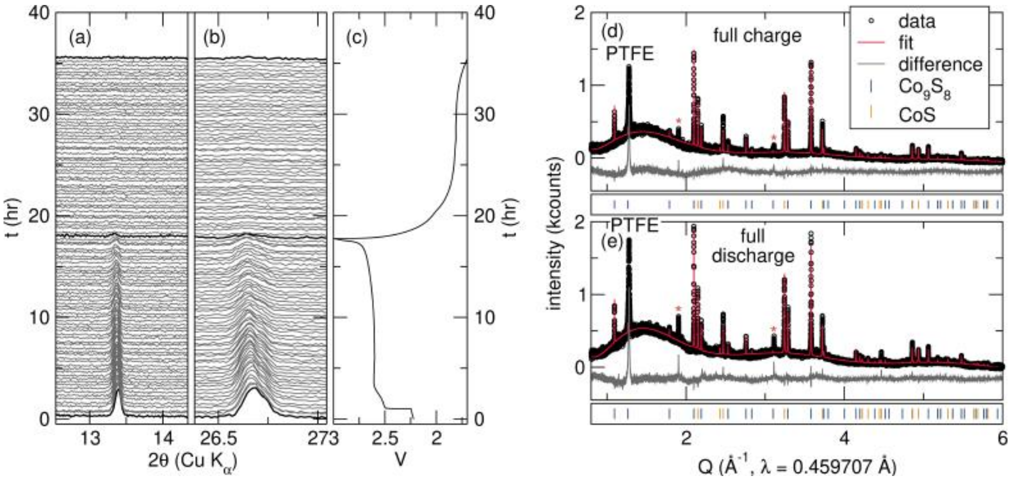

Figure 5.5: *Operando* XRD and sXRD data of $LiNaCoS_2$. (a and b) *Operando* XRD patterns of (001) and (002) reflections of $LiNaCoS_2$ and (c) the corresponding galvanostatic cycling data. (d and e) synchrotron XRD patterns of full charge and full discharge $LiNaCoS_2$. * marks Li_2S reflections in *ex situ* sXRD patterns that are too low in intensity to be fit.

fraction of Co_9S_8 in the pristine material (Figure 5.1) also suggests that the Co_9S_8 observed in *ex situ* sXRD patterns could come from unreacted, residual Co_9S_8 that was observed in the pristine sample. Butala et al. utilized *operando* pair distribution function (PDF) of $Li-CoS_2$ and observed that the formation of spinel phases Co_3S_4 and Co_9S_8 as well as minor recovery of CoS_2 accounted for charge compensation during charge.[182]

The full discharge sXRD patterns shown in Figure 5.5e are fit to the same phases Co_9S_8 and CoS without new reflections nor significant changes in relative phase fractions. This result further indicates that species without long-range order play a major role in the charge compensation mechanism. Additionally, we note that while ssNMR results indicate that re-intercalated alkali metal ion is predominantly Li (Figure 7.4), the intensities of the peaks that align with Li_2S reflections do not increase significantly upon full discharge (Figure 5.5e). The same trend is observed by Butala et al. who reported that the weighting of Li_2S does not increase upon deep discharge in $Li-CoS_2$ below 1.6 V.[182] The Li could be incorporated in small domains of Li_2S that do not result in an increase in the Li_2S reflection intensities, or inserted into the structure through a different pathway. The lower voltage cutoff of 1.7 V suggests that Li_2S is likely not formed.[179,182] Also, ^{7}Li MAS ssNMR indicates that the Li environment in full discharge resembles the one that forms during charge, further suggesting a lithiated phase other than Li_2S such as $Li_xCo_3S_4$.

Next, redox activities and local environments of Co and S are probed with X-ray absorption spectroscopy (XAS) to gain insights into the charge compensation mechanism. Figure 5.6 shows the *ex situ* Co and S K-edge XANES of $LiNaCoS_2$ at various states of charge. The pre-edge feature of pristine $LiNaCoS_2$ in Co XANES confirms the presence of tetrahedrally coordinated Co, arising from the 1s to 3d transition (Figure 5.6a).[182–184] The rising edge does not shift initially until 1.0 e^- and shifts to higher energy (Figure 5.6b), suggesting Co oxidation. Upon full discharge, the rising edge shifts to a lower energy than the pristine state, suggesting Co reduction and an irreversible phase transition.

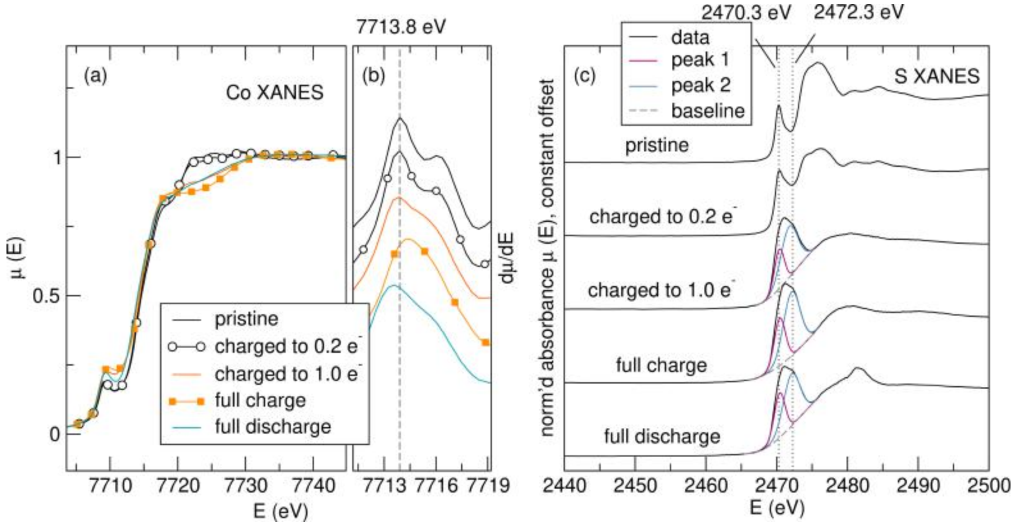

Figure 5.6: Co and S K-edge XANES data of $LiNaCoS_2$ at different states of charge. (a) Co XANES of $LiNaCoS_2$ at different states of charge and (b) the corresponding first derivative plot of the rising edge. (c) S XANES of $LiNaCoS_2$ at different states of charge. Co K-edge rising edge position does not shift in early states of charge and shifts at the end of charge, while S K-edge XANES reveals the emergence of a new feature at early states of charge.

S K-edge XANES at various states of charge (Figure 5.6c) are now investigated. The S K-edge spectrum of pristine $LiNaCoS_2$ exhibits the same profile as its isostructural material $LiNaFeS_2$ with its pre-edge feature at 2470.3 eV. Pristine $LiNaCoS_2$ exhibits a strong pre-edge feature at 2470.3 eV from the S 1s to Co 3d transition.[173,185] Upon charge, a new feature emerges at a higher energy suggesting a new transition associated with more oxidized S relative to S^{2-}. The new feature at 2472.3 eV grows in intensity during charge and does not disappear upon discharge. The phases identified with *ex situ* sXRD – CoS and Co_9S_8 – maintains S^{2-} with a pre-edge feature at 2470 eV and thus do not explain the new feature.[186–188] The presence of this new feature suggests the formation of species with more oxidized S relative to the pristine S states such as $(S_2)^{2-}$, which will be explored further in the next section.

Discussion

$LiNaCoS_2$ exhibits multielectron capacity in the first charge cycle but undergoes an irreversible phase transition. Now, the charge compensation mechanism is discussed. First, to examine the electronic structure of $LiNaCoS_2$ and the role of transition metal-anion covalency, the partial density of states (pDOS) is calculated with DFT. Figure 5.7 illustrates the calculated density of states for $LiNaCoS_2$. $LiNaCoS_2$ exhibits small gap semiconducting electronic ground states with predominantly S states. Comparing isostructural materials $LiNaFeS_2$ and $LiNaCoS_2$ reveals that the $Co^{2+/3+}$-d states are lower compared to the $Fe^{2+/3+}$-d states and overlap more with the S-p states while $LiNaFeS_2$ exhibits $Fe^{2+/3+}$-d states at and immediately below the Fermi level(Figure 5.13).[162,173] The predominant S states below the Fermi level in $LiNaCoS_2$ indicates that S states are accessed first during the plateau in the charge cycle. Although $Co^{2+/3+}$ exhibits more covalent interactions with S p states compared to $Fe^{2+/3+}$, the plateau oxidation voltage appears to be pinned at c.a. 2.6 V in both $LiNaFeS_2$ and $LiNaCoS_2$ in the galvanostatic cycling data.[173] We hypothesize that although transition metal–anion covalency is increased in $LiNaCoS_2$, the S-*nb* states are largely unaffected, which leads to the same anion oxidation potential.

Electrochemical and structural characterization techniques indicate a conversion reaction in $LiNaCoS_2$. GITT of the charge cycle demonstrates that a new phase is formed at each polarization step. There are no visible signs of S dissolution on the separator, and UV-Vis shows no difference between pristine and full charge electrolytes, eliminating the possibility of S dissolution. ^7Li MAS ssNMR reveals that a phase transition happens at early states of charge. Concurrently, a new feature is observed in S XANES during charge. The new feature in S XANES persists at full charge while the new resonance in ^7Li MAS ssNMR is almost absent at full charge, suggesting that these two features arise from different moieties.

S XANES provides further insights into the charge compensation mechanism. The new pre-edge feature at 2472.3 eV suggests the presence of a more oxidized S states compared to S^{2-} in $LiNaCoS_2$. A feature at the same energy is observed in reference spectra of pyrite CoS_2, elemental S_8, or Li_xS_y.[189–192] The new pre-edge feature appears at early states of charge and does not increase significantly upon full charge. Meanwhile, the Co rising edge does not shift until 1.0 e^- and shifts to

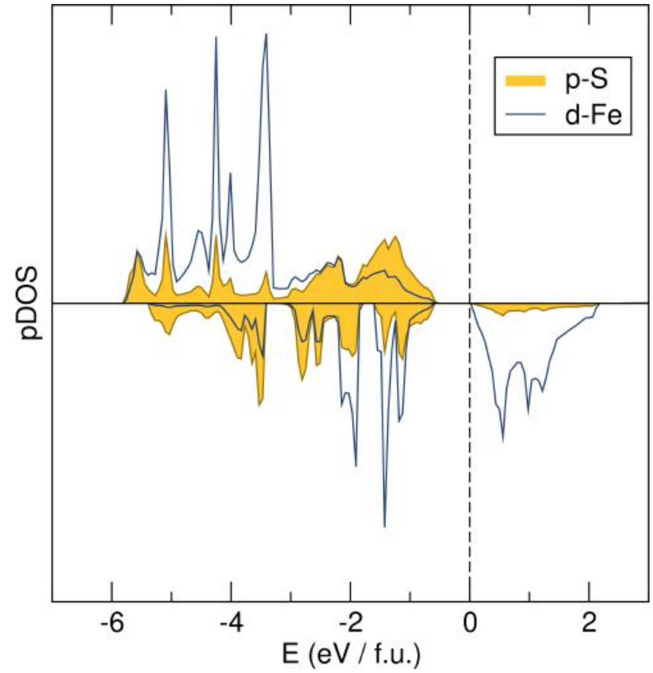

Figure 5.7: Calculated spin-polarized partial density of states of $LiNaCoS_2$. $LiNaCoS_2$ exhibits small gap semiconducting electronic ground states with predominantly S states.

a higher energy upon full charge. This result corroborates the pDOS calculations that S oxidation accounts for most of the charge compensation initially followed by Co oxidation during charge. Based on the pDOS calculations and Co and S K-edge XANES, we propose that S is oxidized initially which forces a phase transition into CoS_2. Previous works have observed the presence of CoS_2 in similar operating conditions. Yan et al. showed that when CoS_2 is discharged to 1.6 V and charged again, CoS_2 initially loses its XRD peak intensities during discharge but recovers them upon the subsequent charge, suggesting that CoS_2 formation can occur when the lower voltage cutoff is at 1.6 V.[179] Butala et al. also reported that CoS_2 weighting appears and remains between 1.6 and 3 V in the *operando* PDF analysis.[182]

Other spectroscopic techniques further elucidate the charge products in $LiNaCoS_2$. *Ex situ* sXRD patterns of full charge and full discharge $LiNaCoS_2$ reveal the presence of CoS and Co_9S_8 that retain long-range order, but fail to detect non-crystalline moieties. Also, sXRD patterns of full charge and full discharge appear almost identical and are both fit to the same phases, suggesting that structural changes are local and not detected by sXRD. Butala et al. illustrated with *ex situ* Co XANES and *operando* PDF that during cycle one charge, spinel phase Co_3S_4 grows at the expense of Co_9S_8 with a slight increase in CoS_2 weighting above 1.6 V.[182] Also,

Li_2S weighting does not increase during discharge, suggesting a Li insertion in the spinel phases as a different pathway for Li incorporation.[182] Li et al. also showed with *in situ* TEM that Li insertion undergoes intercalation followed by conversion in Co_3O_4 during which Li pushes and occupies the tetrahedral *8a* site of Co and forms $Li_xCo_3S_4$, which is ultimately converted into Co + Li_2O upon full reduction.[193] Similar mechanism has been observed with the Co_3S_4 spinel phase with various mobile ions such as Li and Mg[194–197] and in other thiospinel phases.[198–200]

We suggest that during charge, the initial formation of CoS_2 domains alters the structure and yields $Li_xCo_3S_4$ upon further oxidation in small domains that are not detected in sXRD. The emergence of $Li_xCo_3S_4$ also explains the new resonance observed in ^{7}Li MAS ssNMR; during charge, Li ions migrate into the Co_3S_4 domains and give rise to the new Li resonance. Upon full full charge, Li is removed from the structure and Co is oxidized as evidenced by Co XANES (Figure 5.6). Upon full discharge, Co_3S_4 is reduced and more Co_9S_8 domains appear, with the formal oxidation state of Co decreasing (Figure 5.6). Because Li is incorporated into these phases instead of recovering the parent phase, only the new resonance in ^{7}Li MAS ssNMR remains.

Lastly, we discuss the differences between isostructural materials $LiNaFeS_2$ and $LiNaCoS_2$. $LiNaFeS_2$ does not form pyrite FeS_2 while forming S-S bonds during delithiation and maintains its local structural environments.[173] Although the material suffers from particle fracturing, the layered structure and the charge compensation mechanism is maintained.[178] On the other hand, $LiNaCoS_2$ undergoes a rapid phase transition during charge and forms CoS_2 and $Li_xCo_3S_4$. Elucidating the origin of the energetic driving force that leads to phase transition requires further computational calculations. Based on the spectroscopic techniques employed in this work, we hypothesize that while lowering the transition metal *d* states leads to increased transition metal-anion covalency, the states immediately below the Fermi level mainly consists of S-*nb* states. As a result, S is oxidized first in $LiNaCoS_2$ and forms S-S bonds which energetically favor to phase separate into CoS_2. Concurrently, increasing domains of CoS_2 forces the rest of the structure to phase separate and form $Li_xCo_3S_4$. We also point out that ternary Li_2CoS_2 does not form in the same conditions used to synthesize Li_2FeS_2. Therefore, it is also possible that larger Na ions stabilize the structure and enables the formation of $LiNaCoS_2$, and the removal of Na ions leads to phase transition as well. We also note that partial substitution of

Co for Fe does not improve the electrochemical performance of the material (Figure 5.14).

5.5 Conclusions

Layered $LiNaCoS_2$ isostructural to $LiNaFeS_2$ can be synthesized and exhibits multielectron capacity from both cation and anion redox. $LiNaCoS_2$ undergoes an irreversible phase transition in cycle 1, which is summarized in Figure 5.8.

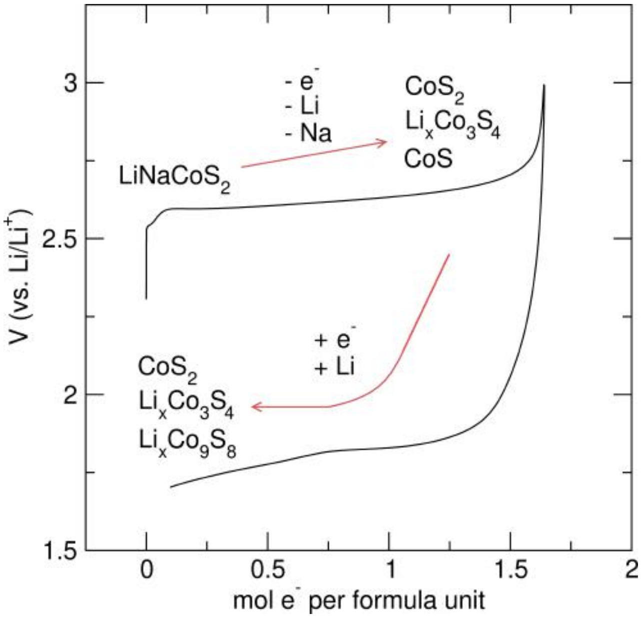

Figure 5.8: Summary of phase transition in $LiNaCoS_2$ in cycle 1 based on structural and spectroscopic characterization.

The charge curve is characterized by a single plateau suggesting a two-phase mechanism. S oxidation occurs first and forms CoS_2, which is followed by the formation of $Li_xCo_3S_4$. During discharge, CoS_2 plays a reduced role in charge compensation while Co is readily reduced. More covalent interactions between $Co^{2+/3+}$ and S states compared to $Fe^{2+/3+}$ cause S-*p* states to be available from the beginning of charge. However, $LiNaCoS_2$ suffers from rapid capacity fade due to the irreversible phase transition. Therefore, this work highlights that the physical structural stability of the delithiated state of a material must be considered and understood in addition to electronic structure to develop high-performance cathode materials with anion redox.

5.A Supplementary Information

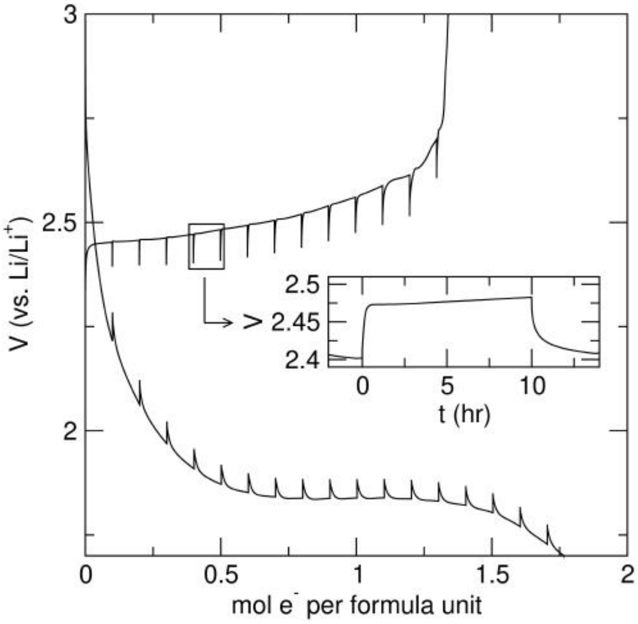

Figure 5.9: Galvanostatic intermittent titration technique of LiNaCoS$_2$ collected at C/100 based on 1 e$^-$ per formula unit. The overpotential spike present in GITT at C/10 is no longer present.

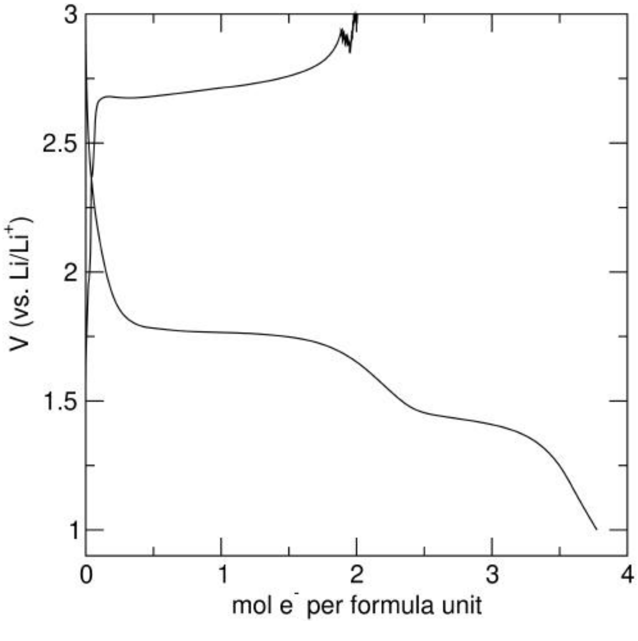

Figure 5.10: Galvanostatic cycling data of LiNaCoS$_2$ charged to 3 V and discharged to 1 V. The discharge curve resembles that of CoS$_2$.

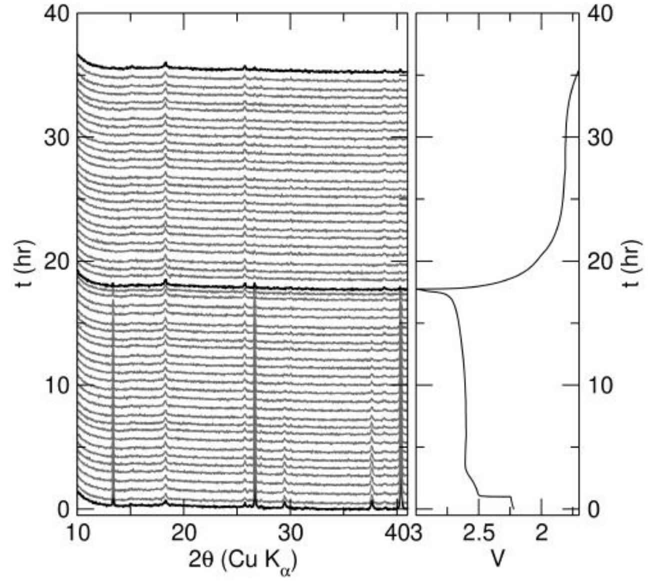

Figure 5.11: *Operando* XRD patterns of $LiNaCoS_2$ in cycle 1.

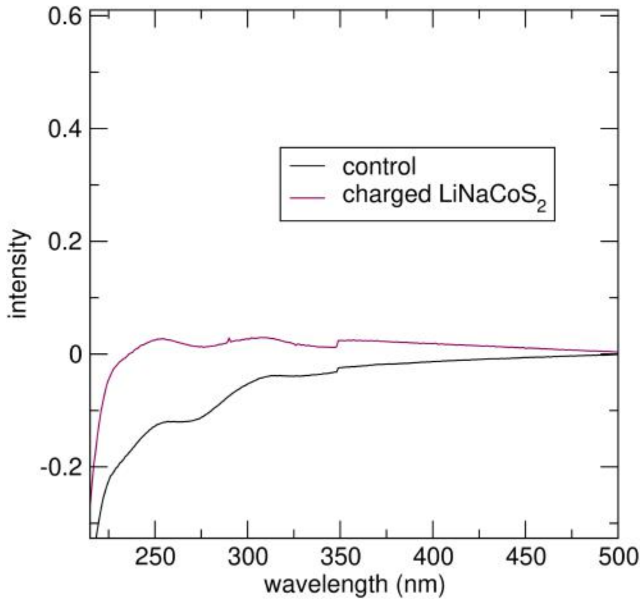

Figure 5.12: UV-Vis spectra of control and charged $LiNaCoS_2$. UV-Vis is conducted on the solution obtained by running dimethyl carbonate on the separator of the disassembled cell and collecting the drops from the separator. Control is from the separator of a dummy cell that contains Li foil, the electrolyte, and the separator without the cathode composite electrode. The charged cell is from the separator of a fully charged LiNaCoS2 cell.

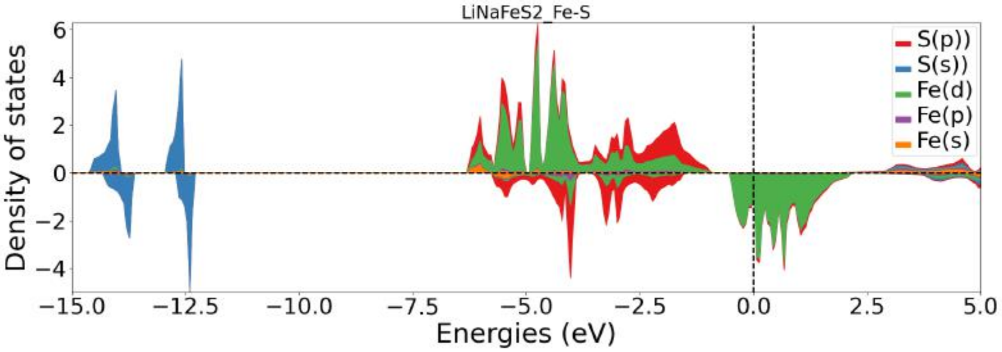

Figure 5.13: pDOS calculations of $LiNaFeS_2$ States at and immediately below the Fermi level are characterized by Fe-*d* states.

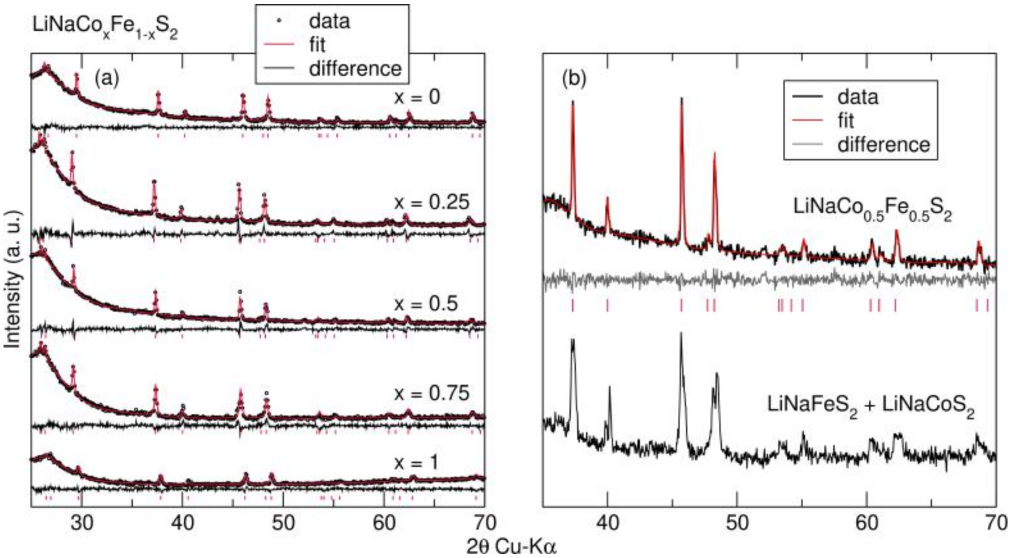

Figure 5.14: (a) XRD patterns of $LiNaCo_xFe_{1\text{-}x}S_2$ and (b) comparison of XRD patterns of $LiNaCo_{0.5}Fe_{0.5}S_2$ and 50:50 wt% mixture of $LiNaFeS_2$ and $LiNaCoS_2$ powders. $LiNaCo_{0.5}Fe_{0.5}S_2$ can be fit to one single phase while the mixture exhibits two peaks, suggesting that $LiNaCo_xFe_{1\text{-}x}S_2$ forms a single-phase material with mixed occupancy of Fe and Co in the same site.

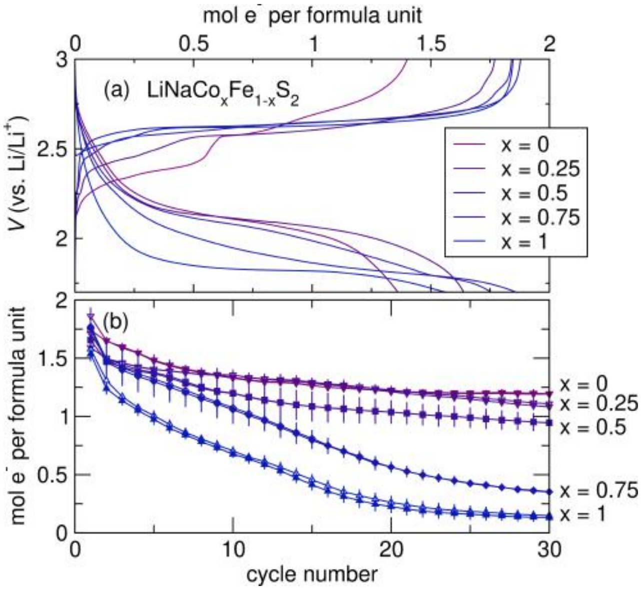

Figure 5.15: Galvanostatic cycling data of LiNaCo$_x$Fe$_{1-x}$S$_2$. (a) Galvanostatic cycling data of LiNaCo$_x$Fe$_{1-x}$S$_2$ and (b) the corresponding cycling data. Partial does not result in improved electrochemical performance of the material.

Chapter 6

ENABLING ANION REDOX THROUGH CATION VACANCIES IN LI-RICH SULFIDE MATERIALS

Contributions: S.S.K. conceived, designed, and performed experiments, and wrote the manuscript. *manuscript submitted*

6.1 Abstract

Conventional Li-ion battery intercalation cathodes leverage charge compensation that is formally associated with redox on the transition metal. Employing the anions in the charge compensation mechanism, so-called anion redox, can yield higher capacities beyond the traditional limitations of intercalation chemistry. Here, we aim to understand the structural considerations that enable anion redox. Using a Li-rich metal sulfide as a model system, we present both first-principles simulations and experimental data that show cation vacancies are required for anion redox. First-principles simulations show that oxidation of sulfide to persulfide only occurs when a neighboring vacancy is present. To experimentally probe the role of vacancies in anion redox processes, we introduce vacancies into the Li_2TiS_3 phase while maintaining a high valency of Ti. When the cationic sublattice is fully occupied and no vacancies can be formed through transition metal oxidation, the material is electrochemically inert. Upon introduction of vacancies, the material can support high degrees of anion redox even in the absence of transition metal oxidation. This system offers fundamental insights to deepen our understanding of structure-property relationships that govern reversible anion redox in sulfides and provides strong evidence that cation vacancies are required for anion redox.

6.2 Introduction

Developments in Li-ion batteries (LIBs) have enabled the modern technological era, and their future applications could have a dramatic impact on sustainability.[7,8] Since the 1990s, LIB cathode chemistry has been dominated by layered transition metal oxides like $LiMO_2$, where M is a combination of transition metals. Upon oxidation of $LiMO_2$, Li^+ is deintercalated and the transition metal is oxidized. While $LiMO_2$ materials can exhibit varying degrees of covalency between the M and O, the charge compensation is largely localized to the M which causes minimal structural changes upon redox. The intercalation mechanism is quite reversible; however, intercalation materials are reaching their theoretical capacity limits.[155]

To increase the energy density of LIBs, cathode materials capable of storing more than one electron per transition metal through the additional redox activity of lattice anions, so-called multielectron redox, have received increasing attention.[201,202] In Li-rich oxides, the charge compensation has been suggested to involve both the transition metal and the oxide anions. However, the underlying mechanism of multielectron capacity observed in these materials remains subject to debate, with proposed mechanisms invoking oxidation of hybridized M-O states,[164,203] transition metal oxidation beyond 4+[204,205] as well as various forms of oxidized O.[204,206–211] Additionally, Li-rich oxides suffer from a number of undesirable side reactions that further complicate both the development of a mechanistic understanding of anion redox and the practical development of Li-rich cathodes.[211–213]

To effectively leverage anion redox, design rules controlling reversible oxidation of anions need to be understood. Hong *et al.* demonstrated that cation vacancies that form as a result of transition metal migration stabilize the formation of short Ir–O π bonds and 1.4 Å O–O dimers through local structural defects that accommodate small distortions in $Li_2Ir_{1-y}Sn_yO_3$.[214] Similarly, House et al. recently demonstrated that the loss of Li from the transition metal layer and transition metal migration during charge result in vacancy clusters in $Na_{0.75}(Li_{0.25}Mn_{0.75})O_2$ that accommodate the formation of molecular O_2 in the bulk.[209] The driving force behind the vacancy cluster formation is ascribed to the lower energy of O_2 dimer–containing structure that promotes Mn migration to disrupt the honeycomb superstructure.[158] In Li-rich oxides, the formation of cationic vacancy clusters is a byproduct of O dimerzation that leads to irreversible transition metal migration and voltage hysteresis.

Unlike Li-rich oxides, anion redox in Li-rich sulfides intrinsically operates at lower voltages due to the higher energy of S-p states compared to O-p states. Multielectron redox in Li-rich sulfides is free of electrolyte decomposition and other degradation reactions. Furthermore, oxidation of sulfides can lead to the formation of persulfide moieties without breaking the transition metal–S bond.[161] The energetics of the S valence states allow S to form relatively covalent metal-anion bonds with the more abundant, less expensive 3d transition metals. In these materials, S exists fully or partially as dimerized $(S_2)^{2-}$ pairs.[163,215–217] Therefore, persulfides can serve as a thermodynamically stable structural feature that can promote increased electrochemical activity.

Activating S oxidation via persulfide formation requires structural motifs that can accommodate local distortions associated with S-S bond formation. d^0 transition metal sulfides such as Li_2TiS_3 and Li_3NbS_4 do not exhibit electrochemical activity in their ordered phases, but show anion oxidation upon ball milling and forming disordered rocksalt phases.[218] Ball milling and the formation of disordered rock salt introduce various types of defects and also further affect the electronic states of S by altering its coordination environment. In this work, we target a specific type of defect–cationic vacancies–and explore its role in activating S oxidation. To determine if anion redox is indeed enabled by the presence of vacancies, a material is needed that cannot be electrochemically oxidized during charge when the cationic sublattice is fully occupied as a negative control and allows for only anion oxidation when cationic vacancies are introduced (Figure 6.1).

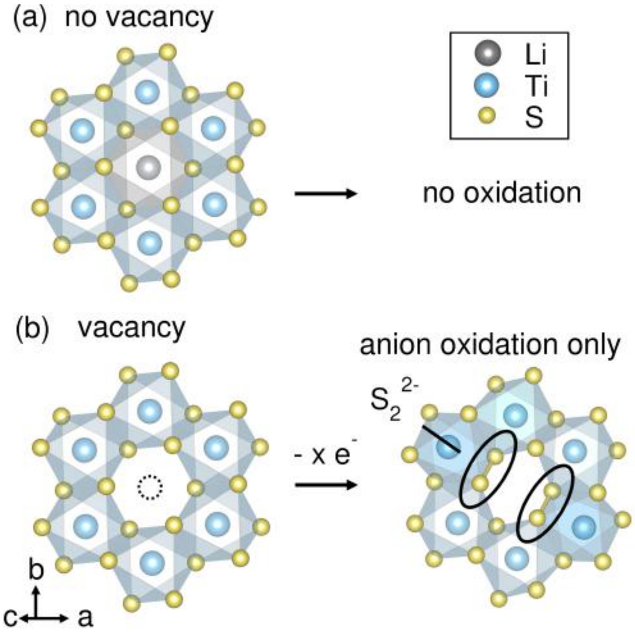

Figure 6.1: Cartoon representation of vacancy enabling S oxidation. (a) Cartoon representation of fully occupied cation sublattice in which no oxidation occurs. (b) Cartoon representation of Li vacancy in the transition metal layer resulting in anion redox.

The negative control thus precludes the use of Li-rich materials with open shell transition metals, since oxidation will simply form vacancies by virtue of transition metal oxidation and Li^+ delithiation and prevent observation of the negative control case. Here, we use Li_2TiS_3 as the negative control since it has a fully occupied cationic sublattice, d^0 Ti^{4+}, and oxidation yields minimal capacity.[163,165,166,218–220] We then demonstrate that anion redox is activated in otherwise inert Li_2TiS_3 by introducing cation vacancies while maintaining the Ti oxidation state at Ti^{4+}. We introduce intrinsic vacancies via solid-state synthesis by increasing the Ti^{4+}:Li^{+} ratio, circumventing complications associated with initial transition metal oxidation. Using spectroscopic techniques and first-principles simulations, we demonstrate that intrinsic cation vacancies in $Li_{1.33-1.33z}Ti_{0.67+0.33z}\square_zS_2$ ($\square$ = vacancy) activates anion redox by allowing for persulfide formation, which is responsible for the observed excess capacity. Thus, we show that cation vacancies are a necessary structural motif to liberate and rehybridize S-p orbitals, activating sulfide anion redox.

6.3 Methods

Material Preparation

All materials were prepared using traditional solid state methods in an Ar-filled glovebox in which O_2 and H_2O levels were < 1 ppm. The Ti:S ratio of commercially available TiS_2 (Thermo Scientific Chemicals, ≥99.8%) based on electron probe microanalysis (EPMA) is 1:1.93. Therefore, materials prepared with the commercially available TiS_2 are labeled as "Ti-rich." Stoichiometric TiS_2 was prepared by grinding a 1:2.1 molar ratio of Ti metal powder (325 mesh, Thermo Scientific Chemicals, ≥99.5%) and S (S_8, Acros Organics, >99.5%) , which was then pressed into 400 mg pellets and sealed in an evacuated vitreous silica ampule. The reactants were heated at 3 °C min^{-1} to 600 °C with a dwell time of 24 h before cooling to room temperature. $Li_{1.33-1.33z}Ti_{0.67+0.33z}\square_zS_2$ was prepared by grinding stoichiometric quantities of Li_2S (Beantown Chemical, 99.9%), stoichiometric TiS_2, and 0.1 molar excess S pressing into 300 mg pellets. Pellets were placed inside carbon-coated vitreous silica ampules and heated at 3 °C min^{-1} to 750°C with a dwell time of 48 h before cooling to room temperature. "Ti-rich" $LiTi_{0.75}\square_{0.25}S_2$ was synthesized by the same procedure, but with stoichiometric quantities of Li_2 and "Ti-rich" TiS_2. $Li_{1+\alpha}Ti_{0.75}\square_{0.25-\alpha}S_2$ was synthesized by the same procedure, but with stoichiometric quantities of Li_2S (Beantown Chemical), stoichiometric TiS_2, Ti, and 0.1 excess S pressing into 300 mg pellets. $Li_{0.83}Mg_{0.25}Ti_{0.67}\square_{0.25}S_2$ was synthesized by the same procedure, but with stoichiometric quantities of Li_2S (Beantown Chemical), stoichiometric TiS_2, Mg powder (Sigma Aldrich, >99%), S (Acros Organics), and 0.1 excess S (Acros Organics) pressing into 300 mg pellets. The color of all materials synthesized was black.

Electrochemical Characterization

All cells were prepared inside Ar-filled gloveboxes in which H_2O and O_2 levels were below 0.1 ppm. Active materials of $Li_{1.33-1.33z}Ti_{0.67+0.33z}\square_{z}S_2$ and $Li_{1+\alpha}Ti_{0.75}\square_{0.25-\alpha}S_2$ were mixed with Super P carbon (Alfa Aesar, $\geq$99%) and polytetrafluoroethylene (PTFE, Sigma-Aldrich) at a ratio of 3:1:1 by mass to make composite electrodes. The active material and carbon were hand-ground together first for 5 minutes, then PTFE was added to the mixture and hand-ground with a mortar and pestle. Approximately 10 mg of the composite mixture was then pressed into 0.25 inch diameter pellets with a hand-operated arbor press. 2032 coin cells were prepared with polished Li metal counter/reference electrodes, dried 18 mm diameter glass fiber separators (Whatman GF/D), and 11 drops of electrolyte (approximately 165 mg). The electrolyte in all cells was a 1 M solution of $LiPF_6$ (Sigma-Aldrich, $\geq$99.99%) in a 1:1:3 mixture of ethylene carbonate (Sigma-Aldrich, >99%), propylene carbonate (Sigma-Aldrich, >99%), and dimethyl carbonate (Sigma-Aldrich, >99%) by volume. All potentials are in reference to the Li metal counter/reference electrode potential, which is approximated to equal to that of Li/Li^+. Galvanostatic cycling data were collected at C/20 based on 1 e^- per formula unit. $LiTi_{0.75}\square_{0.25}S_2$ in a Mg electrolyte system was prepared in a similar manner to a previously reported TiS_2 cathode in a Mg electrolyte.[221] $LiTi_{0.75}\square_{0.25}S_2$ was mixed with Super P carbon (Alfa Aesar, $\geq$ 99%) and polyvinylidene fluoride (PVDF, MTI Corp.) at a mass ratio of 8:1:1 in N-methyl-2-pyrrolindone (NMP, Thermo Scientific) and the slurry was casted onto Mo foil (Alfa Aesar, >99%). 1/4 inch diameter PTFE Swagelok cells were prepared with polished Mg metal (MTI Corp., >99%) counter/reference electrodes, dried 1/4 inch diameter glass fiber separators (Whatman GF/D), and 5 drops of electrolyte (approximately 56 mg). The electrolyte in all cells was 0.2 M all-phenyl complex (APC) using 1:2 aluminum chloride, anhydrous (Beantown Chemical, >99%):phenylmangesium chloride (Sigma Aldrich, 2.0 M in THF) with 10 wt.% excess aluminum chloride in THF (Sigma). Galvanostatic cycling data was collected at C/100 based on 1 e- per formula unit in an oven at 60 °C.

Material Characterization

For powder X-ray diffraction (XRD), the powders were placed on an air-free sample holder (Rigaku) inside the glovebox to prevent air exposure during measurement. XRD patterns were collected on a Rigaku diffractometer with a Cu-Kα X-ray source at 3 $^{\circ}$min^{-1} with 0.04 °step size. The diffraction patterns were fit by the Rietveld method using GSAS-II.[144] Visualization of the crystal structures was aided by VESTA.[174]

High-resolution synchrotron powder X-ray diffraction (XRD) patterns were collected on beamline 11-BM-B (λ = 0.458979 Å) at the Advanced Photon Source at Argonne National Laboratory.[175] The powder of $LiTi_{0.75}\square_{0.25}S_2$ was used for the pristine state, while *ex situ* charged sample was prepared using 16 mg of a 60:20:20 wt% pellet consisting of active material, Super P carbon, and PTFE. A cell fully charged to 3 V was disassembled in an Ar-filled glovebox, and the cathode composite was recovered from the disassembled cell, washed with 200 μl of dimethyl carbonate, and vacuum dried. The sample was sealed under vacuum in 0.7 mm (o.d.) glass capillaries (Hampton Research) to prevent air exposure and placed inside of polyimide capillaries.

Operando XRD data were collected using a Bruker D8 Advance diffractometer in Bragg-Brentano geometry equipped with a Cu Kα source (λ_1 = 1.5406 Å, λ_2 = 1.5444 Å) and a Lynxeye XE-T detector. A custom-made *operando* cell with a PEEK body, stainless steel electrical contacts, and an X-ray transparent Be window (SPI Supplies, 0.25 mm thick) was used. The Be window served as a current collector and allowed for X-ray penetration so that diffraction patterns could be collected while cycling galvanostatically. As with the *ex situ* cells, pellet electrodes composed of 60% active material, 20% carbon black, and 20% polymer binder were used and placed directly on the Be window. The pellet electrodes were cycled against Li foil using a BioLogic SP-200 potentiostat at a C/20 rate with one Whatman glass fiber separator (GF/D) flooded with 1 M LiPF6 in 1:1:1 EC:PC:DMC electrolyte. Patterns were continuously collected over a range of 10°to 45°2θ approximately every 20 min throughout the duration of the electrochemical cycling.

Transmission electron microscopy (TEM) imaging was conducted using Thermofisher Talos F200X G2 S/TEM at an accelerating voltage of 200 keV under High-resolution TEM (HRTEM) mode. TEM samples of pristine $LiTi_{0.75}\square_{0.25}S_2$ and charged $LiTi_{0.75}\square_{0.25}S_2$ were prepared through dry transfer powders onto 200 mesh lacey carbon films on copper grids (Ted Pella, Inc.). The Fast Fourier Transformation (FFT) pattern simulation from the HRTEM image of pristine $LiTi_{0.75}\square_{0.25}S_2$ was performed in ImageJ and was matched to [110] zone axis by CrysTBox diffract-GUI.[222]

Electron probe microanalysis (EPMA) was conducted using the JEOL JXA-8200 with a 10 kV and 5 nA focused beam. The focused electron beam is 150 nm in diameter. Standards for analysis were TiO_2 for Ti and FeS_2 for S. 30 mg of powder was pressed with a hydraulic press for 5 minutes at 2 tons inside an Ar-filled glovebox. C was sputtered onto the pellets using graphite under vacuum, and transferred to the instrument. There was < 30 s of air exposure during transfer. Seven different areas were selected and measured.

Inductively coupled plasma mass spectrometry (ICP-MS) was performed on Agilent 8800. 3 replicates of 3 – 4 mg of LiTi0.75S2 were dissolved in 5% nitic acid solution at 60 °C for 2 hours. Upon complete dissolution, the solutions were diluted twice in 5% nitric acid to reach x2500 dilution. 5 different concentrations were chosen as standards from 100.02 ppm Ti and 998 ppm Li standard solutions.

Solid-state NMR was performed using Bruker Avance 500 MHz spectrometer operating at 194.31 MHz for ^{7}Li. All samples were packed in a 4 mm ZrO_2 HR-MAS rotor with 50 μl PTFE spacer (Cortecnet). 40 mg of pristine powders of $Li(Li_{1/3}Ti_{2/3})S_2$ and $LiTi_{0.75}\square_{0.25}S_2$ were packed into the rotor in an Ar-filled glovebox. *Ex situ* samples were preared in the same way as electrochemical cells in coin cells with a total mass of 20 mg. Upon reaching the appropriate state of charge, the cathode composite was recovered and washed with 300 μl of dimethyl carbonate and vacuum-dried in an Ar-filled glovebox. ^{6}Li and ^{7}Li MAS ssNMR was recorded spinning at 13 kHz. A single RF pulse of 0.5 μs with a 4 μs $\pi/2$ was applied. The ^{7}Li MAS spectra were fit with DMFIT using Quasar. The $Li(Li_{1/3}Ti_{2/3})S_2$ spectrum was fit while fixing the relative areas of the peaks at 50 : 25 : 25 %. ^{6}Li and ^{7}Li spectra were referenced using LiCl as the standard at 0 ppm.

Electron paramagnetic resonance (EPR) spectroscopy data were collected with Bruker EMX X-band CW-EPR Spectrometer operating at 9.4 GHz. In an Ar-filled glovebox, 30 mg of powder was packed into a 1.8 mm O.D. quartz capillary which was then placed inside an EPR tube and sealed with a septum to prevent air exposure. The tube was placed in LN_2 dewar flask and during measurement. Spectra were acquired with microwave power of 2.185 mW and an amplitude modulation of 8 G.

Ti X-ray absorption spectroscopy was conducted at beamline 2-2 at the Stanford Synchrotron Radiation Lightsource at SLAC National Accelerator Laboratory. Data processing including calibration and background correction was performed using Athena.[176] The Ti K-edge data were calibrated to a collinear Ti foil for each sample. *Ex situ* samples were prepared in the same way as electrochemical cells in coin cells with a total mass of 20 mg. Upon reaching the appropriate state of charge, the cathode composite was recovered and washed with 300 μl of dimethyl carbonate and vacuum-dried in an Ar-filled glovebox. *Ex situ* samples were placed onto the sample holder using Kapton tape on each side inside an Ar-filled glovebox. During measurement, the sample holder was placed in a continuous He-flushed chamber with minimal O_2 concentration (< 500 ppm). Each scan lasted about 15 minutes, and 3 scans were averaged.

S X-ray emission spectroscopy was performed using the Brimstone^{TM} laboratory spectrometer (easyXAFS LLC, Renton, WA, USA). The spectrometer utilized a Pd-anode x-ray tube and was operated at 24 kV and 3 mA. The spectrometer uses the easyXAFS Kromo^{TM} cmos-based position-sensitive, energy resolving detector. Using a Si(111) crystal analyzer with radius of curvature 100 mm, the S K_α spectra were measured at a Bragg angle of 59.0 degrees, and S K_β spectra were measured at a Bragg angle of 53.4 degrees. To reduce Johann error for optimal resolution, the 20 mm wide analyzer was masked to use only the central 4 mm. Measurements are performed under helium flushed into the experimental chamber at atmospheric pressure. Samples were prepared by encapsulating the powder samples between a lower layer of Kapton tape and an upper layer of 8 μm thin Kapton film. The sealed samples were then briefly exposed to air during mounting into the spectrometer (15 min) and during the helium flushing (25 min). Some residual air is expected to remain in the chamber, even after flushing. Samples were mounted on an automatic sample changer, and a series of repeated short scans (3 minutes each) were measured alternately between each sample and reference compounds, and 5 scans were averaged. Resulting data were monitored for possible changes due to instrumental drift or changes in sample signal over time from radiation damage, air exposure, or other effects. ZnS and Na_2SO_4 were used as standards for calibration and the spectra are shown in Figure 6.25.

Computational Methods

Density functional theory (DFT) calculations were performed using the Vienna Ab-Initio Simulation Package (VASP), following the protocol recently benchmarked specifically for capturing the behavior of mixed metal-centric and anion-centric redox processes.[164,205] Specifically, we rely on the SCAN exchange-correlation functional and projector-augmented wave method, Gaussian smearing (σ = 0.05 eV), and a reciprocal space discretization of 25 k-points per Å^{-1}. All calculations are converged to 10^{-5} eV in total energy and 20 meV Å^{-1} in forces. No specific symmetry is assumed or enforced, and no further corrections are used. Energies are optimized over all distinct combinations of Li-vacancy configurations, together with zero, one or two S_2 dimers per Ti-vacancy. In the enumeration, we account for both standard octahedral Li sites and tetrahedral Li configurations reported in analogous systems. Configurational enumeration is limited to 1 unit cell shown in Figure 6.2a, that is considering up to 10 total Li and 1 vacancy in the Ti layer. Structural enumeration and calculation postprocessing is performed using the pymatgen python package.

6.4 Results

Mechanism of S Redox in Mixed Valence $Li_{1+x}Ti_{1-x}S_2$

Previous works have shown that Li_2TiS_3 is electrochemically inactive.[163,165,166,218–220] Li_2TiS_3 is similar to $LiTiS_2$ but with 1/3 of the Ti sites in the metal layer substituted by Li to yield a fully occupied cationic sublattice and fully oxidized d^0 Ti^{4+}. The structure of $LiTiS_2$ can be described as a layer of edge-sharing octahedrally coordinated Li separated by a layer of edge-sharing octahedrally coordinated Ti. Thus, the stoichiometry of the Li-rich phase can be written as $Li(Li_{1/3}Ti_{2/3})S_2$ where the alkali stoichiometry outside the parenthesis indicates the composition of cations in the Li layer and the alkali + metal stoichiometry within the parenthesis indicates the composition of the metal layer. Li can also occupy the Ti sites at various ratios and thus the Li-rich phases can be more generally described as $Li(Li_xTi_{1-x})S_2$.[165]

Using the $Li(Li_xTi_{1-x})S_2$ family of materials as a model system, we first turn to density functional theory (DFT) calculations to probe the correlation between anion oxidation and vacancy content. Most compositions of $Li(Li_xTi_{1-x})S_2$ contain mixed valence $Ti^{3+/4+}$ and yield Ti^{3+} oxidation commensurate with the formation of Li^+ vacancies. As a representative example of such mixed valence $Ti^{3+/4+}$ compounds analogous to those reported by Flamary-Mespoulie *et al.*,[165] we computationally examine the oxidation of $Li(Li_{1/9}Ti_{8/9})S_2$, which can be written as $[Li_9][Li_1Ti_6^{3+}Ti_2^{4+}]S_{18}$. We assume that this compound is layered, consistent with the $R\bar{3}m$ space group reported experimentally, with a representative Li-Ti arrangement in the Ti layer shown schematically in Figure 6.2a. Figure 6.2b shows calculated formation energies of enumerated configurations of this compound as Li is extracted for three scenarios: (a) $Ti^{3+/4+}$ oxidation followed by on-lattice S-oxidation with no persulfide formation ($0S_2^{2-}$), (b) $Ti^{3+/4+}$ oxidation followed by the formation of one persulfide ($1S_2^{2-}$), or (c) $Ti^{3+/4+}$ oxidation followed by the formation of two persulfides ($2S_2^{2-}$). The formation of two persulfides at full delithiation is the lowest energy pathway, while on-lattice S-redox ($0S_2^{2-}$) is substantially higher in energy.

The corresponding voltage curve shown in Figure 6.2c reveals close agreement with the experimental data reported by Flamary-Mespoulie *et al.*,[165] with a sloping voltage profile in the $Ti^{3+/4+}$ region and a jump to ≈ 2.8 V at the onset of S-oxidation.

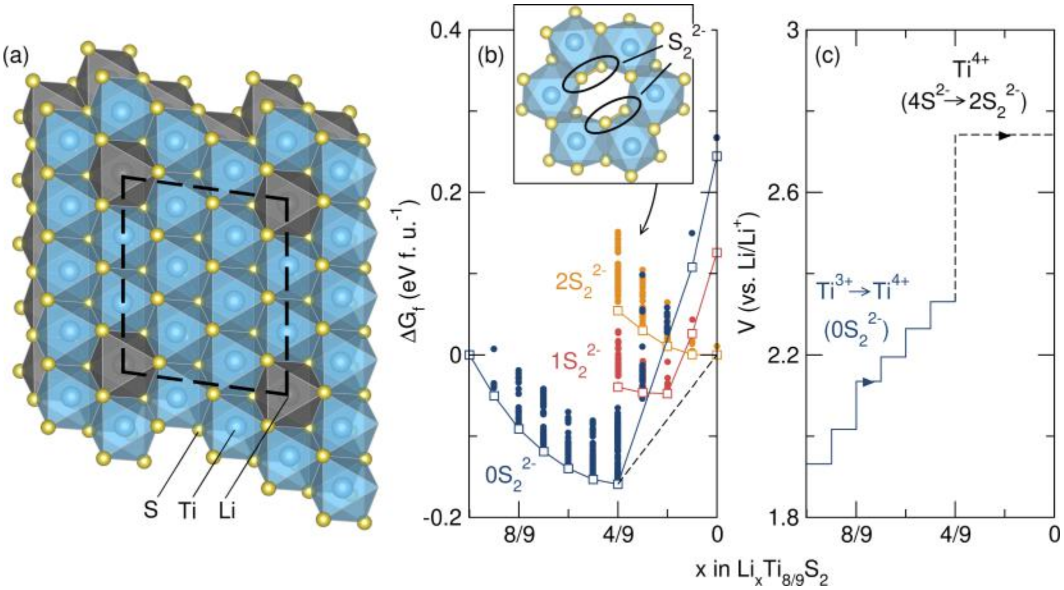

Figure 6.2: Thermodynamic enumeration of delithiated states(a) Structure of model $Li(Li_{1/9}Ti_{8/9})S_2$ compound viewed down the *c*-axis onto the transition metal layer. (b) Thermodynamic enumeration of delithiated states illustrating the relative energies of $Ti^{3+/4+}$ oxidation, on-lattice S-oxidation ($0S_2^{2-}$), and S-oxidation through the formation of persulfides ($1S_2^{2-}$ and $2S_2^{2-}$). (c) Voltage curve corresponding to the equilibrium persulfide pathway on charge. Data collected by Dr. Daniil Kitchaev in the Van der Ven Group at UCSB.

A critical feature of the redox mechanism proposed in Figure 6.2 is that the low-energy persulfide pathway is only possible in the presence of a cation vacancy in the Ti-layer. Persulfide formation requires a distortion of the local environment, which in the absence of a vacancy is structurally unfavorable. However, on-lattice S-oxidation is a high-energy process that requires much higher voltages than those observed experimentally and is unlikely to be observable in practice. We thus propose that the reason Li_2TiS_3 is electrochemically inactive is the insufficient amount of vacancies in the material, which suppresses the formation of persulfides responsible for S-redox activity.

Introduction of Vacancies by Substitution

Based on the proposed vacancy-mediated mechanism in the mixed-valence compounds, we hypothesize that pure S-redox can be activated in Li_2TiS_3 by chemically introducing vacancies into the pristine material. Vacancies can be introduced by aliovalent substitution of Ti for Li in Li_2TiS_3. During synthesis, for every additional Ti^{4+}, four Li^+ are removed to maintain the Ti oxidation state at Ti^{4+} yielding a general stoichiometry of $Li_{1.33-1.33z}Ti_{0.67+0.33z}\square_zS_2$, where $\square$ = vacancy and z = vacancy content. Li_2TiS_3 will be described as $Li_{1.33}Ti_{0.67}S_2$ hereafter for consistency.

Compounds with various vacancy contents are synthesized in the form $Li_{1.33-1.33z}Ti_{0.67+0.33z}\square_zS_2$. Excess S (+0.1 mol) must be used during synthesis to maintain a partial pressure of S in the headspace of the reaction ampoule and drive the formal oxidation state of Ti closer to Ti^{4+}. We choose $LiTi_{0.75}\square_{0.25}S_2$ for in–depth analysis based on its superior electrochemical performance (*vide infra*). The synchrotron XRD (sXRD) pattern and quantitative Rietveld refinement of $LiTi_{0.75}\square_{0.25}S_2$ are shown in Figure 6.3a (see Figure 6.6 for XRD patterns of $Li_{1.33-1.33z}Ti_{0.67+0.33z}\square_zS_2$). The pattern can be refined to a single phase in the O3 $R\bar{3}m$ space group, as opposed to the lower symmetry C2/m space group of the parent phase $Li(Li_{1/3}Ti_{2/3})S_2$, due to a lack of honeycomb ordering within the Ti/Li layer. The lattice parameters of $LiTi_{0.75}\square_{0.25}S_2$ are a = 3.525 Å and c = 18.066 Å, which show that the phase is slightly contracted in the *a* direction and expanded in the *c* direction upon vacancy introduction. Minor impurities observed in the low Q region between 1.6 and 3.1 $Å^{-1}$ are fit to elemental S_8 with 0.0015 phase fraction, or 1.9 wt%, which do not appear when stoichiometric S is used in the synthesis (Figure 6.7). The presence of S_8 is attributed to the excess S used in solid-state synthesis to ensure full oxidization of Ti. Transmission electron microscopy (TEM) images are indexed to the $R\bar{3}m$ space group and reveal a layered structure free of Ti in the Li layer, confirming that additional Ti is only incorporated into the Ti/Li layer (Figure 6.8).

To confirm the stoichiometry of the material, elemental analysis is undertaken with electron probe microanalysis (EPMA). EPMA is a wavelength-based technique that yields elemental ratios 30-40 times more quantitative than those obtained with energy dispersive spectroscopy (EDS).[223,224] A table summarizing the EPMA results and more information can be found in table 6.2. $LiTi_{0.75}\square_{0.25}S_2$ prepared with Li_2S, synthesized (stoichiometric) TiS_2, and 0.1 excess S exhibits a Ti:S ratio of 1:2.67, showing good agreement with the theoretical ratio. The Li:Ti ratio in $LiTi_{0.75}\square_{0.25}S_2$ is probed with inductively coupled plasma mass spectrometry (ICP-MS). We note that S is precluded in the ICP-MS analysis due to its volatility in the solvent which results in inaccurate elemental composition. The Li:Ti ratio obtained from ICP-MS is 1.364 ±0.006, 2% deviating from the theoretical Li:Ti

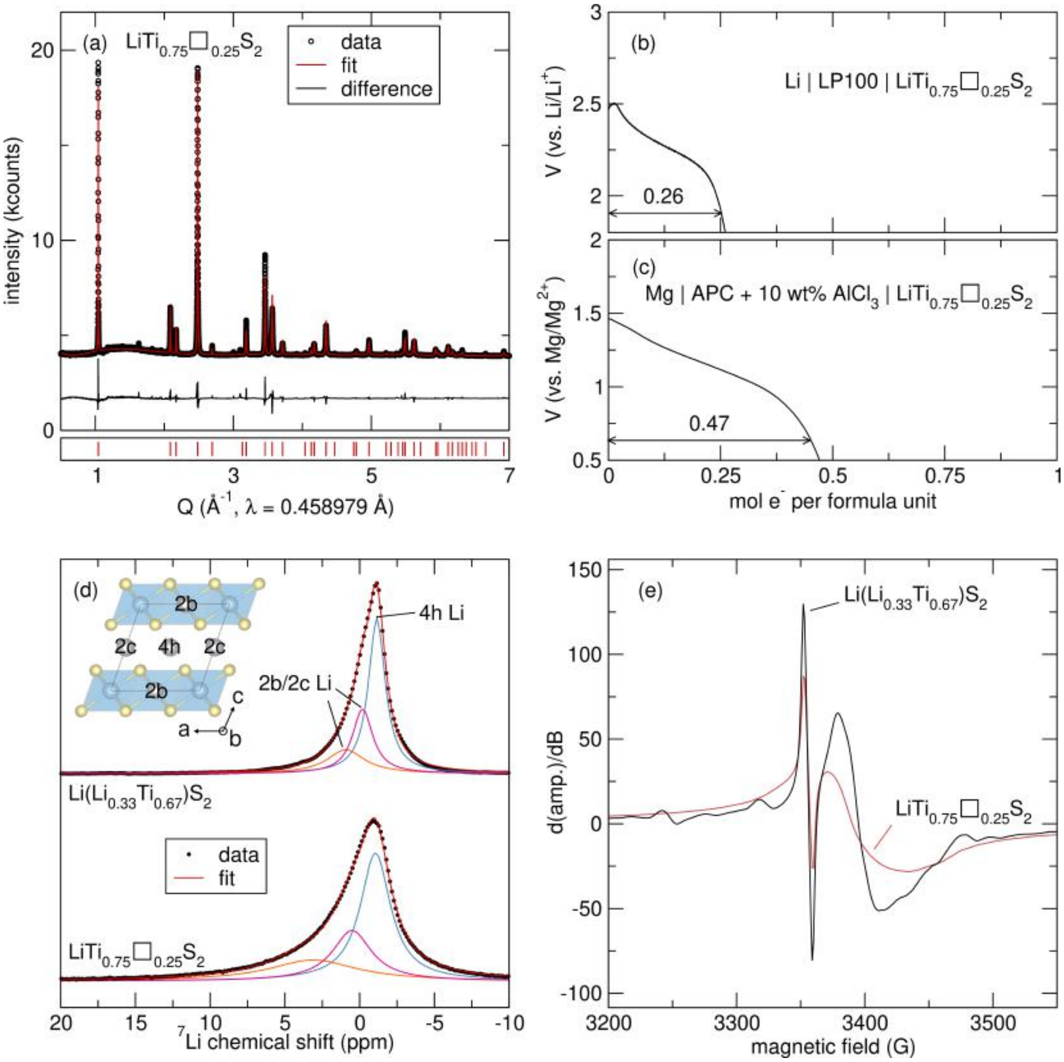

Figure 6.3: sXRD, discharge cycles, ssNMR, and EPR of $\mathrm{LiTi_{0.75}\square_{0.25}S_2}$. (a) Synchrotron powder XRD patterns with quantitative Rietveld refinements of $\mathrm{LiTi_{0.75}\square_{0.25}S_2}$. The tick marks indicate the Bragg reflection positions with the space group $R\bar{3}m$. Discharge curves of $\mathrm{LiTi_{0.75}\square_{0.25}S_2}$ (b) at room temperature and C/500 based on 1 e^- per formula unit in a Li electrolyte and (c) at 60 °C and C/100 based on 1 e^- per formula unit in a Mg electrolyte. The discharge capacities suggest a vacancy concentration of 0.26 and 0.24, respectively. The apparent vacancy concentration is slightly lower when using a Mg^{2+} working ion likely due to kinetic limitations which may prevent occupation of every vacancy. (d) ^{7}Li MAS ssNMR spectra of pristine $\mathrm{Li(Li_{1/3}Ti_{2/3})S_2}$ and $\mathrm{LiTi_{0.75}\square_{0.25}S_2}$ collected at 13 kHz. Both spectra are fit with 3 components, signifying that vacancies are not exclusively formed in the Ti layer. (e) EPR spectra of pristine $\mathrm{Li(Li_{1/3}Ti_{2/3})S_2}$ and $\mathrm{LiTi_{0.75}\square_{0.25}S_2}$ suggesting a small concentration of Ti^{3+} in both materials.

ratio of 1.333, confirming the stoichiometry of $\mathrm{LiTi_{0.75}\square_{0.25}S_2}$ and supporting the presence of cation vacancies in the structure.

With the Ti:S ratio of $LiTi_{0.75}\square_{0.25}S_2$ confirmed by EPMA, the vacancy content can be further probed electrochemically, using the fact that the material can be reduced to incorporate a mobile ion into cation vacancies. Figure 6.3b depicts galvanostatically discharged $LiTi_{0.75}\square_{0.25}S_2$ in a Li electrolyte. When $LiTi_{0.75}\square_{0.25}S_2$ is discharged at a very slow rate of C/500, a discharge capacity of 0.26 mol e^- per formula unit (f.u.) is observed which is in good agreement with the targeted vacancy content of 0.25 mol per f.u. To further confirm the vacancy concentration, we discharge the material with a Mg electrolyte to incorporate a divalent cation. Mg^{2+} can occupy the octahedral sites in layered TiS_2.[221] The discharge curve in a Mg electrolyte is shown in Figure 6.3c. With a Mg^{2+} working ion, we measure a capacity of 0.47 mol e^- per f.u., which would indicate a vacancy concentration of 0.24 mol per f.u. (see Figure 6.9 for replicates).

Next, solid-state nuclear magnetic resonance (ssNMR) spectroscopy is employed to probe the location of the vacancies indirectly by characterizing the local Li environments. ^{7}Li magic-angle spinning (MAS) ssNMR spectra of $Li(Li_{1/3}Ti_{2/3})S_2$ and $LiTi_{0.75}\square_{0.25}S_2$ are shown in Figure 6.3d. The ^{7}Li MAS spectrum of the parent phase $Li(Li_{1/3}Ti_{2/3})S_2$ is fit with three components (Figure 6.3d), consistent with previously reported isostructural materials Li_2TiSe_3 and Li_2TiO_3, representing the two unique Li environments in the Li layer (2*c* and 4*h*) and one Li environment in the Ti/Li layer (2*b*).[219,225,226] The relative areas of the components are determined based on the ratio of the Wyckoff site multiplicity of each Li site. Based on the relative intensities, we assign the most intense peak to the 4*h* Li site. We cannot decouple the remaining 2*b* and 2*c* Li sites as their multiplicities are identical. The resonance broadens with increasing vacancy content (Figure 6.10), suggesting increased disorder. The ^{7}Li MAS spectrum of $LiTi_{0.75}\square_{0.25}S_2$ is fit to 3 components analogously to $Li(Li_{1/3}Ti_{2/3})S_2$ (Figure 6.3d, see Figure 6.12 for 2-component fit). Because all three chemical environments are still present in $LiTi_{0.75}\square_{0.25}S_2$, Li still occupies each Wyckoff site in the material. If all vacancies were present in the Ti/Li layer in $LiTi_{0.75}\square_{0.25}S_2$, there would be no Li in the Ti/Li layer and thus either 2*b* or 2*c* peak would completely disappear. Therefore, vacancies are formed either exclusively in the Li layer or in both the Li and Ti/Li layers. This result is further corroborated by computations which suggest that all low energy configurations of the pristine compound favor vacancy formation in the Li layer(Figure S6). We note that low-field, variable temperature, and ^{6}Li MAS ssNMR cannot resolve the broadened peaks (Figures 6.13 – 6.14).

Next, electron paramagnetic resonance (EPR) is used to investigate local electronic environments in $LiTi_{0.75}\square_{0.25}S_2$ and confirm that vacancy introduction does not alter the Ti electronic structure. Figure 6.3e depicts the EPR spectra of $Li(Li_{1/3}Ti_{2/3})S_2$ and $LiTi_{0.75}\square_{0.25}S_2$ collected at 77 K. Aside from small impurities in $Li(Li_{1/3}Ti_{2/3})S_2$, both spectra are characterized by a sharp feature at g = 2.02 and a broader feature at g = 1.99. The sharp feature at g = 2.02 is observed when electrons are localized in anion vacancies like those in TiO_2 and MoS_2, suggesting that some S vacancies are present in the structure.[227–229] The broader feature at g = 1.99 indicates the presence of Ti^{3+}, which also has been observed in other reports of $Li(Li_{1/3}Ti_{2/3})S_2$.[219,220] The presence of the Ti^{3+} feature in both $Li(Li_{1/3}Ti_{2/3})S_2$ and $LiTi_{0.75}\square_{0.25}S_2$ suggests that there is a residual amount of Ti^{3+} in both materials, and forming completely d^0 Ti^{4+} is extremely difficult even with careful precursor tuning. Indeed, Ti-rich $LiTi_{0.75}\square_{0.25}S_2$ and $Li_{1.25}Ti_{0.75}S_2$, materials containing Ti^{3+} based on electrochemical characterization (*vide infra*), exhibit much larger Ti^{3+} features suggesting that the amount of Ti^{3+} in $Li(Li_{1/3}Ti_{2/3})S_2$ and $LiTi_{0.75}\square_{0.25}S_2$ is very small (Figure 6.15). The similarity between the EPR spectra of $Li(Li_{1/3}Ti_{2/3})S_2$ and $LiTi_{0.75}\square_{0.25}S_2$ indicates that vacancy introduction does not alter the local electronic environments.

Impact of Vacancies on the Electrochemical Activity

The effect of cationic vacancies in $Li_{1.33-1.33z}Ti_{0.67+0.33z}\square_zS_2$ on the electrochemistry is examined with galvanostatic cycling. The galvanostatic cycling data for $Li_{1.33-1.33z}Ti_{0.67+0.33z}\square_zS_2$ are shown in Figure 7.1a-d. All cells are charged first corresponding to oxidation at the cathode. The parent material $Li(Li_{1/3}Ti_{2/3})S_2$ exhibits a minimal capacity of 0.05 e^- per f.u. (Figure 7.1a), consistent with previous reports.[165,219] With increasing vacancy content, the charge capacity increases reaching 0.6 e^- per f.u. in $LiTi_{0.75}\square_{0.25}S_2$ (Figure 7.1b-d). All materials exhibit a single plateau in the charge profiles around 2.77 V, consistent with the calculated voltage for S oxidation (Figure 6.2c). A single plateau above 2.5 V in other Li-rich sulfides has been attributed to S oxidation..[163,173,230] Galvanostatic intermittent titration technique (GITT) of $Li_{1.33}Ti_{0.67}S_2$ exhibits equilibrium V of 2.65 V, suggesting that the same oxidative event occurs with less kinetic overpotentials (Figure 6.16). Also, discharge capacities are higher than charge capacities for all vacancy contents (Figure 7.1a-d). Cation vacancies allow more Li^+ to be inserted into the structure than what was removed during charge. Although d^0 electron configuration of Ti^{4+}

prevents it from partaking in oxidation, Ti^{4+} can act as an additional reduction center during discharge.

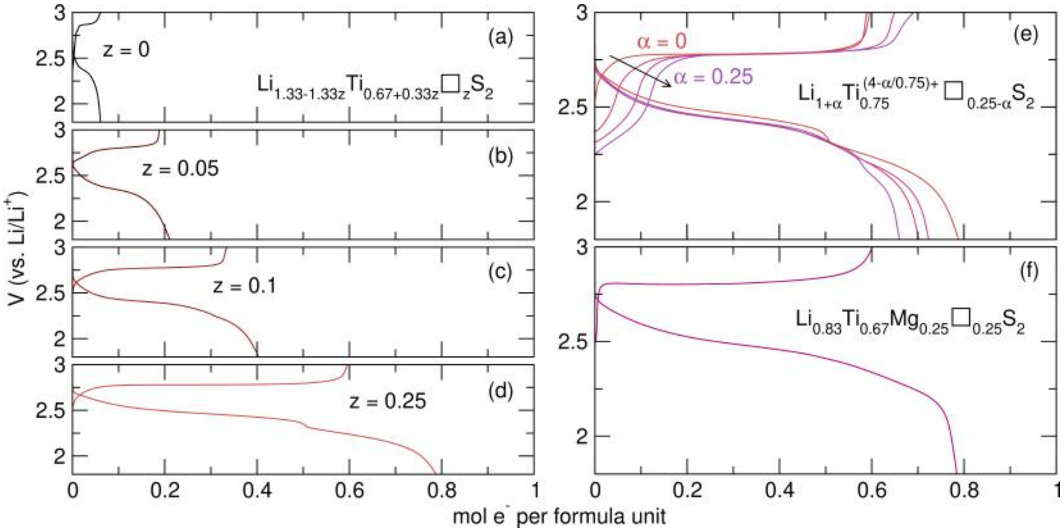

Figure 6.4: First charge and discharge curves of (a-d) $Li_{1.33-1.33z}Ti_{0.67+0.33z}\square_z S_2$ up to z = 0.25 cycled at C/20. Charge capacity is observed upon introduction of vacancies. (e)First charge and discharge curves of $Li_{1+\alpha}Ti_{0.75}\square_{0.25+\alpha}S_2$ cycled at C/20 demonstrating that contributions in the initial sloping region increase with decreasing formal oxidation state of Ti. (f) First charge and discharge curves of $Li_{0.83}Ti_{0.67}Mg_{0.25}\square_{0.25}S_2$ cycled at C/50 showing activation of the material upon vacancy introduction through introduction of Mg^{2+}.

The shape of the curves can indicate the charge compensation mechanism, distinguishing S oxidation from Ti oxidation. For instance, Flamary-Mespoulie *et al.* charged $Li_{1.25}Ti_{0.75}S_2$, which has an average formal oxidation state of $Ti^{3.67+}$, and observed first a sloping region below 2.5 V followed by a plateau around 2.7 V.[165] The two regions were assigned to Ti^{3+} oxidation and S oxidation, respectively.[165] Therefore, the absence of the sloping region in $Li_{1.33-1.33z}Ti_{0.67+0.33z}\square_z S_2$ suggests no contribution from Ti^{3+} on charge.

To confirm that the sloping region appears when Ti^{3+} is oxidized, we systematically varied the formal oxidation state of Ti by maintaining Ti stoichiometry at $Ti_{0.75}$ and filling the vacancies with Li^+. The substitution is done by increasing Li content of the precursors during synthesis to yield $Li_{1+\alpha}Ti_{0.75}\square_{0.25-\alpha}S_2$ (see Figure 6.17 for XRD patterns). Assuming the excess Li^+ is charge compensated by Ti reduction, the Ti oxidation state will decrease as Li^+ is introduced. Indeed, as Li^+ is introduced, we observe a systematic increase in the capacity from the sloping region (Figure 7.1e) suggesting that the formal oxidation state of Ti decreases from Ti^{4+} to $Ti^{3.67+}$ (see Figure 6.18 for individual cycling data). Furthermore, if $LiTi_{0.75}\square_{0.25}S_2$ (formally

Ti^{4+}) is discharged first to reduce the Ti^{4+}, a sloping region is again observed in the subsequent charge (Figure 6.19).

To confirm that the introduction of vacancies activates anion oxidation, we target an additional method to introduce vacancies. Vacancies are introduced through aliovalent substitution of Mg^{2+} for Li^{+} via solid-state synthesis to yield $Li_{0.83}Ti_{0.67}Mg_{0.25}\square_{0.25}S_2$ while maintaining the $R\bar{3}m$ space group (Figure 6.20). Galvanostatic cycling data of $Li_{0.83}Ti_{0.67}Mg_{0.25}\square_{0.25}S_2$ is shown in Figure 7.1f. The charge capacity is substantial, reaching 0.6 e^- per f.u. Similar to $LiTi_{0.75}\square_{0.25}S_2$, only one plateau is observed in the charge profile, and the discharge capacity is higher than the charge capacity. It is notable that Mg substitution will also activate anion oxidation because Mg substitution does not affect the electronic states near the Fermi level, leaving only the effect of vacancies.

Structural and Spectroscopic Characterization of the Oxidized Material

Next, we characterize the physical and electronic structure of charged $LiTi_{0.75}\square_{0.25}S_2$. We note that detailed analysis on the discharge mechanism is outside the scope of this paper and will be the subject of future studies. First, we investigate structural evolution of $LiTi_{0.75}\square_{0.25}S_2$ during charge. *Operando* XRD indicates a two-phase mechanism upon charge (Figure 6.21), in good agreement with the flat plateau of the charge profile.

To get more quantitative information, we turn to the *ex situ* sXRD data of charged $LiTi_{0.75}\square_{0.25}S_2$ depicted in Figure 6.5a. The sXRD pattern cannot be described with a single phase. Fitting the data to two phases in the $R\bar{3}m$ space group yields reasonable fits; however, some features such as line shape are not well described and the reflection at approximately 3 Å is not fit. Because the pattern can be relatively well described by structures related to the parent phase, we suggest that no substantial structural rearrangements have occurred. The most complex changes in peak shape are observed in (102) and (104) reflections, which are both dictated by the S sublattice (Figure 6.22) suggesting that S atoms deviate from the original lattice position as a result of local structural distortions as would be required by formation of persulfides.

Next, changes in Li environments are probed with ^{7}Li MAS ssNMR. Figure 6.5b depicts *ex situ* ^{7}Li MAS ssNMR spectra of $LiTi_{0.75}\square_{0.25}S_2$ at three different states of charge: pristine, partial charge (0.25 e^- removed), and full charge (0.60 e^- removed).

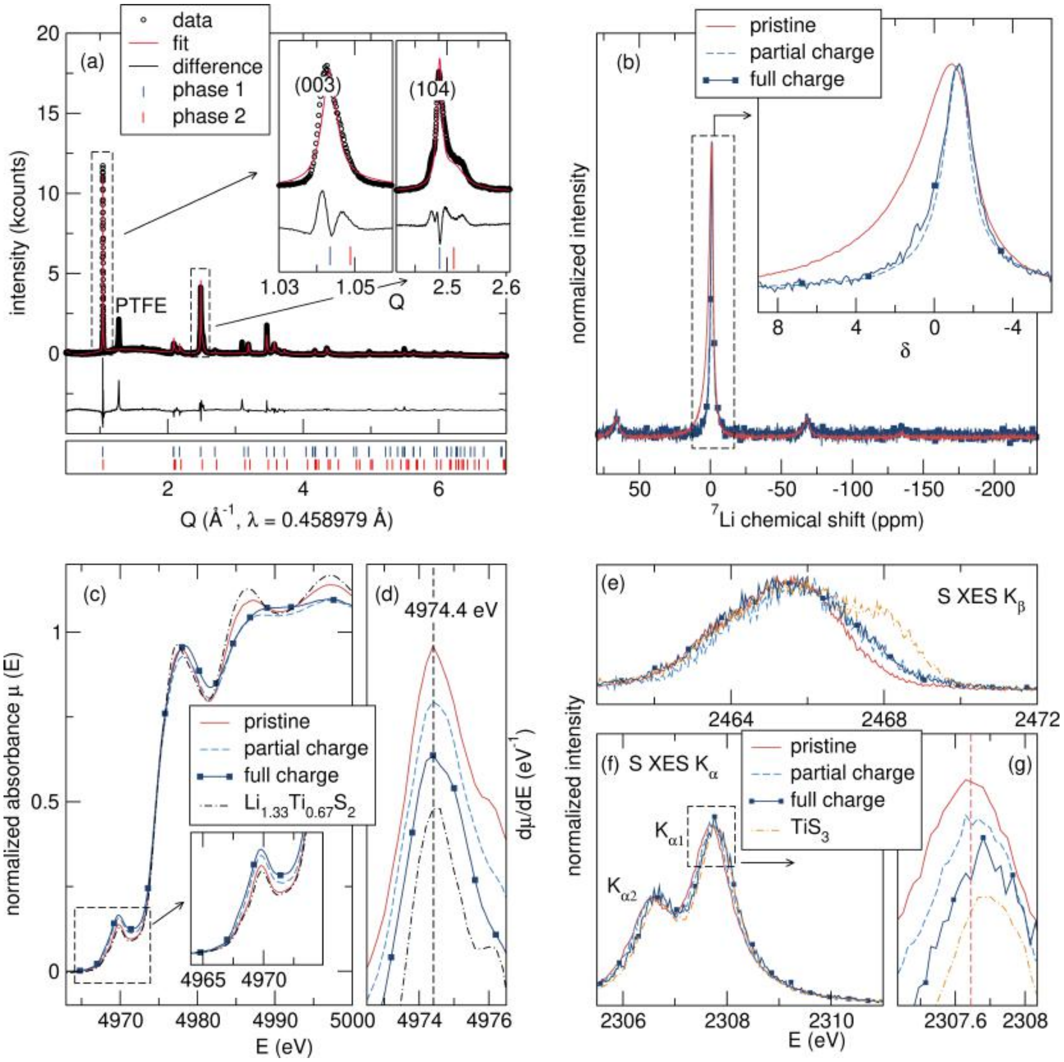

Figure 6.5: *Ex situ* sXRD, ssNMR, Ti XANES, and S XES of $\mathrm{LiTi_{0.75}\square_{0.25}S_2}$. (a) Synchrotron XRD of fully charged $\mathrm{LiTi_{0.75}\square_{0.25}S_2}$ fit to two phases in the $R\bar{3}m$ space group with insets highlighting the (003) and (104) reflections. (b) *Ex situ* ^{7}Li MAS ssNMR of pristine, partially charged, and fully charged $\mathrm{LiTi_{0.75}\square_{0.25}S_2}$ with the inset highlighting the central transition. (c) Ti K-edge XANES of $\mathrm{Li(Li_{1/3}Ti_{2/3})S_2}$ and $\mathrm{LiTi_{0.75}\square_{0.25}S_2}$ at various states of charge and (d) the first derivative of the rising edge. The dashed line represents the peak position of the pristine state. S X-ray emission spectroscopy (XES) of the of pristine, partial charge, full charge $\mathrm{LiTi_{0.75}\square_{0.25}S_2}$ and $\mathrm{TiS_3}$ at the (e) S K$_\beta$ and (f, g) S K$_\alpha$ emission lines.

The pristine spectrum is the same spectrum shown in Figure 6.3e. After partial charge, the ^{7}Li MAS NMR spectrum loses intensity in the region associated with the 2*b* and 2*c* Li sites suggesting that most of the remaining Li resides in the 4*h* Li site in the Li layer. In fact, the spectrum is well described by one single component suggesting that Li is no longer occupying the site in the metal layer (Figure 6.23).

After full charge, the shape of the resonance shows minimal changes suggesting that Li is removed only from the $4h$ Li site (in the Li layer) causing a decrease in the resonance intensity, but no shape change. Again, the resonance can be fit by one single component substantiating the assignment of the partially charged material. Thus, upon oxidation, Li originally present in the Ti/Li layer migrates to the Li layer during delithiation, creating vacancies in the Ti/Li layer.

To probe the role of Ti in the charge compensation mechanism during charge, *ex situ* Ti K-edge X-ray absorption spectroscopy (XAS) is measured at the same states of charge as those measured for ssNMR. Ti K-edge XANES data are plotted in Figure 6.5c. Ti XANES data of standards are shown in Figure 6.24. The rising edge position of pristine $LiTi_{0.75}\square_{0.25}S_2$ at 4974.4 eV aligns with that of $Li(Li_{1/3}Ti_{2/3})S_2$, indicating that the introduction of vacancies does not alter the oxidation state of Ti (Figure 6.5c). In the spectra of the partially charged and fully charged $LiTi_{0.75}\square_{0.25}S_2$, the rising edge does not shift (Figure 6.5d) indicating that Ti is not oxidized. The pre-edge peak is attributed to the $1s$ to $3d$ transition, which is dipole forbidden for absorbers in a centrosymmetric environment.[231,232] The presence of the pre-edge feature suggests slightly distorted TiS_2 octahedra similar to TiS_2.[232] The pre-edge increases in intensity (Figure 6.5c inset) during charge suggesting increased local distortions of TiS_6 octahedra.

To probe the role of S during oxidation, S X-ray emission spectroscopy (XES) is measured on $LiTi_{0.75}\square_{0.25}S_2$ at the same states of charge. XES provides information about the bulk electronic structure of materials and can be conducted without a synchrotron X-ray source.[233,234] The data shown here are taken on a easyXAFS lab instrument. Recently, XES has been employed in various battery systems.[235–238] Figure 6.5e depicts the S K_β measurements of $LiTi_{0.75}\square_{0.25}S_2$ at various states of charge and a TiS_3 standard. K_β XES of S arises from valence-to-core transitions and carries information about the bonding environment around S atoms.[234] The pristine state exhibits a single broad feature at 2465.63 eV. After charge, a new feature appears at 2467.61 eV and is still observed at full charge. The same feature is observed in TiS_3, which has both S^{2-} and oxidized S in the form of $(S_2)^{2-}$ persulfide. Thus, S K_β XES suggests that the bonding environment around S atoms in fully charged $LiTi_{0.75}\square_{0.25}S_2$ resembles that in TiS_3.

Figure 6.5f shows the XES data in the region of the S $K_{\alpha 1}$ and $K_{\alpha 2}$ lines. The position of the core-to-core K_α feature is sensitive to the S oxidation state.[233,234] $K_{\alpha 1}$ peaks are analyzed due to their higher intensities. The pristine state exhibits a

$K_{\alpha 1}$ peak at 2307.70 eV, which shifts to 2307.78 eV after full charge. The shift to higher energy is attributed to oxidation of S^{2-}, providing direct evidence that the charge compensation stems from S oxidation.

6.5 Discussion

Through careful control over structure and crystal chemistry, we have shown that S^{2-} oxidation requires the presence of cation vacancies. We have shown that Ti can chemically substitute Li in $Li(Li_{1/3}Ti_{2/3})S_2$ and introduce vacancies in the structure, keeping the electronic structure of Ti unchanged at predominantly Ti^{4+}. Galvanostatic cycling data of $Li_{1.33-1.33z}Ti_{0.67+0.33z}\square_zS_2$ reveal that while $Li(Li_{1/3}Ti_{2/3})S_2$ exhibits negligible charge capacity (Figure 7.1a), its vacancy-containing analogues such as $LiTi_{0.75}\square_{0.25}S_2$ can be substantially oxidized. The origin of this oxidation is electron removal from states with predominatly S-*p* character, since the S^{2-}-*p* and the empty Ti^{4+}-*d* states lie below and above the Fermi level, respectively.[219] Similarly, first-principles calculations suggest that S oxidation into persulfides is favorable only when accompanied by a large degree of lattice contraction near a vacancy.

In all samples, any accessible S oxidation proceeds via a two-phase mechanism with a high degree of disorder in the S sublattice suggesting distorted S positions. Spectroscopic evidence suggests that Ti does not participate throughout charge, and all charge compensation stems from S oxidation. S K_β indicates that the S bonding environment during charge resembles that of TiS_3 which contains S–S bonds.

The exact mechanism of S oxidation, whether in the form of persulfides ($(S_2)^{2-}$) or S^{n-} ($n<2$), has been debated. Saha *et al.* reported that in $Li_{1.17}Ti_{0.58}Fe_{0.25}S_2$ anion holes are delocalized through Fe-S interaction and no S–S bond with the bond length of 2.1 Å is observed.[163] Leube *et al.* proposed a complex balance between anionic (S^{2-}/S^{n-} and Se^{2-}/Se^{n-}, $n<2$) and cationic ($Ti^{3+/4+}$) redox processes in $Li_2TiS_{3-x}Se_x$.[219] On the other hand, Sakuda *et al.* demonstrated that mechanochemically synthesized rock-salt-like cation-disordered ($Fm\bar{3}m$) Li_2TiS_3 exhibits anion redox resulting in the formation of S–S bonds along the TiS_6 edge, supported by PDF showing a correlation near 2.0 Å.[218,239] Hansen *et al.* demonstrated that a pre-edge feature associated with pyrite FeS_2 (S_2^{2-}) is observed in S XANES of charged Li_2FeS_2.[173] Also, Wang *et al.* showed that a feature around 2 Å associated with S–S is observed in S EXAFS of layered $NaCr_{2/3}Ti_{1/3}S_2$.[240] In this work, based on first-principles simulations, electrochemical performance, and spectroscopic evidence, we propose that S oxidation occurs through persulfide formation due to the dependence of anion oxidation on the presence of cation vacancies. It is likely that vacancies release S-*p* orbitals from M–anion bonding orbitals allowing for rehybridization to form the new S–S bond. The vacancies also provide space for the resulting structural distortions.

We have shown that in sulfides, vacancies are crucial to allow for S–S bond formation. From calculations, vacancies in the transition metal layer are most important, and experimentally we demonstrate that formation of vacancies is a prerequsite for persulfide formation. This contrasts with oxides where anion redox appears to involve transition metal migration and the formation of trapped O_2^{n-} molecular species that detach from the crystalline network.[204,205,209]

6.6 Conclusions

To summarize, we have demonstrated that the introduction of vacancies via chemical substitution activates anion redox in otherwise electrochemically inert $Li(Li_{1/3}Ti_{2/3})S_2$. By introducing intrinsic vacancies, we can engineer the material on the atomic scale to accommodate structural distortions associated with persulfide formation and activate anion redox. By maintaining the electron configuration of Ti at d^0, we are able to isolate the role of vacancies in activating anion redox and demonstrate that anion redox without transition metal oxidation is possible. This finding offers new insights regarding the origin of anion redox that involves partial structural transformations.

6.A Supplementary Information

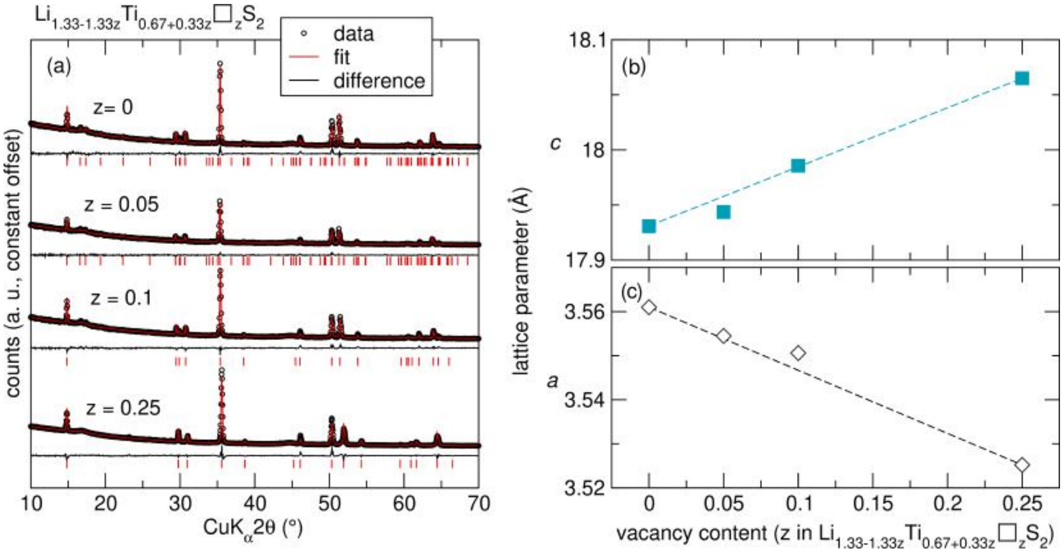

Figure 6.6: XRD patterns of $Li_{1.33-1.33z}Ti_{0.67+0.33z}\square_zS_2$. (a) XRD patterns of $Li_{1.33-1.33z}Ti_{0.67+0.33z}\square_zS_2$. z = 0 and 0.05 are fit to C2/m space group due to the superstructure peaks at low 2θ and z > 0.05 are fit to the R$\bar{3}$m space group. (b and c) Lattice parameters c and a as a function of vacancy content with all XRD patterns fit to the R$\bar{3}$m space group. Lattice parameter c increases and a decreases with increasing vacancy content, demonstrating that Ti substitution and vacancy introduction follow Vegard's law.”

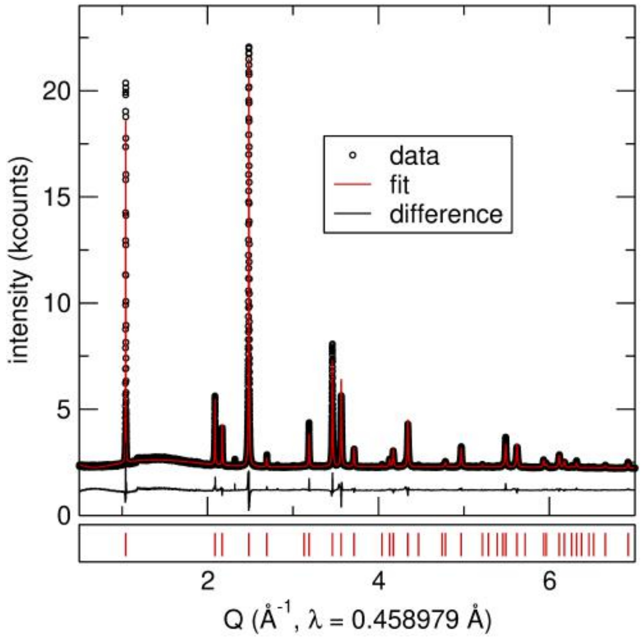

Figure 6.7: Synchrotron XRD patterns of $LiTi_{0.75}\square_{0.25}S_2$ synthesized from Li_2S and stoichiomtric TiS_2. There are no impurities in the low Q region (between 1.2 and 1.6 Q) observed in $LiTi_{0.75}\square_{0.25}S_2$ synthesized from Li_2S + stoichiometric TiS_2 + 0.1 S.

atom	Wyckoff site	x	y	z	occupancy	U_{iso}
Li	3a	0	0	0	0.25	0.21874
Ti	3a	0	0	0	0.75	0.00782
Li	3b	0	0	0.5	0.75	0.01456
S	6c	0	0	0.25616	1	0.019

Table 6.1: Rietveld refinement of $LiTi_{0.75}\square_{0.25}S_2$ in the $R\bar{3}m$ space group (a = 3.52521 Å, c = 18.06502 Å, χ^2 = 4.01, R_W = 10.347). The occupancy of Li 3a and Li 3b is arbitrarily chosen based on the assumption that all vacancies are present in the Li layer. The occupancy of Li does not affect the fit result as Li is too light to affect the diffraction patterns.

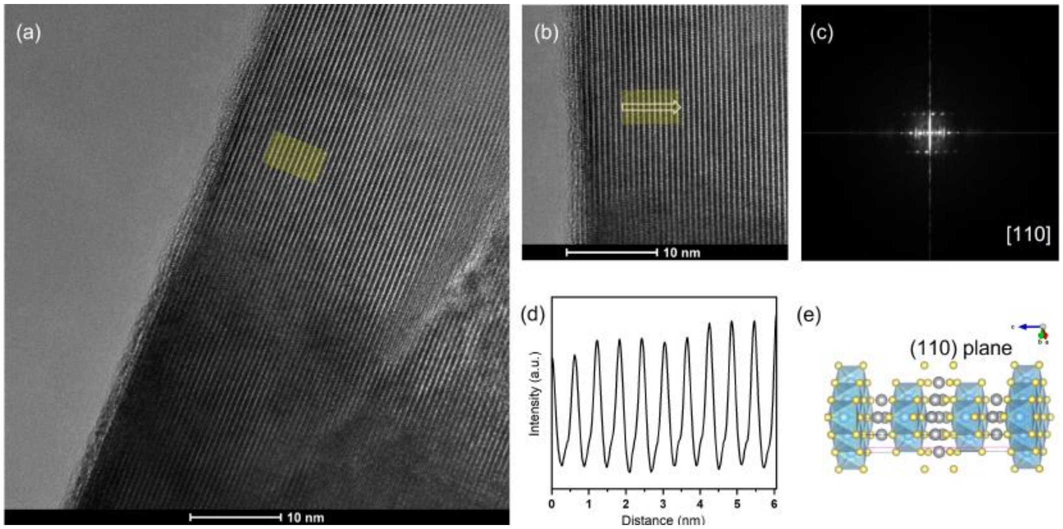

Figure 6.8: TEM of pristine $LiTi_{0.75}\square_{0.25}S_2$. (a) High-resolution TEM image near the edge of pristine $LiTi_{0.75}\square_{0.25}S_2$ particle in the zone axis [110]. The region-of-interest (ROI) was highlighted in the yellow rectangle, magnified in (b). Fast Fourier transform (FFT) pattern in (c) was simulated from ROI in (b). (d) The intensity line profile was collected from the integration of the signal across the arrow direction in (b). The d-spacing calculated from the peak distance was 0.605 nm, which matches the theoretical value from the unit cell model (e) generated from the sXRD patterns.

sample	theoretical ratio		EPMA ratio		precursors
	Ti	S	Ti	S	
commercial TiS_2	1	2	1	1.93±0.01	-
lab TiS_2			1	2.01±0.04	Ti + 2.1 S
Ti-rich $LiTi_{0.75}\square_{0.25}S_2$	1	2.67	1	2.56±0.08	Li_2S + commercial TiS_2
$LiTi_{0.75}\square_{0.25}S_2$			1	2.67±0.05	Li_2S + lab TiS_2 + 0.1 S

Table 6.2: Summary of EPMA results. Theoretical and EPMA Ti:S ratio in TiS_2 and $LiTi_{0.75}\square_{0.25}S_2$. EPMA of commercially available TiS_2 exhibits a Ti:S ratio of 1:1.93. In fact, TiS_2 has been reported to be Ti–rich, with excess Ti atoms occupying the Van der Waals gap in the structure. The Ti:S ratio of commercial TiS_2 indicates that there are excess Ti atoms and thus the overall oxidation state of Ti is not completely 4+. Therefore, we prepared "stoichiometric" TiS_2 by reacting 1:2.1 molar ratio of Ti and S which resulted in a Ti:S ratio of 1:2.01. We note that only Ti:S ratios are reported as Li is too light to be detected.

	spot #	Ti Elemental Percents	S Elemental Percents	Elemental Totals	Ti Atomic Percents	S Atomic Percents	Atomic Totals	S:Ti ratio
commercial TiS_2	1	41.35	53.61	94.96	34.05	65.95	100	1.937
	2	41.45	53.75	95.20	34.04	65.96	100	1.937
	3	41.57	53.60	95.17	34.17	65.83	100	1.926
	4	41.47	53.28	94.76	34.25	65.75	100	1.919
	5	41.29	52.89	94.18	34.32	65.68	100	1.914
							average	**1.927**
							stdev	**0.009**
stoichi. TiS_2 (Ti + 2.1 S)	1	40.01	54.77	94.78	32.84	67.16	100	2.045
	2	40.17	53.18	93.35	33.59	66.41	100	1.978
	3	39.53	54.72	94.24	32.60	67.40	100	2.068
	4	40.75	53.74	94.49	33.67	66.33	100	1.970
	5	40.86	54.41	95.27	33.45	66.55	100	1.989
							average	**2.010**
							stdev	**0.044**
TiS_2 from Ti + 2.05 S	1	41.24	53.63	94.87	33.98	66.02	100	1.943
	2	41.18	53.63	94.81	33.95	66.05	100	1.946
	3	40.88	53.56	94.44	33.82	66.18	100	1.957
	4	40.87	53.65	94.53	33.77	66.23	100	1.961
	5	41.14	53.42	94.56	34.01	65.99	100	1.940
							average	**1.949**
							stdev	**0.008**
Ti-rich $LiTi_{0.75}\square_{0.25}S_2$	1	32.34	55.65	87.98	28.01	71.99	100	2.571
	2	33.18	53.46	86.64	29.35	70.65	100	2.407
	3	32.04	56.44	88.48	27.54	72.46	100	2.631
	4	32.27	55.77	88.04	27.92	72.08	100	2.581
	5	31.93	55.97	87.90	27.64	72.36	100	2.619
							average	**2.562**
							stdev	**0.080**
$LiTi_{0.75}\square_{0.25}S_2$	1	30.73	55.59	86.32	27.01	72.99	100	2.703
	2	29.53	53.82	83.35	26.86	73.14	100	2.723
	3	31.26	54.43	85.69	27.77	72.23	100	2.601
	4	30.29	54.91	85.21	26.97	73.03	100	2.708
	5	29.66	53.52	83.18	27.06	72.94	100	2.696
							average	**2.668**
							stdev	**0.048**

Table 6.3: Electron probe microanalysis (EPMA) results of various compounds. While commercial TiS_2 and TiS_2 prepared from Ti + 2.05 S result in Ti:S ratios of less than 2, TiS_2 prepared by mixing 1:2.1 ratios of Ti and S results in a S:Ti ratio of 2.01. Ti-rich $LiTi_{0.75}\square_{0.25}S_2$ is prepared with stoichiometric ratios of Li_2S and commercial TiS_2 while $LiTi_{0.75}\square_{0.25}S_2$ is prepared with stoichiometric ratios of Li_2S, stoichiometric TiS_2, and 0.1 excess S. Ti-rich $LiTi_{0.75}\square_{0.25}S_2$ exhibits lower S:Ti ratio than theoretical ratio (2.67) while $LiTi_{0.75}\square_{0.25}S_2$ agrees with the theoretical ratio.

	phase fraction	a (Å)	c (Å)	atom	Wyckoff site	x	y	z	occupancy	U_{iso}
phase 1	0.5654	3.5162	18.0656	Ti	3a	0	0	0	0.75	0.03034
				Li	3b	0	0	0.5	0.4	0.0125
				S	6c	0	0	0.25785	1	0.06262
phase 2	0.4346	3.4715	18.0515	Ti	3a	0	0	0	0.75	0.01453
				Li	3b	0	0	0.5	0.4	0.0219
				S	6c	0	0	0.24423	1	0.05211

Table 6.4: Rietveld refinement of charged $LiTi_{0.75}\square_{0.25}S_2$ in the $R\bar{3}m$ space group (χ^2 = 8.778)

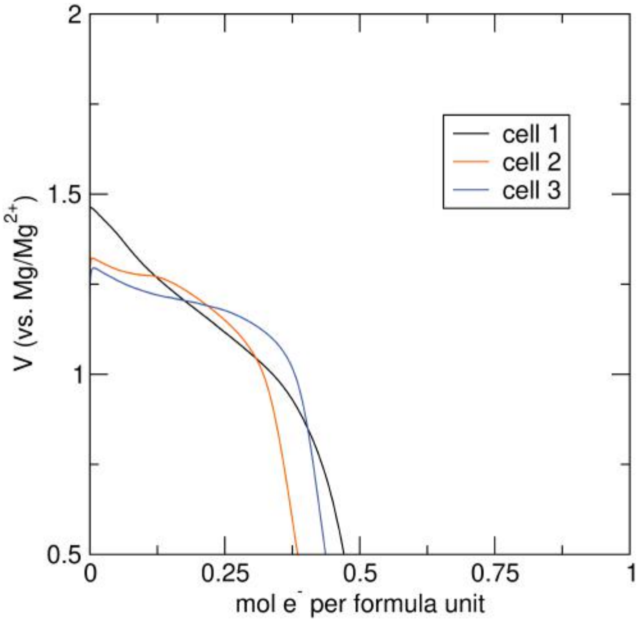

Figure 6.9: Galvanostatic discharge curves of $\mathrm{LiTi_{0.75}\square_{0.25}S_2}$ at 60 °C and C/100 based on 1 e^- per formula unit in a Mg electrolyte.

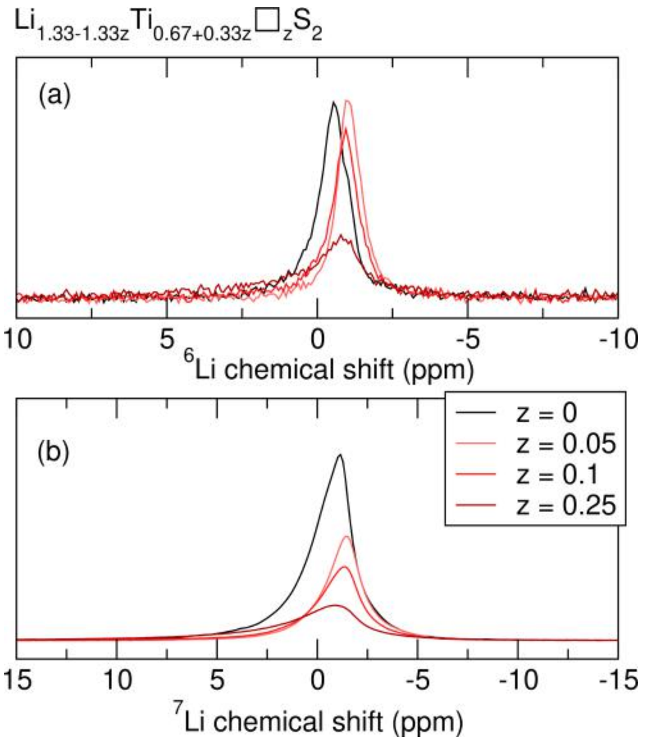

Figure 6.10: ssNMR of $\mathrm{Li_{1.33-1.33\mathit{z}}Ti_{0.67+0.33\mathit{z}}\square_{\mathit{z}}S_2}$. (a) ^{6}Li and (b) ^{7}Li MAS NMR spectra of $\mathrm{Li_{1.33-1.33\mathit{z}}Ti_{0.67+0.33\mathit{z}}\square_{\mathit{z}}S_2}$. ^{6}Li NMR spectra exhibit sharper peaks but cannot isolate them. Both ^{6}Li and ^{7}Li MAS NMR spectra show that the resonance broadens with increasing vacancy content suggesting increased disorder.

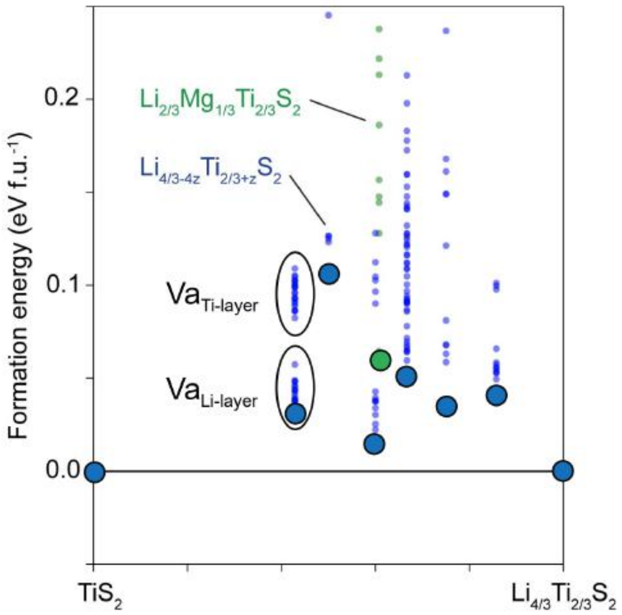

Figure 6.11: In all DFT enumerations of the pristine structure, there is a strong driving force for the Ti layer to be fully occupied by a combination of Ti and Li. The vacancies in the pristine structure form in the Li layer as opposed to the Ti layer. However, as the material is oxidized past the Ti^{4+} limit, the direction of the driving force switches and favors any Li in the Ti layer to migrate to the Li layer, forming the vacancies where the persulfide can then form. In the presence of vacancies in the Li layer, the kinetic barrier for this kind of Li migration is negligible, and in the vast majority of our calculated examples, the structural rearrangement happens spontaneously. Note that the absence of any vacancies in stoichiometric $Li_{1.33}Ti_{0.67}S_2$ precludes this structural rearrangement and thus suppresses persulfide formation. Data collected by Dr. Daniil Kitchaev in the Van der Ven Group at UCSB

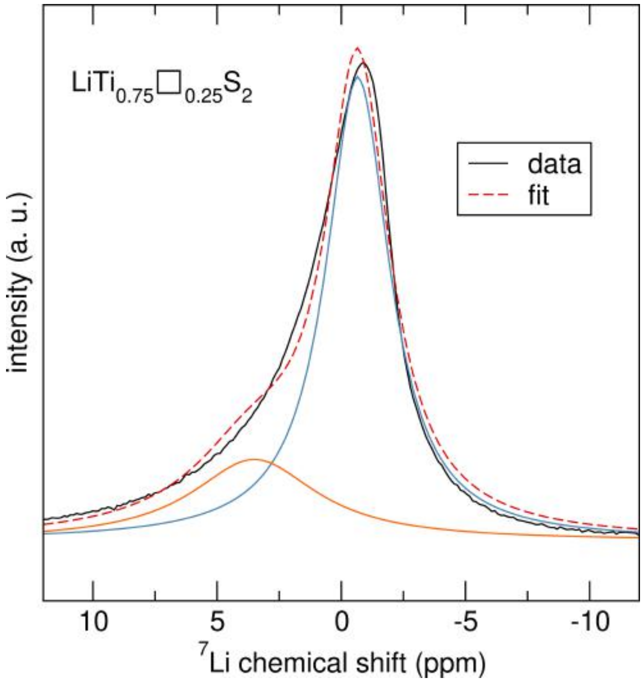

Figure 6.12: MAS ^{7}Li ssNMR spectrum of $\mathrm{LiTi_{0.75}\square_{0.25}S_2}$ fit with two components. Two components cannot adequately fit the spectrum.

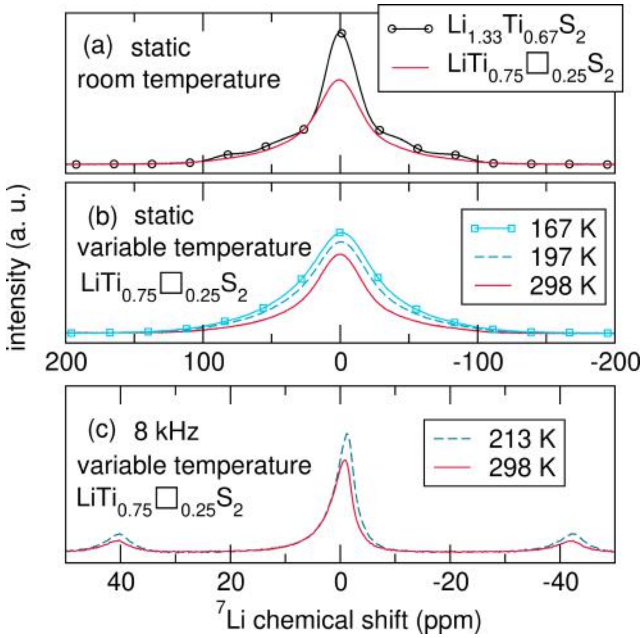

Figure 6.13: ssNMR at various temperatures of $\mathrm{Li_{1.33-1.33\mathit{z}}Ti_{0.67+0.33\mathit{z}}\square_{\mathit{z}}S_2}$. (a) Static ^{7}Li NMR spectra of $\mathrm{Li_{1.33}Ti_{0.67}S_2}$ and $\mathrm{LiTi_{0.75}\square_{0.25}S_2}$, (b) and (c) static and MAS ^{7}Li NMR spectra of $\mathrm{LiTi_{0.75}\square_{0.25}S_2}$ at various temperatures. All of these conditions do not adequately isolate the $\mathrm{LiTi_{0.75}\square_{0.25}S_2}$ resonance for further analysis.

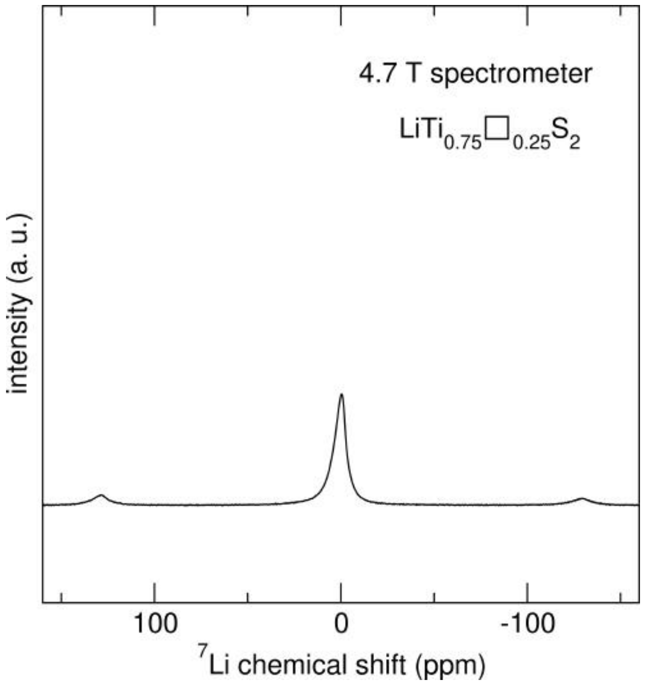

Figure 6.14: ^{7}Li MAS spectrum of $\mathrm{LiTi}_{0.75}\square_{0.25}\mathrm{S}_2$ collected at 10 kHz in a 4.7 T spectrometer.

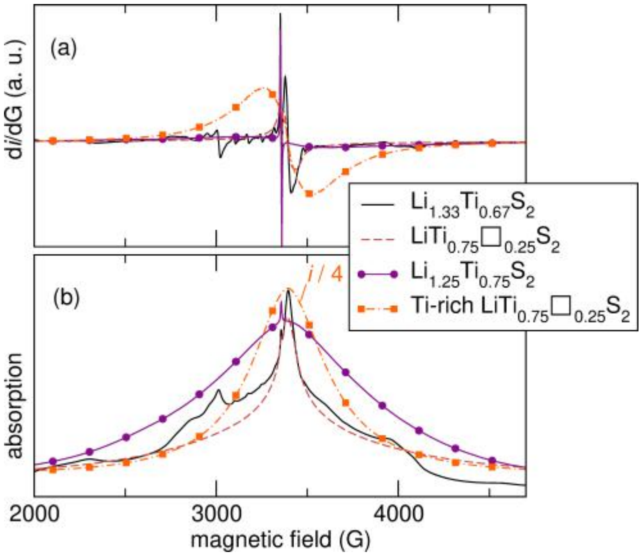

Figure 6.15: EPR of $\mathrm{Li}_{1.33-1.33z}\mathrm{Ti}_{0.67+0.33z}\square_z\mathrm{S}_2$. (a) EPR spectra and (b) integrated absorption spectra of $\mathrm{Li}_{1.33}\mathrm{Ti}_{0.67}\mathrm{S}_2$, $\mathrm{LiTi}_{0.75}\square_{0.25}\mathrm{S}_2$, $\mathrm{Li}_{1.25}\mathrm{Ti}_{0.75}\mathrm{S}_2$, and Ti-rich $\mathrm{LiTi}_{0.75}\square_{0.25}\mathrm{S}_2$. $\mathrm{Li}_{1.25}\mathrm{Ti}_{0.75}\mathrm{S}_2$ and Ti-rich $\mathrm{LiTi}_{0.75}\square_{0.25}\mathrm{S}_2$ exhibit distinctively broader Ti^{3+} features compared to $\mathrm{Li}_{1.33}\mathrm{Ti}_{0.67}\mathrm{S}_2$ and $\mathrm{LiTi}_{0.75}\square_{0.25}\mathrm{S}_2$.

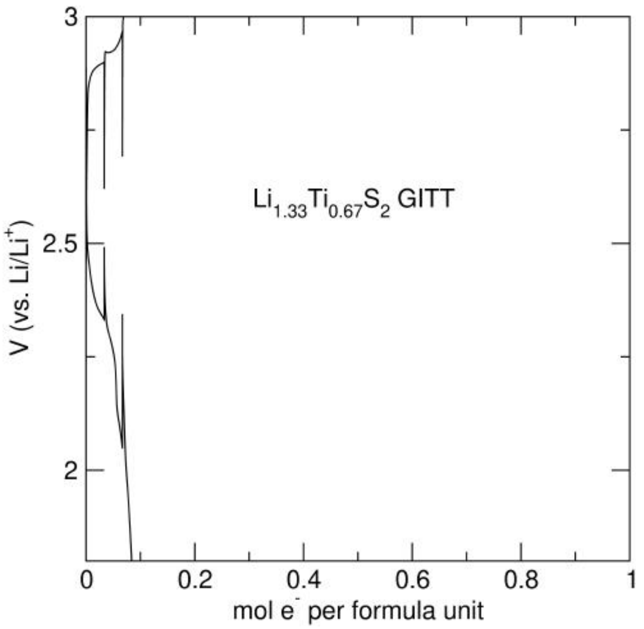

Figure 6.16: GITT of $Li_{1.33}Ti_{0.67}S_2$ reveals that the equilibrium voltage is at 2.65 V, suggesting that $Li_{1.33}Ti_{0.67}S_2$ also undergoes persulfide formation but with much higher overpotentials

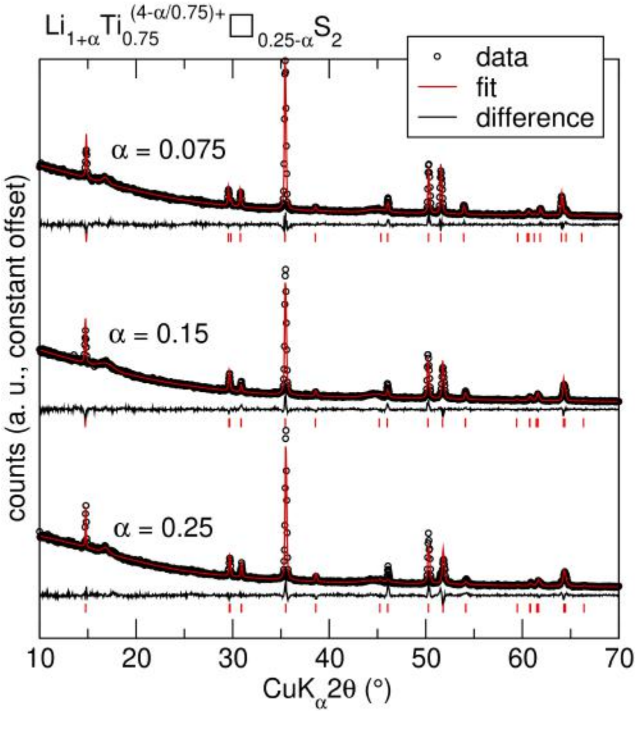

Figure 6.17: XRD patterns of $Li_{1+\alpha}Ti_{0.75}\square_{0.25-\alpha}S_2$.

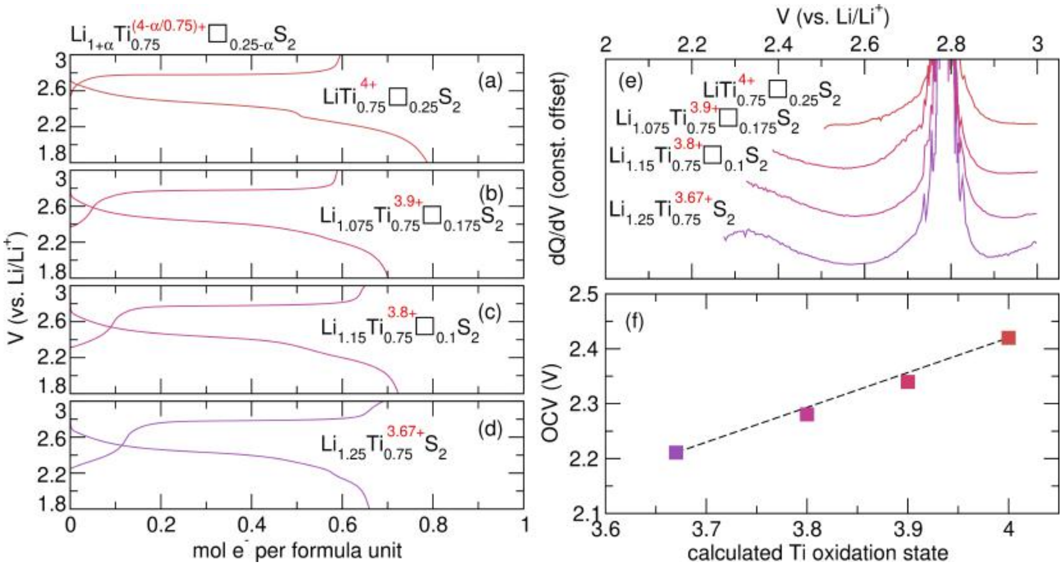

Figure 6.18: First charge and discharge curves of (a-d) $\mathrm{Li}_{1+\alpha}\mathrm{Ti}_{0.75}\square_{0.25-\alpha}\mathrm{S}_2$ up to $\alpha = 0.25$ cycled at C/20 based on 1 e^-. (e) Corresponding dQ/dV plots of $\mathrm{Li}_{1+\alpha}\mathrm{Ti}_{0.75}\square_{0.25-\alpha}\mathrm{S}_2$ and (f) OCV of $\mathrm{Li}_{1+\alpha}\mathrm{Ti}_{0.75}\square_{0.25-\alpha}\mathrm{S}_2$ based on calculated Ti oxidation state. With increasing Li content, the initial sloping region associated with $\mathrm{Ti}^{3+/4+}$ oxidation increases. In the dQ/dV plot, $\mathrm{LiTi}_{0.75}\square_{0.25}\mathrm{S}_2$ exhibits only one sharp peak at 2.77 V corresponding to the plateau associated with S oxidation. With decreasing Ti oxidation state, a new peak grows at 2.32 V that corresponds to the sloping region associated with $\mathrm{Ti}^{3+/4+}$ oxidation. There is a linear trend between the open-circuit voltage (OCV) and the calculated Ti oxidation state based on Li content, further suggesting that altering the precursor ratios can effectively control the oxidation state of Ti and thus the oxidation species.

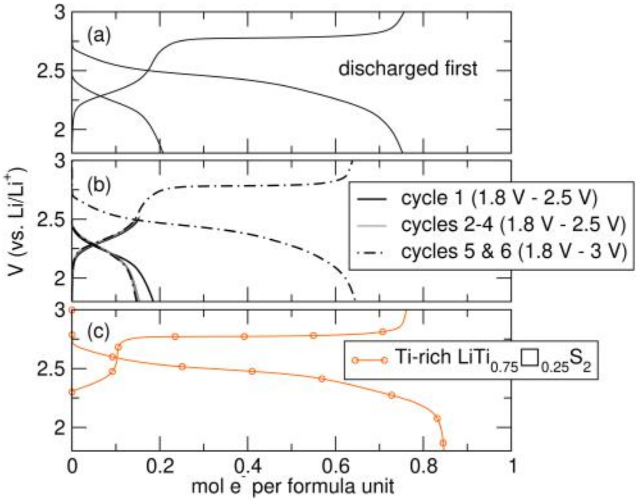

Figure 6.19: Cycling data of Ti^{3+}-containing materials. (a) and (b) Galvanostatic cycling data of $LiTi_{0.75}\square_{0.25}S_2$ discharged first with various V cutoffs at C/20. A capacity of 0.2 is observed during discharge, and the subsequent charge profile is characterized by an initial sloping region whose capacity matches that of the discharge capacity followed by the plateau at 2.77 V. (c) Galvanostatic cycling data of Ti-rich $LiTi_{0.75}\square_{0.25}S_2$ charged first. An initial sloping region is observed similar to the discharged first sample.

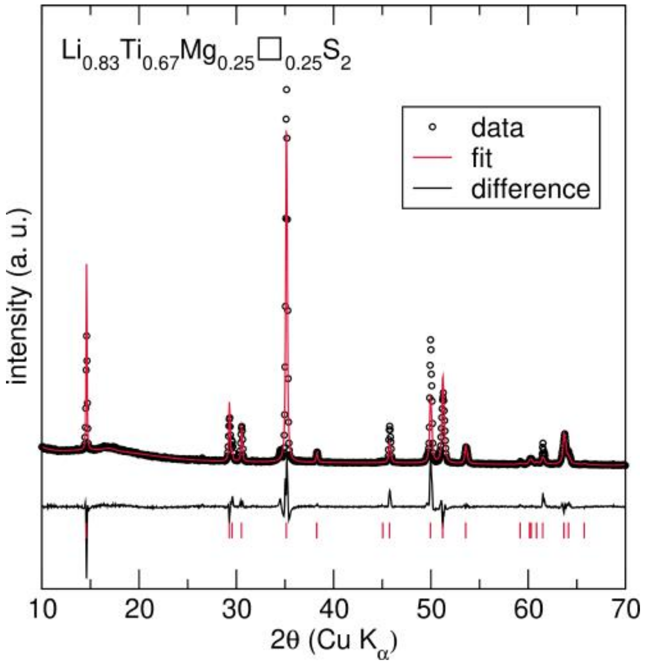

Figure 6.20: XRD patterns of $Li_{0.83}Mg_{0.25}Ti_{0.67}\square_{0.25}S_2$ in the $R\bar{3}m$ space group.

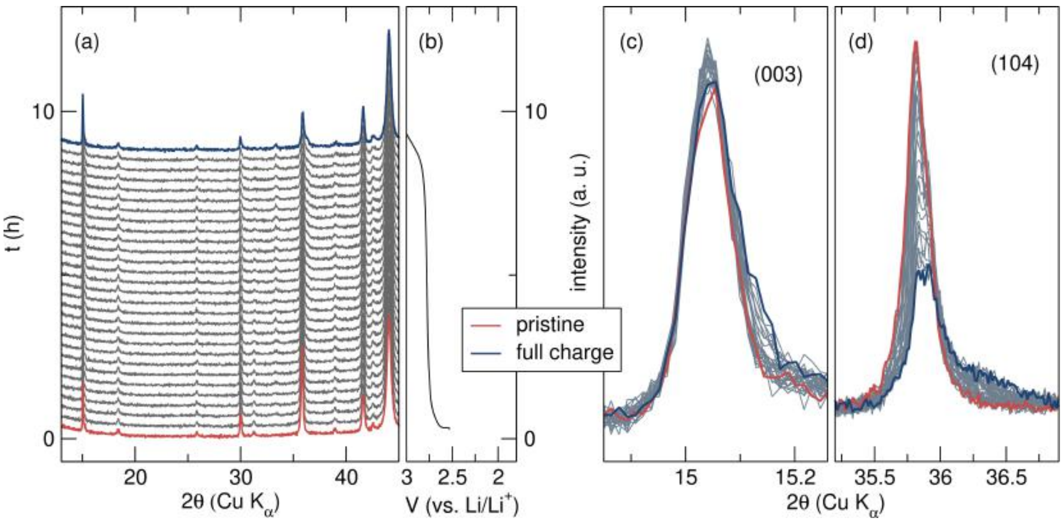

Figure 6.21: *Operando* XRD patterns of LiTi$_{0.75}\square_{0.25}$S$_2$. (a) *Operando* XRD patterns of LiTi$_{0.75}\square_{0.25}$S$_2$ and (b) the corresponding galvanostatic cycling data. LiTi$_{0.75}\square_{0.25}$S$_2$ exhibits a two-phase mechanism during charge as highlighted by changes in (c) (001) and (d) (104) reflections. The second phase is evident as shoulders evolve on the (003) and (104) reflections.

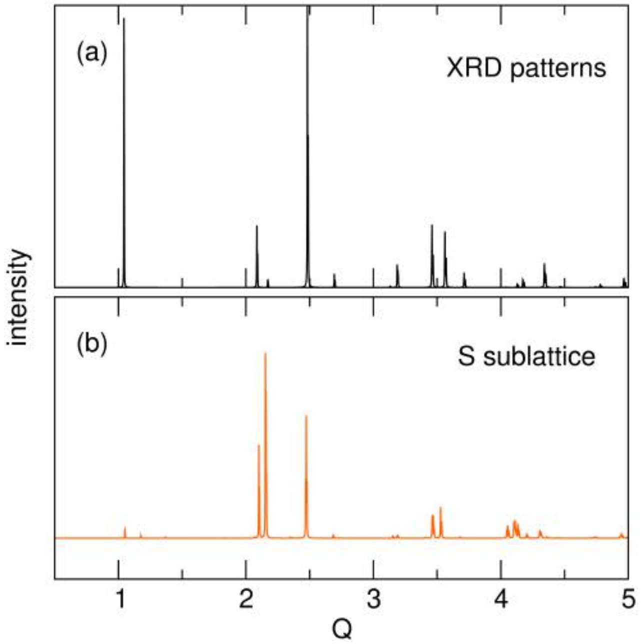

Figure 6.22: Simulated XRD patterns of the S sublattice. (a) Simulated XRD patterns of LiTi$_{0.75}\square_{0.25}$S$_2$ in the R$\bar{3}$m space group and (b) simulated XRD patterns of the S sublattice which was obtained by removing all Li and Ti atoms in the unit cell.

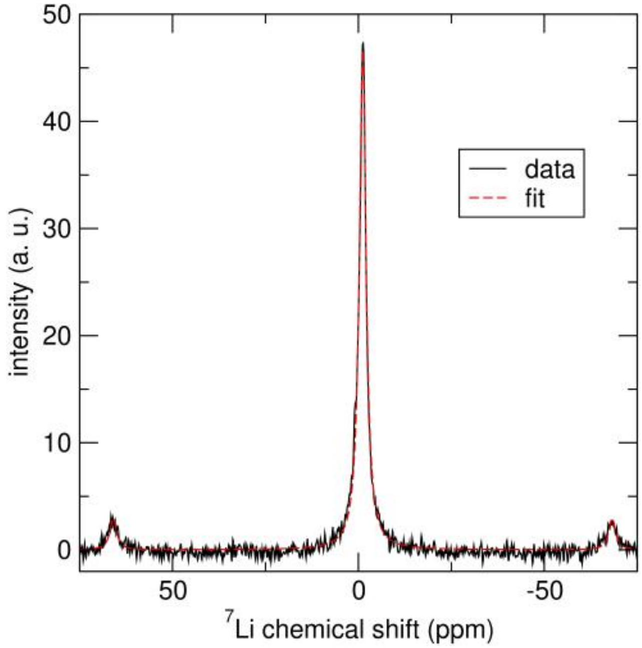

Figure 6.23: ^{7}Li MAS ssNMR spectrum of fully charged $LiTi_{0.75}\square_{0.25}S_2$ and its fit. The resonance can be well represented by one component.

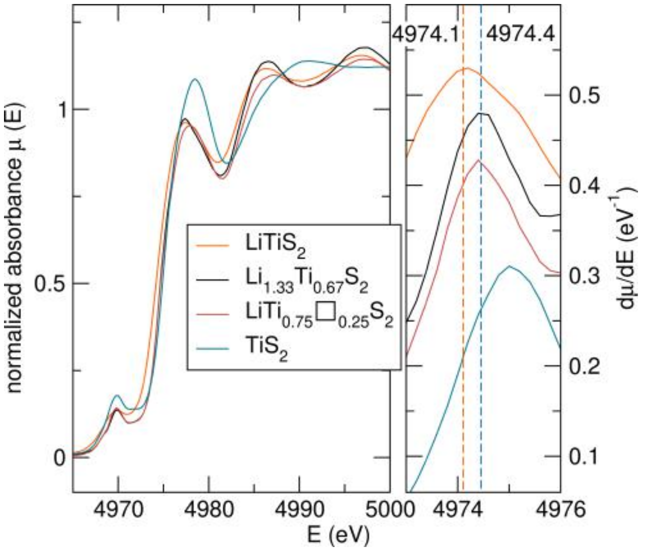

Figure 6.24: Ti XANES spectra of $LiTiS_2$, $Li_{1.33}Ti_{0.67}S_2$, $LiTi_{0.75}\square_{0.25}S_2$, and TiS_2. The rising edge position of $LiTi_{0.75}\square_{0.25}S_2$ aligns with that of $Li_{1.33}Ti_{0.67}S_2$, suggesting that the oxidation state of Ti is the same in both materials.

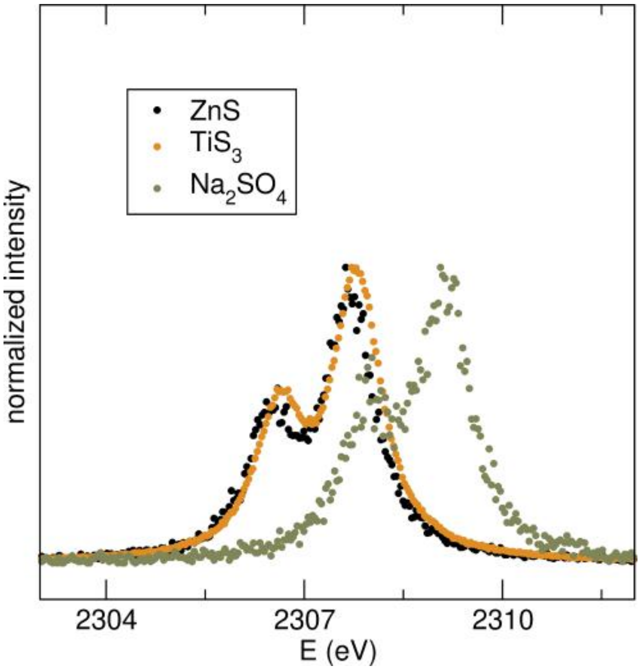

Figure 6.25: S K$_\alpha$ XES spectra of ZnS and Na_2SO_4 which are used for calibration and TiS_3 for reference.

Chapter 7

ORIGIN OF FIRST-CYCLE ACTIVATION AND VOLTAGE HYSTERESIS IN LI-RICH SULFIDE MATERIALS

Contributions: S.S.K. conceived, designed, and performed experiments, and wrote the manuscript. *manuscript submitted*

7.1 Abstract

In many battery systems, asymmetry between charge and discharge curves and voltage hysteresis indicate sluggish kinetics, irreversible processes, or different reaction pathways. Extensive research on Li-rich oxides has shown that first-cycle activation and voltage hysteresis is largely caused by surface O_2 evolution and transition metal migration in the bulk. While layered Li-rich sulfide materials are emerging in the field, the root cause of the first-cycle activation and voltage hysteresis in Li-rich sulfides remains elusive. In this work, we turn to $LiTi_{0.75}\square_{0.25}S_2$ which shows only anion oxidation during charge. By examining the discharge mechanism of $LiTi_{0.75}\square_{0.25}S_2$, we explore first-cycle activation and voltage hysteresis in Li-rich sulfides. Spectroscopic and structural characterization reveals that Ti is overreduced and S is not fully reduced back to S^{2-} during discharge. Voltage hysteresis is caused by the formation of trapped $(S_2)^{2-}$ and the formation of amorphous regions during discharge. We further demonstrate that annealing the cycled material recovers the thermodynamically stable phase and triggers ligand-metal charge transfer and structural reorganization.

7.2 Introduction

The world's growing demand for sustainable energy sources has spurred the development of renewable energy technologies. Li-ion batteries (LIBs) have been well established in powering electronic devices and electric transportation and are also a great candidate for grid storage applications.[7,241] State-of-the-art intercalation cathode materials in the form of $LiMO_2$ (M = a combination of metals) depend on transition metal redox for charge compensation and are reaching their capacity limits. Therefore, the increasing demand for high-energy density systems requires the development of new electrode materials.

One of the most promising ways to achieve high energy density is by substituting and populating some of the transition metal sites with Li and creating nonbonding electron pairs on the lattice anion that can be accessed for additional charge compensation.[156,242] Incorporating both cation and anion redox in the lattice enables multielectron charge storage. Li-rich oxides such as Li-rich NMCs ($\mathrm{Li}M\mathrm{O_2}$ + Li_2MnO_3)) exhibit increased capacities owing to high-voltage O redox processes, but undergo so-called first-cycle activation; the first charge curve is characterized by transition metal oxidation followed by a long plateau above 4.5 V. The following discharge cycle experiences poor Coulombic efficiency, and the subsequent charge curves also change irreversibly, hence the term activation cycle. The exact mechanism and physical phenomena responsible for the activation cycle are still not fully elucidated, but it is generally agreed that there is irreversible O_2 gas evolution directly from the lattice or from electrolyte decomposition as well as transition metal migration.[156,163,243,244] Because irreversible structural changes occurred, large voltage hysteresis is also observed in cycle 1.[157,244,245] Continuing to cycle the cell at high voltages to access O redox exacerbates these problems and leads to further capacity loss and voltage fade in Li-rich oxides. Recently, it was shown that the oxidation of O^{2-} and the lower energy of O_2 dimer–containing structure forces transition metal migration.[158]

In contrast, Li-rich sulfides can stabilize electron holes through dimerization of S and the formation of $(S_2)^{2-}$ that remains coordinated to the transition metal.[162,246] Li-rich sulfides do not experience gas evolution nor irreversible capacity loss in cycle 1 because S redox intrinsically operates at lower voltages. Also, no signs of transition metal migration into the Li layer were observed in $Li_{1.33-2y/3}Ti_{0.67-y/3}Fe_yS_2$ after 40 cycles based on HAADF-STEM.[163] As such, Li-rich sulfides serve as model systems to study structure-property relations of anion redox and also as great candidates as next-generation cathode materials. Despite minimal to no irreversible capacity loss in cycle 1 and no apparent transition metal migration, many layered Li-rich sulfides still experience a change in the charge profile after cycle 1.[163,166,167,177,220] We define the term first-cycle activation as the irreversible change in the charge voltage profile from cycle 1 to subsequent cycles. First-cycle activation in layered alkali-rich sulfides has been largely disregarded in many reports and not been extensively investigated to our knowledge.

In this work, we elucidate the discharge mechanism of $LiTi_{0.75}\square_{0.25}S_2$ to study the nature of first-cycle activation and voltage hysteresis in Li-rich sulfides. $LiTi_{0.75}\square_{0.25}S_2$

serves as a great candidate because it is free of transition metal oxidation during charge owing to the d^0 electronic configuration of Ti^{4+} and solely exhibits S oxidation through the formation of persulfide ($(S_2)^{2-}$). With a multitude of electrochemical, structural, and spectroscopic characterization techniques, we illustrate that $LiTi_{0.75}\square_{0.25}S_2$ exhibits $Ti^{4+/3+}$ overreduction and kinetically trapped $(S_2)^{2-}$ in the structure accompanied by surface amorphization during discharge. We then demonstrate that subjecting cycled $LiTi_{0.75}\square_{0.25}S_2$ to heat treatment recovers the thermodynamically stable phase by promoting ligand–metal charge transfer and structural reorganization.

7.3 Experimental Section

Material Preparation

$LiTi_{0.75}\square_{0.25}S_2$ was synthesized with the same solid-state synthesis method used in our previous report. All materials were prepared in an Ar-filled glovebox in which O_2 and H_2O levels were < 1 ppm using solid-state methods. $LiTi_{0.75}\square_{0.25}S_2$ was prepared by grinding stoichiometric quantities of Li_2S (Beantown Chemical, 99.9%), stoichiometric TiS_2, and 0.1 molar excess S pressing into 300 mg pellets. Pellets were placed inside carbon-coated vitreous silica ampules and heated at 3 °C min^{-1} to 750 °C and heated for 48 hr before cooling to room temperature. The color of the product pellet was black, and so was the ground powder. For annealing experiments, the cell was first charged and discharged at C/20 per formula unit. The cell was disassembled in an Ar-filled glovebox, and the cathode composite was carefully removed from the cell and washed with 400 μl of dimethyl carbonate. The composite was then vacuum dried for at least 4 hours at room temperature. the pellet was placed in a vitreous silica ampule and vacuum sealed. The tube was heated at 2 °C min^{-1} to 200 °C and heated for 24 hours before cooling to room temperature. A new coin cell was assembled with the annealed cathode.

Electrochemical Characterization

All cells were prepared inside an Ar-filled glovebox in which H_2O and O_2 levels were below 0.1 ppm. $LiTi_{0.75}\square_{0.25}S_2$ was mixed with Super P carbon (Alfa Aesar, ≥99%) and polytetrafluoroethylene (PTFE, Sigma-Aldrich) at a 60:20:20 wt% to make composite electrodes. The mixture was ground with a mortar and pestle and pressed into 0.25 inch diameter pellets with a hand-operated arbor press with a mass loading of 8 – 10 mg per pellet. 2032 coin cells were prepared with polished Li metal counter/reference electrodes, dried 18 mm diameter glass fiber separators (Whatman

GF/D), and 11 drops of electrolyte (approximately 160 mg). The electrolyte used in all cells was a 1 M solution of $LiPF_6$ (Sigma-Aldrich, ≥99.99%) in a 1:1:3 mixture of ethylene carbonate (Sigma-Aldrich, >99%), propylene carbonate (Sigma-Aldrich, >99%), and dimethyl carbonate (Sigma-Aldrich, >99%) by volume. All potentials are in reference to the Li metal counter/reference electrode potential, which is approximated to equal to that of Li/Li^+. Galvanostatic cycling data were collected at C/20 based on 1 e^- per formula unit $LiTi_{0.75}\square_{0.25}S_2$. Galvanostatic intermittent titration technique (GITT) was conducted at a rate of C/20 based on 1 e^- per formula unit for 20 minutes with 4 hour open circuit hold rest periods.

Material Characterization

Synchrotron powder X-ray diffraction patterns were collected on 11-BM-B (λ = 0.458979 Å) beamline at the Advanced Photon Source at Argonne National Laboratory.[175] The *ex situ* discharged sample was prepared using 16 mg of a 60:20:20 wt% pellet consisting of active material, Super P carbon, and PTFE. A cell fully charged to 3 V and discharged to 1.8 V was disassembled, and the cathode composite was recovered from the disassembled cell, washed with 400 μl of dimethyl carbonate, and vacuum dried. The sample was sealed under vacuum in 0.7 mm (o.d.) glass capillaries (Hampton Research) to prevent air exposure and placed inside of polyimide capillaries. The diffraction patterns were fit by the Rietveld method using GSAS-II.[144]

Operando XRD data were collected using a Bruker D8 Advance diffractometer in Bragg-Brentano geometry equipped with a Cu Kα source (λ_1 = 1.5406 Å, λ_2 = 1.5444 Å) and a Lynxeye XE-T detector. A custom-made *operando* cell with a PEEK body, stainless steel electrical contacts, and an X-ray transparent Be window (SPI Supplies, 0.25 mm thick) was used. The Be window served as a current collector and allowed for X-ray penetration so that diffraction patterns could be collected while cycling galvanostatically. As with the *ex situ* cells, pellet electrodes composed of 60% active material, 20% carbon black, and 20% polymer binder were used and placed directly on the Be window. The pellet electrodes were cycled against Li foil using a BioLogic SP-200 potentiostat at a C/20 rate with one Whatman glass fiber separator (GF/D) flooded with 1 M LiPF6 in 1:1:1 EC:PC:DMC electrolyte. Patterns were continuously collected over a range of 10°to 45°2θ approximately every 20 min throughout the duration of the electrochemical cycling.

Transmission electron microscopy (TEM) imaging was conducted using Thermofisher Talos F200X G2 S/TEM at an accelerating voltage of 200 keV under High-resolution TEM (HRTEM) mode. TEM samples of pristine $LiTi_{0.75}\square_{0.25}S_2$ and charged $LiTi_{0.75}\square_{0.25}S_2$ were prepared through dry transfer powders onto 200 mesh lacey carbon films on copper grids (Ted Pella, Inc.).

Solid-state NMR was performed with the Bruker Avance 500 MHz spectrometer operating at 194.31 MHz for ^{7}Li. All samples were packed in a 4 mm ZrO_2 HR-MAS rotor with 50 μl PTFE spacer (Cortecnet). *Ex situ* samples were prepared in the same way as electrochemical cells above, with a total mass of 20 mg. ^{7}Li MAS ssNMR was recorded spinning at 13 kHz. A single RF pulse of 0.5 μs with a 4 μs $\pi/2$ was applied. The ^{7}Li MAS spectra were fit with DMFIT using Quasar.

Ti X-ray absorption spectroscopy was conducted at beamline 2-2 at the Stanford Synchrotron Radiation Lightsource at SLAC National Accelerator Laboratory. Data processing including calibration and background correction was performed using Athena.[176] The Ti K-edge data were calibrated to a collinear Ti foil for each sample. *Ex situ* samples were prepared in the same way as electrochemical cells in coin cells with a total mass of 20 mg. *Ex situ* samples were placed onto the sample holder using Kapton tape on each side inside an Ar-filled glovebox. During measurement, the sample holder was placed in a continuous He-flushed chamber with minimal O_2 concentration ($<$ 500 ppm). Each scan lasted about 15 minutes, and 3 scans were averaged.

S X-ray emission spectroscopy was performed using the Brimstone^{TM} laboratory spectrometer (easyXAFS LLC, Renton, WA, USA). The spectrometer utilized a Pd-anode x-ray tube and was operated at 24 kV and 3 mA. The spectrometer uses the easyXAFS Kromo^{TM} cmos-based position-sensitive, energy resolving detector. Using a Si(111) crystal analyzer with radius of curvature 100 mm, the S K_α spectra were measured at a Bragg angle of 59.0 degrees, and S K_β spectra were measured at a Bragg angle of 53.4 degrees. To reduce Johann error for optimal resolution, the 20 mm wide analyzer was masked to use only the central 4 mm. Measurements are performed under helium flushed into the experimental chamber at atmospheric pressure. Samples were prepared by encapsulating the powder samples between a lower layer of Kapton tape and an upper layer of 8 μm thin Kapton film. The sealed samples were then briefly exposed to air during mounting into the spectrometer (15 min) and during the helium flushing (25 min). Some residual air is expected to remain in the chamber, even after flushing. Samples were mounted on an automatic sample changer, and a series of repeated short scans (3 minutes each) were measured alternately between each sample and reference compounds, and 5 scans were averaged. Resulting data were monitored for possible changes due to instrumental drift or changes in sample signal over time from radiation damage, air exposure, or other effects.

7.4 Results

Electrochemical Characterization of $LiTi_{0.75}\square_{0.25}S_2$

First, the electrochemical performance of $LiTi_{0.75}\square_{0.25}S_2$ is examined with galvanostatic cycling. Detailed information regarding the crystal structure and the first charge cycle is reported in our previous report. Galvanostatic cycling data and the corresponding dQ/dV plots of $LiTi_{0.75}\square_{0.25}S_2$ are shown in Figure 7.1. While the parent phase Li_2TiS_3, or $Li_{1.33}Ti_{0.67}S_2$ hereafter, exhibits no meaningful capacity, vacancy-containing $LiTi_{0.75}\square_{0.25}S_2$ exhibits a charge capacity of 0.6 e^- per formula unit activated by the introduction of cation vacancies in the structure. A higher discharge capacity of 0.85 is observed, indicating that more Li can be inserted back in the structure than what was removed during charge and that Ti^{4+} acts as a reduction center during discharge. Thus, the charge profile changes drastically after cycle 1; an initial sloping region is observed below 2.5 V followed by a plateau at a lower voltage than in cycle 1 (Figure 7.1a). The charge profile resembles that of $Li_{1.25}Ti_{0.75}S_2$ reported by Flamary-Mespoulie et al., in which the sloping region below 2.5 V corresponds to $Ti^{3+/4+}$ oxidation and the plateau S oxidation.[165] Although the d^0 electron configuration of Ti^{4+} precludes Ti from participating in oxidation in cycle 1, the presence of Ti^{3+} at the end of cycle 1 allows for $Ti^{3+/4+}$oxidation in cycle 2.

Next, the dQ/dV plots of the galvanostatic cycling data are examined to explore redox processes in $LiTi_{0.75}\square_{0.25}S_2$ (Figure 7.1b). In cycle 1 charge, one sharp peak is observed corresponding to the single plateau associated with S oxidation. During discharge, one sharp peak at 2.46 V and a broad shoulder at 2.3 V are observed. In cycle 2, a new oxidative peak is observed at 2.33 V corresponding to the initial sloping region, and the peak associated with the plateau is shifted to a lower voltage. Upon continued cycling, the second oxidative peak gradually broadens and voltage fade is observed in both charge and discharge suggesting that $Ti^{3+/4+}$ redox couple begins to dominate. While the contribution of $Ti^{3+/4+}$ redox couple increases, S redox is not as reversible. We hypothesize that $(S_2)^{2-}$ formed during charge is kinetically trapped during discharge, resulting in residual $(S_2)^{2-}$ at the end of discharge leading to voltage fade upon continued cycling. This hypothesis will be further probed with spectroscopic characterization.

The kinetics of different redox processes are probed with galvanostatic intermittent titration technique (GITT). The cell is polarized for 20 minutes followed by a 4-hr rest period. Overpotential η is defined as the difference in potential between the

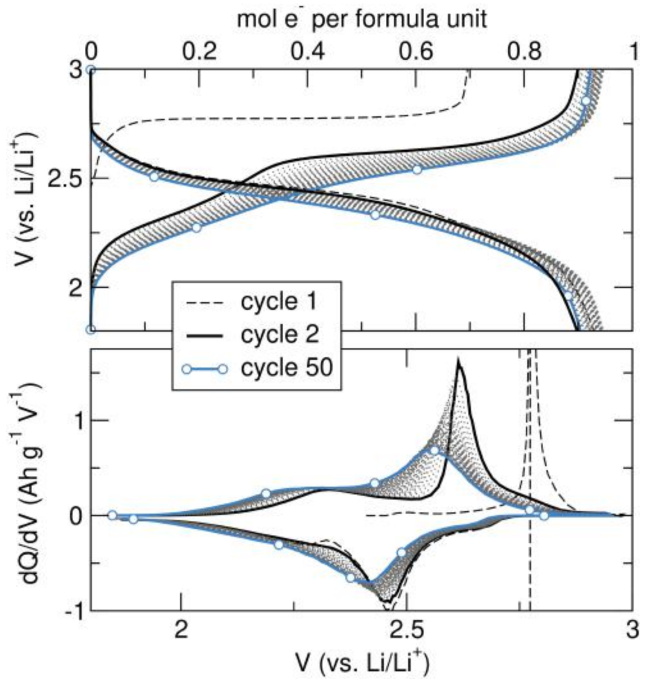

Figure 7.1: Galvanostatic cycling and dQ/dV plots of $LiTi_{0.75}\square_{0.25}S_2$. (a) Galvanostatic cycling data of $LiTi_{0.75}\square_{0.25}S_2$ at C/20 based on 1 e^- per formula unit, (b) the corresponding dQ/dV plots. Voltage hysteresis between charge and discharge is observed in cycle 1, and the plateau shifts to a lower voltage after cycle 1.

beginning and the end of each rest period, and equilibrium potential V_{eq} is the potential at the end of each rest period. GITT of $LiTi_{0.75}\square_{0.25}S_2$ is shown in Figure 7.2. V_{eq} of the first charge cycle is characterized by a single plateau indicating a two-phase mechanism during charge. A uniform η of ~50 mV is observed until the cell polarizes to 3 V (Figure 7.2a). This η is lower than those associated with O oxidation in Li-rich oxides which is greater than 100 mV, suggesting more facile kinetics for S oxidation. η in the first discharge cycle also stays uniform at ~50 mV (Figure 7.2a).

In the second charge cycle, the initial sloping region shows lower η reaching as low as 17 mV, suggesting very facile kinetics associated with Ti^{3+} oxidation. The second plateau exhibits similar η as the first cycle, suggesting that the kinetic barrier does not change despite the lowered voltage.

The second discharge cycle reveals that although η is similar in the beginning, η decreases after 0.4 e^- and reaches 18 mV. This behavior is different from the first discharge cycle that shows a constant η of ~50 mV. GITT of cycle 2 reveals that $Ti^{3+/4+}$ redox exhibits lower kinetic barriers compared to S. Interestingly, although

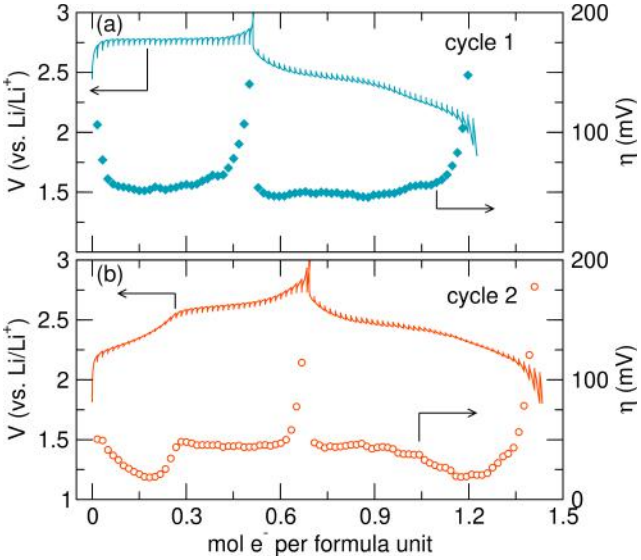

Figure 7.2: GITT data of LiTi$_{0.75}$□$_{0.25}$S$_2$ and the corresponding overpotential η at each step (a) in cycle 1 and (b) in cycle 2.

the higher discharge capacity in cycle 1 indicates Ti reduction in cycle 1 discharge, η remains the same suggesting additional kinetic barriers for Ti reduction during discharge.

Next, entropic potential measurements are performed on LiTi$_{0.75}$□$_{0.25}$S$_2$ during cycling to gain more insights into the charge compensation mechanism. Entropic measurements are collected by polarizing the cell at C/20, relaxing the cell for 4 hr to achieve V$_{eq}$, and applying a 5 °C temperature bias to measure the change in potential dV$_{eq}$/dT at various states of charge.[247] The V$_{eq}$ and entropic potential measurements are depicted in Figure 7.3. Similar to V$_{eq}$ observed in GITT, a single plateau in the entropic potential measurements stems from the common tangent of two phases and thus represents the coexistence of two phases.[247] Therefore, the single plateau in the dV$_{eq}$/dT plot during charge further supports a two-phase mechanism in LiTi$_{0.75}$□$_{0.25}$S$_2$.

During discharge, a different dV$_{eq}$/dT profile is observed compared to the charge profile. First, a short plateau is observed in early states of discharge suggesting a two-phase reaction (region I). The length of the plateau is a lot shorter compared to that in charge, suggesting that the two-phase reaction is short-lived. Subsequently, a fluctuation in the profile with an inflection point is observed (region II). Such a profile of a fluctuation with an inflection point occurs in systems with different site energies that result in initial preferential Li occupancy in one site followed

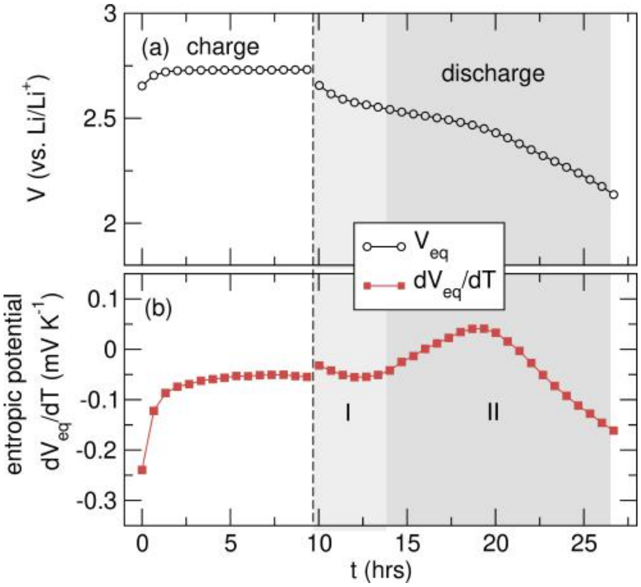

Figure 7.3: Entropic potential measurements of $LiTi_{0.75}\square_{0.25}S_2$. (a)Equilibrium potential V_{eq} of $LiTi_{0.75}\square_{0.25}S_2$ and (b) entropic potential dV_{eq}/dT of $LiTi_{0.75}\square_{0.25}S_2$ in cycle 1. Data collected by Yucheng Zhou in the Pilon Group at UCLA.

by the other site. This behavior is observed in materials that exhibit ion ordering during insertion and removal of Li in single-phase intercalation-type materials such as Li_xTiS_2 and Li_xCoS_2.[247–251] The short plateau followed by a fluctuation in the dV_{eq}/dT plot in discharge therefore suggests a two-phase reaction followed by an ion-ordering event during discharge. In contrast, the charge curve is characterized by one single plateau and does not exhibit any signs of ion ordering or stable intermediate species. Therefore, the discrepancy in the charge and discharge curves of dV_{eq}/dT further suggests asymmetry in charge and discharge pathways and that the hysteresis is structural in origin.

Structural and Spectroscopic Evolution during Cycling

Next, we investigate structural and spectroscopic evolution of $LiTi_{0.75}\square_{0.25}S_2$ during cycling with an emphasis on the discharge mechanism. Detailed analysis during charge can be found in our previous report. First, changes in Li environments are probed with ^{7}Li magic angle spinning (MAS) solid-state NMR (ssNMR). Figure 7.4 illustrates *ex situ* ^{7}Li MAS ssNMR spectra of $LiTi_{0.75}\square_{0.25}S_2$ at the following states of charge: pristine, full charge (charged to 3 V), partial discharge (fully charged then discharged to 2.35 V), and full discharge (fully charged then discharged to 1.8 V). We previously demonstrated that the resonance in the full charge spectrum is well described by the 4*h* Li site in the Li layer. Upon partial discharge, the resonance begins to broaden and is no longer fit to one single component, indicating that other Li sites begin to be filled during Li intercalation (Figure 7.9). Upon full discharge, the resonance broadens significantly. We attribute this peak broadening to the paramagnetic influence of d^1-electron configuration of Ti^{3+}. Indeed, the full discharge spectrum resembles the spectrum of $Li_{1.25}Ti_{0.75}S_2$ prepared via solid-state synthesis that contains mixed $Ti^{3+/4+}$ (Figure 7.10), further indicating Ti reduction during discharge and the effect of paramagnetic peak broadening.

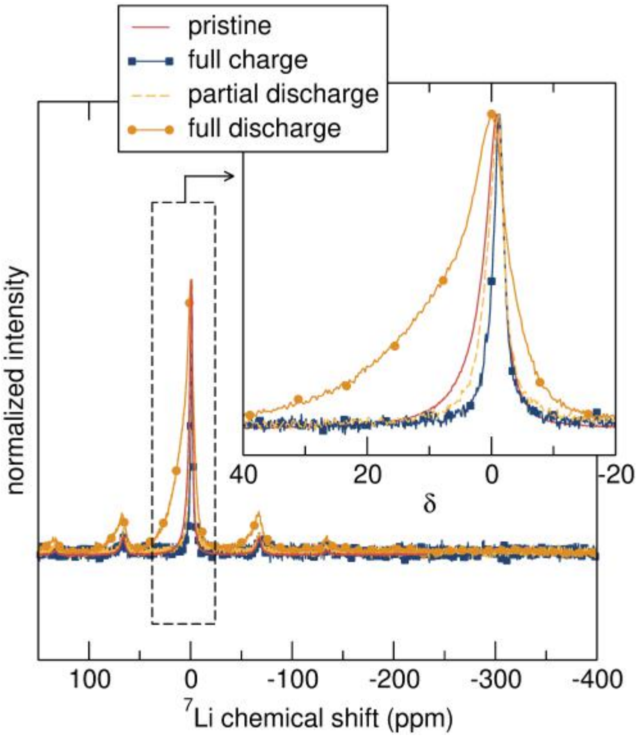

Figure 7.4: *Ex situ* ^{7}Li MAS ssNMR spectra of $LiTi_{0.75}\square_{0.25}S_2$ at different states of charge with the insent showing the magnified section of the isotropic peaks.

Next, the structural evolution during discharge is probed with *operando* X-ray diffraction (XRD) and *ex situ* synchrotron XRD (sXRD). Figure 7.5a depicts the *operando* XRD patterns of $LiTi_{0.75}\square_{0.25}S_2$ during discharge at C/20 based on 1 e^- per formula unit. We have previously shown that at the end of full charge, sXRD patterns of $LiTi_{0.75}\square_{0.25}S_2$ are fit to two phases in the same space group $R\bar{3}m$, with one phase more closely related to the parent phase and the other one associated with a persulfide-containing structure. In initial states of discharge denoted as region I (Figure 7.5c), the (104) reflection exhibits a shift to lower 2θ. Additionally, the shoulder at higher 2θ diminishes in this region suggesting a two-phase mechanism. In the remainder of the discharge curve denoted as region II (Figure 7.5d), the shoulder is no longer present and the main reflection shifts to lower 2θ, suggesting a solid-solution mechanism. This result will be complimented by the entropic potential measurements.

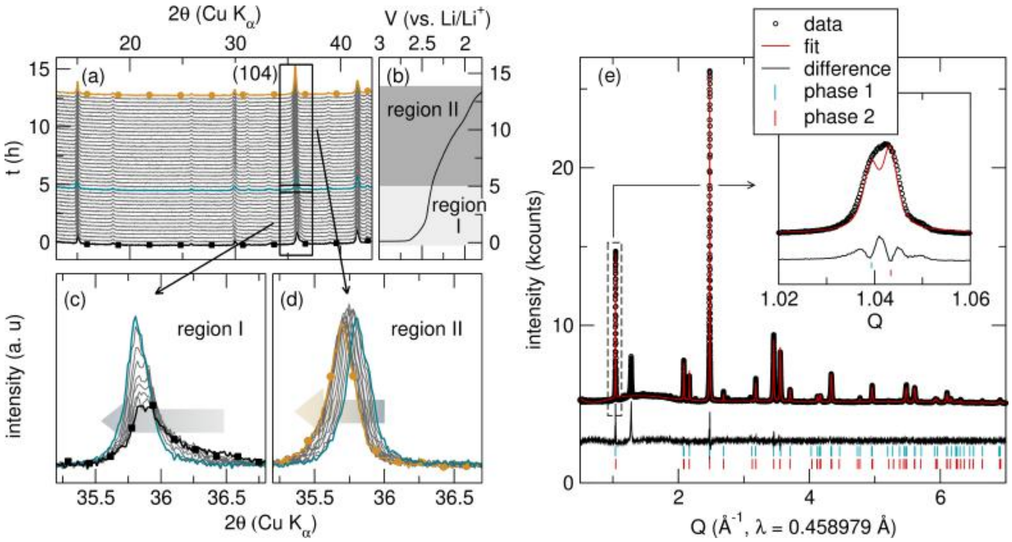

Figure 7.5: XRD patterns of $LiTi_{0.75}\square_{0.25}S_2$. (a)*Operando* XRD patterns of $LiTi_{0.75}\square_{0.25}S_2$ during discharge and (b) the corresponding galvanostatic cycling data. (104) reflection (c) during the initial discharge until 2.35 V, or region I, and (d) from 2.35 V to 1.8 V, or region II. (e) Synchrotron XRD patterns of fully discharged $LiTi_{0.75}\square_{0.25}S_2$ fit to two phases in the $R\bar{3}m$ space group with an inset highlighting the (003) reflection. *Operando* XRD data collected by Jessica Andrews in the Melot Group at UCLA.

More quantitative crystal structure analysis is performed with sXRD on fully discharged $LiTi_{0.75}\square_{0.25}S_2$. The diffraction patterns are fit to two phases (Figure 7.5e) with very similar lattice parameters of a = 3.53554 Å and c = 18.06532 Å(V = 195.564 Å^3) for phase I and a = 3.52842 Å and c = 18.13537 Å (V = 195.531 Å^3) for phase II. Two phases are used to fit the diffraction patterns because the (002) reflection is too broad and bimodal although other reflections are unimodal and can be fit to one single phase (Figure 7.11). Compared to the lattice parameters of pristine $LiTi_{0.75}\square_{0.25}S_2$ a = 3.52508 Å and c = 18.06548 Å (V = 194.410 Å^3), phase I exhibits only a slight expansion in the *a* direction while phase II shows a larger expansion in the *c* direction. This result indicates that there are two phases with different layer stacking distance. Further structural characterization including TEM will be carried out to elucidate the origin of this two-phase behavior.

Charge Compensation by Ti Reduction and Kinetically Trapped $(S_2)^{2-}$ during Discharge

The role of Ti and S in the charge compensation mechanism during discharge is probed with *ex situ* Ti K-edge X-ray absorption spectroscopy (XAS) and S X-ray emission spectroscopy (XES). Ti K-edge XANES data are plotted in Figure 7.6a. As depicted in the first derivative plot in Figure 7.6b for clarity, the Ti rising edge position does not shift from pristine to full charge indicating that Ti remains as Ti^{4+} and does not participate in oxidation during charge. During discharge, the rising edge does not shift in the partial discharge spectrum, suggesting that Ti is not reduced in this region. Upon full discharge, the rising edge position shifts down from 4974.4 eV to 4974.0 eV indicating Ti reduction. This aligns with the edge position of isostructural $LiTiS_2$ with the space group $R\bar{3}m$ in which the formal oxidation state of Ti is 3+. This result further validates the paramagnetic broadening of ^7Li MAS ssNMR spectrum of fully discharged $LiTi_{0.75}\square_{0.25}S_2$.

The electrochemical activity of S in $LiTi_{0.75}\square_{0.25}S_2$ during discharge is probed with *ex situ* XES at the same states of charge. K_α features shown in Figure 7.6c are sensitive to the oxidation state of S while K_β features shown in Figure 7.6d are more sensitive to the bonding environment around S atoms.[234] The $K_{\alpha1}$ peak position shifts from 2307.70 eV to 2307.78 eV after full charge, indicating S oxidation. During discharge, the peak position shifts to lower energy, signifying S reduction. The peak position does not return to the same position as that of pristine $LiTi_{0.75}\square_{0.25}S_2$ upon full discharge which indicates that there is residual oxidized S in the structure, likely in the form of kinetically trapped $(S_2)^{2-}$. K_β spectra reveal that the pristine spectrum is characterized by a broad feature at 2465.63 eV, and a new feature develops at 2467.61 eV upon full charge. The same feature is observed in TiS_3 which contains both S^{2-} and $(S_2)^{2-}$. Upon discharge, the new feature at 2467.61 eV remains, suggesting that the structural element that gives rise to the new feature at 2467.61 eV does not disappear upon discharge. The energy shifts of Ti XANES and S XES are summarized in Figure 7.6e and f.

First-Cycle Activation in Li-Rich Sulfides

Next, we discuss the first-cycle activation in $LiTi_{0.75}\square_{0.25}S_2$ and generalize the implications in Li-rich sulfides. In $LiTi_{0.75}\square_{0.25}S_2$ and in all other reported layered alkali-rich sulfides and selenides in which transition metal is octahedrally coordinated (Li_2TiS_3 + Fe^{2+}, Co^{2+}, Ti^{3+}, Li_2SnS_3 + Fe^{2+}, Na_2TiS_3, $Li_2TiS_{3-x}Se_x$), the charge profile changes after cycle 1; the charge curve after cycle 1 is characterized

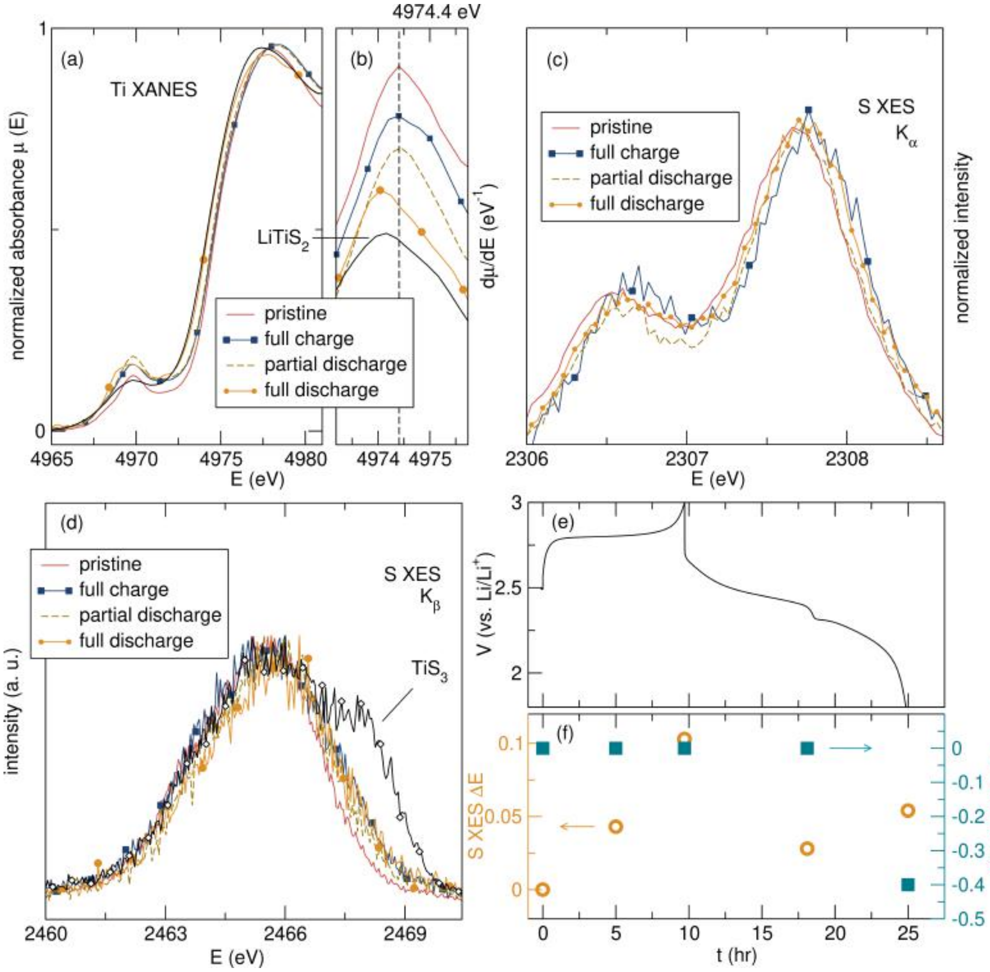

Figure 7.6: Ti XANES and S XES of LiTi$_{0.75}\square_{0.25}$S$_2$ during discharge. (a) *Ex situ* Ti XANES of LiTi$_{0.75}\square_{0.25}$S$_2$ and (b) the corresponding first derivatives of the rising edge. (c) S K$_\alpha$ and (d) S K$_\beta$ XES spectra of LiTi$_{0.75}\square_{0.25}$S$_2$. (e) The galvanostatic cycling data and (f) summary of the edge positions of Ti XANES and S XES.

by lowered anion oxidation potential which remains consistent in subsequent cycles.[163,165–167,177,220] GITT (Figure 7.2) indicates that the V$_{eq}$ in the anion oxidation region in cycle 2 is lower than in cycle 1 suggesting that there is an irreversible thermodynamic change in the material.

Clues about the origin of first-cycle activation can be gathered from structural characterization. To examine the morphological changes that occur during cycling, transmission electron microscopy (TEM) is performed on pristine, fully charged, and fully discharge LiTi$_{0.75}\square_{0.25}$S$_2$ and the results are show in Figure 7.7. Both pristine and fully charged LiTi$_{0.75}\square_{0.25}$S$_2$ exhibit the layered framework stretched to the edge of the particle with a very small loss of crystallinity near the surface due to surface oxidation (Figure 7.7a). Upon full discharge, however, an amorphous region near the surface is observed (Figure 7.7c) indicating that the material undergoes surface amorphization during discharge. Nagaraja et al. also reported that layered Fe^{2+}–substituted Li_2SnS_3 suffers from severe structural distortions and nanopore formation at the end of cycle 1.[177] The layered structural framework continues to degrade, and by the end of cycle 2 disordered amorphous regions form near the surface.[177] We hypothesize that first-cycle activation in Li-rich sulfides can be explained by structural distortions and surface amorphization on the nano scale. These structural changes occurring during the first discharge cycle are short-range in nature and thus are not detected by X-ray diffraction patterns. Also, we point out that the layered materials' disordered rocksalt counterparts – Li_2TiS_3, Na_2TiS_3, and Li_xNbS_4 – show first charge profiles that appear indistinguishable from those in subsequent cycles. We hypothesize that these materials are already highly disordered and amorphous, and thus the structural changes already have occurred during mechanochemical synthesis and consequently exhibit consistent electrochemical behavior. In fact, disordered rocksalt Li-rich oxides also exhibit a similar behavior; the first charge cycle adopts a more sloping shape than layered structures albeit with irreversible capacity loss.[21,252] Other examples of Li-rich sulfides that do not exhibit first-cycle activation include tetrahedrally coordinated Li-rich materials Li_2FeS_2 and antiperovskite structures $(Li_2M)SO$ (M = Fe^{2+} and Co^{2+}). They all exhibit electrochemical activity above 2.5 V ascribed to anion redox, and their charge curve profile does not change after cycle 1. Therefore, we suggest that first-cycle activation is a phenomenon more prevalent in the archetypal layered structures with octrahedrally coordinated transition metal, and further studies are necessary to elucidate the driving force behind surface amorphization.

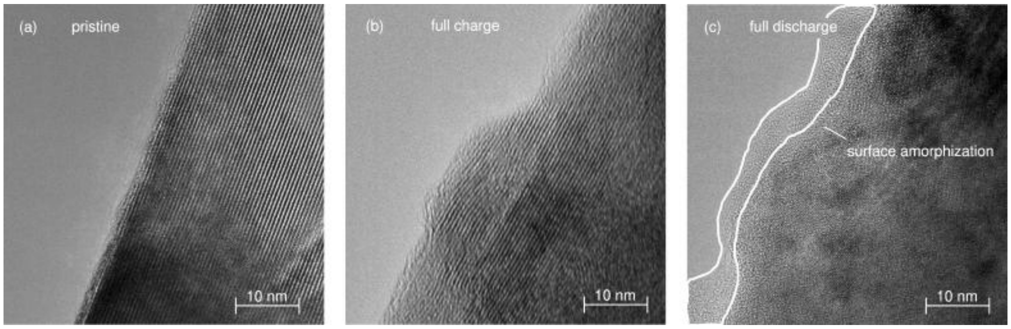

Figure 7.7: TEM images of (a) pristine, (b) full charge, and (c) full discharge $LiTi_{0.75}\square_{0.25}S_2$. Fully discharged $LiTi_{0.75}\square_{0.25}S_2$ exhibits surface amorphization. Data collected by Dr. Qizhang Yan in the Luo Group at UCSD.

Recovery of Thermodynamic Phase by Annealing

Spectroscopic and structural analysis so far demonstrated that the pristine material is not recovered at the end of cycle 1. $LiTi_{0.75}\square_{0.25}S_2$ gains extra capacity in the discharge cycle due to the presence of vacancies and the ability of Ti to act as a reduction center. Also, preliminary TEM analysis revealed that fully discharged $LiTi_{0.75}\square_{0.25}S_2$ exhibits surface amorphization. We hypothesize that Ti reduction is more kinetically facile than S reduction as it requires the breaking of S-S dimers resulting in a metastable phase at the end of discharge. To recover the thermodynamically stable phase at the end of cycle 1, cycled $LiTi_{0.75}\square_{0.25}S_2$ is thermally treated by annealing at 200 °C for 24 hours. The annealed material hereafter refers to the cathode composite that was charged to 3 V, discharged to 1.8 V, recovered from the cell, washed with sovlent, and annealed at 200 °C under vacuum. The galvanostatic cycling data comparison of $LiTi_{0.75}\square_{0.25}S_2$ cycle 2 and annealed $LiTi_{0.75}\square_{0.25}S_2$ is depicted in Figure 7.8a and b. Cycle 2 charge curve of $LiTi_{0.75}\square_{0.25}S_2$ exhibits two distinct regions that exhibit initial $Ti^{3+/4+}$ oxidation followed by S oxidation (Figure 7.8a). 34% of the capacity stems from the sloping region below 2.5 V indicating a large contribution from $Ti^{3+/4+}$ oxidation. On the other hand, the annealed sample exhibits a much smaller fraction below 2.5 V contributing to 11%, meaning that most of the charge compensation is accounted for by S oxidation (Figure 7.8b). We note that the overall capacity is lower in the annealed sample due to the mass of non-active materials added, mainly the separator, during the disassembly and reassembly process. The change in the charge curve after annealing suggests that the relative capacity contribution from $Ti^{3+/4+}$ oxidation decreases while that of S increases. We note that the control – cathode composite recovered from the disassembled cell after cycle 1, washed with solvent, and vacuum dried without annealing at 200 °C – exhibits the same electrochemical behavior as the normal cell indicating that the observed difference in the annealed sample originates from the annealing step (Figure 7.12). Relaxing the cell at room temperature for three weeks also does not alter the subsequent cycling, suggesting that thermal treatment is necessary (Figure 7.13).

To investigate the contribution of Ti and S during annealing, Ti K-edge XANES and S XES spectra shown in Figure 7.8d-f are examined. Ti XANES exhibits that the rising edge shifts to a higher energy compared to full discharge upon annealing suggesting more oxidized Ti (See Figure 7.14 for first derivatives). The rising edge does not return to the exact same position as the pristine material because $LiTi_{0.75}\square_{0.25}S_2$ is reduced more during discharge than it is oxidized during charge indicating a net

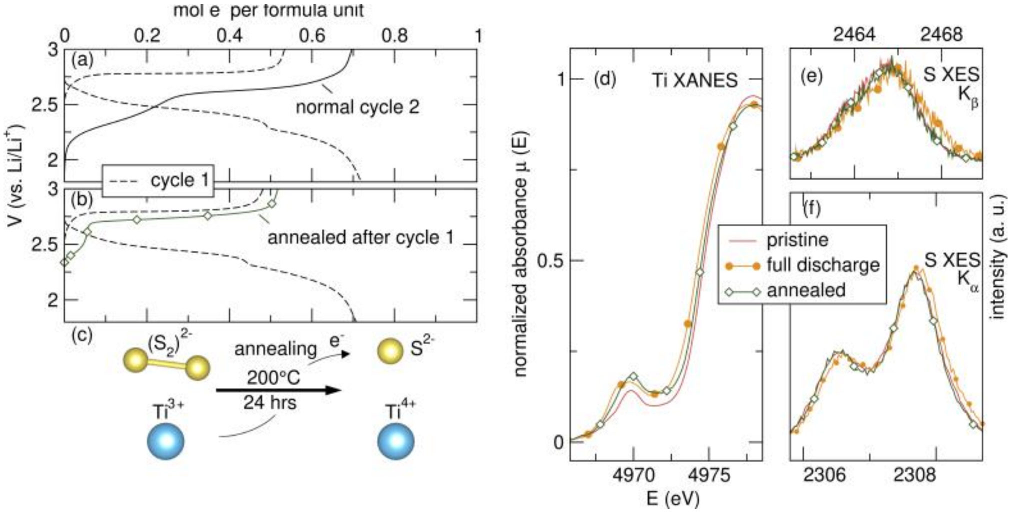

Figure 7.8: Annealing experiment galvanostatic cycling and spectroscopy. (a) normal galvanostatic cycling data of $\mathrm{LiTi}_{0.75}\square_{0.25}\mathrm{S}_2$ highlighting cycle 2 and (b) galvanostatic cycling data of annealed $\mathrm{LiTi}_{0.75}\square_{0.25}\mathrm{S}_2$. (c) Schematic depicting ligand–metal charge transfer during annealing. (d) Ti XANES and (e and f) S XES spectra of annealed $\mathrm{LiTi}_{0.75}\square_{0.25}\mathrm{S}_2$.

reduction in the material. ^{7}Li MAS ssNMR spectrum of annealed $\mathrm{LiTi}_{0.75}\square_{0.25}\mathrm{S}_2$ exhibits a sharper resonance compared to the fully discharged material, suggesting that the effect of paramagnetic broadening is reduced after annealing (Figure 7.15). The decreased but apparent presence of Ti^{3+} as indicated by Ti XANES also explains the decreased yet persistent presence of the sloping region in the charge curve of the annealed material. When the annealing experiment is performed on a cell that is stopped when the discharge capacity is equal to the charge capacity, the initial sloping region completely disappears (Figure 7.16).

S XES data reveals that while full discharge K_α and K_β spectra deviate in energy and exhibit a shoulder compared to the pristine state, both K_α and K_β spectra of annealed $\mathrm{LiTi}_{0.75}\square_{0.25}\mathrm{S}_2$ resemble those of the pristine state very well (Figure 7.8e and f). This result indicates that the formal oxidation state of S in the annealed material returns to S^{2-}. Also, the shoulder is no longer present in the K_β spectrum which indicates that the unique S environment similar to TiS_3 ascribed to $(\mathrm{S}_2)^{2-}$ disappears.

Together, *ex situ* spectroscopy results suggest that the capacity gained from Ti reduction during discharge accounts for more than the extra capacity observed during discharge. We hypothesize that the dissociation of S-S dimers competes with $\mathrm{Ti}^{4+/3+}$ reduction and S–S dimer dissociation is suppressed by a kinetic barrier while the Ti reduction is kinetically favored. Annealing $\mathrm{LiTi}_{0.75}\square_{0.25}\mathrm{S}_2$ after cycle

1 recovers the thermodynamically stable state via a ligand-metal charge transfer mechanism in which e^- is transferred from Ti to S and break the S-S bond (Figure 7.8c).

In addition to triggering ligand metal charge transfer, annealing also causes structural changes. In oxides, transition metal migration causes hysteresis and voltage fade upon continued cycling.[157,158,253] Singer et al. and Qiu et al. reported that Li-rich NMC develops dislocation networks and TM migration upon continued cycling and demonstrated that annealing the cycled material resulted in the recovery of the average discharge voltage and cation ordering as well as the elimination of structural disorder.[254,255] The average discharge voltage of $LiTi_{0.75}\square_{0.25}S_2$ decreases by 30 mV by cycle 50 suggesting that structural changes – surface amorphization as illustrated by TEM – persistently occurs (Figure 7.17). We hypothesize that annealing $LiTi_{0.75}\square_{0.25}S_2$ converts the amorphous region back into the layered structure. Subjecting cation-disordered rocksalt phases to heat treatment has shown to lead to the formation of layered structure in $LiTi_{0.5}MS_2$ (M = Fe^{2+}, Mn^{2+}, and Mg^{2+}).[256]

First-cycle Voltage Hysteresis

The voltage hysteresis in cycle 1 can be summarized in the following way. The charge cycle undergoes a two-phase reaction during which S oxidation occurs in the form of $(S_2)^{2-}$ in the bulk of the material. The discharge cycle proceeds by overreducing Ti in the bulk and leaving kinetically sluggish $(S_2)^{2-}$ in the structure which eventually converts into disordered, amorphous domains. In cycle 2, $Ti^{3+/4+}$ oxidation occurs first in the initial sloping region with low overpotentials followed by S oxidation, and the presence of disordered, amorphous domains lower the overall oxidation potential. The voltage hysteresis in $LiTi_{0.75}\square_{0.25}S_2$ stems from the asymmetry between charge and discharge pathways. Nonetheless, The voltage hysteresis is much less than in Li-rich oxides thanks to more facile kinetics of S redox compared to O redox. We also note that there are other possible causes of hysteresis that result in asymmetry between charge and discharge. For instance, Ti reduction may precede S reduction as it is more kinetically facile during cycle 1 discharge. Once Ti^{4+} is reduced to Ti^{3+}, ligand–metal charge transfer occurs which reduces S. In this case, the intermediate species – Ti^{3+} at early states of discharge – is not observed in *ex situ* spectroscopic techniques because the intermediate species has relaxed to the thermodynamically stable phases during sample preparation and transportation to synchrotron sources which takes 1 to 2 weeks. It is also possible that the ligand–metal charge transfer occurs at a much faster time scale than what *operando* synchrotron XANES can capture, in which case capturing the charge transfer would be extremely difficult.

7.5 Discussion

Lastly, we examine the relationship between first-cycle activation and hysteresis. Cycle 1 discharge is not the reversal of cycle 1 charge and proceeds via a different pathway causing voltage hysteresis. Specifically, surface amorphization occurs during discharge concurrent with Ti overreduction and residual oxidized S. In the subsequent cycle, while the $Ti^{3+/4+}$ redox is reversible with low overpotential, S oxidation occurs at lower voltages compared to cycle 1. We ascribe this to the presence of amorphous regions near the surface and the presence of oxidized S which alter the electronic structure of the material. The thermodynamic state can be restored by annealing the material which triggers ligand-metal charge transfer and structural reorganization. It is possible that most oxidized S at the end of cycle 1 resides in the amorphous region; S-S bonds have been shown to be stable and prevalent in the amorphous rock-salt phase as illustrated by Sakuda et al.[257] In this case, annealing triggers charge transfer by breaking S-S bonds in the amorphous region and recovering the structure. Another possibility is that $(S_2)^{2-}$ is trapped in the bulk of the material. However, *ex situ* sXRD of fully discharged $LiTi_{0.75}\square_{0.25}S_2$ indicates that the (104) reflection is very sharp suggesting very crystalline and ordered anion sublattice. Also, a high degree of lithiation is observed during discharge indicating that the cationic vacancies introduced during synthesis have been filled, eliminating the free space that allowed the distortions associated with persulfide formation. Therefore, we hypothesize that the former is occuring in $LiTi_{0.75}\square_{0.25}S_2$.

7.6 Conclusions

We explored the discharge mechanism of $LiTi_{0.75}\square_{0.25}S_2$ and used it as a model system to investigate first-cycle activation and voltage hysteresis. $LiTi_{0.75}\square_{0.25}S_2$ exhibits higher discharge capacity than charge capacity due to the intrinsic cationic vacancies and the ability of Ti^{4+} to act as a reduction center. While the material maintains the layered framework during charge throughout the particle, nanoscale structural changes are observed during discharge. Surface amorphization indicates that the discharge cycle undergoes a different pathway and thus explains the voltage hysteresis between cycle 1 charge and discharge. Because the resulting structure is different from the pristine state, the voltage profile of the anion oxidation region changes after cycle 1. Annealing cycled $LiTi_{0.75}\square_{0.25}S_2$ effectively recovers the thermodynamically stable phase by triggering ligand–metal charge transfer and structural organization. Unlike Li-rich oxides in which parasitic side reactions occur on the surface and in the bulk, Li-rich sulfides exhibit only surface effects and the bulk is largely unaffected. We highlight in this work the potential of Li-rich sulfides as high energy density cathode materials and the need for surface engineering to stabilize to improve the electrochemical performance of Li-rich sulfides.

7.A Supplementary Information

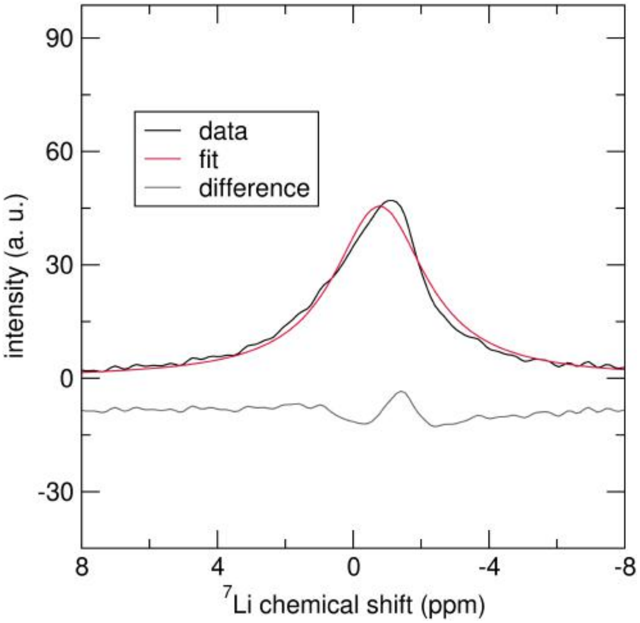

Figure 7.9: ^{7}Li MAS ssNMR spectrum of partially discharged LiTi$_{0.75}\square_{0.25}$S$_2$. The spectrum can no longer be fit to a single phase as highlighted by the difference curve. There is a shoulder at higher chemical shift.

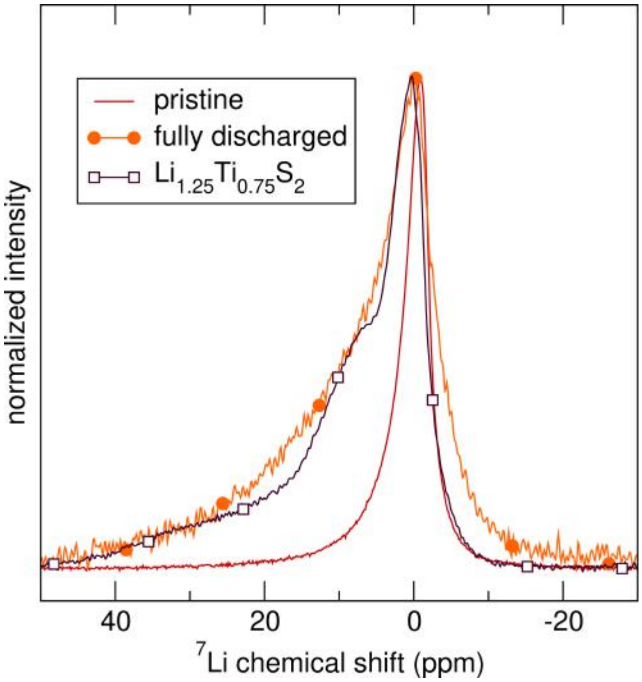

Figure 7.10: ^{7}Li MAS ssNMR spectra of pristine and fully discharged $LiTi_{0.75}\square_{0.25}S_2$ and Li1.25Ti0.75S2. The spectrum of fully discharged $LiTi_{0.75}\square_{0.25}S_2$ resembles that of Li1.25Ti0.75S2 with more broad features likely due to disordered Li environments compared to chemically synthesized Li1.25Ti0.75S2. The extensive broadening compared to the pristine state suggests paramagnetic broadening influenced by the presence of Ti3+.

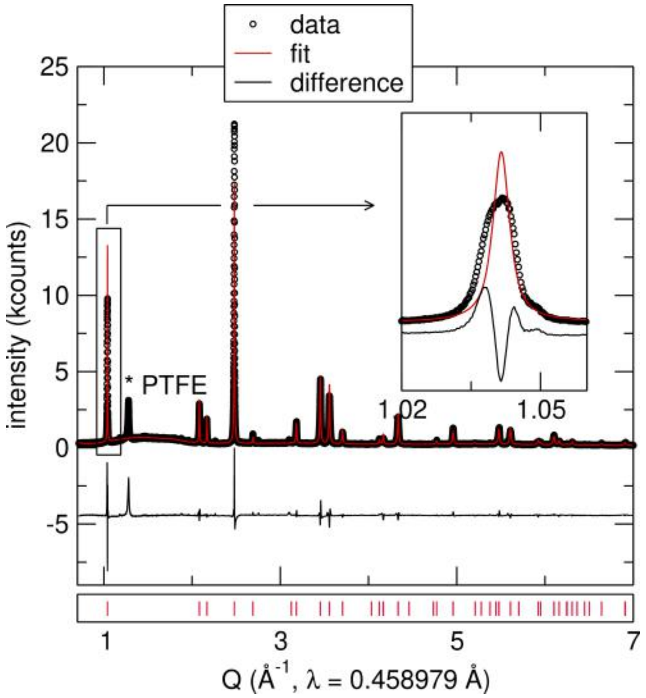

Figure 7.11: *Ex situ* sXRD patterns of full discharge $LiTi_{0.75}\square_{0.25}S_2$ fit to a single phase. While the rest of the reflections are unimodal and thus can be well described by one phase, the (003) reflection is bimodal and cannot be described by one single phase, necessitating a two-phase fit.

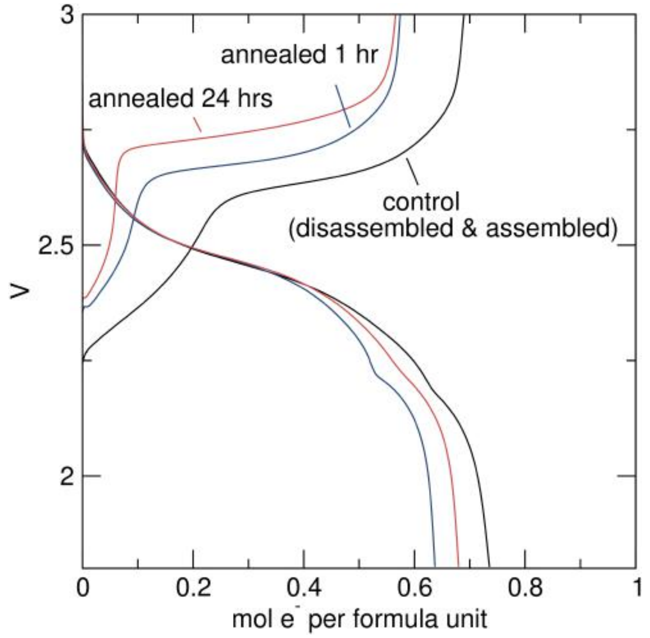

Figure 7.12: Galvanostatic cycling data of control, 1 hr annealed, and 24 hr annealed $LiTi_{0.75}\square_{0.25}S_2$. Control cell is prepared by running a normal cell for cycle 1, disassembling the cell, recovering the composite electrode, washing it with solvent, vacuum drying it, and making a new cell. Control cell is not heat treated. Annealing for 1 hr begins to show the recovery of the plateau but as much as the 24 hr annealed sample.

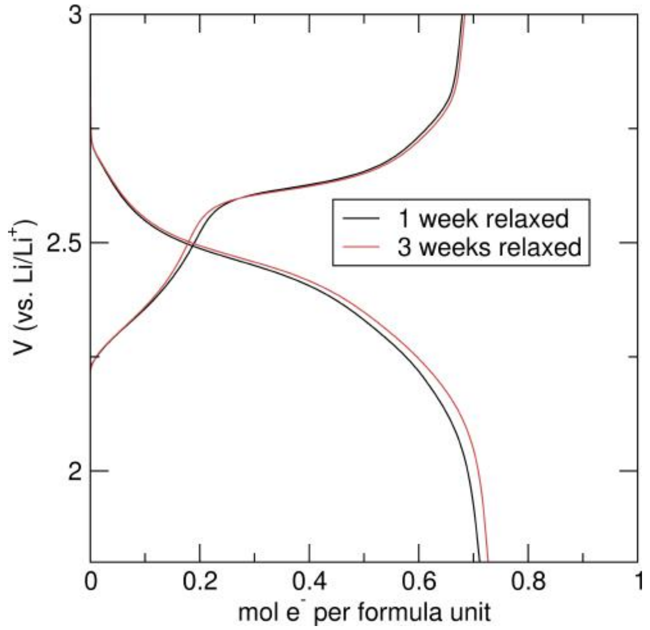

Figure 7.13: Cycle 2 of $LiTi_{0.75}\square_{0.25}S_2$ after relaxing for 1 week or 3 weeks. The voltage profile remains the same regardless of relaxation period after cycle 1, suggesting that heat treatment is necessary to recover the thermodynamic phase.

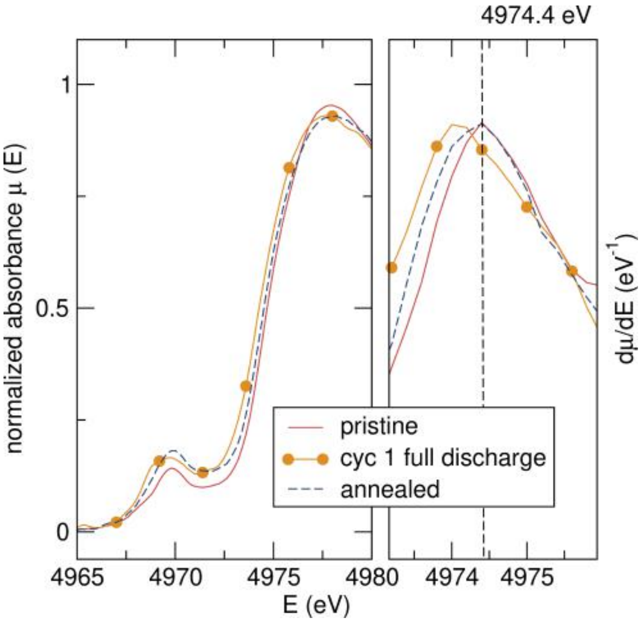

Figure 7.14: Ti XANES and the first derivatives of the rising edge of pristine, full discharge, and annealed $LiTi_{0.75}\square_{0.25}S_2$.

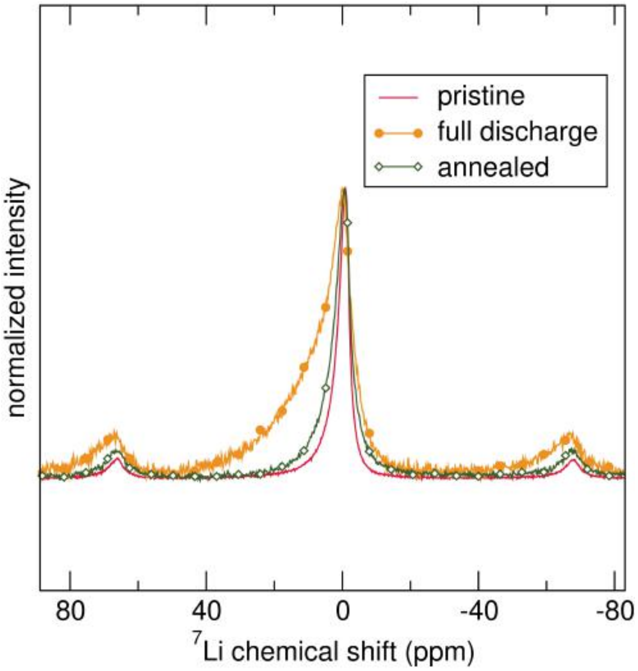

Figure 7.15: ^{7}Li MAS ssNMR spectra of pristine, full discharge, and annealed $LiTi_{0.75}\square_{0.25}S_2$. Upon annealing, the resonance becomes sharper, suggesting that paramagnetic broadening decreases significantly.

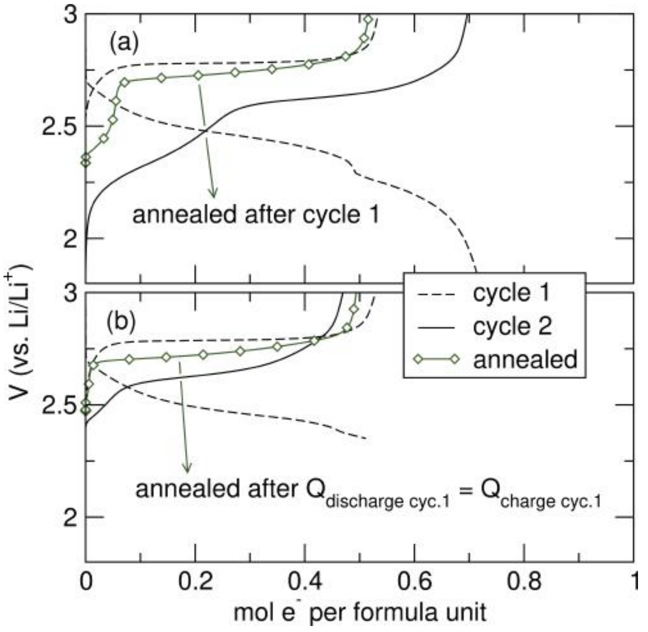

Figure 7.16: Galvanostatic cycling comparison of $\mathrm{LiTi}_{0.75}\square_{0.25}\mathrm{S}_2$ (a) cycled to 1.8 V during discharge and (b) cycled to $Q_{discharge} = Q_{charge}$. When cycled to $Q_{discharge} = Q_{charge}$, the subsequent charge cycle exhibits an initial sloping region and a plateau. When this material is annealed after $Q_{discharge} = Q_{charge}$, the initial sloping region disappears completely. and the plateau is recovered at a higher potential.

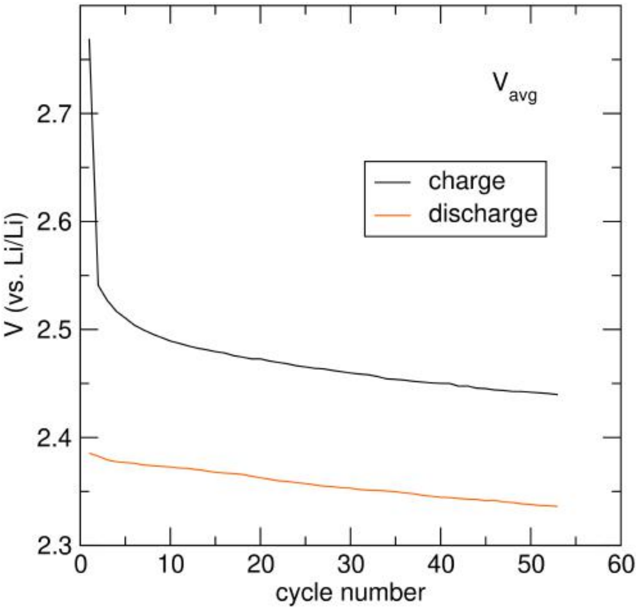

Figure 7.17: Average V of charge and discharge over 50 cycles. The average V in cycle 1 is higher because there is no Ti oxidation below 2.5 V.

Chapter 8

THESIS SUMMARY AND PERSPECTIVE

8.1 Thesis Summary

This thesis tackles two multi-electron systems–Mg electrolytes and Li-rich sulfide materials–to deepen our understanding of next-generation battery materials. In Chapters 2 and 3, I demonstrated that while MACC electrolyte requires electrolytic conditioning to activate the electrolyte, adding small amounts of $Mg(HMDS)_2$ into the electrolyte chemically activates the electrochemical behavior. Adding just 2 mM of $Mg(HMDS)_2$ suppresses Al^{3+} reduction and promotes Mg^{2+} electrodeposition and stripping. The fact that a small amount of $Mg(HMDS)_2$ drastically improves the electrochemical performance of the electrolyte indicates that changes in the electrolyte speciation are directly affecting structure of the electrode-electrolyte interface. With a multitude of solution-phase characterization techniques, I identified the reactions responsible for Al deposition suppression and increased reversibility of Mg deposition and stripping. First, $Mg(HMDS)_2$ scavenges trace levels of water present in the solution and prevents the formation of passive films on the Mg surface. Also, $Mg(HMDS)_2$ reacts with $AlCl_4^-$ to release Cl^- which is an important species that activates the Mg electrode-electrolyte interface. With these two papers, I highlighted the importance of activating the Mg electrode surface and the role of Cl^- in Mg charge transfer.

In Chapters 4 to 7, three different Li-rich sulfide materials were examined. In Chapter 4, we saw that transmission X-ray microscopy was performed on Li_2FeS_2 and $LiNaFeS_2$ to elucidate the root cause of the rapid capacity fade in $LiNaFeS_2$ and identified parallel particle fracturing to be the culprit. Although Li_2FeS_2 and $LiNaFeS_2$ exhibit the same spectroscopic behavior based on Fe and S XANES, $LiNaFeS_2$ exhibits particle fracturing due to high strain induced by the removal of bigger Na ions. This highlights that events across different length scales–from crystallographic changes from (de)lithiation to possible phase transformations and also changes in the particle morphology–must be taken considered with care when developing battery materials. Cryomilling $LiNaFeS_2$ decreases crystallite size and increases microstrain which successfully prevents particle fracturing and mitigates capacity fade. Increased defect density help accommodate strain associated with

Na removal in $LiNaFeS_2$. With a better understanding of differences between Li_2FeS_2 and $LiNaFeS_2$, transition metal substitution was done on $LiNaFeS_2$ to form $LiNaCoS_2$ to study the role of transition metal-anion covalency. pDOS comparison of $LiNaFeS_2$ and $LiNaCoS_2$ reveals that $Co^{2+/3+}$ d states are lower compared to $Fe^{2+/3+}$ d states and overlap more with the S p states. For this reason, while $Fe^{2+/3+}$ oxidation occurs first in $LiNaFeS_2$, S p states are access first during the two-phase reaction in $LiNaCoS_2$. It is still unclear why $LiNaFeS_2$ is able to maintain its structure and form S–S bonds at the same time while $LiNaCoS_2$ converts as soon as the material is oxidized. Based on the spectroscopic and structural characterization, we hypothesize that once S–S bonds are formed during charge, converting to CoS_2 is more stable than maintaining the parent phase. Once CoS_2 begins to form, the Li environment changes in $LiNaCoS_2$ and forms a structure similar to $Li_xCo_3S_4$. After full charge, the speciation actually resembles those of CoS_2 cycled between 1.6 and 3 V. It is also possible that the presence of Na stabilizes the structure and the removal of Na disrupts the structural stability and forces conversion. Unfortunately, partial substitution of Co for Fe did not improve electrochemistry as well.

Chapters 6 and 7 focus on $LiTi_{0.75}\square_{0.25}S_2$. Studying Li_2FeS_2 revealed that S–S bonds form in delithiated Li_2FeS_2 without changing the coordination environment of Fe, hinting at a mechanism that requires vacancies in the structure. The hypothesis for S–S bond formation became that a material needs to be able to support local distortions associated with dimer formation. To directly probe this hypothesis, we turned to Li_2TiS_3, a Li-rich sulfide material that does not exhibit any electrochemical activity due to the d^0 electron configuration of Ti^{4+} although S redox should be accessible from electronic structure perspective. By increasing the Ti^{4+} content in the material, intrinsic cationic vacancies are introduced by removing Li in the structure. Various characterization techniques confirmed the stoichiometry of $LiTi_{0.75}\square_{0.25}S_2$ and the presence of vacancies. Vacancy–containing $LiTi_{0.75}\square_{0.25}S_2$ exhibits 150 mAh g^{-1} with a plateau indicating that introducing cationic vacancies indeed activated S oxidation. By showing that S oxidation is possible by virtue of vacancy introduction and without transition metal oxidation, we revealed a crucial design rule for S oxidation in Li-rich materials. Because the charge cycle is not convoluted by both cation and anion oxidation, $LiTi_{0.75}\square_{0.25}S_2$ serves as a great candidate to study first-cycle activation and voltage hysteresis. Our results indicate that cycle 1 discharge is not the reversal of the charge pathway. Although S reduction is more thermodynamically favorable compared to $Ti^{4+/3+}$ reduction, Ti reduction is more kinetically facile than S reduction. Therefore, we end up with overreduced Ti and

S that is not fully reduced back to S^{2-}. Also, surface amorphization is observed during discharge as well. The voltage hysteresis therefore may be attributed to both of these phenomena together. These results suggest possible future research avenues to achieve more reversible anion redox in Li-rich sulfide materials.

8.2 Perspective

There have been advancements in our knowledge about charge compensation mechanisms in Li-rich cathode materials. For instance, Li-rich NMC materials undergo O_2 evolution from the surface, surface densification and phase transition into rock-salt/spinel phase, and both inter- and intra-layer transition metal migration in the bulk. Recent works have shown that although the oxidation of O^{2-} in the lattice introduces a high driving force for irreversible transition metal migration, structural treatments such as different stacking order or superstructure in the transition metal layer can prevent transition metal migration and reduce hysteresis. These works highlight the importance of understanding not just the electronic structure, but also physical structural changes to develop new materials.

Although the fundamental nature of sulfides differs from oxides, the same trend holds true. The key in metal sulfides is to leverage the stable TM-S-S coordination and achieve reversible anion redox. A major challenge for Li-rich sulfides is its anion redox potential. Most S oxidation occurs near 2.5 V vs Li/Li^+, so it is important to increase the thermodynamic redox potential of S. One way would be by designing oxysulfides whose p bands overlap. Another challenge that Li-rich sulfides face is surface amorphization and S dissolution. While surface anions in oxides lead to O_2 gas evolution at high voltages, those in sulfides can react with the electrolyte and lead to S dissolution. To that end, developing compatible electrolytes or pairing with solid-state electrolytes would be a viable avenue. Another fundamental question that Li-rich sulfides need to answer is an effective spectroscopic tool to capture the presence of persulfide ($(S2)^{2-}$). S XANES offers valuable information about S environments, but it does not always yield definitive evidence for persulfides. S XES K_β can be explored further with more experiments and DFT calculations to have a bigger pool of materials database. Also, many Li-rich sulfide materials exhibit low but apparent V_{eq} hysteresis of less than 100 mV. Developing a material that definitively exhibits hole chemistry of $S^{2-/n-}$ ($n < 2$) redox and comparing its V_{eq} hysteresis would offer insights about reversible anion redox in Li-rich sulfides. Lastly, there has been increasing reports of ligand–metal charge transfer during cycling in Li-rich materials. Capturing such a phenomenon with a *operando* spectroscopic technique would offer valuable information about the root cause of voltage hysteresis.

BIBLIOGRAPHY

(1) Berrang-Ford, L.; Ford, J. D.; Paterson, J. Are We Adapting to Climate Change? *Global Environmental Change* **2011**, *21*, 25–33.

(2) Hayhoe, K.; Wuebbles, D. J.; Easterling, D. R.; Fahey, D. W.; Doherty, S.; Kossin, J. P.; Sweet, W. V.; Vose, R. S.; Wehner, M. F. *Chapter 2 : Our Changing Climate. Impacts, Risks, and Adaptation in the United States: The Fourth National Climate Assessment, Volume II*; U.S. Global Change Research Program, 2018.

(3) Anderson, B. T.; Knight, J. R.; Ringer, M. A.; Yoon, J.-H.; Cherchi, A. Testing for the Possible Influence of Unknown Climate Forcings upon Global Temperature Increases from 1950 to 2000. *Journal of Climate* **2012**, *25*, 7163–7172.

(4) Fawzy, S.; Osman, A. I.; Doran, J.; Rooney, D. W. Strategies for Mitigation of Climate Change: A Review. *Environ Chem Lett* **2020**, *18*, 2069–2094.

(5) Armstrong, R. et al. The Future of Energy Storage. **2022**.

(6) Olabi, A. Renewable Energy and Energy Storage Systems. *Energy* **2017**, *136*, 1–6.

(7) Whittingham, M. S. Lithium Batteries: 50 Years of Advances to Address the Next 20 Years of Climate Issues. *Nano Lett.* **2020**, *20*, 8435–8437.

(8) Chen, T.; Jin, Y.; Lv, H.; Yang, A.; Liu, M.; Chen, B.; Xie, Y.; Chen, Q. Applications of Lithium-Ion Batteries in Grid-Scale Energy Storage Systems. *Trans. Tianjin Univ.* **2020**, *26*, 208–217.

(9) Winter, M.; Besenhard, J. O.; Spahr, M. E.; Novµk, P. Insertion Electrode Materials for Rechargeable Lithium Batteries. *Advanced Materials* **1999**, *10*, 725–763.

(10) Aurbach, D.; Levi, M. D.; Levi, E.; Teller, H.; Markovsky, B.; Salitra, G.; Heider, U.; Heider, L. Common Electroanalytical Behavior of Li Intercalation Processes into Graphite and Transition Metal Oxides. *J. Electrochem. Soc.* **1998**, *145*, 3024–3034.

(11) Nagaura, T.; Tozawa, K. Lithium Ion Rechargeable Battery. *Prog. Batteries Sol. Cells* **1990**, *9*, 209–217.

(12) Whittingham, M. S. Electrical Energy Storage and Intercalation Chemistry. *Science* **1976**, *192*, 1126–1127.

(13) Mizushima, K.; Jones, P.; Wiseman, P.; Goodenough, J. LixCoO2 (0. *Materials Research Bulletin* **1980**, *15*, 783–789.

(14) Manthiram, A. A Reflection on Lithium-Ion Battery Cathode Chemistry. *Nat Commun* **2020**, *11*, 1550.

(15) Amatucci, G. G.; Tarascon, J. M.; Klein, L. C. CoO_2, The End Member of the Li_x CoO_2 Solid Solution. *J. Electrochem. Soc.* **1996**, *143*, 1114–1123.

(16) Blomgren, G. E. The Development and Future of Lithium Ion Batteries. *J. Electrochem. Soc.* **2017**, *164*, A5019–A5025.

(17) Märker, K.; Reeves, P. J.; Xu, C.; Griffith, K. J.; Grey, C. P. Evolution of Structure and Lithium Dynamics in $LiNi_{0.8}Mn_{0.1}Co_{0.1}O_2$ (NMC811) Cathodes during Electrochemical Cycling. *Chem. Mater.* **2019**, *31*, 2545–2554.

(18) Chakraborty, A.; Kunnikuruvan, S.; Kumar, S.; Markovsky, B.; Aurbach, D.; Dixit, M.; Major, D. T. Layered Cathode Materials for Lithium-Ion Batteries: Review of Computational Studies on $LiNi_{1-x-y}Co_xMn_yO_2$ and $LiNi_{1-x-y}Co_xAl_yO_2$. *Chem. Mater.* **2020**, *32*, 915–952.

(19) Albertus, P. et al. Challenges for and Pathways toward Li-Metal-Based All-Solid-State Batteries. *ACS Energy Lett.* **2021**, 1399–1404.

(20) Tian, Y.; Zeng, G.; Rutt, A.; Shi, T.; Kim, H.; Wang, J.; Koettgen, J.; Sun, Y.; Ouyang, B.; Chen, T.; Lun, Z.; Rong, Z.; Persson, K.; Ceder, G. Promises and Challenges of Next-Generation “Beyond Li-ion” Batteries for Electric Vehicles and Grid Decarbonization. *Chem. Rev.* **2021**, *121*, 1623–1669.

(21) Lee, J.; Kitchaev, D. A.; Kwon, D.-H.; Lee, C.-W.; Papp, J. K.; Liu, Y.-S.; Lun, Z.; Clément, R. J.; Shi, T.; McCloskey, B. D.; Guo, J.; Balasubramanian, M.; Ceder, G. Reversible Mn^{2+}/Mn^{4+} Double Redox in Lithium-Excess Cathode Materials. *Nature* **2018**, *556*, 185–190.

(22) He, P.; Yan, M.; Liao, X.; Luo, Y.; Mai, L.; Nan, C.-W. Reversible V3+/V5+ Double Redox in Lithium Vanadium Oxide Cathode for Zinc Storage. *Energy Storage Materials* **2020**, *29*, 113–120.

(23) Nitta, N.; Wu, F.; Lee, J. T.; Yushin, G. Li-ion battery materials: present and future. *Materials Today* **2015**, *18*, 252–264.

(24) Aurbach, D.; Gofer, Y.; Lu, Z.; Schechter, A.; Chusid, O.; Gizbar, H.; Cohen, Y.; Ashkenazi, V.; Moshkovich, M.; Turgeman, R. A short review on the comparison between Li battery systems and rechargeable magnesium battery technology. *Journal of Power Sources* **2001**, *97-98*, 28–32.

(25) Doe, R. E.; Han, R.; Hwang, J.; Gmitter, A. J.; Shterenberg, I.; Yoo, H. D.; Pour, N.; Aurbach, D. Novel, electrolyte solutions comprising fully inorganic salts with high anodic stability for rechargeable magnesium batteries. *Chem. Commun.* **2014**, *50*, 243–245.

(26) Matsui, M. Study on electrochemically deposited Mg metal. *J. Power Sources* **2011**, *196*, 7048–7055.

(27) Davidson, R.; Verma, A.; Santos, D.; Hao, F.; Fincher, C.; Xiang, S.; Buskirk, J. V.; Xie, K.; Pharr, M.; Mukherjee, P. P.; Banerjee, S. Formation of Magnesium Dendrites during Electrodeposition. *ACS Energy Letters* **2019**, 375–376.

(28) Gaddum, L. W.; French, H. E. The Electrolysis of Grignard Solutions. *J. Am. Chem. Soc.* **1927**, *49*, 1295–1299.

(29) Overcash, D. M.; Mathers, F. C. The Electrodeposition of Magnesium. *Trans. Electrochem. Soc.* **1933**, *64*, 305–311.

(30) Evans, W. V.; Lee, F. H.; Lee, C. H. The Decomposition Voltage of Grignard Reagents in Ether Solution. **1935**, *57*, 489–490.

(31) Liebenow, C. Reversibility of electrochemical magnesium deposition from Grignard solutions. *Journal of Applied Electrochemistry* **1997**, *27*, 221–225.

(32) Gregory, T. D. Nonaqueous Electrochemistry of Magnesium. *J. Electrochem. Soc.* **1990**, *137*, 775.

(33) Aurbach, D.; Lu, Z.; Schechter, A.; Gofer, Y.; Gizbar, H.; Turgeman, R.; Cohen, Y.; Moshkovich, M.; Levi, E. Prototype systems for rechargeable magnesium batteries. *Nature* **2000**, *407*, 724–727.

(34) Mizrahi, O.; Amir, N.; Pollak, E.; Chusid, O.; Marks, V.; Gottlieb, H.; Larush, L.; Zinigrad, E.; Aurbach, D. Electrolyte Solutions with a Wide Electrochemical Window for Rechargeable Magnesium Batteries. *J. Electrochem. Soc.* **2008**, *155*, A103–A109.

(35) Mohtadi, R.; Matsui, M.; Arthur, T. S.; Hwang, S.-J. Magnesium Borohydride: From Hydrogen Storage to Magnesium Battery. *Angewandte Chemie International Edition* **2012**, *51*, 9780–9783.

(36) Keyzer, E. N.; Glass, H. F. J.; Liu, Z.; Bayley, P. M.; Dutton, S. E.; Grey, C. P.; Wright, D. S. Mg(PF6)2-Based Electrolyte Systems: Understanding Electrolyte–Electrode Interactions for the Development of Mg-Ion Batteries. *J. Am. Chem. Soc.* **2016**, *138*, 8682–8685.

(37) Lu, Z.; Schechter, A.; Moshkovich, M.; Aurbach, D. On the electrochemical behavior of magnesium electrodes in polar aprotic electrolyte solutions. *Journal of Electroanalytical Chemistry* **1999**, *466*, 203–217.

(38) Ha, S.-Y.; Lee, Y.-W.; Woo, S. W.; Koo, B.; Kim, J.-S.; Cho, J.; Lee, K. T.; Choi, N.-S. Magnesium(II) Bis(trifluoromethane sulfonyl) Imide-Based Electrolytes with Wide Electrochemical Windows for Rechargeable Magnesium Batteries. *ACS Appl. Mater. Interfaces* **2014**, *6*, 4063–4073.

(39) Baskin, A.; Prendergast, D. Exploration of the Detailed Conditions for Reductive Stability of Mg(TFSI)2 in Diglyme: Implications for Multivalent Electrolytes. *J. Phys. Chem. C* **2016**, *120*, 3583–3594.

(40) Carter, T. J.; Mohtadi, R.; Arthur, T. S.; Mizuno, F.; Zhang, R.; Shirai, S.; Kampf, J. W. Boron Clusters as Highly Stable Magnesium-Battery Electrolytes. *Angewandte Chemie International Edition* **2014**, *53*, 3173–3177.

(41) Tutusaus, O.; Mohtadi, R.; Arthur, T. S.; Mizuno, F.; Nelson, E. G.; Sevryugina, Y. V. An Efficient Halogen-Free Electrolyte for Use in Rechargeable Magnesium Batteries. *Angewandte Chemie International Edition* **2015**, *54*, 7900–7904.

(42) Zhao-Karger, Z.; Bardaji, M. E. G.; Fuhr, O.; Fichtner, M. A new class of non-corrosive, highly efficient electrolytes for rechargeable magnesium batteries. *J. Mater. Chem. A* **2017**, *5*, 10815–10820.

(43) Du, A.; Zhang, Z.; Qu, H.; Cui, Z.; Qiao, L.; Wang, L.; Chai, J.; Lu, T.; Dong, S.; Dong, T.; Xu, H.; Zhou, X.; Cui, G. An efficient organic magnesium borate-based electrolyte with non-nucleophilic characteristics for magnesium–sulfur battery. *Energy & Environmental Science* **2017**, *10*, 2616–2625.

(44) Zhao-Karger, Z.; Liu, R.; Dai, W.; Li, Z.; Diemant, T.; Vinayan, B. P.; Bonatto Minella, C.; Yu, X.; Manthiram, A.; Behm, R. J.; Ruben, M.; Fichtner, M. Toward Highly Reversible Magnesium–Sulfur Batteries with Efficient and Practical Mg[B(hfip)4]2 Electrolyte. *ACS Energy Lett.* **2018**, *3*, 2005–2013.

(45) Guo, Y.-s.; Zhang, F.; Yang, J.; Wang, F.-f.; NuLi, Y.; Hirano, S.-i. Boron-based electrolyte solutions with wide electrochemical windows for rechargeable magnesium batteries. *Energy Environ. Sci.* **2012**, *5*, 9100–9106.

(46) Zhang, Z.; Cui, Z.; Qiao, L.; Guan, J.; Xu, H.; Wang, X.; Hu, P.; Du, H.; Li, S.; Zhou, X.; Dong, S.; Liu, Z.; Cui, G.; Chen, L. Novel Design Concepts of Efficient Mg-Ion Electrolytes toward High-Performance Magnesium–Selenium and Magnesium–Sulfur Batteries. *Advanced Energy Materials* **2017**, *7*, 1602055.

(47) Xu, H.; Zhang, Z.; Cui, Z.; Du, A.; Lu, C.; Dong, S.; Ma, J.; Zhou, X.; Cui, G. Strong anion receptor-assisted boron-based Mg electrolyte with wide electrochemical window and non-nucleophilic characteristic. *Electrochemistry Communications* **2017**, *83*, 72–76.

(48) Xu, H.; Zhang, Z.; Li, J.; Qiao, L.; Lu, C.; Tang, K.; Dong, S.; Ma, J.; Liu, Y.; Zhou, X.; Cui, G. Multifunctional Additives Improve the Electrolyte Properties of Magnesium Borohydride Toward Magnesium–Sulfur Batteries. *ACS Appl. Mater. Interfaces* **2018**, *10*, 23757–23765.

(49) Liebenow, C.; Yang, Z.; Lobitz, P. The electrodeposition of magnesium using solutions of organomagnesium halides, amidomagnesium halides and magnesium organoborates. *Electrochemistry Communications* **2000**, *2*, 641–645.

(50) Kim, H. S.; Arthur, T. S.; Allred, G. D.; Zajicek, J.; Newman, J. G.; Rodnyansky, A. E.; Oliver, A. G.; Boggess, W. C.; Muldoon, J. Structure and compatibility of a magnesium electrolyte with a sulphur cathode. *Nature Communications* **2011**, *2*, 427.

(51) Zhao-Karger, Z.; Zhao, X.; Fuhr, O.; Fichtner, M. Bisamide based non-nucleophilic electrolytes for rechargeable magnesium batteries. *RSC Advances* **2013**, *3*, 16330.

(52) Zhao-Karger, Z.; Mueller, J. E.; Zhao, X.; Fuhr, O.; Jacob, T.; Fichtner, M. Novel transmetalation reaction for electrolyte synthesis for rechargeable magnesium batteries. *RSC Adv.* **2014**, *4*, 26924–26927.

(53) Zhao-Karger, Z.; Zhao, X.; Wang, D.; Diemant, T.; Behm, R. J.; Fichtner, M. Performance Improvement of Magnesium Sulfur Batteries with Modified Non-Nucleophilic Electrolytes. *Advanced Energy Materials* **2015**, *5*, 1401155.

(54) Merrill, L. C.; Schaefer, J. L. Electrochemical Properties and Speciation in Mg(HMDS)2-Based Electrolytes for Magnesium Batteries as a Function of Ethereal Solvent Type and Temperature. *Langmuir* **2017**, *33*, 9426–9433.

(55) Bieker, G.; Salama, M.; Kolek, M.; Gofer, Y.; Bieker, P.; Aurbach, D.; Winter, M. The Power of Stoichiometry: Conditioning and Speciation of $MgCl_2$ /$AlCl_3$ in Tetraethylene Glycol Dimethyl Ether-Based Electrolytes. *ACS Appl. Mater. Interfaces* **2019**, 24057–24066.

(56) Liao, C.; Sa, N.; Key, B.; Burrell, A. K.; Cheng, L.; Curtiss, L. A.; Vaughey, J. T.; Woo, J.-J.; Hu, L.; Pan, B.; Zhang, Z. The unexpected discovery of the Mg(HMDS) complex as a magnesium electrolyte for rechargeable magnesium batteries. *Journal of Materials Chemistry A* **2015**, *3*, 6082–6087.

(57) Merrill, L. C.; Schaefer, J. L. Conditioning – Free Electrolytes for Magnesium Batteries Using Sulfone – Ether Mixtures with Increased Thermal Stability. *Chem. Mater.*, *30*, 3971–3974.

(58) Barile, C. J.; Barile, E. C.; Zavadil, K. R.; Nuzzo, R. G.; Gewirth, A. A. Electrolytic Conditioning of a Magnesium Aluminum Chloride Complex for Reversible Magnesium Deposition. *J. Phys. Chem. C* **2014**, *118*, 27623–27630.

(59) See, K. A.; Chapman, K. W.; Zhu, L.; Wiaderek, K. M.; Borkiewicz, O. J.; Barile, C. J.; Chupas, P. J.; Gewirth, A. A. The Interplay of Al and Mg Speciation in Advanced Mg Battery Electrolyte Solutions. *J. Am. Chem. Soc.* **2016**, *138*, 328–337.

(60) Liu, T.; Shao, Y.; Li, G.; Gu, M.; Hu, J.; Xu, S.; Nie, Z.; Chen, X.; Wang, C.; Liu, J. A facile approach using $MgCl_2$ to formulate high performance Mg^{2+} electrolytes for rechargeable Mg batteries. *J. Mater. Chem. A* **2014**, *2*, 3430.

(61) See, K. A.; Liu, Y.-M.; Ha, Y.; Barile, C. J.; Gewirth, A. A. Effect of Concentration on the Electrochemistry and Speciation of the Magnesium Aluminum Chloride Complex Electrolyte Solution. *ACS Applied Materials & Interfaces* **2017**, *9*, 35729–35739.

(62) Luo, J.; He, S.; Liu, T. L. Tertiary Mg/$MgCl_2$/$AlCl_3$ Inorganic Mg^{2+} Electrolytes with Unprecedented Electrochemical Performance for Reversible Mg Deposition. *ACS Energy Lett.* **2017**, *2*, 1197–1202.

(63) Bevilacqua, S. C.; Pham, K. H.; See, K. A. Effect of the Electrolyte Solvent on Redox Processes in Mg–S Batteries. *Inorg. Chem.* **2019**, *58*, 10472–10482.

(64) Hoon Ha, J.; Adams, B.; Cho, J.-H.; Duffort, V.; Hak Kim, J.; Yoon Chung, K.; Won Cho, B.; F. Nazar, L.; Hyoung Oh, S. A conditioning-free magnesium chloride complex electrolyte for rechargeable magnesium batteries. *Journal of Materials Chemistry A* **2016**, *4*, 7160–7164.

(65) He, Y.; Li, Q.; Yang, L.; Yang, C.; Xu, D. Electrochemical-Conditioning-Free and Water-Resistant Hybrid $AlCl_3$/$MgCl_2$/$Mg(TFSI)_2$ Electrolytes for Rechargeable Magnesium Batteries. *Angewandte Chemie International Edition* **2019**, *58*, 7615–7619.

(66) Ta, K.; See, K. A.; Gewirth, A. A. Elucidating Zn and Mg Electrodeposition Mechanisms in Nonaqueous Electrolytes for Next-Generation Metal Batteries. *The Journal of Physical Chemistry C* **2018**, *122*, 13790–13796.

(67) Esbenshade, J. L.; Barile, C. J.; Fister, T. T.; Bassett, K. L.; Fenter, P.; Nuzzo, R. G.; Gewirth, A. A. Improving Electrodeposition of Mg through an Open Circuit Potential Hold. *J. Phys. Chem. C* **2015**, *119*, 23366–23372.

(68) Yamane, H.; Inoue, T.; Fujita, M.; Sano, M. A causal study of the capacity fading of $Li_{1.01}Mn_{1.99}O_4$ cathode at 80°C, and the suppressing substances of its fading. *Journal of Power Sources* **2001**, *99*, 60–65.

(69) Kang, S.-J.; Kim, H.; Hwang, S.; Jo, M.; Jang, M.; Park, C.; Hong, S.-T.; Lee, H. Electrolyte Additive Enabling Conditioning-Free Electrolytes for Magnesium Batteries. *ACS Applied Materials & Interfaces* **2019**, *11*, 517–524.

(70) Shterenberg, I.; Salama, M.; Yoo, H. D.; Gofer, Y.; Park, J.-B.; Sun, Y.-K.; Aurbach, D. Evaluation of $(CF_3SO_2)_2N$ (TFSI) Based Electrolyte Solutions for Mg Batteries. *J. Electrochem. Soc.* **2015**, *162*, A7118–A7128.

(71) Connell, J. G.; Genorio, B.; Lopes, P. P.; Strmcnik, D.; Stamenkovic, V. R.; Markovic, N. M. Tuning the Reversibility of Mg Anodes via Controlled Surface Passivation by H_2O/Cl^- in Organic Electrolytes. *Chem. Mater.* **2016**, *28*, 8268–8277.

(72) Wedepohl, K. H. The composition of the continental crust. 16.

(73) Choi, J. W.; Aurbach, D. Promise and Reality of Post-Lithium-Ion Batteries with High Energy Densities. *Nat Rev Mater* **2016**, *1*, 16013.

(74) Matsui, M. Study on Electrochemically Deposited Mg Metal. *J. Power Sources* **2011**, *196*, 7048–7055.

(75) Davidson, R.; Verma, A.; Santos, D.; Hao, F.; Fincher, C.; Xiang, S.; Buskirk, J. V.; Xie, K.; Pharr, M.; Mukherjee, P. P.; Banerjee, S. Formation of Magnesium Dendrites during Electrodeposition. *ACS Energy Lett.* **2019**, 375–376.

(76) Davidson, R. et al. Mapping Mechanisms and Growth Regimes of Magnesium Electrodeposition at High Current Densities. *Mater. Horiz.* **2020**, *7*, 843–854.

(77) McArthur, Scott. G.; Geng, L.; Guo, J.; Lavallo, V. Cation Reduction and Comproportionation as Novel Strategies to Produce High Voltage, Halide Free, Carborane Based Electrolytes for Rechargeable Mg Batteries. *Inorg. Chem. Front.* **2015**, *2*, 1101–1104.

(78) McArthur, S. G.; Jay, R.; Geng, L.; Guo, J.; Lavallo, V. Below the 12-Vertex: 10-Vertex Carborane Anions as Non-Corrosive, Halide Free, Electrolytes for Rechargeable Mg Batteries. *Chem. Commun.* **2017**, *53*, 4453–4456.

(79) Zhao-Karger, Z.; Bardaji, M. E. G.; Fuhr, O.; Fichtner, M. A New Class of Non-Corrosive, Highly Efficient Electrolytes for Rechargeable Magnesium Batteries. *Journal of Materials Chemistry A* **2017**, *5*, 10815–10820.

(80) Zhang, Z.; Cui, Z.; Qiao, L.; Guan, J.; Xu, H.; Wang, X.; Hu, P.; Du, H.; Li, S.; Zhou, X.; Dong, S.; Liu, Z.; Cui, G.; Chen, L. Novel Design Concepts of Efficient Mg-Ion Electrolytes toward High-Performance Magnesium–Selenium and Magnesium–Sulfur Batteries. *Advanced Energy Materials* **2017**, *7*, 1602055.

(81) Aurbach, D.; Gizbar, H.; Schechter, A.; Chusid, O.; Gottlieb, H. E.; Gofer, Y.; Goldberg, I. Electrolyte Solutions for Rechargeable Magnesium Batteries Based on Organomagnesium Chloroaluminate Complexes. *J. Electrochem. Soc.* **2002**, *149*, A115.

(82) Kim, H. S.; Arthur, T. S.; Allred, G. D.; Zajicek, J.; Newman, J. G.; Rodnyansky, A. E.; Oliver, A. G.; Boggess, W. C.; Muldoon, J. Structure and Compatibility of a Magnesium Electrolyte with a Sulphur Cathode. *Nat. Commun.* **2011**, *2*, DOI: `10.1038/ncomms1435`.

(83) Bieker, G.; Salama, M.; Kolek, M.; Gofer, Y.; Bieker, P.; Aurbach, D.; Winter, M. The Power of Stoichiometry: Conditioning and Speciation of $MgCl_2$ /$AlCl_3$ in Tetraethylene Glycol Dimethyl Ether-Based Electrolytes. *ACS Appl. Mater. Interfaces* **2019**, acsami.9b05307.

(84) Liao, C.; Sa, N.; Key, B.; Burrell, A. K.; Cheng, L.; Curtiss, L. A.; Vaughey, J. T.; Woo, J.-J.; Hu, L.; Pan, B.; Zhang, Z. The Unexpected Discovery of the Mg(HMDS) Complex as a Magnesium Electrolyte for Rechargeable Magnesium Batteries. *J. Mater. Chem. A* **2015**, *3*, 6082–6087.

(85) Doe, R. E.; Han, R.; Hwang, J.; Gmitter, A. J.; Shterenberg, I.; Yoo, H. D.; Pour, N.; Aurbach, D. Novel, Electrolyte Solutions Comprising Fully Inorganic Salts with High Anodic Stability for Rechargeable Magnesium Batteries. *Chem Commun* **2014**, *50*, 243–245.

(86) Carter, T. J.; Mohtadi, R.; Arthur, T. S.; Mizuno, F.; Zhang, R.; Shirai, S.; Kampf, J. W. Boron Clusters as Highly Stable Magnesium-Battery Electrolytes. *Angew. Chem. Int. Ed.* **2014**, *53*, 3173–3177.

(87) Huang, D.; Tan, S.; Li, M.; Wang, D.; Han, C.; An, Q.; Mai, L. Highly Efficient Non-Nucleophilic $Mg(CF_3SO_3)_2$-Based Electrolyte for High-Power Mg/S Battery. *ACS Appl. Mater. Interfaces* **2020**, *12*, 17474–17480.

(88) See, K. A.; Chapman, K. W.; Zhu, L.; Wiaderek, K. M.; Borkiewicz, O. J.; Barile, C. J.; Chupas, P. J.; Gewirth, A. A. The Interplay of Al and Mg Speciation in Advanced Mg Battery Electrolyte Solutions. *J. Am. Chem. Soc.* **2016**, *138*, 328–337.

(89) Liu, T.; Shao, Y.; Li, G.; Gu, M.; Hu, J.; Xu, S.; Nie, Z.; Chen, X.; Wang, C.; Liu, J. A Facile Approach Using MgCl2 to Formulate High Performance Mg2+ Electrolytes for Rechargeable Mg Batteries. *J. Mater. Chem. A* **2014**, *2*, 3430.

(90) Esbenshade, J. L.; Barile, C. J.; Fister, T. T.; Bassett, K. L.; Fenter, P.; Nuzzo, R. G.; Gewirth, A. A. Improving Electrodeposition of Mg through an Open Circuit Potential Hold. *J. Phys. Chem. C* **2015**, *119*, 23366–23372.

(91) Canepa, P.; Jayaraman, S.; Cheng, L.; Nidhi Rajput, N.; D. Richards, W.; Sai Gautam, G.; A. Curtiss, L.; A. Persson, K.; Ceder, G. Elucidating the Structure of the Magnesium Aluminum Chloride Complex Electrolyte for Magnesium-Ion Batteries. *Energy Environ. Sci.* **2015**, *8*, 3718–3730.

(92) Canepa, P.; Gautam, G. S.; Malik, R.; Jayaraman, S.; Rong, Z.; Zavadil, K. R.; Persson, K.; Ceder, G. Understanding the Initial Stages of Reversible Mg Deposition and Stripping in Inorganic Nonaqueous Electrolytes. *Chem. Mater.* **2015**, *27*, 3317–3325.

(93) Benmayza, A.; Ramanathan, M.; Arthur, T. S.; Matsui, M.; Mizuno, F.; Guo, J.; Glans, P.-A.; Prakash, J. Effect of Electrolytic Properties of a Magnesium Organohaloaluminate Electrolyte on Magnesium Deposition. *J. Phys. Chem. C* **2013**, *117*, 26881–26888.

(94) Ta, K.; See, K. A.; Gewirth, A. A. Elucidating Zn and Mg Electrodeposition Mechanisms in Nonaqueous Electrolytes for Next-Generation Metal Batteries. *J. Phys. Chem. C* **2018**, *122*, 13790–13796.

(95) Muldoon, J.; Bucur, C. B.; Oliver, A. G.; Zajicek, J.; Allred, G. D.; Boggess, W. C. Corrosion of Magnesium Electrolytes: Chlorides – the Culprit. *Energy Environ. Sci.* **2013**, *6*, 482–487.

(96) Kim, S. S.; Bevilacqua, S. C.; See, K. A. Conditioning-Free Mg Electrolyte by the Minor Addition of Mg(HMDS) $_2$. *ACS Appl. Mater. Interfaces* **2020**, *12*, 5226–5233.

(97) Thiry, P. A.; Ghijsen, J.; Sporken, R.; Pireaux, J. J.; Johnson, R. L.; Caudano, R. Incipient Oxidation of Magnesium: A High-Resolution Electron-Energy-Loss and Photoemission Study. *Phys. Rev. B* **1989**, *39*, 3620–3631.

(98) He, S.; Luo, J.; Leo Liu, T. MgCl 2 /AlCl 3 Electrolytes for Reversible Mg Deposition/Stripping: Electrochemical Conditioning or Not? *J. Mater. Chem. A* **2017**, *5*, 12718–12722.

(99) Kang, S.-J.; Kim, H.; Hwang, S.; Jo, M.; Jang, M.; Park, C.; Hong, S.-T.; Lee, H. Electrolyte Additive Enabling Conditioning-Free Electrolytes for Magnesium Batteries. *ACS Appl. Mater. Interfaces* **2019**, *11*, 517–524.

(100) Shterenberg, I.; Salama, M.; Yoo, H. D.; Gofer, Y.; Park, J.-B.; Sun, Y.-K.; Aurbach, D. Evaluation of (CF $_3$ SO $_2$) $_2$ N (TFSI) Based Electrolyte Solutions for Mg Batteries. *J. Electrochem. Soc.* **2015**, *162*, A7118–A7128.

(101) Luo, J.; He, S.; Liu, T. L. Tertiary Mg/MgCl2/AlCl3 Inorganic Mg2+ Electrolytes with Unprecedented Electrochemical Performance for Reversible Mg Deposition. *ACS Energy Lett.* **2017**, *2*, 1197–1202.

(102) Yamane, H.; Inoue, T.; Fujita, M.; Sano, M. A Causal Study of the Capacity Fading of Li1.01Mn1.99O4 Cathode at 80°C, and the Suppressing Substances of Its Fading. *Journal of Power Sources* **2001**, *99*, 60–65.

(103) Fulmer, G. R.; Miller, A. J. M.; Sherden, N. H.; Gottlieb, H. E.; Nudelman, A.; Stoltz, B. M.; Bercaw, J. E.; Goldberg, K. I. NMR Chemical Shifts of Trace Impurities: Common Laboratory Solvents, Organics, and Gases in Deuterated Solvents Relevant to the Organometallic Chemist. *Organometallics* **2010**, *29*, 2176–2179.

(104) See, K. A.; Liu, Y.-M.; Ha, Y.; Barile, C. J.; Gewirth, A. A. Effect of Concentration on the Electrochemistry and Speciation of the Magnesium Aluminum Chloride Complex Electrolyte Solution. *ACS Appl. Mater. Interfaces* **2017**, *9*, 35729–35739.

(105) Pour, N.; Gofer, Y.; Major, D. T.; Aurbach, D. Structural Analysis of Electrolyte Solutions for Rechargeable Mg Batteries by Stereoscopic Means and DFT Calculations. *J. Am. Chem. Soc.* **2011**, *133*, 6270–6278.

(106) Alves, C. C.; Campos, T. B.; Alves, W. A. FT-Raman Spectroscopic Analysis of the Most Probable Structures in Aluminum Chloride and Tetrahydrofuran Solutions. *Spectrochimica Acta Part A: Molecular and Biomolecular Spectroscopy* **2012**, *97*, 1085–1088.

(107) Robinson, E. A.; Hamada, K. The Vibrational Spectra and Structures of Hexachlorodisilazane and Hexamethyldisilazane. *Sci Bull Fac Educ* **1972**, *23*, 69–73.

(108) Gallinella, E.; Cadiolia, B.; Pierre Flament, J.; Berthier, G. A Scaled Force Field for Tetrahydrofuran and Its Isotopomers from Quantum Mechanical Calculations and Infrared and Raman Spectra. *Journal of Molecular Structure: THEOCHEM* **1994**, *315*, 137–148.

(109) Cadioli, B.; Gallinella, E.; Coulombeau, C.; Jobic, H.; Berthier, G. Geometric Structure and Vibrational Spectrum of Tetrahydrofuran. *J. Phys. Chem.* **1993**, *97*, 7844–7856.

(110) Derouault, J.; Granger, P.; Forel, M. T. Spectroscopic Investigation of Aluminum Trihalides-Tetrahydrofuran Complexes. 2. Solutions of Aluminum Chloride or Bromide in Tetrahydrofuran and in (Tetrahydrofuran-Dichloromethane). *Inorg. Chem.* **1977**, *16*, 3214–3218.

(111) Kitada, A.; Nakamura, K.; Fukami, K.; Murase, K. Electrochemically Active Species in Aluminum Electrodeposition Baths of AlCl 3 /Glyme Solutions. *Electrochimica Acta* **2016**, *211*, 561–567.

(112) Akiit, W. Multinuclear Studies of Aluminum Compounds. *Prog. NMR Spectrosc.* **1989**, *21*, 1–149.

(113) Nöth, H.; Rurländer, R.; Wolfgardt, P. An Investigation of AlCl3 Solutions in Ethers by 27Al NMR Spectroscopy. *Z. Für Naturforschung B J. Chem. Sci.* **1982**, *37*, 29–37.

(114) Lefebvre, M. C.; Conway, B. E. 27Al NMR Spectroscopy Studies on Speciation of Al Complex Ions in AlCl3 q LiAlH 4 Solutions in Tetrahydrofuran for Electroplating of Al. **1998**, 11.

(115) Benn, R.; Rufińska, A.; Lehmkuhl, H.; Janssen, E.; Krüger, C. ^{27} AI-NMR Spectroscopy: A Probe for Three-, Four-, Five-, and Sixfold Coordinated Al Atoms in Organoaluminum Compounds. *Angew. Chem. Int. Ed. Engl.* **1983**, *22*, 779–780.

(116) Černý, Z.; Macháček, J.; Fusek, J.; Čásenský, B.; Křiž, O.; Tuck, D. G. 27Al NMR Studies of the Hydrolysis of Aluminium(III) Chloride in Non-Aqueous Media. *Inorganica Chimica Acta* **2000**, *300-302*, 556–564.

(117) Connell, J. G.; Genorio, B.; Lopes, P. P.; Strmcnik, D.; Stamenkovic, V. R.; Markovic, N. M. Tuning the Reversibility of Mg Anodes via Controlled Surface Passivation by H $_2$ O/Cl $^-$ in Organic Electrolytes. *Chem. Mater.* **2016**, *28*, 8268–8277.

(118) Whittingham, M. S. Lithium Batteries and Cathode Materials. *Chem. Rev.* **2004**, *104*, 4271–4302.

(119) Liang, Y.; Zhao, C.-Z.; Yuan, H.; Chen, Y.; Zhang, W.; Huang, J.-Q.; Yu, D.; Liu, Y.; Titirici, M.-M.; Chueh, Y.-L.; Yu, H.; Zhang, Q. A Review of Rechargeable Batteries for Portable Electronic Devices. *InfoMat* **2019**, *1*, 6–32.

(120) Assat, G.; Tarascon, J.-M. Fundamental Understanding and Practical Challenges of Anionic Redox Activity in Li-ion Batteries. *Nat Energy* **2018**, *3*, 373–386.

(121) Hy, S.; Felix, F.; Rick, J.; Su, W.-N.; Hwang, B. J. Direct *In Situ* Observation of Li_2O Evolution on Li-Rich High-Capacity Cathode Material, $Li[Ni_xLi_{1-2x/3}Mn_{(2-x)/3}]O_2$ ($0 \le x \le 0.5$). *J. Am. Chem. Soc.* **2014**, *136*, 999–1007.

(122) Luo, K.; Roberts, M. R.; Hao, R.; Guerrini, N.; Pickup, D. M.; Liu, Y.-S.; Edström, K.; Guo, J.; Chadwick, A. V.; Duda, L. C.; Bruce, P. G. Charge-Compensation in 3d-Transition-Metal-Oxide Intercalation Cathodes through the Generation of Localized Electron Holes on Oxygen. *Nature Chem* **2016**, *8*, 684–691.

(123) Luo, K.; Roberts, M. R.; Guerrini, N.; Tapia-Ruiz, N.; Hao, R.; Massel, F.; Pickup, D. M.; Ramos, S.; Liu, Y.-S.; Guo, J.; Chadwick, A. V.; Duda, L. C.; Bruce, P. G. Anion Redox Chemistry in the Cobalt Free 3d Transition Metal Oxide Intercalation Electrode $Li[Li_{0.2}Ni_{0.2}Mn_{0.6}]O_2$. *J. Am. Chem. Soc.* **2016**, *138*, 11211–11218.

(124) Renfrew, S. E.; McCloskey, B. D. Residual Lithium Carbonate Predominantly Accounts for First Cycle CO_2 and CO Outgassing of Li-Stoichiometric and Li-Rich Layered Transition-Metal Oxides. *J. Am. Chem. Soc.* **2017**, *139*, 17853–17860.

(125) Kaufman, L. A.; McCloskey, B. D. Surface Lithium Carbonate Influences Electrolyte Degradation via Reactive Oxygen Attack in Lithium-Excess Cathode Materials. *Chem. Mater.* **2021**, *33*, 4170–4176.

(126) Rana, J.; Papp, J. K.; Lebens-Higgins, Z.; Zuba, M.; Kaufman, L. A.; Goel, A.; Schmuch, R.; Winter, M.; Whittingham, M. S.; Yang, W.; McCloskey, B. D.; Piper, L. F. J. Quantifying the Capacity Contributions during Activation of Li_2MnO_3. *ACS Energy Lett.* **2020**, *5*, 634–641.

(127) Sathiya, M.; Rousse, G.; Ramesha, K.; Laisa, C. P.; Vezin, H.; Sougrati, M. T.; Doublet, M.-L.; Foix, D.; Gonbeau, D.; Walker, W.; Prakash, A. S.; Ben Hassine, M.; Dupont, L.; Tarascon, J.-M. Reversible Anionic Redox Chemistry in High-Capacity Layered-Oxide Electrodes. *Nature Mater* **2013**, *12*, 827–835.

(128) Sathiya, M.; Abakumov, A. M.; Foix, D.; Rousse, G.; Ramesha, K.; Saubanère, M.; Doublet, M. L.; Vezin, H.; Laisa, C. P.; Prakash, A. S.; Gonbeau, D.; VanTendeloo, G.; Tarascon, J.-M. Origin of Voltage Decay in High-Capacity Layered Oxide Electrodes. *Nature Mater* **2015**, *14*, 230–238.

(129) Zhang, X.; Shyy, W.; Marie Sastry, A. Numerical Simulation of Intercalation-Induced Stress in Li-Ion Battery Electrode Particles. *J. Electrochem. Soc.* **2007**, *154*, A910.

(130) Kondrakov, A. O.; Schmidt, A.; Xu, J.; Geßwein, H.; Mönig, R.; Hartmann, P.; Sommer, H.; Brezesinski, T.; Janek, J. Anisotropic Lattice Strain and Mechanical Degradation of High- and Low-Nickel NCM Cathode Materials for Li-Ion Batteries. *J. Phys. Chem. C* **2017**, *121*, 3286–3294.

(131) Hansen, C. J.; Zak, J. J.; Martinolich, A. J.; Ko, J. S.; Bashian, N. H.; Kaboudvand, F.; Van der Ven, A.; Melot, B. C.; Nelson Weker, J.; See, K. A. Multielectron, Cation and Anion Redox in Lithium-Rich Iron Sulfide Cathodes. *J. Am. Chem. Soc.* **2020**, *142*, 6737–6749.

(132) Witkin, D.; Lavernia, E. Synthesis and Mechanical Behavior of Nanostructured Materials via Cryomilling. *Progress in Materials Science* **2006**, *51*, 1–60.

(133) Song, X.; Valset, K.; Graff, J.; Thøgersen, A.; Gunnæs, A.; Luxsacumar, S.; Løvvik, O.; Snyder, G.; Finstad, T. Nanostructuring of Undoped ZnSb by Cryo-Milling. *Journal of Elec. Materi.* **2015**, *44*, 2578–2584.

(134) Kumar, N.; Biswas, K. Cryomilling: An Environment Friendly Approach of Preparation Large Quantity Ultra Refined Pure Aluminium Nanoparticles. *J. Mater. Res. Technol.* **2019**, *8*, 63–74.

(135) Yan, Q.; Ko, S.-T.; Zhao, Y.; Whang, G.; Dawson, A.; Tolbert, S. H.; Dunn, B. S.; Luo, J. Cryogenic Milling Method to Fabricate Nanostructured Anodes. *ACS Appl. Energy Mater.* **2020**, 11285–11292.

(136) Xun, Y.; Mohamed, F. A.; Lavernia, E. J. Synthesis of Nanocrystalline Zn-22 Pct Al Using Cryomilling. *Metall and Mat Trans A* **2004**, *35*, 573–581.

(137) Nelson, J.; Misra, S.; Yang, Y.; Jackson, A.; Liu, Y.; Wang, H.; Dai, H.; Andrews, J. C.; Cui, Y.; Toney, M. F. In Operando X-ray Diffraction and Transmission X-ray Microscopy of Lithium Sulfur Batteries. *J. Am. Chem. Soc.* **2012**, *134*, 6337–6343.

(138) Liu, Y.; Meirer, F.; Wang, J.; Requena, G.; Williams, P.; Nelson, J.; Mehta, A.; Andrews, J. C.; Pianetta, P. 3D Elemental Sensitive Imaging Using Transmission X-ray Microscopy. *Anal Bioanal Chem* **2012**, *404*, 1297–1301.

(139) Weker, J. N.; Liu, N.; Misra, S.; Andrews, J. C.; Cui, Y.; Toney, M. F. Insitu Nanotomography and Operando Transmission X-ray Microscopy of Micron-Sized Ge Particles. *Energy Environ. Sci.* **2014**, *7*, 2771–2777.

(140) Cook, J. B.; Lin, T. C.; Detsi, E.; Weker, J. N.; Tolbert, S. H. Using X-ray Microscopy To Understand How Nanoporous Materials Can Be Used To Reduce the Large Volume Change in Alloy Anodes. *Nano Lett.* **2017**, *17*, 870–877.

(141) Lin, T. C.; Dawson, A.; King, S. C.; Yan, Y.; Ashby, D. S.; Mazzetti, J. A.; Dunn, B. S.; Weker, J. N.; Tolbert, S. H. Understanding Stabilization in Nanoporous Intermetallic Alloy Anodes for Li-Ion Batteries Using *Operando* Transmission X-ray Microscopy. *ACS Nano* **2020**, *14*, 14820–14830.

(142) Nelson Weker, J.; Wise, A. M.; Lim, K.; Shyam, B.; Toney, M. F. Operando Spectroscopic Microscopy of $LiCoO_2$ Cathodes Outside Standard Operating Potentials. *Electrochimica Acta* **2017**, *247*, 977–982.

(143) Xu, Y.; Hu, E.; Zhang, K.; Wang, X.; Borzenets, V.; Sun, Z.; Pianetta, P.; Yu, X.; Liu, Y.; Yang, X.-Q.; Li, H. In Situ Visualization of State-of-Charge Heterogeneity within a LiCoO $_2$ Particle That Evolves upon Cycling at Different Rates. *ACS Energy Lett.* **2017**, *2*, 1240–1245.

(144) Toby, B. H.; Von Dreele, R. B. *GSAS-II* : The Genesis of a Modern Open-Source All Purpose Crystallography Software Package. *J. Appl. Crystallogr.* **2013**, *46*, 544–549.

(145) Williamson, G.; Hall, W. X-Ray Line Broadening from Filed Aluminium and Wolfram. *Acta Metallurgica* **1953**, *1*, 22–31.

(146) Su, X.; Wu, Q.; Li, J.; Xiao, X.; Lott, A.; Lu, W.; Sheldon, B. W.; Wu, J. Silicon-Based Nanomaterials for Lithium-Ion Batteries: A Review. *Adv. Energy Mater.* **2014**, *4*, 1300882.

(147) Zhang, M.; Li, Y.; Wu, F.; Bai, Y.; Wu, C. Boost Sodium-Ion Batteries to Commercialization: Strategies to Enhance Initial Coulombic Efficiency of Hard Carbon Anode. *Nano Energy* **2021**, *82*, 105738.

(148) Xu, G.; Hao, F.; Weng, M.; Hong, J.; Pan, F.; Fang, D. Strong Influence of Strain Gradient on Lithium Diffusion: Flexo-Diffusion Effect. *Nanoscale* **2020**, *12*, 15175–15184.

(149) Abbasi, A.; Mirhabibi, A.; Arabi, H.; Golmohammad, M.; Brydson, R. Synthesis, Characterization and Electrochemical Performances of γ-Fe_22O_3 Cathode Material for Li-ion Batteries. *J Mater Sci: Mater Electron* **2016**, *27*, 7953–7961.

(150) Rolison, D. R.; Long, J. W.; Lytle, J. C.; Fischer, A. E.; Rhodes, C. P.; McEvoy, T. M.; Bourg, M. E.; Lubers, A. M. Multifunctional 3D Nanoarchitectures for Energy Storage and Conversion. *Chem. Soc. Rev.* **2009**, *38*, 226–252.

(151) Oakes, L.; Carter, R.; Pint, C. L. Nanoscale Defect Engineering of Lithium Sulfur Battery Composite Cathodes for Improved Performance. *Nanoscale* **2016**, *8*, 19368–19375.

(152) Gu, M.; He, Y.; Zheng, J.; Wang, C. Nanoscale Silicon as Anode for Li-ion Batteries: The Fundamentals, Promises, and Challenges. *Nano Energy* **2015**, *17*, 366–383.

(153) Zeng, X.; Li, M.; Abd El-Hady, D.; Alshitari, W.; Al-Bogami, A. S.; Lu, J.; Amine, K. Commercialization of Lithium Battery Technologies for Electric Vehicles. *Adv. Energy Mater.* **2019**, *9*, 1900161.

(154) Fichtner, M. Recent Research and Progress in Batteries for Electric Vehicles. *Batteries & Supercaps* **2022**, DOI: `10.1002/batt.202100224`.

(155) Radin, M. D.; Hy, S.; Sina, M.; Fang, C.; Liu, H.; Vinckeviciute, J.; Zhang, M.; Whittingham, M. S.; Meng, Y. S.; Van der Ven, A. Narrowing the Gap between Theoretical and Practical Capacities in Li-Ion Layered Oxide Cathode Materials. *Adv. Energy Mater.* **2017**, *7*, 1602888.

(156) Assat, G.; Tarascon, J.-M. Fundamental Understanding and Practical Challenges of Anionic Redox Activity in Li-Ion Batteries. *Nat. Energy* **2018**, 1.

(157) House, R. A.; Rees, G. J.; Pérez-Osorio, M. A.; Marie, J.-J.; Boivin, E.; Robertson, A. W.; Nag, A.; Garcia-Fernandez, M.; Zhou, K.-J.; Bruce, P. G. First-Cycle Voltage Hysteresis in Li-rich 3d Cathodes Associated with Molecular O_2 Trapped in the Bulk. *Nat Energy* **2020**, *5*, 777–785.

(158) House, R. A.; Maitra, U.; Pérez-Osorio, M. A.; Lozano, J. G.; Jin, L.; Somerville, J. W.; Duda, L. C.; Nag, A.; Walters, A.; Zhou, K.-J.; Roberts, M. R.; Bruce, P. G. Hysteresis: Honeycomb vs Riboon Superstructure. Superstructure Control of First-Cycle Voltage Hysteresis in Oxygen-Redox Cathodes. *Nature* **2020**, *577*, 502–508.

(159) House, R. A.; Rees, G. J.; McColl, K.; Marie, J.-J.; Garcia-Fernandez, M.; Nag, A.; Zhou, K.-J.; Cassidy, S.; Morgan, B. J.; Saiful Islam, M.; Bruce, P. G. Delocalized Electron Holes on Oxygen in a Battery Cathode. *Nat. Energy* **2023**, *8*, 351–360.

(160) McColl, K.; House, R. A.; Rees, G. J.; Squires, A. G.; Coles, S. W.; Bruce, P. G.; Morgan, B. J.; Islam, M. S. Kit's Paper on TM Migration on O2 Formation in Hysteresis of Disordered Rock Salt. *Nat Commun* **2022**, *13*, 5275.

(161) Zak, J. J.; Kim, S. S.; Laskowski, F. A. L.; See, K. A. An Exploration of Sulfur Redox in Lithium Battery Cathodes. *J. Am. Chem. Soc.* **2022**, *144*, 10119–10132.

(162) Rouxel, J. TM-anion Redox by Rouxel in 1996. *Chem. Eur. J.* **1996**, *2*, 1053–1059.

(163) Saha, S.; Assat, G.; Sougrati, M. T.; Foix, D.; Li, H.; Vergnet, J.; Turi, S.; Ha, Y.; Yang, W.; Cabana, J.; Rousse, G.; Abakumov, A. M.; Tarascon, J.-M. Exploring the Bottlenecks of Anionic Redox in Li-Rich Layered Sulfides. *Nat Energy* **2019**, *4*, 977–987.

(164) Kitchaev, D. A.; Vinckeviciute, J.; Van der Ven, A. Delocalized Metal–Oxygen -Redox Is the Origin of Anomalous Nonhysteretic Capacity in Li-Ion and Na-Ion Cathode Materials. *J. Am. Chem. Soc.* **2021**, *143*, 1908–1916.

(165) Flamary-Mespoulie, F.; Boulineau, A.; Martinez, H.; Suchomel, M. R.; Delmas, C.; Pecquenard, B.; Le Cras, F. Flamary - Li1.25Ti0.75S2. *Energy Storage Materials* **2020**, *26*, 213–222.

(166) Li, B.; Jiang, N.; Huang, W.; Yan, H.; Zuo, Y.; Xia, D. In Li, B. *Studies on Anionic Redox in Li-Rich Cathode Materials of Li-Ion Batteries*; Springer Singapore: Singapore, 2019, pp 99–121.

(167) Leube, B. T.; Robert, C.; Foix, D.; Porcheron, B.; Dedryvère, R.; Rousse, G.; Salager, E.; Cabelguen, P.-E.; Abakumov, A. M.; Vezin, H.; Doublet, M.-L.; Tarascon, J.-M. Activation of Anionic Redox in D0 Transition Metal Chalcogenides by Anion Doping. *Nat Commun* **2021**, *12*, 5485.

(168) Mohamed, M. A. A.; Gorbunov, M. V.; Valldor, M.; Hampel, S.; Gräßler, N.; Mikhailova, D. Tuning the Electrochemical Properties by Anionic Substitution of Li-rich Antiperovskite (Li$_2$Fe)S$_{1x}$Se$_x$O Cathodes for Li-ion Batteries. *J. Mater. Chem. A* **2021**, *9*, 23095–23105.

(169) Lai, K. T.; Antonyshyn, I.; Prots, Y.; Valldor, M. *Anti* -Perovskite Li-Battery Cathode Materials. *J. Am. Chem. Soc.* **2017**, *139*, 9645–9649.

(170) Mikhailova, D.; Giebeler, L.; Maletti, S.; Oswald, S.; Sarapulova, A.; Indris, S.; Hu, Z.; Bednarcik, J.; Valldor, M. Operando Studies of Antiperovskite Lithium Battery Cathode Material (Li$_2$Fe)SO. *ACS Appl. Energy Mater.* **2018**, *1*, 6593–6599.

(171) Gorbunov, M. V.; Carocci, S.; Gonzalez Martinez, I. G.; Baran, V.; Mikhailova, D. Studies of Li$_2$Fe0.9M0.1SO Antiperovskite Materials for Lithium–Ion Batteries: The Role of Partial Fe^{2+} to M^{2+} Substitution. *Front. Energy Res.* **2021**, *9*, 657962.

(172) Kim, Y.; Goodenough, J. B. Lithium Insertion into Transition-Metal Monosulfides: Tuning the Position of the Metal 4s Band. *J. Phys. Chem. C* **2008**, *112*, 15060–15064.

(173) Hansen, C. J.; Zak, J. J.; Martinolich, A. J.; Ko, J. S.; Bashian, N. H.; Kaboudvand, F.; Van der Ven, A.; Melot, B. C.; Nelson Weker, J.; See, K. A. Multielectron, Cation and Anion Redox in Lithium-Rich Iron Sulfide Cathodes. *J. Am. Chem. Soc.* **2020**, *142*, 6737–6749.

(174) Momma, K.; Izumi, F. *VESTA 3* for Three-Dimensional Visualization of Crystal, Volumetric and Morphology Data. *J. Appl. Crystallogr.* **2011**, *44*, 1272–1276.

(175) Wang, J.; Toby, B. H.; Lee, P. L.; Ribaud, L.; Antao, S. M.; Kurtz, C.; Ramanathan, M.; Von Dreele, R. B.; Beno, M. A. A Dedicated Powder Diffraction Beamline at the Advanced Photon Source: Commissioning and Early Operational Results. *Review of Scientific Instruments* **2008**, *79*, 085105.

(176) Ravel, B.; Newville, M. *ATHENA* , *ARTEMIS* , *HEPHAESTUS* : Data Analysis for X-ray Absorption Spectroscopy Using *IFEFFIT*. *J Synchrotron Rad* **2005**, *12*, 537–541.

(177) Nagarajan, S.; Hwang, S.; Balasubramanian, M.; Thangavel, N. K.; Arava, L. M. R. Mixed Cationic and Anionic Redox in Ni and Co Free Chalcogen-Based Cathode Chemistry for Li-Ion Batteries. *J. Am. Chem. Soc.* **2021**, 15732–15744.

(178) Kim, S. S.; Agyeman-Budu, D. N.; Zak, J. J.; Dawson, A.; Yan, Q.; Cában-Acevedo, M.; Wiaderek, K. M.; Yakovenko, A. A.; Yao, Y.; Irshad, A.; Narayan, S. R.; Luo, J.; Nelson Weker, J.; Tolbert, S. H.; See, K. A. Promoting Reversibility of Multielectron Redox in Alkali-Rich Sulfide Cathodes through Cryomilling. *Chem. Mater.* **2022**, *34*, 3236–3245.

(179) Yan, J.; Huang, H.; Zhang, J.; Liu, Z.; Yang, Y. A study of novel anode material CoS_2 for lithium ion battery. *Journal of Power Sources* **2005**, *146*, 264–269.

(180) Pei, A.; Zheng, G.; Shi, F.; Li, Y.; Cui, Y. Nucleation - Yi Cui. Nanoscale Nucleation and Growth of Electrodeposited Lithium Metal. *Nano Lett.* **2017**, *17*, 1132–1139.

(181) Mohammadi, A.; Monconduit, L.; Stievano, L.; Younesi, R. Measuring the Nucleation Overpotential in Lithium Metal Batteries: Never Forget the Counter Electrode! *J. Electrochem. Soc.* **2022**, *169*, 070509.

(182) Butala, M. M.; Doan-Nguyen, V. V. T.; Lehner, A. J.; Göbel, C.; Lumley, M. A.; Arnon, S.; Wiaderek, K. M.; Borkiewicz, O. J.; Chapman, K. W.; Chupas, P. J.; Balasubramanian, M.; Seshadri, R. Operando Studies Reveal Structural Evolution with Electrochemical Cycling in Li–CoS_2. *J. Phys. Chem. C* **2018**, *122*, 24559–24569.

(183) Bouwens, S. M. A. M.; Koningsberger, D. C.; de Beer, V. H. J.; Prins, R. The Structure of the Cobalt Sulfide Phase in Carbon-Supported Co and Co-Mo Sulfide Catalysts as Studied by Exafs and Xanes. *Catal Lett* **1988**, *1*, 55–59.

(184) Shulman, G. R.; Yafet, Y.; Eisenberger, P.; Blumberg, W. E. Observations and Interpretation of X-Ray Absorption Edges in Iron Compounds and Proteins. *Proc. Natl. Acad. Sci. U.S.A.* **1976**, *73*, 1384–1388.

(185) Dey, A.; Jiang, Y.; Ortiz de Montellano, P.; Hodgson, K. O.; Hedman, B.; Solomon, E. I. S K-edge XAS and DFT Calculations on Cytochrome P450: Covalent and Ionic Contributions to the Cysteine-Fe Bond and Their Contribution to Reactivity. *J. Am. Chem. Soc.* **2009**, *131*, 7869–7878.

(186) Soldatov, A. V.; Kravtsova, A. N.; Fleet, M. E.; Harmer, S. L. Electronic structure of MeS (Me = Ni, Co, Fe): X-ray absorption analysis. *J. Phys.: Condens. Matter* **2004**, *16*, 7545–7556.

(187) Farrell, S. P. Sulfur K-edge XANES study of local electronic structure in ternary monosulfide solid solution [(Fe, Co, Ni)$_{0.923}$S]. *Phys. Chem. Minerals* **2000**, *28*, 17–27.

(188) Farrell, S. P. XAS S - CoS.

(189) Guo, Q.; Lau, K. C.; Pandey, R. A XANES study of lithium polysulfide solids: a first-principles study. *Mater. Adv.* **2021**, *2*, 6403–6410.

(190) Cuisinier, M.; Cabelguen, P.-E.; Evers, S.; He, G.; Kolbeck, M.; Garsuch, A.; Bolin, T.; Balasubramanian, M.; Nazar, L. F. XAS S - Li-S Operando by Linda Nazar. *J. Phys. Chem. Lett.* **2013**, *4*, 3227–3232.

(191) Patel, M. U. M.; Arčon, I.; Aquilanti, G.; Stievano, L.; Mali, G.; Dominko, R. XAS S - in Li-S Battery S and LixSy. *ChemPhysChem* **2014**, *15*, 894–904.

(192) Mosselmans, J. F. W.; Pattrick, R. A. D.; van der Laan, G.; Charnock, J. M.; Vaughan, D. J.; Henderson, C. M. B.; Garner, C. D. X-Ray Absorption near-Edge Spectra of Transition Metal Disulfides FeS2 (Pyrite and Marcasite), CoS_2, NiS_2 and CuS_2, and Their Isomorphs FeAsS and CoAsS. *Phys Chem Minerals* **1995**, *22*, 311–317.

(193) Li, J.; He, K.; Meng, Q.; Li, X.; Zhu, Y.; Hwang, S.; Sun, K.; Gan, H.; Zhu, Y.; Mo, Y.; Stach, E. A.; Su, D. Spinel - Co_3O_4 Intercalation and Conversion. *ACS Nano* **2016**, *10*, 9577–9585.

(194) Li, H.; Yang, H.; Sun, Z.; Shi, Y.; Cheng, H.-M.; Li, F. A Highly Reversible Co_3S_4 Microsphere Cathode Material for Aluminum-Ion Batteries. *Nano Energy* **2019**, *56*, 100–108.

(195) Cai, X.; Yu, L.; Dong, J.; Cen, Y.; Zhu, T.; Yu, D.; Chen, C.; Zhang, D.; Liu, Y.; Pan, F. Revealing the Electrochemical Mechanism of the Conversion-Type Co_3S_4 in a Novel High-Capacity Mg-Li Hybrid Battery. *Electrochimica Acta* **2022**, *401*, 139403.

(196) Mahmood, N.; Zhang, C.; Jiang, J.; Liu, F.; Hou, Y. Multifunctional Co $_3$ S $_4$ /Graphene Composites for Lithium Ion Batteries and Oxygen Reduction Reaction. *Chem. Eur. J.* **2013**, *19*, 5183–5190.

(197) Shi, J.; Liu, G.; Weng, W.; Cai, L.; Zhang, Q.; Wu, J.; Xu, X.; Yao, X. Co $_3$ S $_4$ @Li $_7$ P $_3$ S $_{11}$ Hexagonal Platelets as Cathodes with Superior Interfacial Contact for All-Solid-State Lithium Batteries. *ACS Appl. Mater. Interfaces* **2020**, *12*, 14079–14086.

(198) Bonnick, P.; Sun, X.; Lau, K.-C.; Liao, C.; Nazar, L. F. Monovalent versus Divalent Cation Diffusion in Thiospinel Ti $_2$ S $_4$. *J. Phys. Chem. Lett.* **2017**, *8*, 2253–2257.

(199) James, A.; Goodenough, J. Lithium Ion Diffusion in the Defect Thiospinel $Li_xCu_{0.07}Ti_2S_4$. *Solid State Ionics* **1988**, *27*, 37–43.

(200) Sinha, S.; Murphy, D. Lithium Intercalation in Cubic TiS_2. *Solid State Ionics* **1986**, *20*, 81–84.

(201) Assat, G.; Tarascon, J.-M. Fundamental Understanding and Practical Challenges of Anionic Redox Activity in Li-Ion Batteries. *Nat Energy* **2018**, *3*, 373–386.

(202) Zhang, M.; Kitchaev, D. A.; Lebens-Higgins, Z.; Vinckeviciute, J.; Zuba, M.; Reeves, P. J.; Grey, C. P.; Whittingham, M. S.; Piper, L. F. J.; Van der Ven, A.; Meng, Y. S. Pushing the Limit of 3d Transition Metal-Based Layered Oxides That Use Both Cation and Anion Redox for Energy Storage. *Nat. Rev. Mater.* **2022**, *7*, 522–540.

(203) Sudayama, T.; Uehara, K.; Mukai, T.; Asakura, D.; Shi, X.-M.; Tsuchimoto, A.; Mortemard de Boisse, B.; Shimada, T.; Watanabe, E.; Harada, Y.; Nakayama, M.; Okubo, M.; Yamada, A. Multiorbital Bond Formation for Stable Oxygen-Redox Reaction in Battery Electrodes. *Energy Environ. Sci.* **2020**, *13*, 1492–1500.

(204) Radin, M. D.; Vinckeviciute, J.; Seshadri, R.; Van der Ven, A. Manganese Oxidation as the Origin of the Anomalous Capacity of Mn-Containing Li-Excess Cathode Materials. *Nat Energy* **2019**, *4*, 639–646.

(205) Vinckeviciute, J.; Kitchaev, D. A.; Van der Ven, A. A Two-Step Oxidation Mechanism Controlled by Mn Migration Explains the First-Cycle Activation Behavior of Li_2MnO_3-Based Li-Excess Materials. *Chem. Mater.* **2021**, *33*, 1625–1636.

(206) Sathiya, M.; Rousse, G.; Ramesha, K.; Laisa, C. P.; Vezin, H.; Sougrati, M. T.; Doublet, M.-L.; Foix, D.; Gonbeau, D.; Walker, W.; Prakash, A. S.; Ben Hassine, M.; Dupont, L.; Tarascon, J.-M. Reversible Anionic Redox Chemistry in High-Capacity Layered-Oxide Electrodes. *Nature Mater* **2013**, *12*, 827–835.

(207) Li, X.; Qiao, Y.; Guo, S.; Xu, Z.; Zhu, H.; Zhang, X.; Yuan, Y.; He, P.; Ishida, M.; Zhou, H. Direct Visualization of the Reversible O^{2}/O Redox Process in Li-Rich Cathode Materials. *Adv. Mater.* **2018**, *30*, 1705197.

(208) McCalla, E.; Abakumov, A. M.; Saubanère, M.; Foix, D.; Berg, E. J.; Rousse, G.; Doublet, M.-L.; Gonbeau, D.; Novák, P.; Van Tendeloo, G.; Dominko, R.; Tarascon, J.-M. Visualization of O-O Peroxo-like Dimers in High-Capacity Layered Oxides for Li-ion Batteries. *Science* **2015**, *350*, 1516–1521.

(209) House, R. A.; Rees, G. J.; Pérez-Osorio, M. A.; Marie, J.-J.; Boivin, E.; Robertson, A. W.; Nag, A.; Garcia-Fernandez, M.; Zhou, K.-J.; Bruce, P. G. First-Cycle Voltage Hysteresis in Li-rich 3d Cathodes Associated with Molecular O2 Trapped in the Bulk. *Nat Energy* **2020**, *5*, 777–785.

(210) Kaufman, L. A.; McCloskey, B. D. Surface Lithium Carbonate Influences Electrolyte Degradation via Reactive Oxygen Attack in Lithium-Excess Cathode Materials. *Chem. Mater.* **2021**, *33*, 4170–4176.

(211) Renfrew, S. E.; McCloskey, B. D. Quantification of Surface Oxygen Depletion and Solid Carbonate Evolution on the First Cycle of $LiNi_{0.6}Mn_{0.2}Co_{0.2}O_2$ Electrodes. *ACS Appl. Energy Mater.* **2019**, *2*, 3762–3772.

(212) Hu, E.; Yu, X.; Lin, R.; Bi, X.; Lu, J.; Bak, S.; Nam, K.-W.; Xin, H. L.; Jaye, C.; Fischer, D. A.; Amine, K.; Yang, X.-Q. Evolution of Redox Couples in Li- and Mn-Rich Cathode Materials and Mitigation of Voltage Fade by Reducing Oxygen Release. *Nat. Energy* **2018**, 1.

(213) Rana, J.; Papp, J. K.; Lebens-Higgins, Z.; Zuba, M.; Kaufman, L. A.; Goel, A.; Schmuch, R.; Winter, M.; Whittingham, M. S.; Yang, W.; McCloskey, B. D.; Piper, L. F. J. Quantifying the Capacity Contributions during Activation of Li_2MnO_3. *ACS Energy Lett.* **2020**, *5*, 634–641.

(214) Hong, J. et al. Metal–Oxygen Decoordination Stabilizes Anion Redox in Li-rich Oxides. *Nature Mater.* **2019**, *18*, 256–265.

(215) Murphy, D. W.; Trumbore, F. A. The Chemistry of TiS_3 and $NbSe_3$ Cathodes. *J. Electrochem. Soc.* **1976**, *123*, 960–964.

(216) Rouxel, J. Anion–Cation Redox Competition and the Formation of New Compounds in Highly Covalent Systems. *Chem. Eur. J.* **1996**, *2*, 1053–1059.

(217) Whittingham, M. Chemistry of Intercalation Compounds: Metal Guests in Chalcogenide Hosts. *Progress in Solid State Chemistry* **1978**, *12*, 41–99.

(218) Sakuda, A.; Takeuchi, T.; Okamura, K.; Kobayashi, H.; Sakaebe, H.; Tatsumi, K.; Ogumi, Z. Rock-Salt-Type Lithium Metal Sulphides as Novel Positive-Electrode Materials. *Scientific Reports* **2014**, *4*, 4883.

(219) Leube, B. T.; Robert, C.; Foix, D.; Porcheron, B.; Dedryvère, R.; Rousse, G.; Salager, E.; Cabelguen, P.-E.; Abakumov, A. M.; Vezin, H.; Doublet, M.-L.; Tarascon, J.-M. Activation of Anionic Redox in D0 Transition Metal Chalcogenides by Anion Doping. *Nat Commun* **2021**, *12*, 5485.

(220) Leube, B. T.; Salager, E.; Chesneau, E.; Rousse, G.; Vezin, H.; Abakumov, A. M.; Tarascon, J.-M. Layered Sodium Titanium Trichalcogenide Na_2TiCh_3 Framework (Ch = S, Se): A Rich Crystal and Electrochemical Chemistry. *Chem. Mater.* **2022**, *34*, 2382–2392.

(221) Sun, X.; Bonnick, P.; Nazar, L. F. Layered TiS_2 Positive Electrode for Mg Batteries. *ACS Energy Lett.* **2016**, *1*, 297–301.

(222) Klinger, M. More Features, More Tools, More *CrysTBox*. *J. Appl. Crystallogr.* **2017**, *50*, 1226–1234.

(223) Llovet, X.; Moy, A.; Pinard, P. T.; Fournelle, J. H. Electron Probe Microanalysis: A Review of Recent Developments and Applications in Materials Science and Engineering. *Progress in Materials Science* **2021**, *116*, 100673.

(224) Lavrent'ev, Y. G.; Karmanov, N. S.; Usova, L. V. Electron Probe Microanalysis of Minerals: Microanalyzer or Scanning Electron Microscope? *Russian Geology and Geophysics* **2015**, 1154–1161.

(225) Baklanova, Y. V.; Arapova, I. Y.; Shein, I. R.; Maksimova, L. G.; Mikhalev, K. N.; Denisova, T. A. 2021/03/05 Charge Distribution and Mobility of Lithium Ions in Li2TiO3 from 6,7Li NMR Data. *J Struct Chem* **2013**, *54*, 111–118.

(226) Vijayakumar, M.; Kerisit, S.; Yang, Z.; Graff, G. L.; Liu, J.; Sears, J. A.; Burton, S. D.; Rosso, K. M.; Hu, J. Combined ^{6,7} Li NMR and Molecular Dynamics Study of Li Diffusion in Li $_2$ TiO $_3$. *J. Phys. Chem. C* **2009**, *113*, 20108–20116.

(227) Li, L.; Qin, Z.; Ries, L.; Hong, S.; Michel, T.; Yang, J.; Salameh, C.; Bechelany, M.; Miele, P.; Kaplan, D.; Chhowalla, M.; Voiry, D. Role of Sulfur Vacancies and Undercoordinated Mo Regions in MoS $_2$ Nanosheets toward the Evolution of Hydrogen. *ACS Nano* **2019**, *13*, 6824–6834.

(228) Carter, E.; Carley, A. F.; Murphy, D. M. Evidence for O $_2$ $^-$ Radical Stabilization at Surface Oxygen Vacancies on Polycrystalline TiO $_2$. *J. Phys. Chem. C* **2007**, *111*, 10630–10638.

(229) Nakamura, I.; Negishi, N.; Kutsuna, S.; Ihara, T.; Sugihara, S.; Takeuchi, K. Role of Oxygen Vacancy in the Plasma-Treated TiO_2 Photocatalyst with Visible Light Activity for NO Removal. *Journal of Molecular Catalysis A: Chemical* **2000**, *161*, 205–212.

(230) Martinolich, A. J.; Zak, J. J.; Agyeman-Budu, D. N.; Kim, S. S.; Bashian, N. H.; Irshad, A.; Narayan, S. R.; Melot, B. C.; Nelson Weker, J.; See, K. A. Controlling Covalency and Anion Redox Potentials through Anion Substitution in Li-Rich Chalcogenides. *Chem. Mater.* **2021**, *33*, 378–391.

(231) Wu, Z. Y.; Ouvrard, G.; Moreau, P.; Natoli, C. R. Interpretation of Preedge Features in the Ti and S K-edge x-Ray-Absorption near-Edge Spectrain the Layered Disulfides TiS 2 and TaS 2. *Phys. Rev. B* **1997**, *55*, 9508–9513.

(232) Zhang, L.; Sun, D.; Kang, J.; Wang, H.-T.; Hsieh, S.-H.; Pong, W.-F.; Bechtel, H. A.; Feng, J.; Wang, L.-W.; Cairns, E. J.; Guo, J. Tracking the Chemical and Structural Evolution of the TiS $_2$ Electrode in the Lithium-Ion Cell Using Operando X-ray Absorption Spectroscopy. *Nano Lett.* **2018**, *18*, 4506–4515.

(233) Parratt, L. G. Effects of Chemical Binding on the X-Ray K_α Doublet Lines of Sulphur Studied with a Two-Crystal Spectrometer. *Phys. Rev.* **1936**, *49*, 14–16.

(234) Holden, W. M.; Jahrman, E. P.; Govind, N.; Seidler, G. T. Probing Sulfur Chemical and Electronic Structure with Experimental Observation and Quantitative Theoretical Prediction of K and Valence-to-Core K X-ray Emission Spectroscopy. *J. Phys. Chem. A* **2020**, *124*, 5415–5434.

(235) Alonso Mori, R.; Paris, E.; Giuli, G.; Eeckhout, S. G.; Kavčič, M.; Žitnik, M.; Bučar, K.; Pettersson, L. G. M.; Glatzel, P. Electronic Structure of Sulfur Studied by X-ray Absorption and Emission Spectroscopy. *Anal. Chem.* **2009**, *81*, 6516–6525.

(236) Petric, M.; Rajh, A.; Vizintin, A.; Talian, S. D.; Dominko, R.; Kavčič, M. Sulfur Valence-to-Core X-ray Emission Spectroscopy Study of Lithium Sulfur Batteries. *Chem. Commun.* **2021**, *57*, 7573–7576.

(237) Kavčič, M.; Petric, M.; Rajh, A.; Isaković, K.; Vizintin, A.; Talian, S. D.; Dominko, R. Characterization of Li–S Batteries Using Laboratory Sulfur X-ray Emission Spectroscopy. *ACS Appl. Energy Mater.* **2021**, *4*, 2357–2364.

(238) Ali, S. E.; Olszewski, W.; Marini, C.; Kazzazi, A.; Choi, H.; Kuenzel, M.; Bresser, D.; Passerini, S.; Tonti, D.; Simonelli, L. Quantification of Charge Compensation in Lithium- and Manganese-Rich Li-ion Cathode Materials by x-Ray Spectroscopies. *Materials Today Physics* **2022**, *24*, 100687.

(239) Sakuda, A. A Reversible Rocksalt to Amorphous Phase Transition Involving Anion Redox. *Scientific Reports* **2018**, *8*, 15086.

(240) Wang, T.; Ren, G.-X.; Shadike, Z.; Yue, J.-L.; Cao, M.-H.; Zhang, J.-N.; Chen, M.-W.; Yang, X.-Q.; Bak, S.-M.; Northrup, P.; Liu, P.; Liu, X.-S.; Fu, Z.-W. Anionic Redox Reaction in Layered NaCr2/3Ti1/3S2 through Electron Holes Formation and Dimerization of S–S. *Nat Commun* **2019**, *10*, 4458.

(241) Chen, T.; Jin, Y.; Lv, H.; Yang, A.; Liu, M.; Chen, B.; Xie, Y.; Chen, Q. Applications of Lithium-Ion Batteries in Grid-Scale Energy Storage Systems. *Trans. Tianjin Univ.* **2020**, *26*, 208–217.

(242) Seo, D.-H.; Lee, J.; Urban, A.; Malik, R.; Kang, S.; Ceder, G. The Structural and Chemical Origin of the Oxygen Redox Activity in Layered and Cation-Disordered Li-excess Cathode Materials. *Nature Chem* **2016**, *8*, 692–697.

(243) Strehle, B.; Kleiner, K.; Jung, R.; Chesneau, F.; Mendez, M.; Gasteiger, H. A.; Piana, M. The Role of Oxygen Release from Li- and Mn-Rich Layered Oxides during the First Cycles Investigated by On-Line Electrochemical Mass Spectrometry. *J. Electrochem. Soc.* **2017**, *164*, A400–A406.

(244) Luo, K.; Roberts, M. R.; Hao, R.; Guerrini, N.; Pickup, D. M.; Liu, Y.-S.; Edström, K.; Guo, J.; Chadwick, A. V.; Duda, L. C.; Bruce, P. G. Charge-Compensation in 3d-Transition-Metal-Oxide Intercalation Cathodes through the Generation of Localized Electron Holes on Oxygen. *Nature Chem* **2016**, *8*, 684–691.

(245) Van der Ven, A.; See, K. A.; Pilon, L. Hysteresis in electrochemical systems. *Battery Energy* **2022**, 20210017.

(246) House, R. A.; Marie, J.-J.; Park, J.; Rees, G. J.; Agrestini, S.; Nag, A.; Garcia-Fernandez, M.; Zhou, K.-J.; Bruce, P. G. House and Bruce - Covalency Does Not Suppress O2 Formation in 4d and 5d Li-rich O-redox Cathodes. *Nat Commun* **2021**, *12*, 2975.

(247) Baek, S. W.; Saber, M.; Van Der Ven, A.; Pilon, L. Thermodynamic Analysis and Interpretative Guide to Entropic Potential Measurements of Lithium-Ion Battery Electrodes. *J. Phys. Chem. C* **2022**, *126*, 6096–6110.

(248) Van Der Ven, A.; Aydinol, M. K.; Ceder, G.; Kresse, G.; Hafner, J. First-Principles Investigation of Phase Stability in $\mathrm{Li}_x\ \mathrm{CoO}_2$. *Phys. Rev. B* **1998**, *58*, 2975–2987.

(249) Reimers, J. N.; Dahn, J. R. Electrochemical and In Situ X-Ray Diffraction Studies of Lithium Intercalation in Li x CoO2. *J. Electrochem. Soc.* **1992**, *139*, 2091–2097.

(250) Dahn, J. R.; Haering, R. R. Entropy Measurements on $\mathrm{Li}_{\ x}\ \mathrm{TiS}_{\ 2}$. *Can. J. Phys.* **1983**, *61*, 1093–1098.

(251) Van Der Ven, A.; Thomas, J. C.; Xu, Q.; Swoboda, B.; Morgan, D. Nondilute Diffusion from First Principles: Li Diffusion in Li x TiS 2. *Phys. Rev. B* **2008**, *78*, 104306.

(252) House, R. A.; Jin, L.; Maitra, U.; Tsuruta, K.; Somerville, J. W.; Förstermann, D. P.; Massel, F.; Duda, L.; Roberts, M. R.; Bruce, P. G. Lithium Manganese Oxyfluoride as a New Cathode Material Exhibiting Oxygen Redox. *Energy Environ. Sci.* **2018**, *11*, 926–932.

(253) House, R. A.; Marie, J.-J.; Pérez-Osorio, M. A.; Rees, G. J.; Boivin, E.; Bruce, P. G. Review: The Role of O_2 in O-redox Cathodes for Li-ion Batteries. *Nat Energy* **2021**, *6*, 781–789.

(254) Singer, A. et al. Nucleation of Dislocations and Their Dynamics in Layered Oxide Cathode Materials during Battery Charging. *Nat Energy* **2018**, *3*, 641–647.

(255) Qiu, B.; Zhang, M.; Lee, S.-Y.; Liu, H.; Wynn, T. A.; Wu, L.; Zhu, Y.; Wen, W.; Brown, C. M.; Zhou, D.; Liu, Z.; Meng, Y. S. Metastability and Reversibility of Anionic Redox-Based Cathode for High-Energy Rechargeable Batteries. *Cell Reports Physical Science* **2020**, *1*, 100028.

(256) Shinoda, M.; Rajendra, H. B.; Yabuuchi, N. Rocksalt and Layered Metal Sulfides for Li Storage Applications: $\mathrm{LiMe}_{0.5}\mathrm{Ti}_{0.5}\mathrm{S}_2$ (Me = Fe^{2+}, Mn^{2+}, and Mg^{2+}). *ACS Appl. Energy Mater.* **2022**, *5*, 2642–2646.

(257) Sakuda, A.; Ohara, K.; Kawaguchi, T.; Fukuda, K.; Nakanishi, K.; Arai, H.; Uchimoto, Y.; Ohta, T.; Matsubara, E.; Ogumi, Z.; Kuratani, K.; Kobayashi, H.; Shikano, M.; Takeuchi, T.; Sakaebe, H. A Reversible Rocksalt to Amorphous Phase Transition Involving Anion Redox. *Sci Rep* **2018**, *8*, 15086.